Charles University in Prague

Faculty of Mathematics and Physics

DOCTORAL THESIS

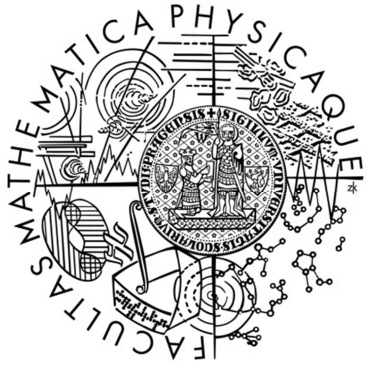

Hana Karousová

Teleseismic Tomography of the Upper Mantle beneath the Bohemian Massif

Department of Geophysics

Supervisor: RNDr. Jaroslava Plomerová, DrSc.
Consultant: RNDr. Vladislav Babuška, DrSc.

Study programme: Physics
Specialization: Geophysics

Prague 2013

.

I declare that I carried out this doctoral thesis independently, and only with the cited sources, literature and other professional sources.

I understand that my work relates to the rights and obligations under the Act No. 121/2000 Coll., the Copyright Act, as amended, in particular the fact that the Charles University in Prague has the right to conclude a license agreement on the use of this work as a school work pursuant to Section 60 paragraph 1 of the Copyright Act.

In Prague date: ..... signature

Název práce	Teleseismická tomografie svrchního pláště pod Českým masívem (střední Evropa)
Autor	Hana Karousová
Katedra	Katedra geofyziky, Matematicko-fyzikální fakulta
Univerzita	Karlova Univerzita v Praze
Vedoucí doktorské práce	RNDr. Jaroslava Plomerová, DrSc., Geofyzikální Ústav, Akademie Věd České Republiky (AV ČR)
Konzultant	RNDr. Vladislav Babuška, DrSc., Geofyzikální Ústav, AV ČR
Školící pracoviště	Geofyzikální Ústav, AV ČR
Klíčová slova	seismická tomografie, struktura svrchního pláště, Český masív, rychlostní model kůry

Abstrakt

Na území Českého masívu (ČM) se uskutečnilo několik pasivních seismických experimentů, např. MOSAIC, BOHEMA I-III, EgerRift nebo PASSEQ, na základě jejichž dat můžeme podrobněji studovat stavbu svrchního pláště. Předmětem této práce jsou nové tomografické modely svrchního pláště zaměřené na severo-východní a jižní části ČM, které byly získány z dat experimentů BOHEMA II a BOHEMA III (2004-2006). Přestože oblasti s nejvyšším rozlišením se v obou modelech liší, rychlostní odchylky v překrývajících se částech modelů jsou podobné. Ukazuje se, že ve svrchním plášti pod ČM převládají nízké rychlosti vůči radiálně symetrickému modelu Země. Malá vysokorychlostní heterogenita táhnoucí se v SV-JZ směru pod moldanubickou jednotkou může být odrazem ztluštění litosféry v důsledku variské kolize ČM a brunovistulické jednotky. V nejjižnější části tomografického modelu založeného na datech z experimentu BOHEMA III se vymezuje výrazná vysokorychlostní heterogenita, kterou lze interpretovat jako litosféru subdukovanou v oblasti východních Alp.

Tomografické testy ukázaly, že vliv nekorigovaných rychlostních heterogenit v kůře se může projevit až do hloubek kolem 100 km a vést k chybné interpretaci rychlostních odchylek ve svrchním plášti. Pro korekci časů šíření teleseismických vln na vliv kůry jsme vytvořili trojrozměrný rychlostní model kůry ČM z profilových modelů refrakční a reflexní seismiky a výsledků lokální seismické tomografie.

Title	Teleseismic Tomography of the Upper Mantle beneath the Bohemian Massif (central Europe)
Author	Mgr. Hana Karousová
Department	Department of Geophysics, Faculty of Mathematics and Physics
University	Charles University in Prague
Supervisor of the doctoral thesis	RNDr. Jaroslava Plomerová, DrSc., Institute of Geophysics, Academy of Sciences, Czech Republic (AS CR)
Consultant:	RNDr. Vladislav Babuška, DrSc., Institute of Geophysics, AS CR
Training Institution:	Institute of Geophysics, AS CR
Keywords	seismic tomography, structure of the upper mantle, Bohemian Massif, velocity model of the crust

Abstract

Passive seismic experiments, MOSAIC, BOHEMA I-III, EgerRift, or, PASSEQ, carried out in the region of the Bohemian Massif (BM), allowed a detailed study of velocity structure of the upper mantle. We present results of tomography studies of the upper mantle beneath the north-eastern and southern parts of the BM based on the data from the BOHEMA II and BOHEMA III experiments (2004-2006). Despite the fact that regions with the highest resolution of velocity perturbations differ in the models, tomography images are similar in overlapping parts. Models of the upper mantle show mostly low-velocity perturbations relatively to radially symmetric velocity model of the Earth beneath the BM. Limited high-velocity heterogeneity beneath the Moldanubian unit, extended in the NE-SW direction, reflects thickening of the lithosphere due to a collision of the BM with the Brunovistulian micro-plate during the Variscan orogeny. The tomography based on the data from the BOHEMA III experiment revealed significant high-velocity heterogeneity in the southern margin of the model with a subduction of the lithosphere beneath the Eastern Alps.

Tomographic tests showed that effects of uncorrected velocity heterogeneities within the crust can appear as deep as 100 km and, therefore, they could lead to erroneous interpretation of velocity perturbations in the upper mantle. A three-dimensional velocity model of the BM crust was created in order to take into account effects of the crust when calculating teleseismic travel-time residuals. The model is based on crustal velocity models derived from refraction and reflection measurements collected during deep seismic soundings and from a local seismic tomography.

Contents

PART I

1 Introduction

Seismic tomography (e.g., Nolet, 2008; Rawlinson et al., 2010) is a widely used technique for depicting velocity structures of the Earth. The origins of the tomography technique date back to the late 70's of the 20th century when Aki and Lee (1976) determined the three-dimensional (3D) velocity structure beneath California based on travel-time data from local earthquakes. A year later, Aki et al. (1977) developed the ACH method (Aki – Christoffersson - Husebye) with the aim to resolve velocity perturbations in the upper mantle. The perturbations were calculated from teleseismic travel times relatively to a one-dimensional (1D) reference velocity model of the Earth. This early method works with a model of blocks, each having constant velocity, and ray paths approximated by straight lines and turned out to be a starting point for all following teleseismic travel-time tomography studies (e.g., Babuška et al., 1984). Since then, major improvements of the teleseismic tomography method include refinements of model parameterization (e.g., Kissling et al., 2001; Nolet and Montelli, 2005), 3D ray tracing (e.g., Rawlinson and Sambridge, 2005), inversion algorithms, and resolution and error analyses (Evans and Achauer, 1993; Sandoval et al., 2003; Tromp et al., 2004; Roeker et al., submitted).

Regional teleseismic tomography provides the highest resolution in the upper mantle (e.g., Bijwaard et al., 1998; Poupinet et al., 2002; Sandoval et al., 2004; Di Stefano et al., 2009; Kissling et al., 2006; Handy et al., 2010). Among others, the technique enables the depiction of velocity structures typical for subducting of lithospheric plates (e.g., Widiyantoro and Van Der Hilst, 1997; Li and Van der Hilst, 2010; Pesicek et al., 2010), uprising plumes (e.g., Ellsworth and Koyanagi, 1977; Granet et al., 1995; Tilmann, 1999; Nataf, 2000; Ritter et al., 2001; Pilidou et al., 2005; Zhao, 2007; Lei et al., 2009) and significant changes in the thickness of the lithosphere (Achauer et al., 2002; Levin et al, 2002; Arrowsmith et al., 2005; Wortel et al., 2009; Mercier et al., 2010).

Our motivation is to create a velocity model of the upper mantle beneath the Bohemian Massif (BM, e.g., Plomerová et al., 2003; 2005), particularly its lithospheric part, with the aim to enhance the understanding of the evolution of the region. However, the network of permanent observatories is too sparse to efficiently conduct a detailed tomographic investigation of the upper mantle. Therefore, several passive experiments were carried out, during which the network of permanent stations was complemented with temporary arrays of stations. During the first of these experiments in 1992, four stations were installed in the western part of the BM as an elongation of the GRF (Gräfenberg) array (Plomerová and

Babuška, 1998). In the MOSAIC project (Plomerová et al., 2005), the Czech Regional Seismic Network was complemented by eight temporary broadband stations in a joint operation carried out by Prague and Strasbourg geophysical institutions with the aim of detecting general features of the uppermost mantle of the BM.

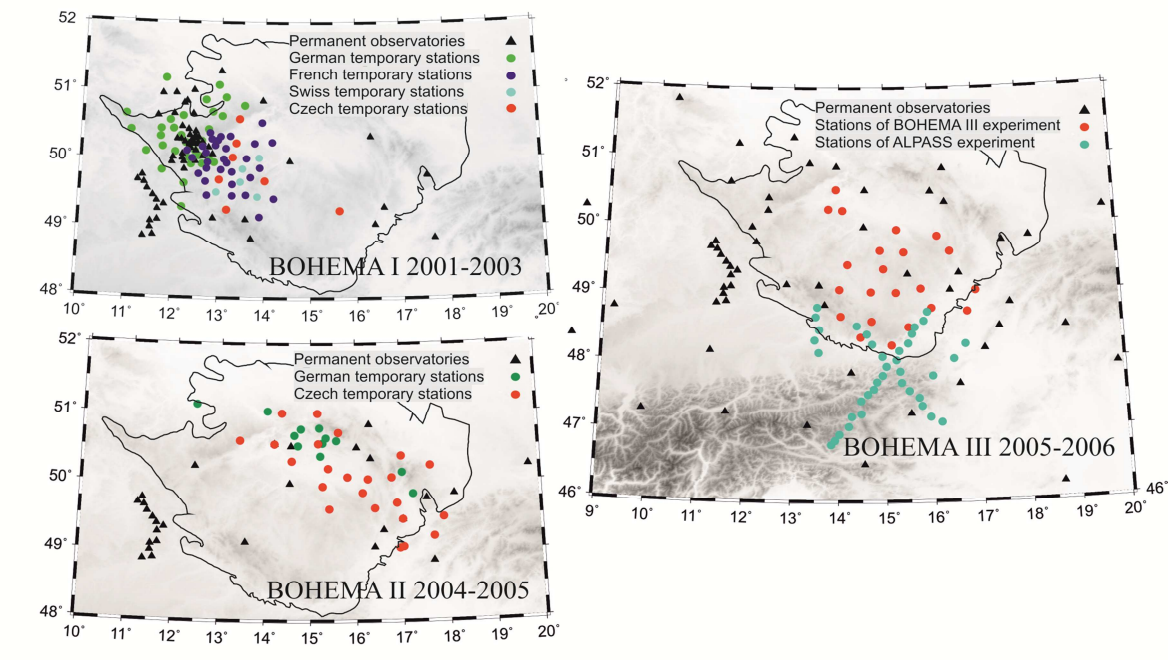

Figure 1.1 Seismic stations of passive seismic BOHEMA I, BOHEMA II, BOHEMA III experiments shown in topography maps. The region of the Bohemian Massif is indicated by black contour.

This pilot project was followed by a series of three international passive seismic experiments BOHEMA I-III (Bohemian Massif Heterogeneity and Anisotropy; Fig. 1.1; Babuška and Plomerová, 2003; Plomerová et al., 2003) which covered consequently the BM with three arrays of seismic stations. During BOHEMA I, 92 Czech, German, French and Swiss temporary stations were deployed in the western part of the BM (Plomerová et al., 2007). The seismic array, with station spacing of 10-15 km in the central part, was designed to reveal a possible mantle plume beneath the Eger Rift (ER). The plume was anticipated based on analogy between the ER and rifts in the French Massif Central and the Eifel region in Germany where narrow sub-vertical low-velocity anomalies interpreted as plumes have been detected (Granet et al., 1995; Ritter et al., 2001). Results of teleseismic travel-time tomography based on the data from BOHEMA I did not show any narrow plume-like anomaly, but depicted a broad low-velocity region beneath the ER, which was

interpreted as upwelling of the lithosphere-asthenosphere boundary (Plomerová et al., 2007; 1998).

The following stages of the investigation of the BM lithosphere, namely the BOHEMA II and BOHEMA III experiments, with average station spacing around 30-40 km covered the north-eastern and southern parts of the BM, respectively (Fig. 1.1., Babuška et al., 2005, Plomerová et al., 2013; Geissler et al., 2012; Karousová et al., 2012b; Babuška and Plomerová, 2013; Karousová et al., 2013). To enhance station coverage, the station arrays of these experiments were complemented by a number of German stations (Geissler et al., 2012) and by several stations from the ALPASS project (Mitterbauer et al., 2011).

Results of the two tomography studies of isotropic velocity structure beneath the BM are summarized in this thesis, consisting of two parts. The first part describes the tomography technique, shows data pre-processing and analyses of the inversion parameters (Chapters 2 and 3), provides general information about the tomographic code used (Chapter 4), shows summary of the main results, and indicates future perspectives (Chapter 5).

The second part comprises three published papers and a detailed User's Guide to the updated TELINV2012 tomography code. In the first paper (**P1** - Karousová et al. 2012a), the 3D velocity model of the crust of the BM and its effects on the tomographic images of the upper mantle are presented. The second (**P2** - Karousová et al. 2012b) and the third (**P3** - Karousová et al., 2013) papers focus on tomographic images of the upper mantle beneath the north-eastern part of the BM and beneath the southern part of the BM, based on data from the BOHEMA II and BOHEMA III experiments, respectively. The TELINV tomographic code was used for calculations (Chapter 4). We updated the code and complemented it with auxiliary FORTRAN, GMT and Matlab scripts, and with the User's Guide (**P4** - Karousová, 2013).

2 Theory

In this part, theory of seismic travel-time tomography based on approaches of Menke (1984), Evans and Achauer (1993) and Nolet (2008) is briefly described.

The travel time is a function of velocity distribution along a ray-path and it can be stated that

$$T = \int_L \frac{dl}{v} + \xi\,, \tag{2.1}$$

where T is the total travel time along ray path L, v is velocity and ξ is an error of travel-time measurement. The relation between travel time and velocity is non-linear. Moreover, the ray path depends on velocity as well. To linearize the integral in the equation (2.1), v_0 is defined as a reference velocity and Δv as velocity perturbation relative to the reference velocity. Assumably, velocity perturbations are relatively small in comparison with the reference velocities:

$$\Delta v \ll v_0. \tag{2.2}$$

According to Fermat's principle, the travel time of a ray must be stationary for small perturbations in the ray path (e.g., Nolet, 2008). It implies that changes of the ray path due to velocity perturbations, as well as those of the second order velocity perturbations, are negligible:

$$\Delta v^2 \sim 0 \text{ and } L \sim L_0, \tag{2.3}$$

where L_0 is a ray path corresponding to the reference velocity model. To utilise equation (2.3), we rewrite the integral in (2.1) in the following form

$$\begin{aligned} T &= \int_L \frac{dl}{v_0 + \Delta v} \cdot \frac{v_0 - \Delta v}{v_0 - \Delta v} + \xi \\ &= \int_L \frac{v_0 - \Delta v}{v_0^2 - \Delta v^2} dl + \xi\,. \end{aligned} \tag{2.4}$$

Then, we separate reference travel time T_0 , which is calculated according to the reference velocity model, and a travel-time residual ΔT , which is directly proportional to velocity perturbations relative to the reference model, and write

$$T = \int_{L_0} \frac{dl}{v_0} + \int_{L_0} \frac{-\Delta v}{v_0^2} dl + \xi = T_0 + \Delta T + \xi + \eta, \tag{2.5}$$

where η is an error of linearization approximation. Then the relation between travel-time residual and velocity perturbation is

$$\Delta T = \int_{L_0} \frac{-\Delta v}{v_0^2} dl + \xi + \eta. \qquad (2.6)$$

To solve equation (2.6) numerically, we have to discretize the velocity model. We divide the velocity model into a system of non-overlapping cells and approximate the integral by summation over these cells. The travel-time residual is then

$$\Delta T = \sum_{j=1}^{M} \frac{\Delta s_j}{v_{0j}^2} \cdot \left(-\Delta v_j\right) + e, \qquad (2.7)$$

where M is the number of cells, Δs_j is the ray length in the jth cell, v_{0j} is reference velocity in the jth cell of the model and e is an error, which contains errors of linearization and discretization and picking error. Based on equation (2.7), a set of travel-time residuals can be generalized to

$$d = Am + e\ , \qquad (2.8)$$

where d is a vector of travel-time residuals (data), A is a matrix relating the data to model parameters and m is a vector of searched velocity perturbations (model parameters). Velocity perturbations are searched with the use of the damped least-squares (DLSQ) method with data weighting and model smoothing. The solution for an over-determined case can be written to

$$m_{est} = (A^T W_d A + \varepsilon W_m)^{-1} A^T W_d d, \qquad (2.9)$$

where m_{est} is vector of estimated model parameters, W_d is a data weighting matrix, ε is the damping factor and W_m is a model smoothing matrix (Menke, 1984).

3 Data pre-processing and parameter analysis of teleseismic travel-time tomography

This chapter deals with procedural details of teleseismic tomography based on data from the BOHEMA III experiment not included in the **P3** paper - Karousová et al. (2013)**.** The target volume is the upper mantle beneath the BOHEMA III station array. Travel times of body waves from distant events are measured at the station array, the size of which is small in comparison with epicentral distances of the events used. The method cannot resolve velocities along the whole ray paths (Fig. 3.2). To fit the equation (2.9), travel-time deviations inverted for the velocity perturbations need to reflect velocity structure in the target volume. Therefore, effects generated outside the target volume must be taken into consideration. These effects are minimized by crustal corrections and by calculation of relative residuals (Chapters 3.1 and 3.2). Data quality is controlled with a-priori data analyses (Chapter 3.3). In Chapters 3.4-3.6, a guideline for the selection of the optimal model parameterization, inversion parameters, and reliability evaluation of the final velocity model are given. The ray-tracing technique, calculation of the matrix *A* in equation (2.8) and the inversion algorithm are explained in detail in the User's Guide to the TELINV2012 (**P4** - Karousová, 2013) and **P2** - Karousová et al. (2012b).

3.1 Crustal corrections

Removing the effects of crustal velocities from travel-time residuals is a crucial task, because the teleseismic tomography cannot reveal small-scale velocity perturbations in shallow depths (e.g., Arlitt et al., 1999; Waldhauser et al., 2002). Rays from distant events propagate in the crust along near-vertical paths and illuminate only volumes in narrow cones beneath stations where rays do not intersect. Moreover, teleseismic P waves on short-period recordings having typical wavelengths of around 8 km are not able to detect small-size heterogeneities, typical for the crustal structure.

In teleseismic regional studies, we find several approaches to minimizing effects of crustal structures (e.g., Granet et al., 1995). The first method applies static corrections which can be calculated as average delay times measured at each station. These static corrections represent travel-time variations due to velocities in the conical volume beneath each station. The static corrections can be a-priori applied to the travel times before inverting them or the static corrections can be resolved within the inversion for the velocity structure of the upper mantle (e.g., Dando et al., 2011). The drawback of static corrections

lies in the fact that they may absorb a part of travel-time variations associated with velocity perturbations in the upper mantle.

The second method inverts teleseismic travel-time residuals for the crustal structure (e.g., Granet et al., 1995, Weiland et al., 1995, Masson et al., 1998; Plomerová et al., 2007). This approach requires station spacing and model parameterization comparable to the size of crustal heterogeneities which is not usually the case in passive seismic experiments (e.g., Artlitt et al., 1999; Shomali et al., 2006; Benoit et al., 2011). On the other hand, this method decreases leakage of crustal velocity perturbations and effects of data errors into the upper mantle images.

And the third method corrects travel-time residuals on the basis of results of active and/or passive seismic studies of the crust, such as two-dimensional (2D) reflection and refraction surveys, local earthquake tomography, or receiver-function technique. One can consider crustal and sediment thicknesses and corresponding average velocities and correct thus for 1D crustal structure beneath each station. However, more accurate crustal corrections can be calculated based on a 3D crustal model (e.g., Lippitch et al., 2003; Shomali et al., 2006, Sandoval et al., 2004; 2004; Martin et al., 2005; Souriau et al., 2008). These crustal corrections depend strongly on resolutions of crustal models used. The errors due to inter-/extrapolation can be significant (**P1** – Karousová et al., 2012a).

The approaches to minimizing effects of crustal velocity structures can be also combined. For instance, Dando et al. (2011) as well as Mitterbauer et al. (2011) correct the travel-time residuals according to a 3D crustal model and then invert for static corrections. In tomographic studies of the BM upper mantle (**P2**– Karousová et al., 2012a; **P3** – Karousová et al., 2013), we also combine several methods. Corrections according to a 3D crustal model are applied, complemented with static corrections to compensate for sediments beneath stations not included in the 3D model and invert for crustal velocities. In this way, we make use of all available information about the crust as well as the inversion technique to deal with travel-time residuals.

3.2 Calculation of relative travel-time residuals

The travel times of teleseismic waves are also affected by velocity structure along the whole ray paths, i.e., outside the target volume, and by errors both in event locations and determination of origin times. Because the ray paths from distant events to stations of a relatively small-size array are similar, such effects can be reduced by calculating relative residuals (e.g., Achauer at el., 1986). Absolute travel time residuals at each station express absolute travel-time deviations relative to a 1D reference velocity Earth's model. Relative travel-time residuals are those from which a representative event mean is subtracted. This method is called travel-time normalization and is described in detail e.g., in Babuška and Plomerová (1992) or in Evans and Achauer (1993).

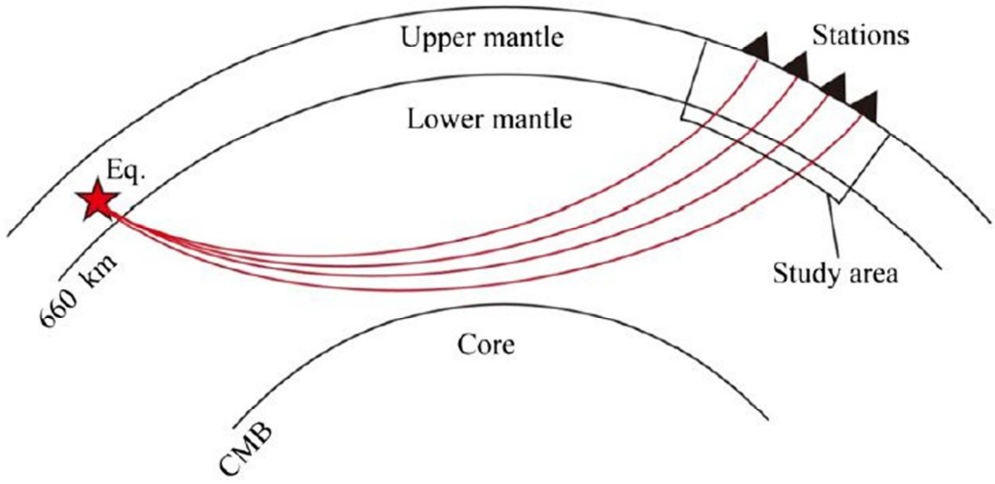

Figure 3.1 Ray paths from a distant event (star) to individual stations (triangles) above the upper mantle studied (contoured), redrawn from Zhao et al. (2013).

3.3 Tests of mislocation/origin-time errors and their effects on imaging the upper mantle heterogeneities

To show the importance of the normalization, we tested results of several inversions with synthetic travel times distorted by systematic time shifts mimicking event mislocation or origin-time errors. After that we performed the same synthetic test without these additional errors for comparison. Both calculations were performed with identical inversion parameters (Table 3.1).

We inserted two anomalies (-3% and +5%, Fig. 3.2) into a reference IASP91 velocity model (Kennett, 1995). To retrieve the synthetic travel time residuals (for details see **P4** - Karousová, 2013), we performed modelling using the Simplex 3D ray-tracing technique (Steck and Prothero, 1991). First, we calculated the "observed" travel times according to the velocity model with the synthetic anomalies. After that, we calculated theoretical travel times according to the reference IASP91 velocity model. Then, we added systematic time shifts of 2 s, 4 s, 6 s and 8 s to the "observed" travel times corresponding to four selected events.

Table 3.1 Inversion parameters for tests of mislocation/origin-time error effects

Number of station	140
Number of events	169
Number of rays	13 541
Number of inverted parameters	3 800
Horizontal node spacing [km]	40
Vertical node spacing [km]	45
Damping factor	100
Number of iterations	2
Variance of synthetic data with additional time shifts	0.059 s^2
Variance of synthetic data without additional time shifts	0.019 s^2

Results of the first test, with variance reduction of 88%, show significant artefacts due to the inserted event mislocation/origin-time errors (Fig. 3.3). Although both velocity anomalies are well-resolved in the horizontal dimension, the amplitude of the low-velocity anomaly is comparable with amplitudes of velocity perturbation noise. All velocity perturbations at depths of 80 km, 260 km, and 305 km are artefacts having the largest amplitudes in regions with a low resolution, particularly at margins of the model.

In the second synthetic test, we tried to retrieve the inserted velocity anomalies (Fig. 3.2) from synthetic "observed" travel times without any additional noise. The recovered velocity perturbations (Fig. 3.4) show good horizontal resolution and minor vertical smearing to neighbouring depth slices. We observed a slight decrease of the amplitudes of both anomalies and also over-swinging effects around the inserted synthetic anomalies. The over-swinging effect is indicated by perturbations of opposite sign compared to the real (inserted) heterogeneity. The data variance reduction of the first synthetic test attains 89% after the 2nd iteration. From comparison of Figures 3.3 and 3.4, it can be concluded that the artefacts resulting from mislocation and origin-time errors can complicate the

interpretation of upper mantle heterogeneities. The results of the test also show that the travel-time normalization removes most of these artefacts.

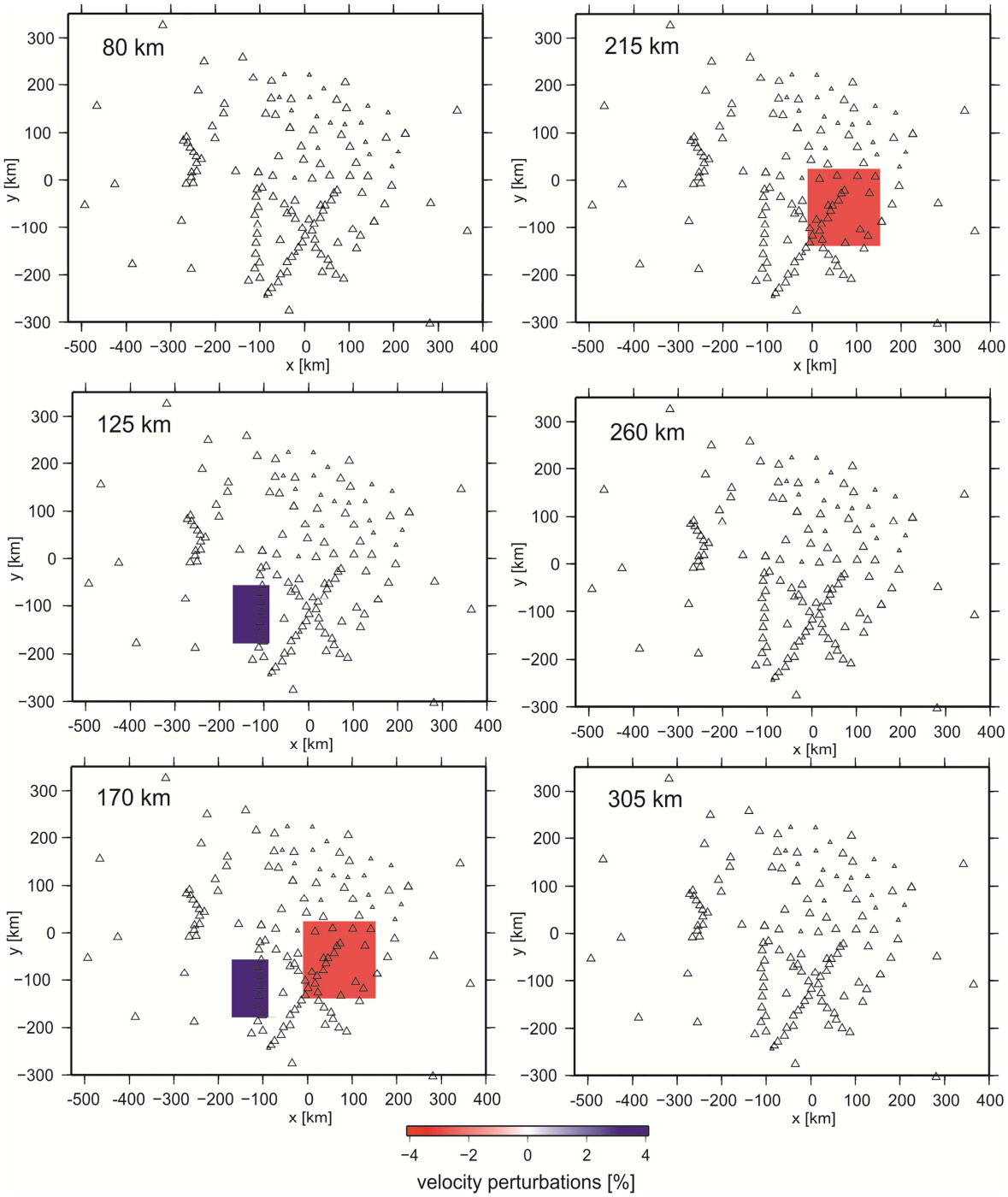

Figure 3.2 The input synthetic model with -3% (red) and +5% (blue) velocity anomalies relative to the 1D reference Earth IASP91 velocity model for eight horizontal depth slices of the upper mantle model. The depths are indicated in the upper left corner of each slice. Locations of stations are marked with triangles. Stations with less than 20 P-waveforms used are indicated with small triangles.

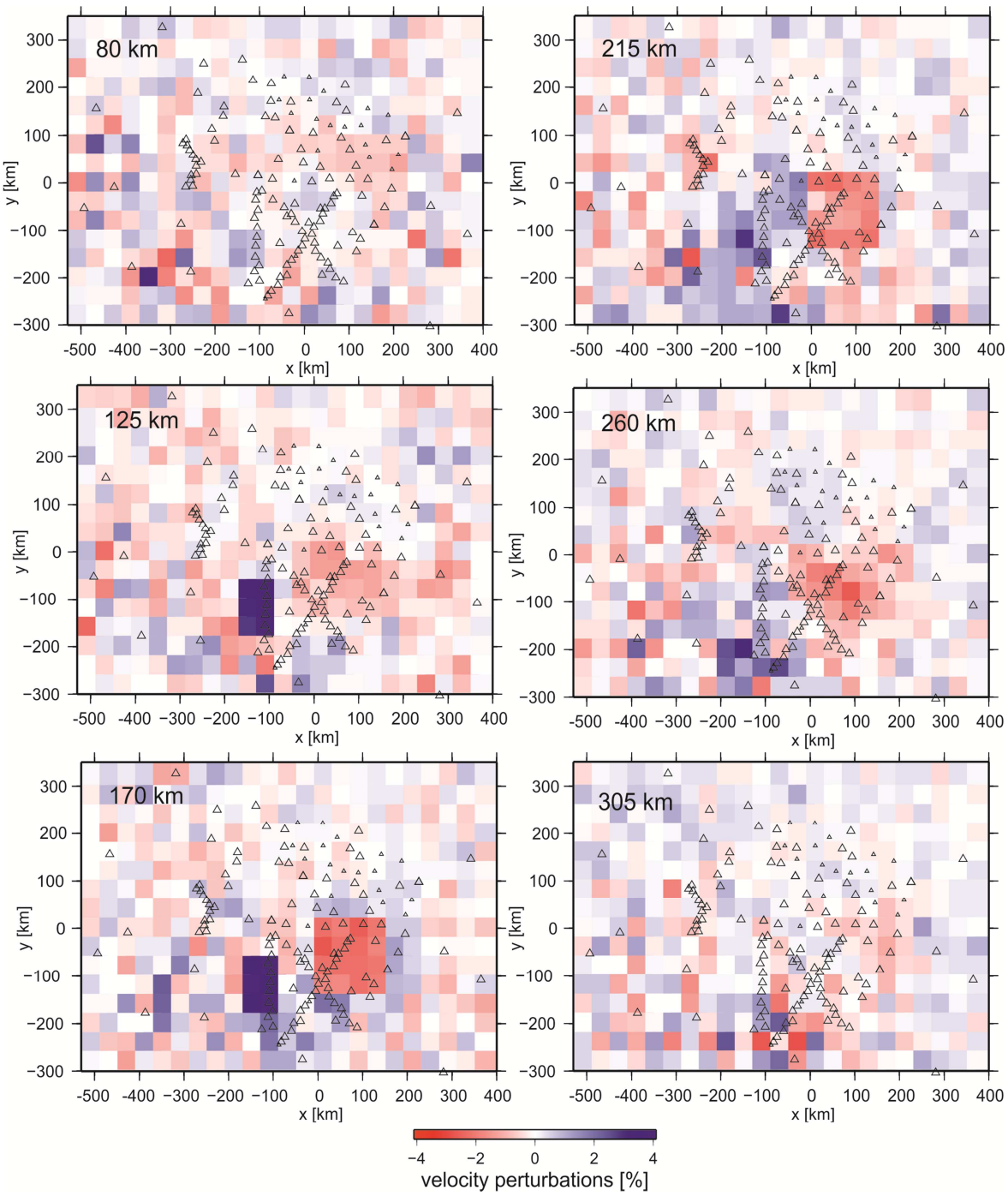

Figure 3.3 Results of inversion of the synthetic travel times according to the model in Fig. 3.2 with additional systematic time shifts mimicking event mislocation errors. Although both positive and negative velocity anomalies are well-resolved in the horizontal dimension, the amplitude of the low-velocity anomaly is low, at a level of noise. For a detail description see a caption of Fig. 3.2.

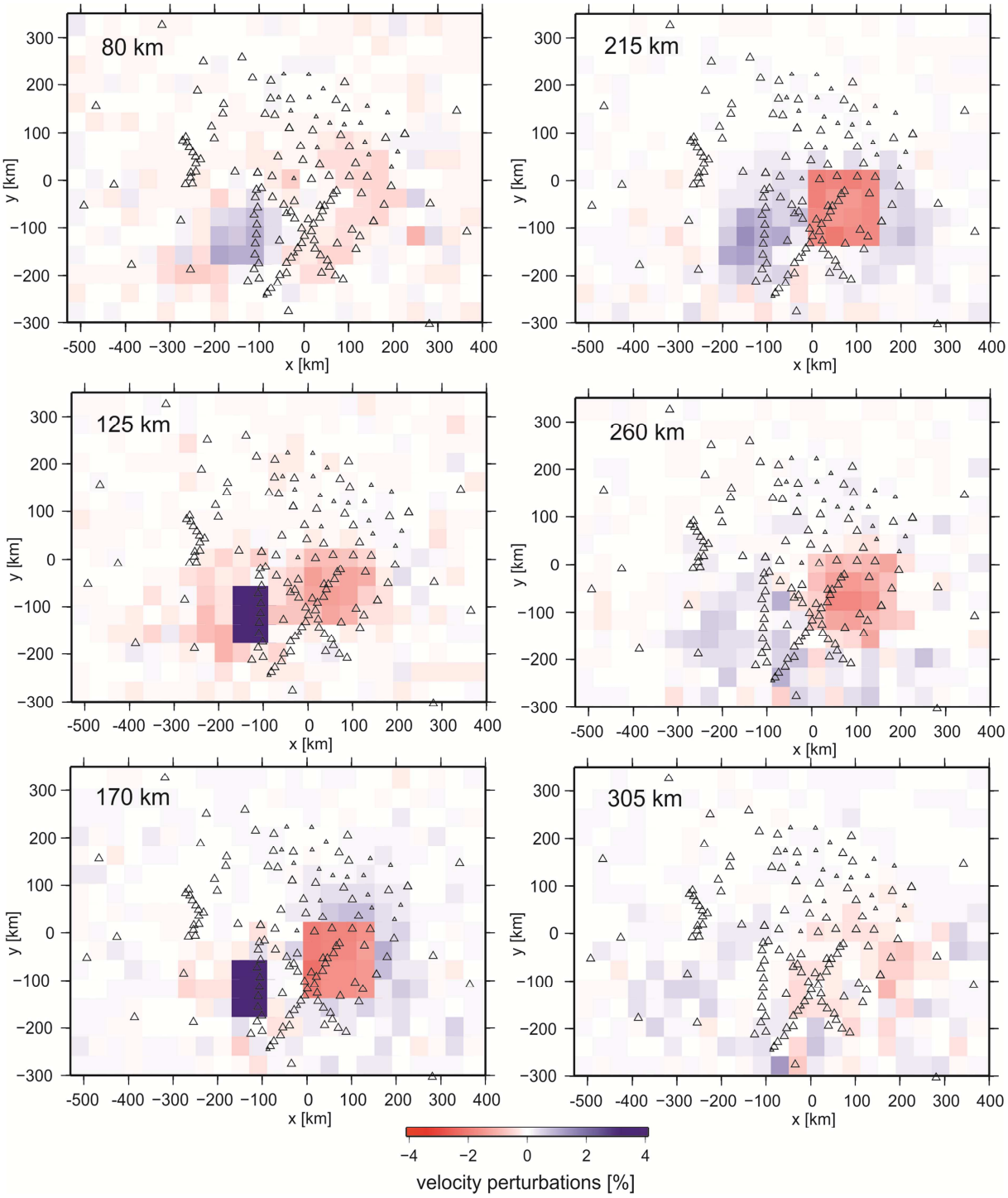

Figure 3.4 Results of inversion of the synthetic travel times according to the model in Fig. 3.2. For a detail description see a caption of Fig. 3.2. We observe a slight decrease of the amplitudes of both anomalies and also over-swinging effects around the inserted synthetic anomalies.

3.4 Testing different types of travel-time normalizations

Normalization of absolute travel-time residuals is a procedure reducing the effects originating out of the target volume, i.e., in the deep mantle, in the source region as well as effects of mislocation and origin-time errors. Normalization means that a representative event mean residual is subtracted from all absolute travel-time residuals of each event. Such travel-time event mean is most often calculated either as an average of all travel-time residuals at the array or as an average across a set of selected stations, or a residual at one reference station can be used. Each of the methods has its advantages and disadvantages. To analyse potential effects of various types of normalizations (NORM1 – NORM5) on the tomographic images of the upper mantle, we prepared five different sets of relative residuals using different normalizations and inverted them for the velocity structure of the upper mantle.

We selected different stations and calculated the event means from their absolute travel-time residuals. Events with less than a pre-defined minimum number of normalizing stations were excluded from the inversion (Table 3.2).

Table 3.2 Types of normalization used for testing

Type of normalization	Station code (total number of stations used for normalization)	Minimum number of stations (percentage relative to declared stations for normalization)
NORM1	All stations (140)	45 stations (32 %)
NORM2	KHC, NKC (2)	2 stations (100 %)
NORM3	CLL, GRB1, KHC, KRUC, MIL, MOA, MORC, NKC (8)	8 stations (100 %)
NORM4	CLL, GRB1, KHCB, KRUC, MIL, MOA, MORC, NKC (8)	4 stations (50 %)
NORM5	KHC (1)	1 station (100 %)

The first normalization (NORM1) represents the most common procedure with the reference residual calculated as an average from all travel-time residuals of an event. The second normalization NORM2 is formed by residuals from stations KHC and NKC, located in the middle of the region. These stations have opposite patterns of the P-wave residual spheres (Babuška and Plomerová et al., 2012). NORM2 and NORM3, which require measurements from all the selected stations, provide the most stable normalizing levels but, due to this requirement, exclude significant amount of events (Tab. 3.3). Normalization NORM4 allows event residuals normalized by only 50 % of stations

selected. NORM5 is an example of normalization where residuals of one reference station are used.

To be able to compare the results, we calculated the inversions with identical inversion parameters: damping factor of 200, two iterations and number of inverted velocity perturbations of 3800. However, numbers of rays and their distribution differ due to different conditions in the normalization (Table 3.3).

Table 3.3 The inversion parameters according to different normalizations.

	NORM1	NORM2	NORM3	NORM4	NORM5
Number of stations	140	140	124	140	140
Number of events	168	144	92	167	167
Number of relative residuals	13551	11533	7569	13461	13461
Variance reduction	66 %	57 %	69 %	44 %	48 %

Despite the fact that the tested normalizations are very diverse and variance reductions of the results vary from 44% to 69%, the resulting velocity perturbations from the five inversions are very similar (Fig. 3.5). Only results of NORM3 show deviations from the others and have generally lower amplitudes of perturbations, especially in the edges of the model. We associate this with considerably different ray-geometry due to significantly lower number of rays (Tab. 3.3). This test shows that for the southern part of the BM, the type of normalization is not as important as the ray geometry (**P3** – Karousová et al., 2013).

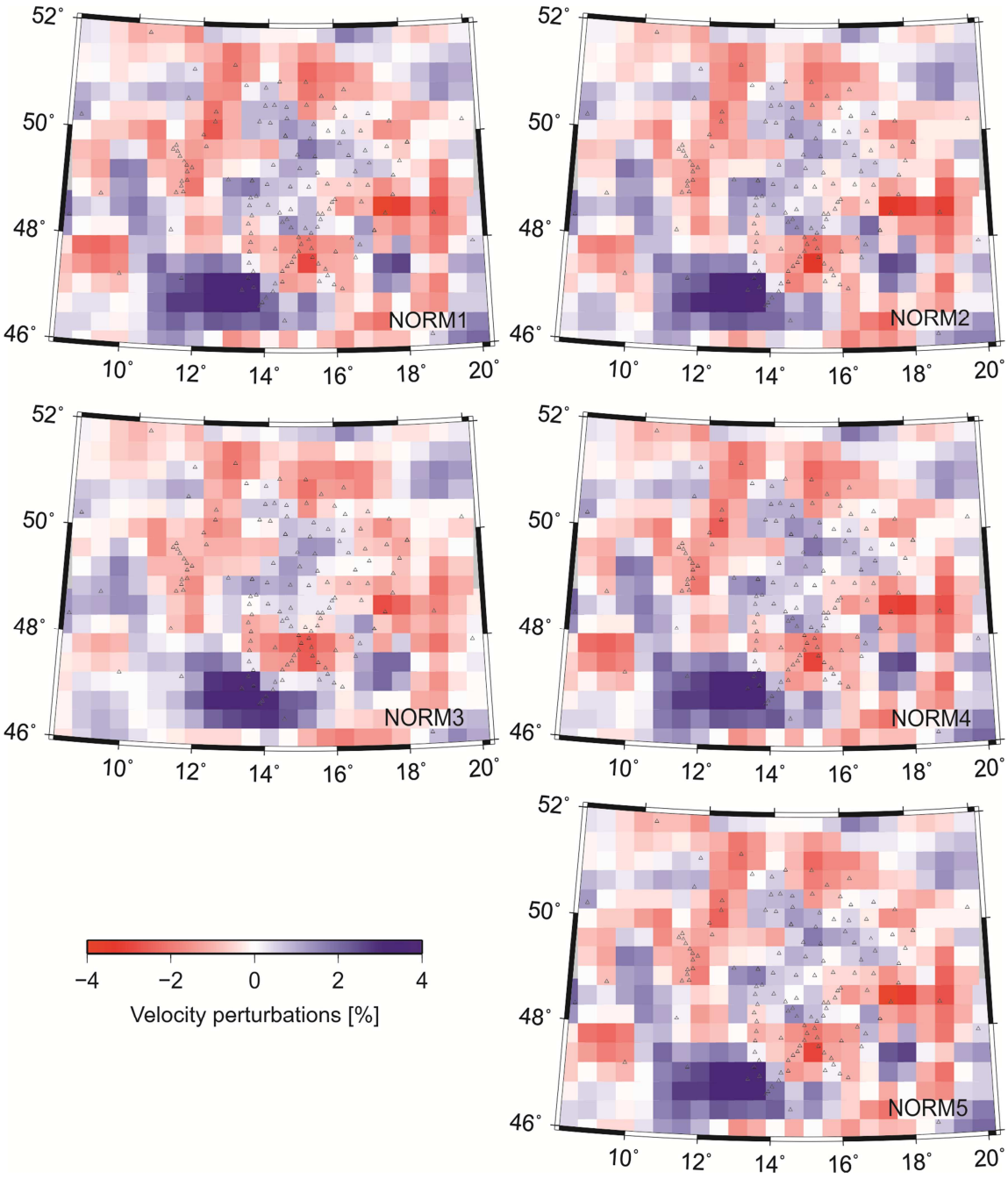

Figure 3.5 Horizontal cross-sections through five velocity perturbation models at depth of 125 km from inversions of five different sets of relative residuals calculated according to normalizations NORM1-NORM5. Type of normalization has negligible effect on tomography images of the upper mantle beneath the BM, the ray geometry appears as the most important.

3.5 A-priori data analysis

Presented velocity-perturbation models of the upper mantle are based on the DLSQ method (**P1 -** Karousová et al., 2012a; **P2** – Karousová et al., 2012b; **P3** – Karousová et al., 2013) which is very sensitive to outliers (Menke, 1984). Therefore, the data set has to be carefully cleaned of the outliers before the inversion. We showed several types of time instabilities (**P2** – Karousová et al., 2012b) and proposed how to clean the data. In case of the dataset from the BOHEMA III and a part of data from the ALPASS projects (**P3** – Karousová et al., 2013), we modified the cleaning procedure. Not only time dependence of the residuals was analysed, but also a dependence of relative residuals on back-azimuth was considered (Figs. 3.6 and 3.7).

Figure 3.6 shows dependence of relative residuals both on time and on back-azimuth for eight selected stations with different kinds of time instabilities. The relative residuals at stations GRA1, KRUC and PRUB are considered as examples of stable stations. The relative residuals are differences between absolute travel-time residuals and an event mean residual calculated from stable stations.

At some stations the relative residuals vary significantly. For example, at station A404 the residuals range from -4.1 s to 6.6 s and seem to be dependent on event back-azimuth. The variation of residuals is too large to be explained purely by velocity perturbations in the crust and/or the upper mantle. The variations also reflect some technical problems of the station. For that reason we excluded all measurements from the A404 station from the data set.

More frequently, we found several sequences of relative residuals deviated from stable mean values, e.g., at stations GFO, OKC and KON (Fig. 3.6, green rectangles). These trends are most probably caused by poor time synchronization of the data acquisition system and GPS (Global Positioning System) in the particular periods. Therefore, we excluded those measurements from the data set.

Some of the measurements could be corrected in accordance with information from station log files. For example, relative residuals corresponding to events with indexes from 130 to 150 at station GFO are grouped into two time levels. We found out from the station log files that some of these relative residuals (Fig. 3.6, red rectangle) have been delayed systematically by 2 s.

At station A306, a group of relative residuals (Fig. 3.6, dark blue rectangle) for events with similar back-azimuths seems to deviate slightly from the mean value. Clustered

deviations of residuals associated with these events are distinguishable also at other stations, (e.g., stations GRA1, KRUC, KON), which means that they may have a physical meaning and we keep such residuals in the data set.

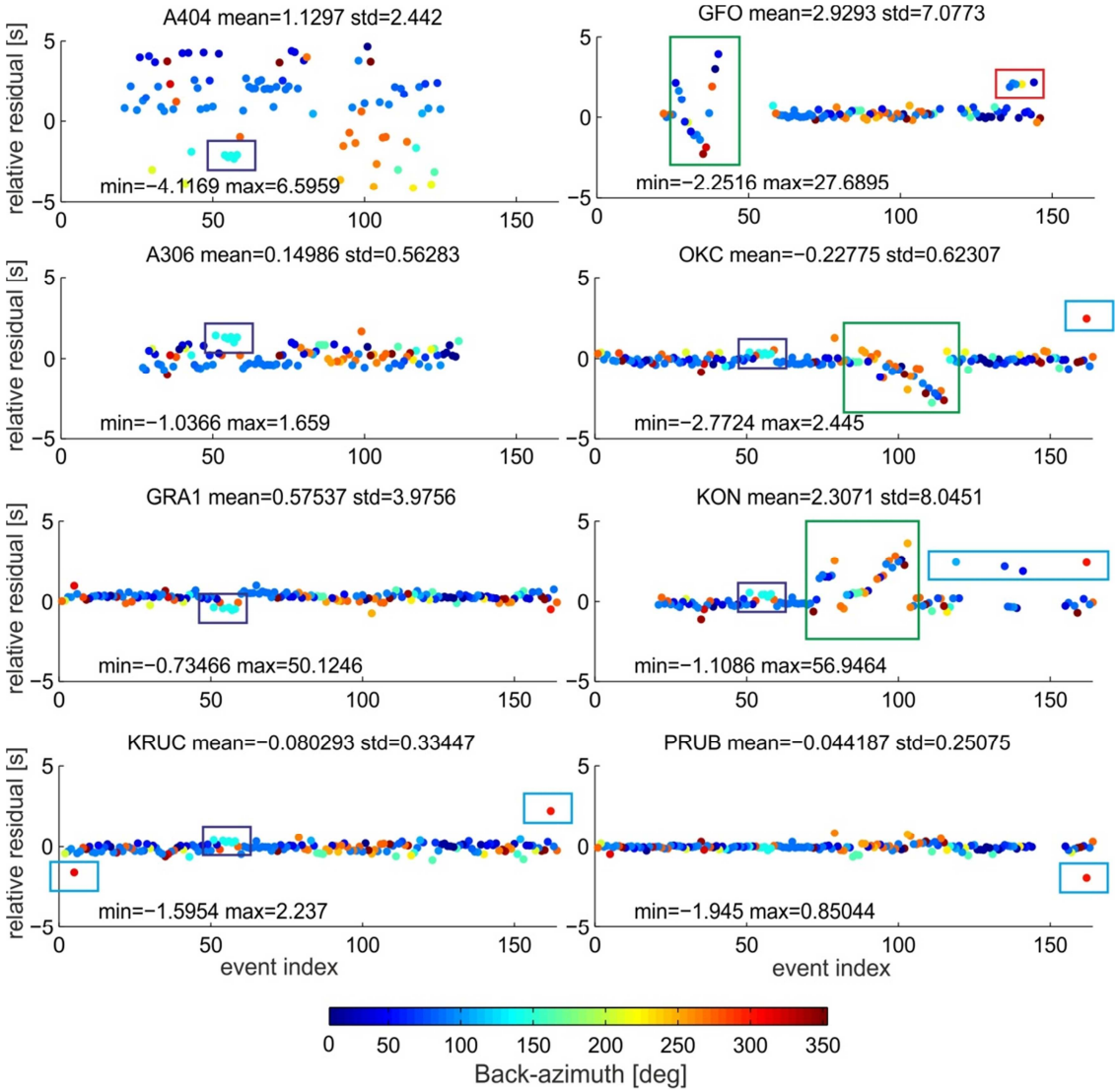

Figure 3.6 Relative residuals for selected eight stations included in the BOHEMA III and ALPASS experiments for events ordered chronologically. The rectangles show different kinds of time instabilities. For each station, the mean, the standard deviation (std), the minimum (min) and the maximum (max) of relative residuals are given in seconds.

We also checked single residuals which significantly differ from the stable mean value at each station (Fig. 3.6, stations KRUC, OKC, KON and PRUB, blue rectangles). We re-measured the arrival times on the P-wave recordings. Residual deviations were usually caused by errors resulting from a small signal-to-noise ratio or a phase misinterpretation. We either corrected the P-wave arrival time or removed the measurement from the data set.

To be able to explain lateral and back-azimuthal variations of the relative residuals with realistic velocity variations, we analysed the residuals corrected for crustal effects averaged in 45° azimuth segments (Fig. 3.7). This allowed us to identify effects of other sources than those coming from the upper mantle structure. Differences of residuals at nearby stations were suspiciously large (~ 1 s) in some regions (see circles in Fig. 3.7). Since these differences were significant only for one group of event back-azimuths, they could reflect complex shallow crustal structure, which had not been included in the crustal corrections. As mentioned in Chapter 3.1, errors due to imperfect crustal corrections were minimized by inverting also at nodes in the lower crust. Nevertheless, the 45°-segment analysis was useful for careful interpretation of velocity perturbations in some regions.

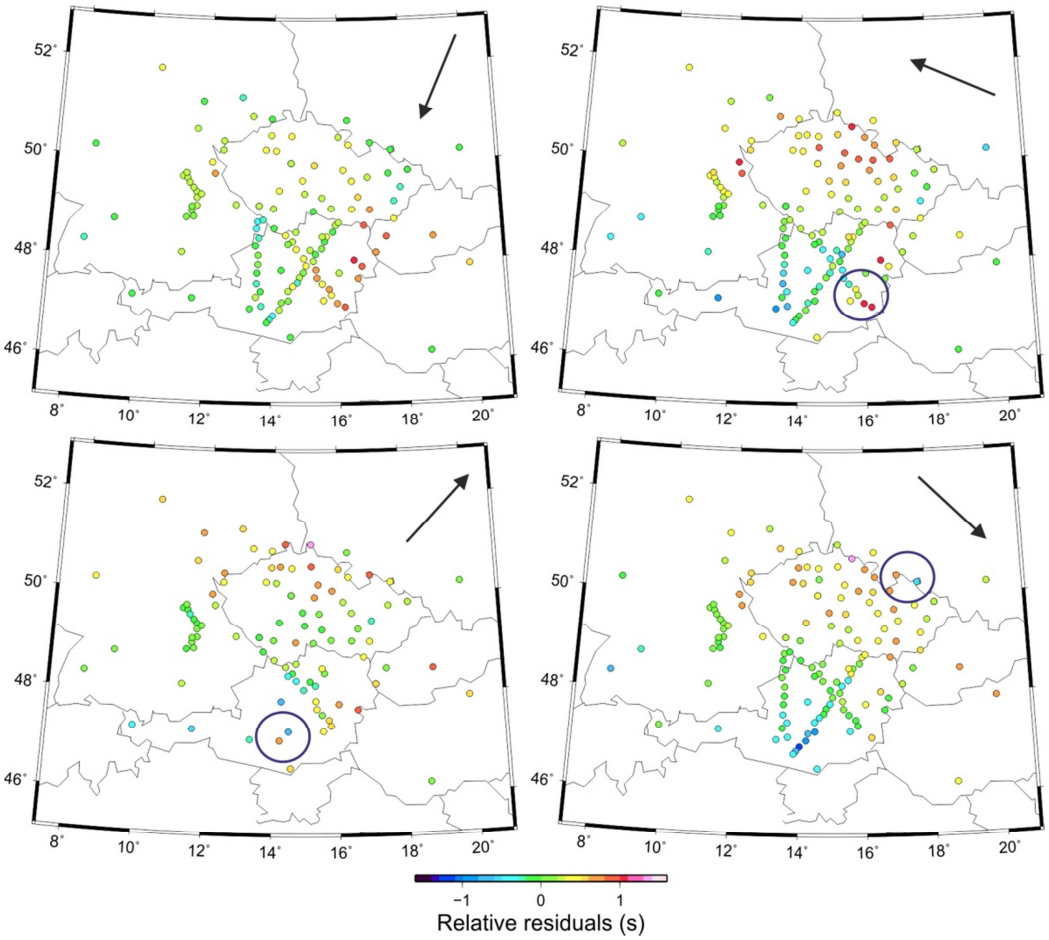

Figure 3.7 Four examples of relative residual distributions corrected for crustal effects averaged in 45° azimuthal segments. The arrows mark the central back-azimuths of the selected segments. The circles mark regions where differences among near-by stations were suspiciously large (> 1 s).

3.6 Model parameterization

The TELINV code calculates velocity perturbations in a grid of nodes, among which velocities are linearly interpolated (**P4** - Karousová, 2013). Because node spacing affects both complexity and stability of the model, selection of the optimal parameterization is crucial for interpretation of resulting perturbations. There are basic rules according to which the nodes spacing can be selected. The spacing is usually regular, at least in horizontal dimensions, in order to prevent misinterpretation of tomographic images (e.g., Spakman and Bijwaard, 2001; Kissling et al., 2001; Nolet and Montelli, 2005). The node spacing should at least double a typical wavelength of teleseismic data (e.g., Evans and Achauer, 1993; **P3** – Karousová et al., 2013).

To illustrate basic characteristics of a dependence of velocity perturbations on the size of node spacing (Fig. 3.8, Table 3.1), we show tomography images from two inversions which differ only in horizontal parameterizations. The inversions are calculated with the horizontal node spacing of 30 km and 40 km. In both cases, we use absolute residuals from the BOHEMA III and ALPASS experiments, i.e. residuals without corrections for the source and deep-path effects.

Main features of velocity perturbations are similar in both models (Fig. 3.8). The model with the 30 km node spacing (Fig. 3.8a) shows significantly smaller amplitudes of perturbations in comparison with the model with the 40 km node spacing (Fig. 3.8b), but a higher amount of unresolved nodes, around which less than 10 rays propagate. The denser node grid parameterization increases variance reduction (Menke, 1984) and reduces the effect of model parameterization, which can cause difficulties if the nodes are located just on a border of two structures **P2** – Karousová et al., 2012b. The drawback of the smaller spacing is that it can lead to complex models with many unresolved nodes.

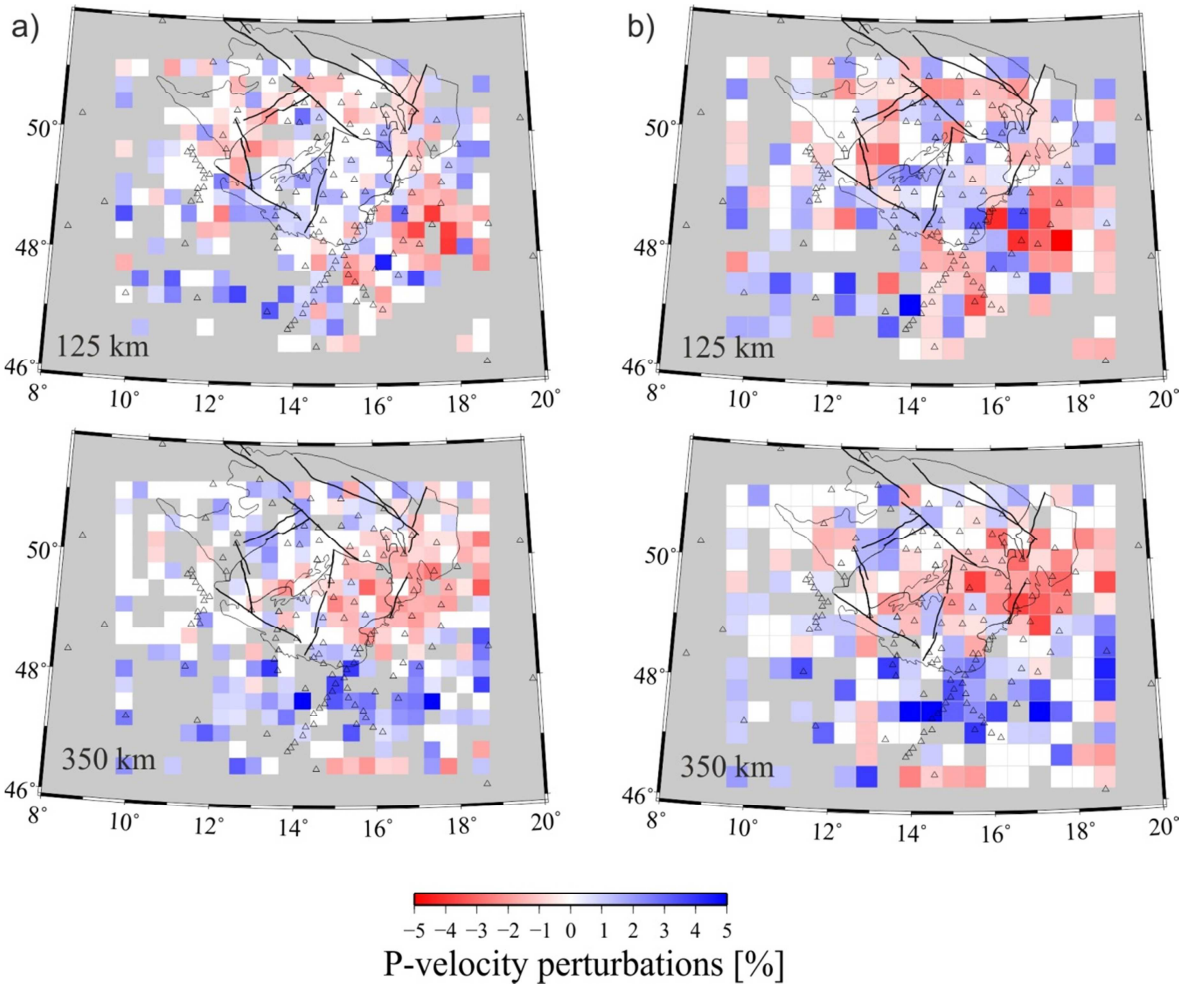

Figure 3.8 Tomography of the upper mantle at depths of 125 km and 350 km based on data from the BOHEMA III and ALPASS experiments with horizontal node spacing of 30 km (a) and 40 km (b), respectively. Only perturbations from more than 10 hit-counts are shown.

3.7 Regularization of the inversion

In dependence on station and event distributions, the optimal ray geometry should be as even as possible (e.g., Kissling, 1988; Nolet, 2008; **P3** – Karousová et al., 2013). Nevertheless, the real ray geometry in teleseismic tomography is irregular and many of the rays are parallel without intersecting, especially in the margins of the upper mantle model. Consequently, the kernel matrix in equations (2.9) tends to be singular. Regularization methods introduce additional constrains in order to limit the number of different solutions of calculating the inverse of the kernel matrix. The TELINV code provides two kinds of regularizations based on: (1) the damping factor and (2) truncated singular value decomposition (TSVD), (e.g., **P4** - Karousová, 2013; Menke, 1984). We have shown that

the DLSQ method is more convenient option for the teleseismic tomography of the upper mantle beneath the BM (**P2 -** Karousová et al., 2012b). The DLSQ method resulted in smoother velocity perturbation images compared to those from the TSVD method which indicated a larger sensitivity to the uneven ray distribution.

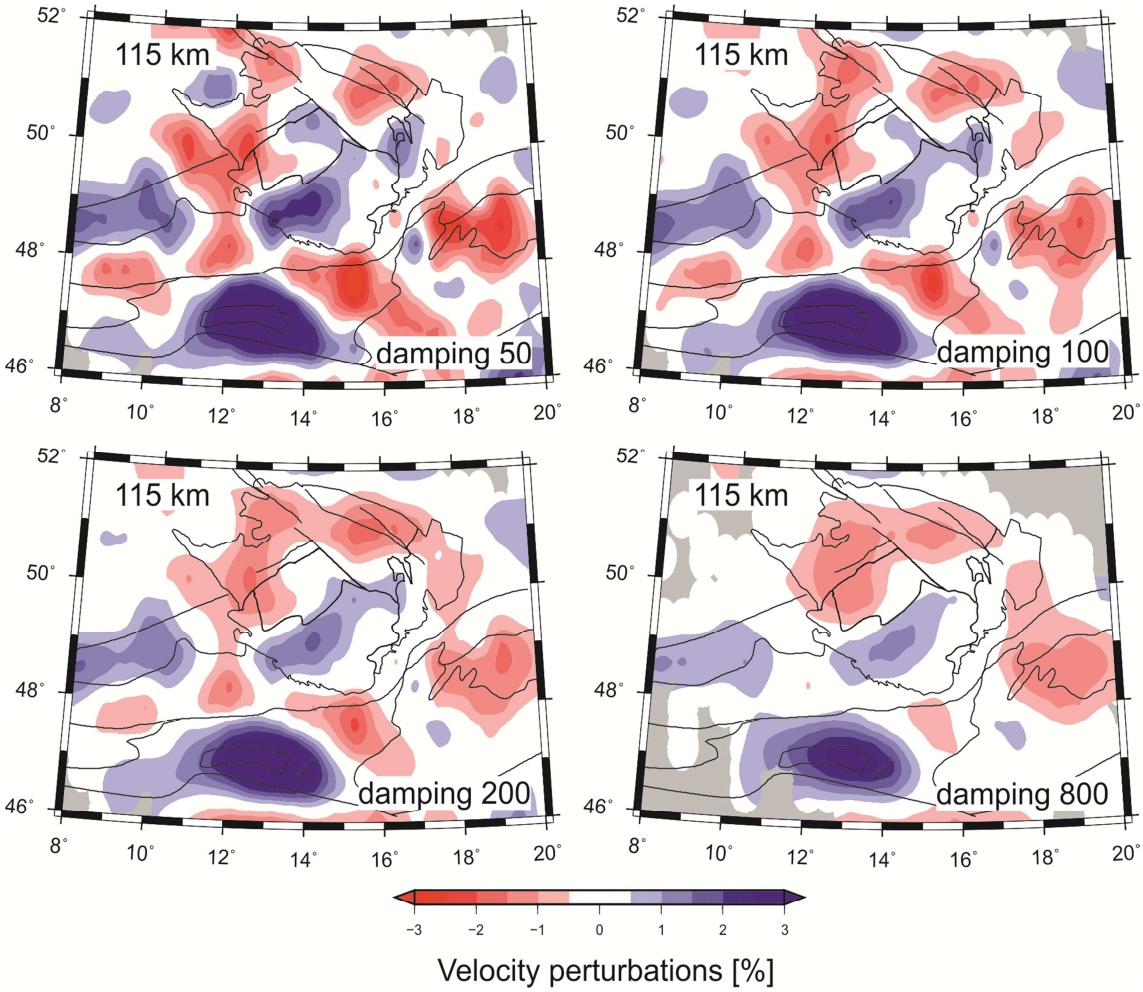

Figure 3.9 Tomography of the upper mantle at depth of 115 km from inversions with the use of different damping factors after the 1st iteration.

To have a stable solution with realistic P-wave velocities it is necessary to test different damping factors and run a number of iterations. Amplitudes of velocity perturbations decrease with increasing damping factor (Fig. 3.9). On the other hand, if the damping factor is too small, the velocity perturbation model becomes very complex because of random perturbations in unresolved nodes. Number of iterations has an opposite effect on the perturbations (Fig. 3.10). Therefore, these two inversion parameters – the damping factor and the number of iterations – have to be selected simultaneously to guarantee that the resulting tomographic model is a stable one and that the corresponding perturbations

have a physical meaning (**P2** - Karousová et al., 2012b). We determined the optimal damping factor and number of iterations according to trade-off curves and synthetic tests (**P2** - Karousová et al., 2012b; **P3** - Karousová et al., 2013).

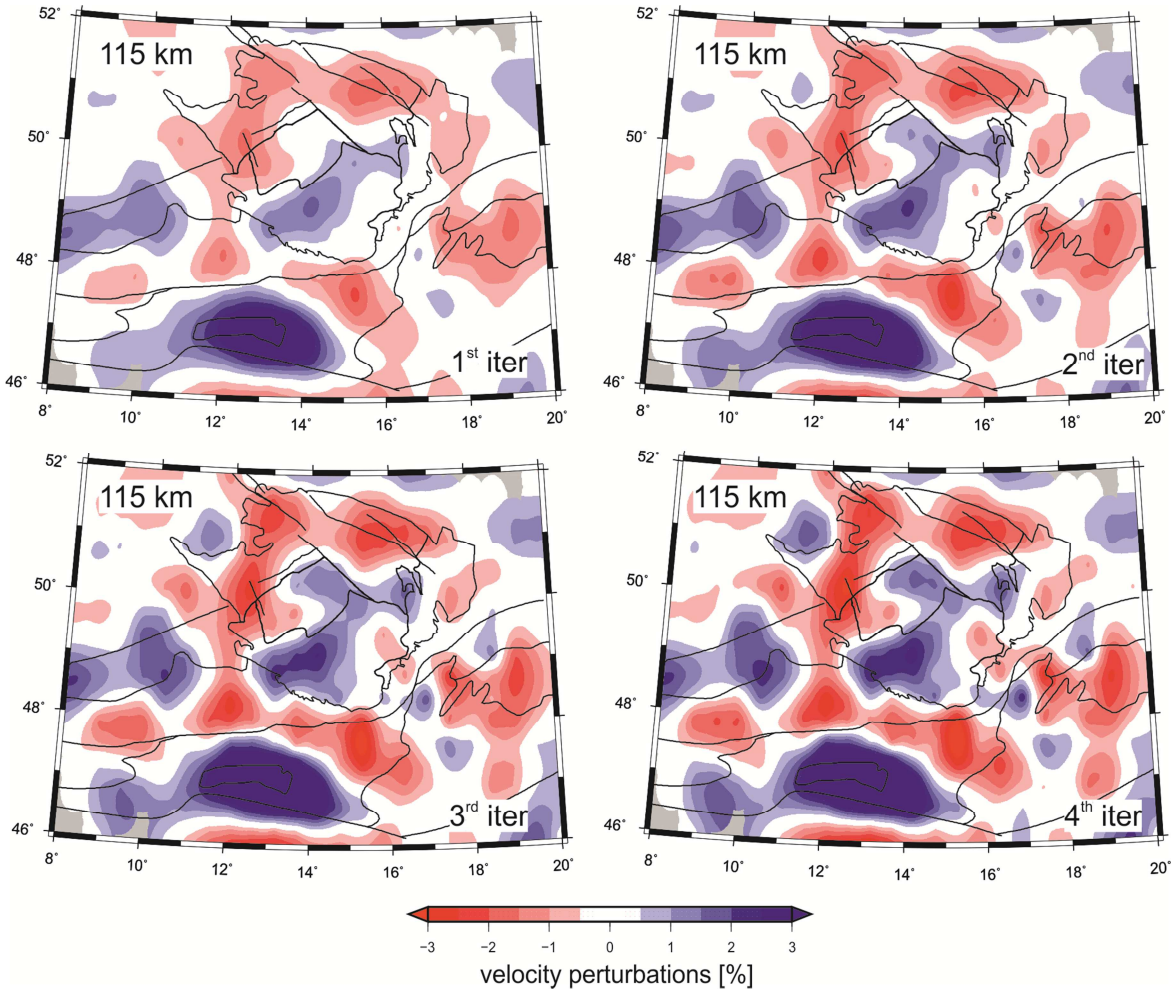

Figure 3.10 Tomography of the upper mantle at depth of 115 km from inversions after the 1st, 2nd, 3rd and 4th iterations.

3.8 Assessment of model quality

Resolution of the velocity perturbations has to be evaluated prior to interpretation. Resolution depends on ray distribution as well as on inversion parameters, e.g., damping factors, or number of iterations. The ray geometry can be visualized in different ways (Fig. 3.11), e.g., as hit counts, derivative weighted sums (DWS), ray paths, or as diagonal elements of resolution matrix (e.g., Kissling, 1988; **P3** - Karousová et al. 2013). According to these methods, we sort the velocity perturbations at all depths into three categories:

well-resolved, poorly-resolved and unresolved. According to these categories we distinguish the velocity perturbations graphically (Figs. 5.2, 5.3).

Reliability of the velocity perturbations can be also indicated by testing various inversion parameters. Velocity perturbations, which remain stable in such tests, are the most robust features of the model. These perturbations reflect usually the most prominent tectonic structures. However, to interpret small-size or weak velocity anomalies and/or anomalies which are located in margins of the model, we need to perform specific synthetic tests (**P2** - Karousová et al. 2012b; **P3** - Karousová et al. 2013).

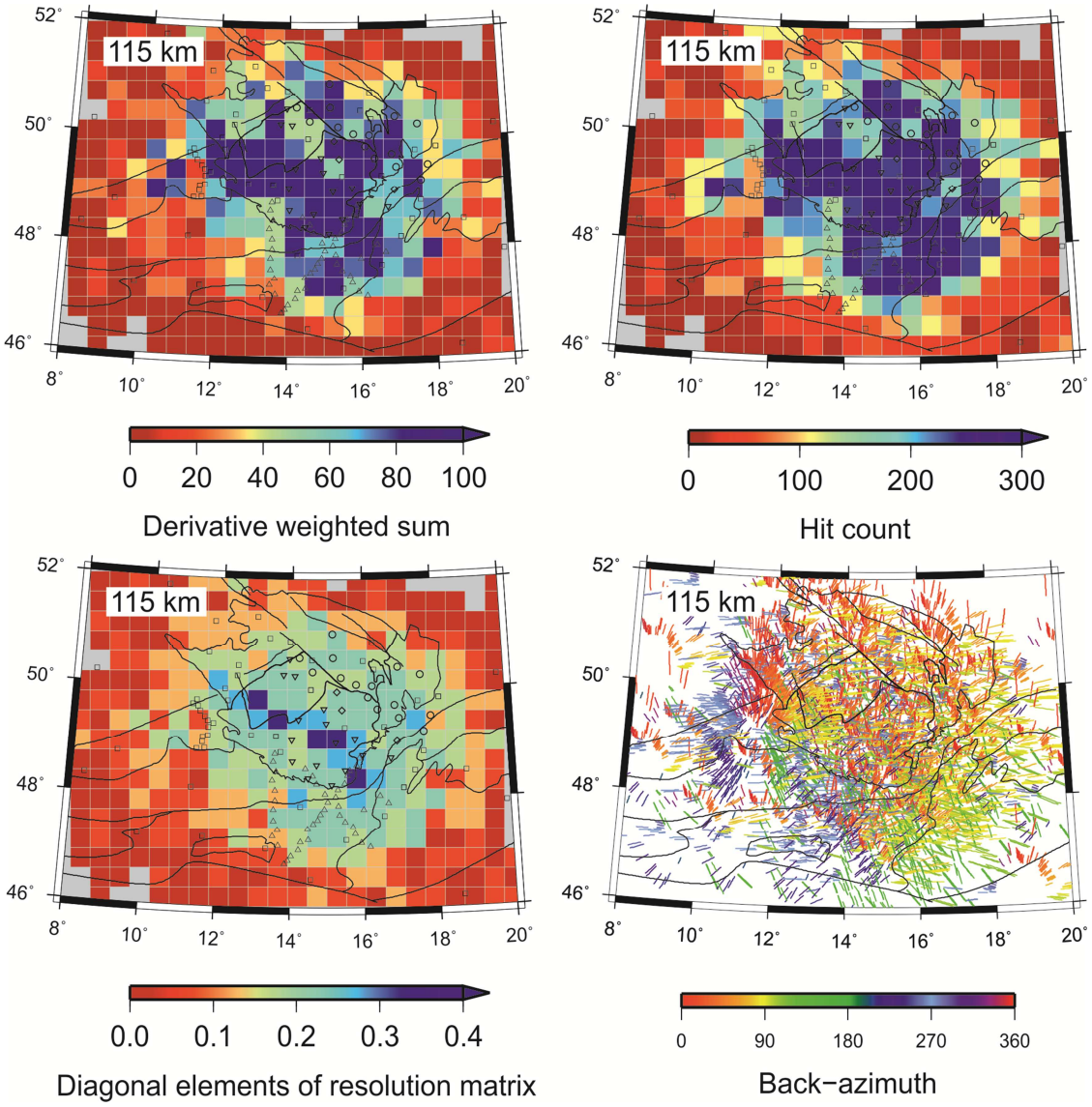

Figure 3.11 Derivative weighted sums, hit counts, diagonal elements of resolution matrix and ray distribution based on data from BOHEMA III and ALPASS experiments for the layer at depth of 115 km.

4 TELINV code

The TELINV code is a FORTRAN code which (1) inverts teleseismic travel-time residuals for three-dimensional velocity structure of the upper mantle and (2) calculates synthetic travel times according to a given velocity model. Three-dimensional ray tracing is implemented in accordance with the Simplex ray-tracing bending technique (Steck and Prothero, 1991). Velocity perturbations are searched in a 3D grid of nodes, among which velocities are linearly interpolated. The velocity perturbations are calculated in subsequent iteration steps, in which the ray-paths and travel-time residuals are updated.

The TELINV code was developed by several authors - J. Taylor, E. Kissling, U. Achauer, C. M. Weiland, L. Steck and later modified and used by many other users (Weiland et al., 1995; Arlitt et al., 1999; Lippitsch et al., 2003; Sandoval et al., 2004; Shomali et al., 2006; Eken et al., 2007). However, significant modifications were done without proper documentation. We first applied a code version provided from the Uppsala University by Tuna Eken (now at GFZ Postdam) to data from the BOHEMA II experiment (**P1** - Karousová et al., 2012a; **P2** - Karousová et al., 2012b). This version does not have a user-friendly structure. Therefore, we have modified the code in cooperation with Prof. Kissling (ETH Zürich), complemented it with a thorough documentation and created a User's Guide (**P4** - Karousová, 2013).

We developed a new modified version, called TELINV2012, which is based on the TELINV99 code, the last version revised by E. Kissling. The TELINV2012 code is written in FORTRAN 77 with several subroutines in FOTRAN 95 (however, compiled by ifort compiler). We complemented the code with comments and error and warning messages which should help users to solve potential problems. We also added different analyses of input travel-time residuals, ray-path geometry, node hit-counts and derivative weighted sums. We simplified formats of the input and output files. The detailed User's Guide (**P4** - Karousová, 2013) describes the most important parts of the tomographic code and provides a step-by-step navigation through the travel-time residual inversion and modelling. Important parts of the TELINV2012 package are the new auxiliary GMT (General Mapping Tools), Matlab and FORTRAN scripts for simple visualization of input data and final model parameters as well as preparation of most of the input files. The TELINV2012 code was tested and applied on data from the BOHEMA III experiment (**P3** - Karousová et al. 2013).

5 Summary of the main results

5.1 3D model of the crust of the Bohemian Massif

Teleseismic travel times are significantly affected by velocity structures of the crust. To correct for these effects, we compiled a 3D crustal model based on independent data sets (**P1** - Karousová et al. 2012a). The BM is well covered with control-source seismic (CSS) profiles (Fig. 5.1). We collected all accessible velocity models along many wide-angle refraction and reflection profiles as well as a model derived from 3D local tomography (Beránek et al., 1975; Behr et al., 1994; Enderle et al., 1998; Hrubcová et al., 2005; Majdański et al., 2006; Růžek et al., 2007; Hrubcová and Środa, 2008; Grad et al., 2008; Růžek et al., 2011). We did not include crustal thicknesses derived from receiver functions (Geissler et al., 2005; Heuer et al., 2006) because they were grossly inconsistent with those from the CSS methods (Hrubcová et al., 2005; Hrubcová and Geissler, 2009) in some parts of the BM. Interpretation of crustal thicknesses according to receiver function method required additional velocity model (e.g., Julia et al., 1990).

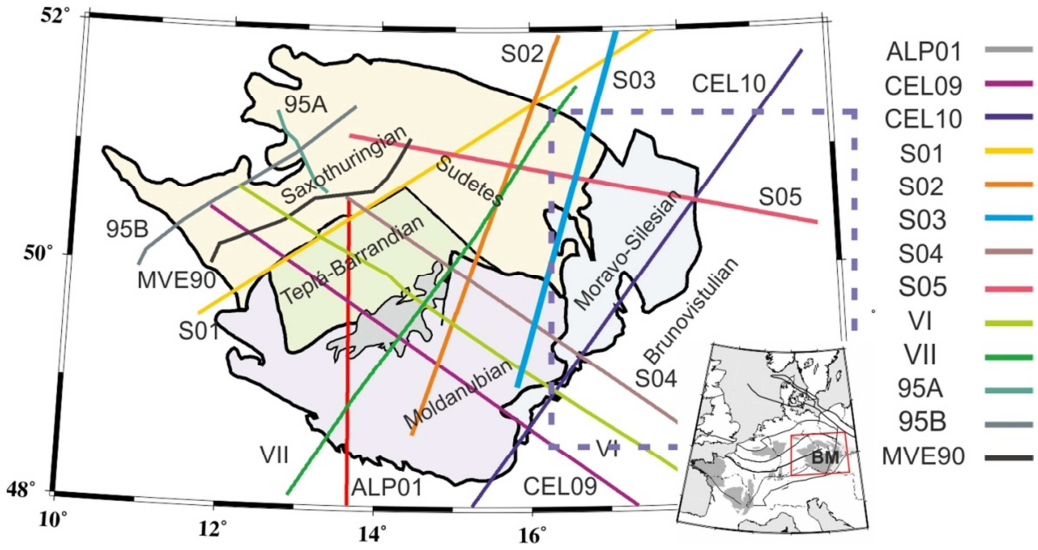

Figure 5.1 Map of refraction and reflection profiles (Beránek et al., 1975; Behr et al., 1994; Enderle et al., 1998; Hrubcová et al., 2005; Majdański et al., 2006; Růžek et al., 2007; Hrubcová and Środa, 2008; Grad et al., 2008) intersecting the Bohemian Massif (BM). The dashed rectangle marks the coverage of the tomographic model of the Moravo-Silesian region by Růžek et al. (2010). The inset locates the BM within the European Variscides.

We tested two types of interpolation of crustal velocities, linear and the nearest-neighbour interpolation methods, which resulted in two different models. The model in which the latter method was applied was complemented by velocities based on the 1D

IASP91 Earth reference model (Kennet and Engdahl, 1991) at sites where data were missing.

Reliability of both models was tested in tomographic inversions of synthetic and observed travel times recorded during the BOHEMA II experiment. The tests showed that errors due to inter/extrapolation can be significant. For this reason, we prefer the model using the nearest-neighbour interpolation resulting in smaller magnitudes of velocity perturbations. The tomographic tests showed that the crustal residuals can produce velocity-perturbation artefacts of magnitude comparable with those caused by heterogeneities of real upper-mantle structures. Therefore, the crustal corrections are of a great importance especially for interpretations of the uppermost mantle velocities down to depths of about 100 km.

5.2 Tomography of the upper mantle based on data from the BOHEMA II experiment

Tomography images based on data from the BOHEMA II experiment show the upper mantle beneath the BM as prevailingly low-velocity region with relatively small velocity variations (Fig. 5.2; **P2** - Karousová et al. 2012b). This finding is in line with results of regional tomography derived from data from permanent observatories (Amaru, 2007; Koulakov et al., 2009; Piromallo and Morralli, 2003). Additionally, the model based on the BOHEMA II data indicates a southward thickening of the lithosphere, which correlates well with tomography findings from BOHEMA I, the preceding experiment focused on the western BM (Plomerová et al., 2007) and the lithosphere thickness studies (e.g., for review Plomerová and Babuška, 2010).

The overall low-velocity pattern of the tomography images is disturbed by small-size high-velocity perturbation in the eastern part of the model (Fig. 5.2). A comparison of the velocity perturbations in this part of the model with depth variations of lithosphere-asthenosphere boundary derived from the static terms of teleseismic P-wave travel-time deviations (Plomerová et al., 2013) and from Sp receiver functions (Geissler et al., 2012) indicates a complex structure beneath areas of contact of the Sudetes/Moravo-Silesian crustal units (Fig. 5.2).

Another discrepancy related to different seismic techniques emerges from a comparison of isotropic velocity perturbations with anisotropic studies of the BM upper mantle. Joint inversions of shear-wave splitting parameters and P-wave travel-time residuals, resulting in

3D self-consistent anisotropic models (e.g., Plomerová et al., 2000; 2007; 2012; Babuška et al., 2008; Babuška and Plomerová, 2013), revealed that the BM mantle lithosphere is formed by several domains with consistent olivine fabric. However, these domains, characterized by different orientation of dipping symmetry axes, remain hidden in the isotropic tomography images. This may be due to the fact that the BM domains delimited by changes in orientation of the fossil anisotropy need not vary in average isotropic velocities, or, velocity differences among them are too small to be resolved by isotropic tomography, namely due to an uneven ray geometry of the BOHEMA II array.

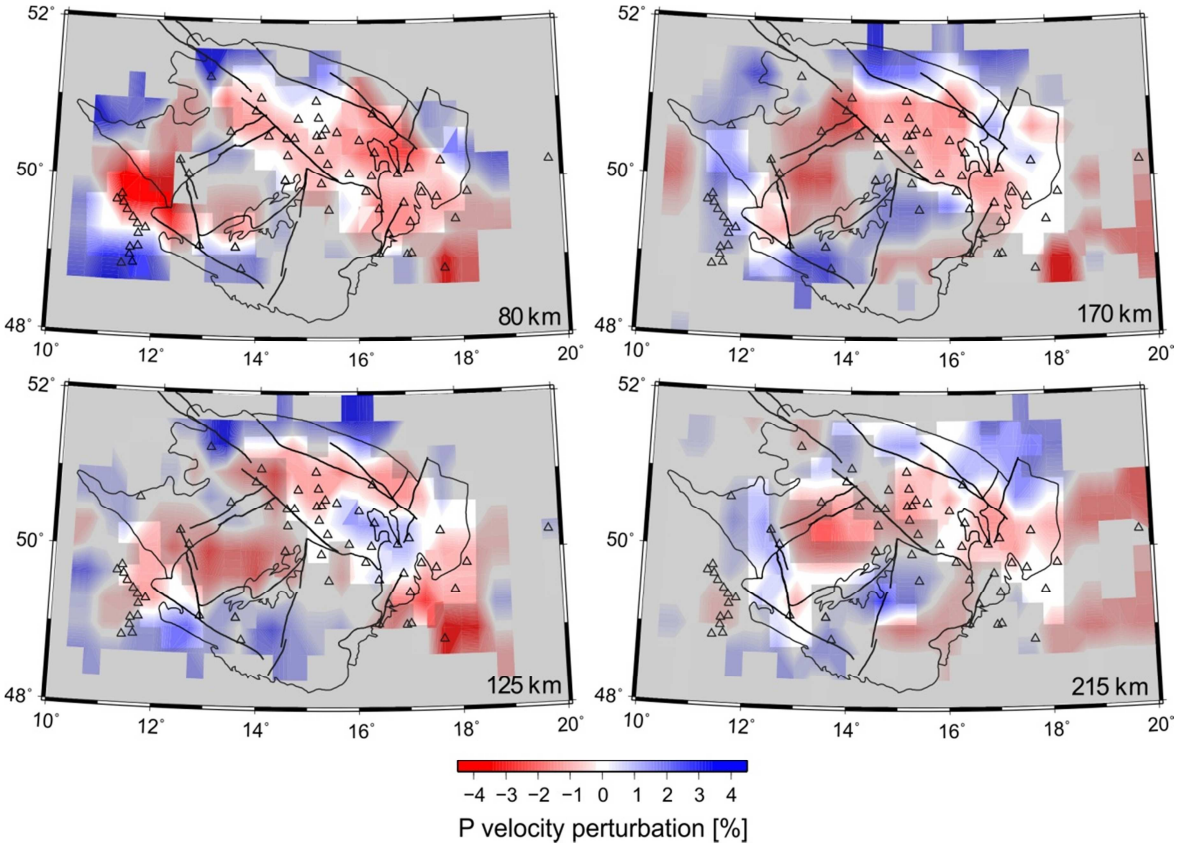

Figure 5.2 Velocity-perturbation model of the upper mantle based on data from the BOHEMA II experiment at four selected horizontal slices. Regions with well resolved nodes are illuminated, while poorly resolved areas are shaded with respect to the values of the diagonal elements of resolution matrix. The black lines show tectonic units of the BM and main faults as in Figure 5.1. The prevailing low-velocity trend is distorted in the NE of the BM by a small high-velocity anomaly beneath the boundary between the Sudetes and Moravo-Silesian units (see Fig. 5.1) particularly at depths of 125 km.

5.3 Tomography of the upper mantle based on data from the BOHEMA III experiment

Tomography based on data from the BOHEMA III and a part of the ALPASS projects images the massif as a part of an extensive large-scale low-velocity region in the upper mantle beneath central Europe (Fig. 5.3a,b; **P3** - Karousová et al. 2013), similarly to results of BOHEMA II in the northern part of BM (**P2** - Karousová et al., 2012b). The low-velocity upper mantle beneath the BM is sharply separated from the extensive high-velocity heterogeneity beneath the Eastern Alps. Within the BM, the low-velocity perturbations concentrate in the shallow mantle layers beneath the Eger Rift (ER) and move from the SW end of the rift toward its NE continuation. The images show also two high-velocity heterogeneities. The smaller one, both in terms of size and amplitude, is located beneath the Moldanubian part of the BM (Fig. 5.3a). We interpret this prominent feature as a manifestation of lithosphere thickening reflecting the collision of the Brunovistulian micro-plate with the eastern rim of the BM during the Variscan orogeny and a consequent underthrusting of this micro-plate beneath the Moldanubian unit (Babuška and Plomerová, 2013). We associate the most distinct high-velocity heterogeneity, located near the southern margin of the model and well-resolved in its deeper parts, with the Eastern Alpine lithosphere root (Fig. 5.3). The tomographic images indicate the northward dip of this subduction (Fig. 5.3c). The high-velocity heterogeneity extends towards the east (Fig. 5.3b), beneath the Pannonian Basin at the bottom of the model and may relate to delaminated parts of down-welling lithosphere residing within the transition zone (Dando et al., 2011).

In order to correct travel times from the BOHEMA III and ALPASS experiments for effects of the crust, we extended the 3D crustal model for the BM to the south (Fig. 5.4). We merged the model of the crust used in a tomographic stu dy of the north-eastern part of the BM (**P2** - Karousová et al., 2012b) and the model of Behm et al. (2007) used in the tomography study of Mitterbauer et al. (2011). First, we combined Moho depths from well-resolved regions of both models and then interpolated velocities from the two models. The Moho depths (Fig. 5.4) vary in range from 28 km to 40 km in the region of the BM, with the shallowest Moho depth beneath the ER and the deepest one beneath the Moldanubian unit. The Moho relief east and south from the BM is more complex. The thickest crust up to 50 km is observed beneath the Eastern Alps, and the shallowest one beneath the western Carpathians with thicknesses of only 24 km.

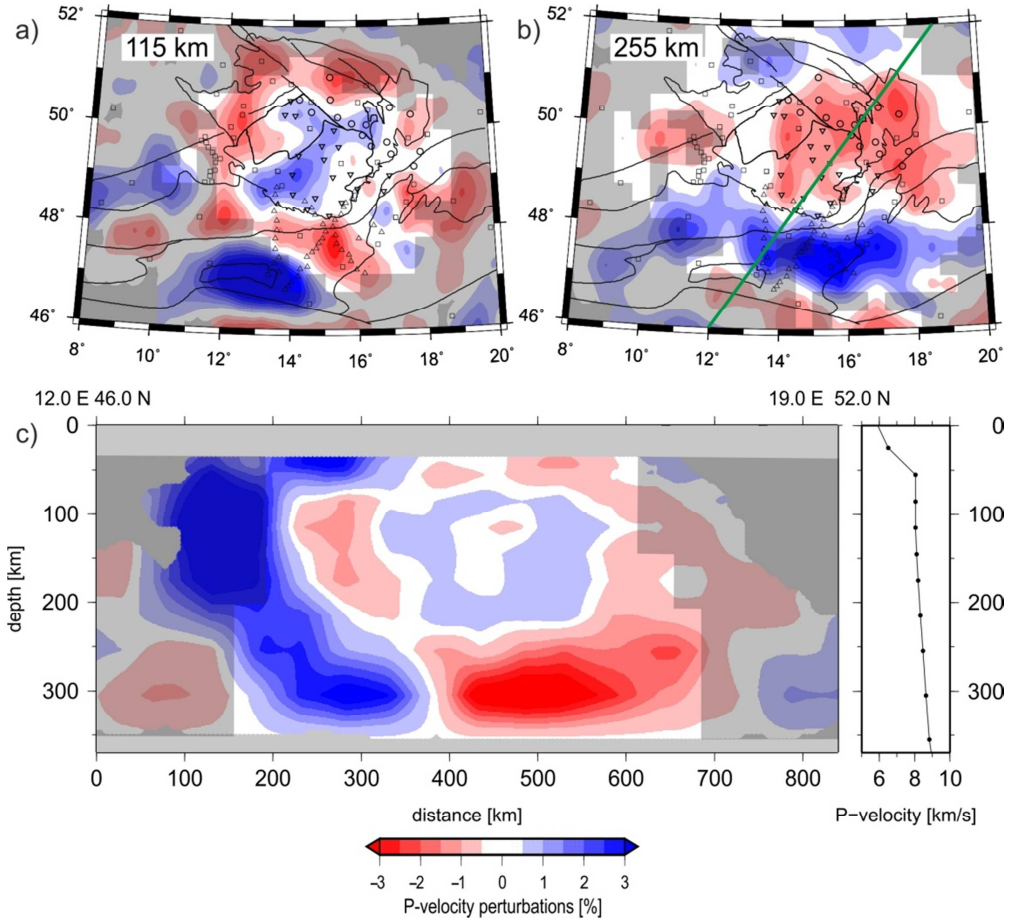

Figure 5.3 Two horizontal slices at depths of 115 and 255 km and a vertical cross-section through the velocity-perturbation model of the upper mantle based on data from the BOHEMA III experiment and a part of the ALPASS project. Regions with well resolved nodes are illuminated, while fairly and poorly resolved areas are shaded with respect to the values of the diagonal elements of the resolution matrix.

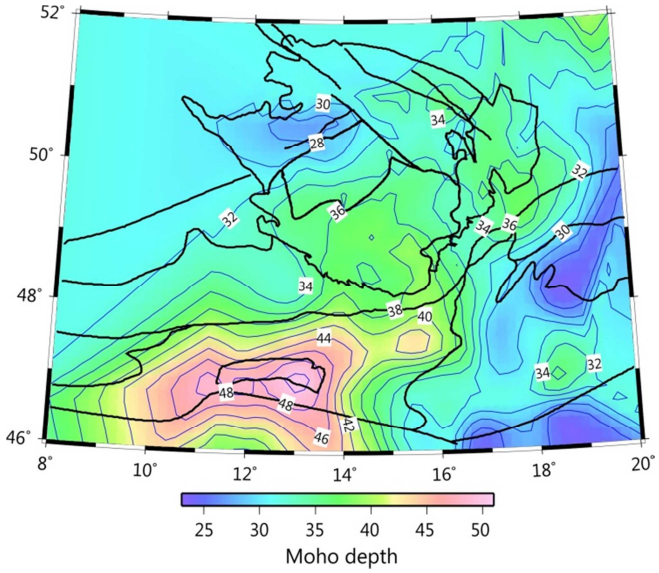

Figure 5.4 The Moho depths beneath the Bohemian Massif and its surroundings based on models of P1 - Karousová et al. (2012a) and Behm et al. (2007).

5.4 Outlook

Teleseismic travel-time tomography is a powerful tool for imaging velocity structure of the upper mantle. However, one has to keep in mind that the method has several limitations. For example, its results may suffer from imperfect crustal corrections, a velocity model simplification, a high-frequency approximation of wave propagation as well as from neglecting seismic anisotropy. The anisotropic signal affects teleseismic travel times and may significantly bias results of tomography studies. To overcome this problem, the next step is developing an advanced anisotropic version of the teleseismic tomographic code TELINV2012 aiming at modelling both isotropic and anisotropic structures and thus providing more realistic images of the upper mantle. Modelling anisotropic velocity parameters is even more sensitive to uneven ray geometry and to ray-path coverage, in general. To improve the resolution of tomography images of the upper mantle beneath the BM, data sets of all recent passive seismic experiments, e.g., BOHEMA I-III, EgerRift and PASSEQ (Plomerová et al., 2007; **P2** - Karousová et al. 2012b; **P3** - Karousová et al. 2013; Vecsey et al., 2013; Wilde-Piorko et al., 2008) will be merged. Besides the P/PKP phases, also shear-waves will be used in joint inversions and results on velocity anisotropy achieved by other methods will be incorporated.

6 List of papers included in the thesis

P1 Karousová, H., Plomerová, J., Babuška, V., 2012a. A three-dimensional velocity model of the crust of the Bohemian Massif,
Studia Geophys. Geod., **56**, 249-267, doi: 10.1007/s11200-010-0065-z.

P2 Karousová, H., Plomerová, J., Vecsey, L., 2012b. Seismic tomography of the upper mantle beneath the north-eastern Bohemian Massif (central Europe),
Tectonophysics, **564–565**, 1-11, doi:10.1016/j.tecto.2012.06.031

P3 Karousová, H., Plomerová, J., Babuška, V., 2013. Upper-mantle structure beneath the southern Bohemian Massif and its surroundings imaged by high-resolution tomography,
Geoph. J. Int.; 1-13, doi: 10.1093/gji/ggt159

P4 Karousová, H., 2013. User's Guide for tomographic code TELINV2012
http://www.ig.cas.cz/en/research-teaching/software-download

7 Acknowledgements

I would like to thank to all my colleagues and friends who helped and encouraged me during my studies. First of all, I express my gratitude to RNDr. Jaroslava Plomerová, DrSc., my supervisor, who guided me through most of my university studies, taught me much about various aspects of research, tomography and presentation scientific work and dedicated countless hours of her time to me. I also thank RNDr. Vladislav Babuška, DrSc. for his valuable advice, thoughtful reading of drafts and cheerful attitude to life. Next, I would like to thank Luděk Vecsey, my colleague, who was always ready to help, especially in shell and Matlab programming, as well as to Helena Munzarová for many hours of consultation and her friendly support. I am also grateful to Prof. Edi Kissling for his enthusiasm and fruitful discussions over the TELINV tomography code and to Tuna Eken who introduced me to the method of teleseismic tomography and helped me with first synthetic tests.

My special thanks belong to all the people in my workplace, the Institute of Geophysics of Academy of Sciences of the Czech Republic, for a nice and friendly work environment. I also thank all my teachers in the Department of Geophysics, Faculty of Mathematics and Physics, for their inspiring lectures and for their enthusiasm for work.

I would like to express special thanks to my family for their continuous interest and support. Finally, I thank to Tadeáš for his love, patience and encouragement during all this time.

The research was partly supported by grants Nos. 205/071088 and 210/12/2381 of the Grant Agency of the Czech Republic, by grant No. IAA300120709 of the Grant Agency of the Academy of Sciences of the Czech Republic, by grants Nos. SVV-2012-265308 and SVV-2013-267308 of Ministry of Education, Youth and Sports of the Czech Republic and by grant No.111-926 10/253101 of the Grant Agency of Charles University. Data acquisition from permanent observatories was supported through the project of large research infrastructure CzechGeo, grant no. LM2010008.

8 References

Achauer, U., Greene, L., Evans, J.R., Iyer, H.M., 1986. Nature of the Magma Chamber Underlying the Mono Craters Area Eastern California, as Determined From Teleseismic Travel Time Residuals. *J. Geoph. Res.*, 91, **B14**, 13873-13897.

Achauer, U., Masson, F., 2002. Seismic tomography of continental rifts revisited: from relative to absolute heterogeneities. *Tectonophysics*, **358**, 17-37, ISSN 0040-1951, 10.1016/S0040-1951(02)00415-8.

Aki, K., Lee, W. H. K. (1976). Determination of three-dimensional velocity anomalies under a seismic array using first P arrival time from local earthquakes: 1. A homogeneous initial model. *J. Geophys. Res.*, **81**, 4381-4399.

Aki K., Christoffersson, A., Husebye E.S., 1977. Determination of 3-dimensional seismic structure of lithosphere. *J. Geophys. Res.*, **82**, 277−296.

Arlitt, R., Kissling, E., Ansorge, J., 1999. Three-dimensional crustal structure beneath the TOR array and effects on teleseismic wavefronts. *Tectonophysics*, **314**, 309–319.

Arrowsmith, S.J., Kendall, M., White, N., VanDecar, J.C., Booth, D.C., 2005. Seismic imaging of a hot upwelling beneath the British Isles. *Geology*, **33**, 345-348.

Babuška, V., Plomerová, J., Šílený, J., 1984. Spatial variations of P residuals and deep structure of the European lithospere. Geophys. J.R. astr. Soc., **79**, 363-383.

Babuška, V., Plomerová, J., 2003. Seismic Experiment Searches for Active Magmatic Source in Deep Lithosphere, Central Europe. Eos, Transactions, Amer. *Geophys. U.*, **84**, 416-417.

Babuška, V., Plomerová, J., Vecsey, L., Jedlička, P., Růžek B., 2005. Ongoing passive seismic experiments unravel deep lithosphere structure of the Bohemian Massif. *Stud. Geophys. Geod.*, **49**, 423−430.

Babuška, V., Plomerová, J., Vecsey, L., 2008. Mantle fabric of western Bohemian Massif (central Europe) constrained by 3D seismic P and S anisotropy. *Tectonophysics*, **462**, 149-163, doi:10.1016/j.tecto.2008.01.020.

Babuška, V., Plomerová, J., 2013. Boundaries of mantle–lithosphere domains in the Bohemian Massif as extinct exhumation channels for high-pressure rocks. *Gondwana Research*, **23**, 973–987, doi.org/10.1016/j.gr.2012.07.005.

Benoit, M. H., Torpey, M., Liszewski, K., Levin, V., Park, J., 2011. P and S wave upper mantle seismic velocity structure beneath the northern Apennines: New evidence for the end of subduction. *Geochem. Geophys. Geosyst.*, **12**, Q06004, doi:10.1029/2010GC003428.

Behr, H.J., Dürbaum, H.J., Bankwitz, P., 1994. Crustal structure of the Saxothuringian Zone: Results of the deep seismic profile MVE-90 (East). *Z. Geol. Wiss.*, **22**, 647−769.

Beránek, B., Dudek, A., Zounková, M., 1975. Velocity models of the crust in the Bohemian Massif and the Western Carpathians (Rychlostní modely stavby zemské kůry v Českém masívu a Západních Karpatech). J. *Geol. Sci. Appl. Geophys. (Sborník geologických věd, Užitá Geofyzika)*, **13**, 7−17 (in Czech).

Behm, M., Brückl, E., Chwatal, W. Thybo, H., 2007. Application of stacking and inversion techniques to three-dimensional wide-angle reflection and refraction seismic data of the Alps. *Geophys. J. Int*., **170**, 275–298.

Bijwaard, H., Spakman, W., Engdahl, E.R., 1998. Closing the gap between regional and global travel time tomography. *J. Geophys. Res.*, **103**, 30055–30078.

Bijwaard, H., Spakman, W., 2000. Non-linear global P-wave tomography by iterated linearized inversion. *Geophys. J. Int.*, **141**, 71-82.

Dando, B. D. E., Stuart, G. W., Houseman, G. A., Heged, E., Brückl, E., Radovanovi, S., 2011. Teleseismic tomography of the mantle in the Carpathian–Pannonian region of central Europe. *Geophys. J. Int.*, **186**, 11–31, doi: 10.1111/j.1365-246X.2011.04998.x

Di Stefano, R., Kissling E, Chiarabba, C., Amato, A., Giardini D, 2009. Shallow subduction beneath Italy: Three-dimensional images of the Adriatic-European-Tyrrhenian lithosphere system based on high-quality P wave arrival times. *J. Geophys. Res. Solid Earth,* **114**, B05305.

Enderle, U., Schuster, K., Prodehl, C., Schulz, A., Bribach, J., 1998. The refraction seismic experiment GRANU95 in the Saxothuringian belt, southeastern Germany. *Geoph. J. Int.*, **133**, 245−259.

Eken, T., Shomali, H., Roberts, R., Bodvarsson, R., 2007. Upper mantle structure of the Baltic Shield below the Swedish National Seismological Networks (SNSN) resolved by teleseismic tomography. *Geophys. J. Int.*, **169**, 617–630.

Ellsworth, W., Koyanagi, R., 1977. Three-dimensional crust and mantle structure of Kilauea Volcano, Hawaii. *J. Geophys. Res.*, **82**, 5379–5394.

Evans, J. R., Achauer, U., 1993. Teleseismic velocity tomography using the ACH method: theory and application to continental scale studies, in: Iyer, H.M., Hirahara, K. (Eds.), Seismic Tomography. Chapman and Hall, London, 319–360.

Franke,W., 2000. Themid-European segment of the Variscides: tectonostratigraphic units, terrane boundaries and plate tectonic evolution. In: Franke,W., Haak, V., Oncken, O., Tanner, D. (Eds.),Orogenic Processes: Quantification and Modelling in the Variscan Belt: *Special Publication of the Geological Society,* **179**, 35-61 (London).

Geissler, W., Plenefisch T., Kind, R., 2005. The Moho structure in the western Eger Rift: A receiver function experiment. *Stud. Geophys. Geod.*, **44**, 188−194.

Geissler, W.H., Kämpf, H., Skácelová, Z., Plomerová, J., Babuška, V., Kind, R., 2012. Lithosphere structure of the NE Bohemian Massif (Sudetes) — A teleseismic receiver function study. *Tectonophysics*, 10.1016/j.tecto.2012.05.005.

Grad, M., Guterch, A., Mazur, S., Keller, G.R., Špičák, A., Hrubcová, P., Geissler W., 2008. Lithosperic structure of the Bohemian Massif and adjacent Variscian belt in central Europe based on profile S01 from SUDETES 2003 experiment. *J. Geophys. Res.*,**113**, B10304, doi: 10.1029/2007JB005497.

Granet, M., Wilson, M., Achauer, U., 1995. Imaging a mantle plume beneath the French Massif Central. *Earth Planet. Sci. Lett.*, **136**, 281–96.

Handy, M.R., Schmid, S.M., Bousquet, R., Kissling, E., Bernoulli, D., 2010. Reconciling plate-tectonic reconstructions of Alpine Tethys with the geological–geophysical record of spreading and subduction in the Alps. *Earth-Sci. Rev.*, **102**, 121–158.

Heuer, B., Geissler, W., Kind, R., 2006. Seismic evidence for asthenospheric updoming beneath the western Bohemian Massif, central Europe. *Geophys. Res. Lett.*, **33**, L05311, doi: 10.1029/2005GL025158.

Hrubcová, P., Środa, P., Špičák, A., Guterch, A., Grad, M., Keller, G.R., Brückl, E., Thybo H., 2005. Crustal and uppermost mantle stucture of the Bohemian Massif based on CELEBRATION 2000 data. *J. Geophys. Res.*, **110**, B11305, DOI: 10.1029/2004JB003080.

Hrubcová, P., Środa P., 2008. Crustal structure at the easternmost termination of the Variscan belt based on CELEBRATION 2000 and ALP 2002 data. Tectonophysics, **460**, 55−75.

Hrubcová, P., and Geissler W., 2009. The crust-mantle transition and the Moho beneath the Vogtland/West Bohemian region in the light of different seismic methods. *Stud. Geophys. Geod.*, **53**, 275−294.

Julia, J., Ammon, C.J., Herrmann, R.B., Correig, A.M., 2000. Joint inversion of the receiver function and the surface-wave dispersion observations. *Geophys. J. Int.*, **143**, 99−112.

Karousová, H., Plomerová, J., Babuška, V., 2012a. A three-dimensional velocity model of the crust of the Bohemian Massif. *Studia Geophys. Geod.*, **56**, 249-267, doi: 10.1007/s11200-010-0065-z.

Karousová, H., Plomerová, J., Babuška, V., 2012b. Seismic tomography of the upper mantle beneath the north-eastern Bohemian Massif (central Europe). *Tectonophysics*, **564–565**, 1-11, doi:10.1016/j.tecto.2012.06.031.

Karousová, H., Plomerová, J., Babuška, V., 2013. Upper-mantle structure beneath the southern Bohemian Massif and its surroundings imaged by high-resolution tomography. *Geoph. J. Int.*; 1-13, doi: 10.1093/gji/ggt159.

Karousová, H., 2013. TELINV2012 – User's Guide, http://www.ig.cas.cz/en/research-teaching/software-download

Kissling, E., 1988. Geotomography with local earthquake data. *Rev. Geophy.*, **26**, 659-698.

Kissling, E., Husen, S., Haslinger, F. 2001. Model parameterization in seismic tomography: a choise of consequence for the solution quality. *Phys. Earth Planet.In.,* **123**, 89-101pp.

Kissling, E., Schmid, S. M., Lippitsch, R., Ansorge, J., Fügenschuh, B., 2006. Lithosphere structure and tectonic evolution of the Alpine arc: New evidence from high-resolution teleseismic tomography. In European Lithosphere Dynamics, edited by D. G. Gee and R. A. Stephenson, *Mem. Gel. Soc.*, **32**, 129-145.

Kennett, B. L. N., Engdahl E. R., 1991. Traveltimes for global earthquake location and phase identification. *Geophys. J. Int.,* **105**, 429–465.

Koulakov I., Kaban M.K., Tesauro M., Cloetingh S., 2009. P- and S-velocity anomalies in the upper mantle beneath Europe from tomographic inversion of ISC data. *Geophys. J. Int.,* **179**, 345−366.

Lei, J., Zhao, D., Steinberger, B., Wu, B., Shen, F, Li, Z., 2009. New seismic constraints on the upper mantle structure of the Hainan plume. *Phys. Earth Planet.In.*,**173**, 33–50.

Levin, V., Shapiro, N., Park, J., Ritzwoller, M., 2002. Seismic evidence for catastrophic slab loss beneath Kamchatka. *Nature,* **418**, 763-767.

Li, C., van der Hilst, R., 2010. Structure of the upper mantle and transition zone beneath Southeast Asia from traveltime tomography. *J. Geophys. Res.*, **115**, B07308, 1-19.

Lippitsch, R., Kissling, E., Ansorge J., 2003. Upper mantle structure beneath the Alpine orogen from high-resolution teleseismic tomography. *J.Geophys. Res*., **108**, 2376.

Majdański, M., Grad, M., Guterch, A., 2006. 2-D seismic tomographic and ray tracing modelling of the crustal structure across the Sudetes Mountains basing on SUDETES 2003 experiment data. *Tectonophysics*, **413**, 249−269.

Martin, M., Ritter, J.R.R. and CALIXTO working group, 2005. High-resolution teleseismic bodywave tomography beneath SE Romania – I. Implications for three-dimensional versus onedimensional crustal correction strategies with a new crustal velocity model. *Geophys. J. Int.*, **162**, 448-460.

Masson, F., Achauer, U., Wittlinger, G., 1998. Joint analysis of P-traveltimes teleseismic tomography and gravity modelling for northern Tibet. *J. Geodynamics*, **26**, 85-109.

Menke, W., 1984. Geophysical data analysis: Discrete Inverse Theory. College of Oceanography, Oregon State University, Academic Press, Inc., pp. 303.

Mercier, J.-P., Bostock, M.G., Cassidy, J.F., Dueker, K., Gaherty, J.B., Garnero, E.J., Revenaugh, J., Zandt, G., 2010. Body-wave tomography of western Canada. *Tectonophysics*, **475**, 480–492.

Mitterbauer, U., Behm, M., Brückl, E., Lippitsch, R., Guterch, A., Keller, G. R., Koslovskaya, E., Rumpfhuber, E-M., Šumanovac, F., 2011. Shape and origin of the East-Alpine slab constrained by the ALPASS teleseismic model, *Tectonophysics*, **510**, 195–206.

Nataf, H.C., 2000. Seismic imaging of mantle plumes. *Annu. Rev. Earth Planet. Sci.,* **28**, 391–417.

Nolet, G., Montelli, R., 2005. Optimal parametrization of tomographic models. *Geophys. J. Int*., **161**, 365-372, doi: 10.1111/j.1365-246X.2005.02596.x.

Nolet, G., 2008. A Breviary of Seismic Tomography: Imaging the Interior of the Earth and Sun, Cambridge University Press, ISBN-10: 0521882443.

Pesicek, J.D., Thurber, C. H., Widiyantoro, S., Zhang, H., DeShon, H. R., Engdahl, E. R., 2010. Sharpening the tomographic image of the subducting slab below Sumatra, the Andaman Islands and Burma. *Geophys. J. Int.*, **182**, 433–453.

Pilidou, S., Priestley, K., Debayle, E., Gudmundsson, O., 2005. Rayleigh wave tomography in the North Atlantic: high resolution images of the Iceland, Azores and Eifel mantle plumes. *Lithos*, **79**, 453 – 474.

Piromallo, C., Morelli, A., 2003. P wave tomography of the mantle under the Alpine-Mediterranean area. *J. geophys. Res*., **108**, B22065, doi:10.1029/2002JB001757.

Plomerová J., Babuška V., Šílený J., Horálek J., 1998. Seismic anisotropy and velocity variations in the mantle beneath the Saxothuringicum-Moldanubicum contact in central Europe, *Pure and Appl. Geophys.*, **151**, 365-394.

Plomerová, J., Granet, M., Judenherc, S., Achauer, U., Babuška V. , Jedlička, P., Kouba, D., Vecsey, L., 2000. Temporary array data for studying seismic anisotropy of Variscan Massifs – The Armorican Massif, French Massif Central and Bohemian Massif. *Stud. Geophys. Geod.*, **44**, 195-209.

Plomerová J., Achauer U., Babuška V., Granet M., 2003. BOHEMA 2001-2003. Passive seismic experiment to study lithosphere-asthenosphere system in the western part of the Bohemian Massif. *Stud. Geophys. Geod.*, **47**, 691−701.

Plomerová, J., Vecsey, L., Babuška, V., Granet, M., Achauer, U., 2005. Passive seismic experiment MOSAIC - a pilot study of mantle lithosphere anisotropy of the Bohemian Massif. *Stud. Geophys. Geod*., **49**, 541−560.

Plomerová, J., Achauer, U., Babuška, V., Vecsey, L., 2007. Upper mantle beneath the Eger Rift (Central Europe): plume or asthenosphere upwelling? *Geophys. J. Int*., **169**, 675-682.

Plomerová, J.,, Babuška, V., 2010. Long memory of mantle lithosphere fabric — European LAB constrained from seismic anisotropy. *Lithos*, **120**, 131–143.

Plomerová, J., Vecsey, L., Babuška, V., 2013. Mapping seismic anisotropy of the lithospheric mantle beneath the northern and eastern Bohemian Massif (central Europe). *Tectonophysics*, **564–565**, 38–53.

Poupinet, G., Avouac, J.P., Jiang, M., 2002. Intracontinental subduction and Palaeozoic inheritance of the lithosphere suggested by a teleseismic experiment across the Chinese Tien Shan. *Terra Nova*, **14**, 18-24.

Rawlinson, N. Sambridge, M., 2005. The fast marching method: an effective tool for tomographic imaging and tracking multiple phases in complex layered media, *Exploration Geophysics*, **36**, 341 – 350, doi:10.1071/EG05341.

Rawlinson, N., Pozgay, S., Fishwick, S., 2010. Seismic tomography: A window into deep Earth, *Phys. Earth Planet.In.*, **178**, 101-135, ISSN 0031-9201, 10.1016/ j.pepi.2009.10.002.

Ritter, J.R.R., Jordan, M., Christensen, U.R., Achauer, U., 2001. A mantle plume below the Eifel volcanic fields, Germany. *Earth Planet. Sc. Lett.*, **186**, 7-14.

Roecker, S., Baker, B., McLaughlin, J., 2013. A Finite-Difference Algorithm for Full-Waveform Teleseismic Tomography, submitted to *Geophys. J. Int.*

Růžek, B., Hrubcová, P., Novotný, M., Špičák, A., Karousová, O., 2007. Inversion of travel times obtained during active seismic refraction experiment CELEBRATION 2000, ALP 2002 and SUDETES 2003. *Stud. Geophys. Geod*., **51**, 141−164.

Růžek, B., Holub K., Rušajová, J., 2011. Three-dimensional crustal model of the Moravo- Silesian region obtained by seismic tomography. *Stud. Geophys. Geod.*, **55**, 87−107.

Sandoval, S., Kissling, E., Ansorge, J. and SVEKALAPKO Seismic Tomography Working Group, 2003. High-resolution body wave tomography beneath the SVEKALAPKO array: I. A priory three dimensional crustal model and associated travel-time effects on teleseismic tomographic wave fronts. *Geophys. J. Int.*, **153**, 75-87.

Sandoval, S., Kislling, E., Ansorge, J., SVEKALAKO Seismic Tomography working Group, 2004. High-resolution body wave tomography beneath the SVEKALAPKO array — II. Anomalous upper mantle structure beneath the central Baltic Shield. *Geophys. J. Int.*, **157**, 200–214, doi: 10.1111/j.1365-246X.2004.02131.x.

Shomali, Z.H., Roberts, R.G., Pedersen, L.B., the TOR Working Group, 2006. Lithospheric structure of the Tornquist Zone resolved by nonlinear P and S teleseismic tomography along the TOR array. *Tectonophysics*, **416**, 133–149.

Spakman, W., Bijwaard, H., 2001. Optimization of Cell Parameterizations for Tomographic Inverse Problems. *Pure appl. geophys.*, **158**, 1401-1423.

Souriau, A., Chevrot, S., Olivera, C., 2008. A new tomographic image of the Pyrenean lithosphere from teleseismic data. *Tectonophysics*, **460**, 206–214.

Steck, L. K., Prothero, W.A., 1991. A 3-D ray-tracer for teleseismic body-wave arrival-times. *B. Seismol. Soc. Am.*, **81**, 1332-1339.

TELINV2012 code http://www.ig.cas.cz/en/research-teaching/software-download

Tilmann, J.T., 1999. The seismic structure of the upper mantle beneath Hawaii. PhD. thesis, Cambridge, 177.

Tromp, J., Tape, C., Liu, Q., 2004. Seismic tomography, adjoint methods, time reversal and banana-doughnut kernels. *Geophys. J. Int.*, **160**, doi: 10.1111/j.1365-246X.2004.02453.x.

Vecsey, L., Plomerová., J., Babuška, V. and PASSEQ Working Group, 2013. Structure of the mantle lithosphere around the TESZ - from the East European Craton to the Variscan Belt. EGU 2013-3133.

Waldhauser, F., Lippitsch, R., Kissling, E., Ansorge, J., 2002. High-resolution teleseismic tomography of the upper mantle structure using a-priori three-dimensional crustal model. *Geophys. J. Int.*, **150**, 403-414.

Weiland, C.M., Steck, L.K., Dawson, P.B., Korneev, V.A., 1995. Nonlinear teleseismic tomography at Long Valley caldera, using three-dimensional minimum travel time ray tracing. *J. Geophys. Res.*, **100**, 20379–20390.

Widiyantoro, S., van der Hilst, R.D., 1997. Mantle structure beneath Indonesia inferred from high-resolution tomographic imaging. *Geophys.J. Int.*, **130**, 167–182.

Wilde-Piórko, M., Geissler, W. H., Plomerová, J., Grad, M., Babuška, V., Brückl, E., Cyziene, J., Czuba, W., England, R., Gaczyński, E., Gaždová, R., Gregersen, S., Guterch, A., Hanka, W., Hegedűs, E., Heuer, B. Jedlička, P., Lazauskiene, J., Keller, G. R., Kind, R., Klinge, K., Kolinský, P., Komminaho, K., Kozlovskaya, E., Krüger, F., Larsen, T., Majdański, M. , Málek, J., Motuza, G., Novotný, O., Pietrasiak, R., Plenefisch, Th., Růžek, B., Sliaupa, S. , Środa, P., Świeczak, M., Tiira, T., Voss, P., Wiejacz, P., 2008. PASSEQ 2006-2008: Passive seismic experiment in Trans-European Suture Zone. *Stud. Geophys. Geod.*, **52**, 439−448.

Wortel, R., Govers, R., Spakman, W., 2009. Continental Collision and the STEP-wise Evolution of Convergent Plate Boundaries, in: Lallemand, S.; Funiciello, F. (Eds.), From Structure to Dynamics, Subduction Zone Geodynamics. Book Series: Frontiers in Earth Sciences, 47-59.

Zhao, D., 2004. Global tomographic images of mantle plumes and subducting slabs: insight into deep Earth dynamics. *Phys. Earth Planet.Int.*, **146**, 3–34.

Zhao, D., 2007. Seismic images under 60 hotspots: Search for mantle plumes. *Gondwana Research*, **12**, 335–355.

PART II

P1

A three-dimensional velocity model of the crust of the Bohemian Massif

Karousová, H., Plomerová, J. and Babuška, V.

Studia Geophys. Geod., 56, 249-267, Doi: 10.1007/S11200-010-0065-Z., 2012

Three-dimensional velocity model of the crust of the Bohemian Massif and its effects on seismic tomography of the upper mantle

HANA KAROUSOVÁ, JAROSLAVA PLOMEROVÁ AND VLADISLAV BABUŠKA

Institute of Geophysics, Acad. Sci. Czech Republic, Boční II/1401, 141 31 Praha 4, Czech Republic (hanak@ig.cas.cz, jpl@ig.cas.cz, babuska@ig.cas.cz)

Received: August 6, 2010; Revised: March 31, 2011; Accepted: June 20, 2011

ABSTRACT

We have compiled a representative three-dimensional P-velocity model of the crust of the Bohemian Massif (BM) to provide a basis for removing effects of the crustal structure in teleseismic tomography of the upper mantle. The model is primarily based on recently published 2D velocity models from findings of wide-angle refraction and near-vertical reflection seismic profiles of CELEBRATION 2000, ALP 2002, and SUDETES 2003 experiments. The best fitting 3D model of the BM crust (NearNeighbour model) is complemented by velocities according to the reference Earth model at sites where data are sparse, which precludes creating artificial heterogeneities that are products of interpolation method. To test the model, we have performed tomographic inversions of the P-wave travel times measured during the BOHEMA II experiment and compared the results obtained with and without crustal corrections. The tests showed that the presented crustal model decreases magnitudes of velocity perturbations leaking from the crust to the mantle in the western part of the BM. The tomographic images also indicated a high-velocity anomaly in the lower crust or just beneath the crust in the Brunovistullian unit. Such anomaly is not described by our model of the crust since no seismic profile intersects this part of the unit. The tests also indicated that crustal corrections are of the great importance especially for interpretations of the uppermost mantle down to depths of about 100 km.

Keywords: crustal structure, seismic methods, Bohemian Massif, teleseismic tomography

1. INTRODUCTION

A number of active and passive seismic experiments accomplished on the territory of the Bohemian Massif (BM) provided numerous data interpreted in several mostly 2D models of the crust. A research of the structure of the BM crust began in 1960's along two perpendicular refraction profiles VI and VII (e.g., *Beránek et al., 1975*; see Fig. 1 for the locations of seismic profiles) and resulted in Moho depth estimates. The authors found the deepest Moho at about 40 km in the Moldanubian part of the BM and the shallowest Moho at about 27 km beneath the Saxothuringian part. The highly reflective lower crust

of the Saxothuringian was detected along reflection profile MVE90 (*Behr et al., 1994*), two refraction profiles 95A and 95B in GRANU 95 experiment (*Enderle et al., 1998*), and along the Saxothuringian part of wide-angle refraction seismic profile CEL09 (*Hrubcová et al., 2005*). Several seismic refraction profiles, namely CEL09, CEL10, S01-S06, and ALP01 from active refraction experiments CELEBRATION 2000, ALP 2002, and SUDETES 2003, resulted in the 2D velocity-depth models (*Hrubcová et al., 2005*; *Majdanski et al., 2006*; *Brückl et al, 2007*; *Růžek et al., 2007*; *Grad et al., 2008*; *Hrubcová and Sroda, 2008*). A local 3D model of the northern part of the BM was developed from travel times of POLONAISE'97, CELEBRATION 2000, and SUDETES 2003 experiments (*Majdanski et al., 2007*). *Málek et al. (2005)* derived 1D velocity model of the upper crust for the west Bohemia/Vogtland earthquake swarm region from travel times of controlled shots and from earthquakes recorded at stations of the local network. Pg and Sg phases, recorded during the several active experiments with mostly 2D geometry, were employed in seismic tomographic model of the Moravo-Silesian region (Fig. 1) by *Růžek et al. (2011).* Velocity structure and the Moho depth were also modelled from surface-wave dispersions (*Wielandt et al., 1987*; *Novotný et al., 1995, 1997*; *Neunhöfer et al., 1981, 1983*) and from receiver functions (*Wilde-Piórko et al., 2005*; *Geissler et al., 2005*; *2010; Heuer et al., 2006*; *Růžek et al., manuscript in preparation, 2011*).

Velocity models from active seismic experiments and local tomography provide enough data for developing a 3D model of the crust. Such model is essential for high-resolution studies of velocity structure and anisotropy of the lithospheric mantle, which has been a main target of passive seismic experiments in central Europe, particularly the MOSAIC, BOHEMA I-III, and PASSEQ 2006-2008 (*Plomerová et al., 2003, 2005*; *Babuška et al., 2005*; *Wilde-Piorko et al., 2008*). Teleseismic tomography represents one of the most powerful methods to look into the Earth interior. Due to the ray geometry of teleseismic waves, the regional tomography requires a-priori information about the crustal structure to separate effects from the crust and those from the upper mantle. *Waldhauser at el. (1998, 2002)*, *Martin et al. (2005)*, or *Sandoval et al. (2003)* point out that crustal models from independent datasets are of a great importance for tomographic studies, but also warn that application of unrealistic models of the crust, or neglecting crustal corrections, can distort results of tomographic images of the upper mantle. Objective of this paper is to compile a 3D velocity distribution from all available individual results, particularly from the CSS (control source seismology), and to create a representative tree-dimensional P-velocity model of the BM crust defined in a regular grid. This paper also aims at testing effects of this model on tomographic images of the upper mantle with the use of inversions of observed and synthetic teleseismic P-wave travel times, and ray-geometry of the BOHEMA II experiment.

2. TECTONIC SETTING

The BM is the most prominent surface exposure of basement rocks in central Europe. It is a part of the Variscan orogenic belt (Fig. 1) representing a collage of magmatic arcs and microcontinents resulting from the collision of supercontinents Laurasia (Laurentia-Baltica) and Africa (Gondwana). The principal division of the BM into the Saxothuringian, Moldanubian, Teplá-Barrandian, and the Moravo-Silesian units was

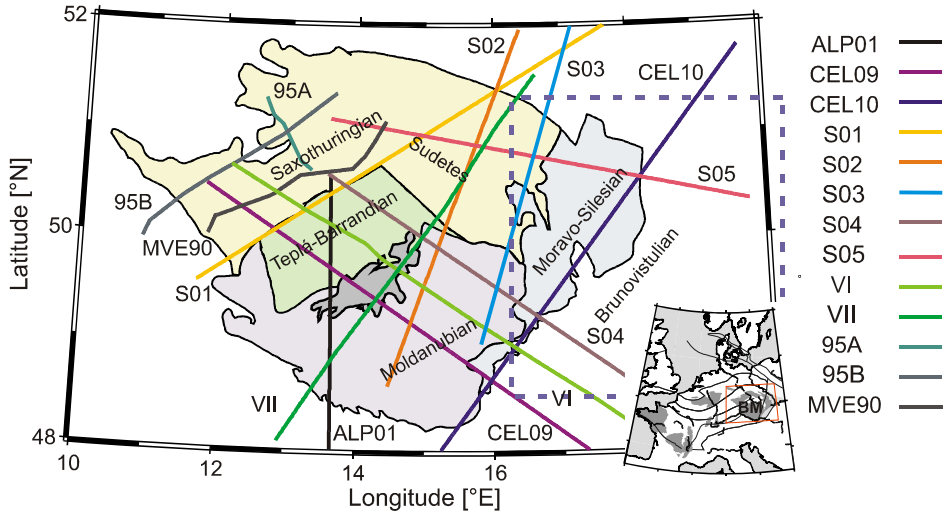

Fig. 1. Map of refraction and reflection profiles (*Beránek et al., 1975*; *Behr et al., 1994*; *Enderle et al., 1998*; *Hrubcová et al., 2005*; *Majdanski et al., 2006*; *Růžek et al., 2007*; *Hrubcová and Sroda, 2008*; *Grad et al., 2008*) intersecting the Bohemian Massif (BM). The dashed rectangle marks location of the tomographic model of the Moravo-Silesian region by *Růžek et al. (2011)*. The inset locates the BM within the European Variscides.

introduced into the literature by various authors starting with *Kossmat (1927)* (see also *McCann et al., 2008*).

The Saxothuringian unit (ST, see, e.g., *Linnemann et al, 2000* and references therein) is situated along the northern rim of the BM. The autochtonous Saxothuringian unit, including non-metamorphic nappes (*Dallmeyer et al., 1995*), contains Cadomian basement of Neoproterozoic to Early Cambrian arc-related volcano-sedimentary low-grade rock complexes and plutonic massifs, transgressed by Cambro-Ordovician overstep sequences with passive margin signatures. The principal tectonometamorphic overprint is of the Variscan age and locally reaches the amphibolite-facies grade. Variscan evolution terminates by post-tectonic intrusions of granitoid rocks, as in the whole BM.

The Teplá-Barrandian (TB), separated from the ST unit by a relict Devonian oceanic suture, is the best-preserved fragment of a peri-Gondwanan microplate incorporated in Central European Variscides (for a review see *Franke, 2000*). Its Cadomian basement is formed by arc-related Neoproterozoic sediments and volcanic rocks, which have undergone a very low-grade to amphibolite-facies metamorphism and deformation at ca. 550–540 Ma (*Zulauf et al., 1997*). The Cadomian basement is transgressed by Cambrian to Ordovician passive-margin sequences. The sedimentation and volcanism then continued up to the Middle Devonian in the Prague Basin (*Patočka and Štorch, 2004*).

The Moldanubian unit (MD) outcropping in the SW part of the studied region represents the largest high-grade crystalline segment within the BM, most probably also of Gondwanan origin (e.g., *Pharaoh, 1999*). The unit contains mainly gneisses and migmatites, locally with quartzites and marbles of supracrustal original lithology, orthogneisses, amphibolites, as well as exotic rocks, such as granulites, various

peridotites, and eclogites. Numerous Variscan syn- to post-tectonic granitoid intrusions are characteristic throughout the whole Moldanubian area. The orthogneiss magmatic protoliths vary in ages from Middle Proterozoic (*Wendt et al., 1993*) through Neoproterozoic, Cambrian up to Devonian (*Vrána, 1997*). The Sudetes, forming the northeastern part of the BM, include diverse parts of the Saxothuringian and Moldanubian units.

The easternmost part of the BM is occupied by the Moravo-Silesian unit (MS) that comprises syn-orogenic Early Carboniferous and a pre-orogenic Devonian sedimentary succession of the former Moravo-Silesian Basin. This succession, up to 7.5 km thick, was strongly deformed by Variscan thrusting and folding (*McCann et al., 2008*). Its overall tectonics is the result of the collisional interaction of the late Neoproterozoic basement unit named the Brunovistulian block with the Variscan collage consisting of the Moldanubian and the Sudetes to the west (*Matte et al., 1990*). The Brunovistulian, originally described by *Dudek (1980)* as Brunovistulicum, represents according to *Kalvoda et al. (2008)* a microcontinent that was located at the southern margin of Baltica in the early Paleozoic.

3. DATA AND METHOD

The BM is well-covered by CSS profiles (Fig. 1). We collected velocity models along wide-angle refraction and reflection profiles VI, VII, MVE90, 95A, 95B, ALP01, CEL09, CEL10, S01-S05, and 3D local tomography (Fig. 1 and references therein).

The 1D velocity-depth distributions along profiles VI and VII (*Beránek et al., 1975*) derived from traveltime curves of refracted and reflected waves and spaced at steps of about 70 km were reviewed in *Novotný and Urban (1988)*. We digitized manually the graphic images of a velocity distribution along profiles MVE90 (*Behr et al., 1994*), 95A and 95B (*Enderle et al., 1998*) with vertical sampling from 1 to 6 km. Horizontal spacing of the velocity distribution along profile MVE90 was 25 km, while the models along profiles 95A and 95B are sampled at sites of explosions (*Enderle et al., 1998*). All the models mentioned above supplied the velocities from the surface to the Moho discontinuity. Data from numerical models of CEL09 (*Hrubcová et al., 2005*), CEL10 (*Hrubcová and Sroda, 2008*), S01 (*Grad et al., 2008*), S02 and S03 (*Majdanski et al., 2006*) were provided in a grid of 10 km in horizontal and 1 km in vertical directions down to depths of 70 km. Velocity models along MVE90 (*Behr et al., 1994*), 95A and 95B (*Enderle et al., 1998*) , CEL09 (*Hrubcová et al., 2005*), CEL10 (*Hrubcová and Sroda, 2008*), S01 (*Grad et al., 2008*), S02 and S03 (*Majdanski et al., 2006*) profiles were interpreted by combination of tomographic inversions and ray tracing modelling of both refracted and reflected phases. The velocity models along profiles ALP01, CEL09, CEL10, and S01-S05 (*Růžek et al., 2007*) were provided with a horizontal spacing of 10 km and irregular vertical sampling down to depths of 45 km. These models resulted from inversion with two steps: parametric one in which interfaces were parameterized and tomographic step, in which velocity perturbations were introduced (*Růžek et al., 2007*). In the Moravo-Silesian region (Fig. 1), we selected only those parts of a 3D local tomography (*Růžek et al., 2011*), where diagonal terms of the resolution matrix were higher than 0.5; the model is parameterized in irregular grid to depths of 15 km.

Along some of the profiles, two different velocity models were published in original papers. In such cases, we chose only the models that authors interpreted also by trial-and-error ray tracing modeling where quality of agreement of observed and synthetic data could be evaluated. Thus we did not use the models along S02, S03, CEL09, CEL10 profiles by *Růžek et al. (2007)*. We also did not include the model along the S04 profile by *Růžek et al. (2007)* because it has very complex structure with unlikely strong lateral heterogeneities e.g., velocities lower than 5.5 km/s observed down to depths at about 30 km surrounded by velocities up to 7.5 km/s in the SE part of the profile S04.

For the model of the crust, the geographical coordinate system was transformed into the Cartesian coordinate system with an origin in longitude of 16°E and latitude of 50°N using commands of General Mapping Tools (GMT; *Wessel and Smith, 1995*). The origin of coordinate system is selected according to distribution of seismic stations in passive seismic experiment BOHEMA II. We derived two new 3D models of the crust by applying two interpolation methods. First, we have used a 3D linear interpolation that led to a LinInterp model (Fig. 2). Second, we have applied a nearest neighbour method to derive velocities at bands - 60 km wide - along 2D velocity profiles and at sites up to

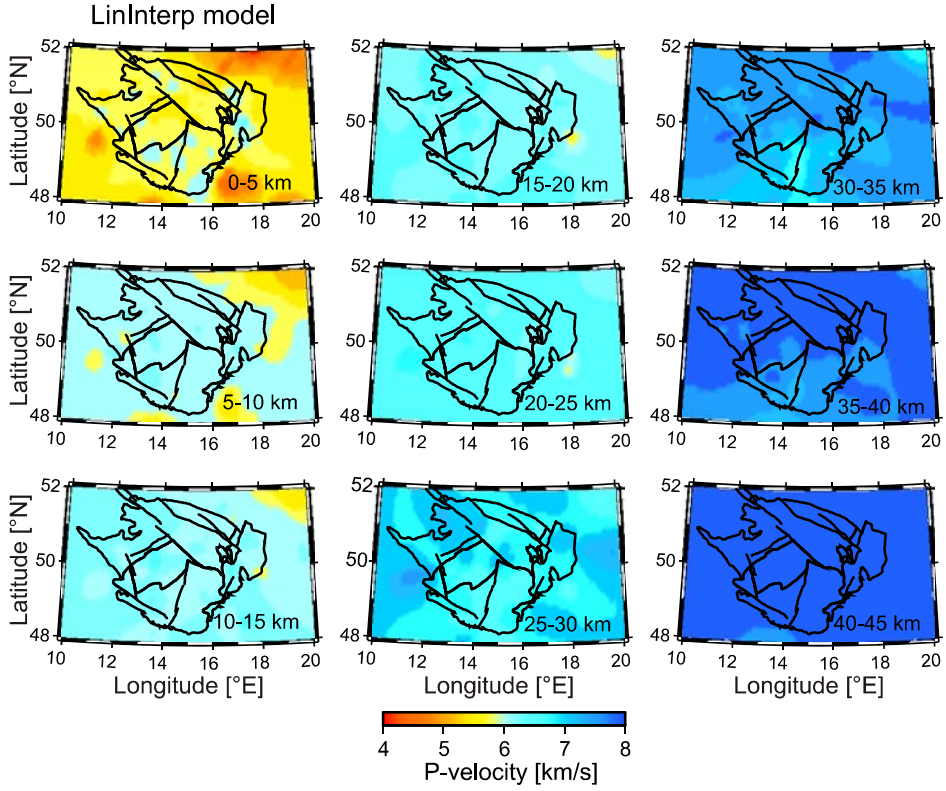

Fig. 2. P-velocities averaged for 5 km thick layers of the 3D LinInterp model of the crust. Lines show tectonic units of BM (as shown in Fig. 1) and main faults.

30 km from individual nodes of well-resolved parts of the 3D local tomography model (*Růžek et al., 2011*). The different sizes of bands along profiles and diameters around nodes were tested. These velocities were complemented by the 1D reference model IASP91 (*Kennet and Engdahl, 1991*). The procedure resulted in a NearNeighbour model (Fig. 3). Both models were smoothed by weighted averaging of velocities at a particular node and at six nearest nodes - four nodes in the horizontal dimension and two nodes in the vertical dimension. The models of the crust have a size of 650 × 400 × 50 km and the velocities are defined in regular grid of 5 × 5 × 1 km.

To complement the models by information about sediments which cannot be described either by 2D velocity profiles or by 3D local tomography in detail, we have found from unpublished sources approximate thicknesses and P-wave velocities of sediments (Fig. 4) for the stations of the BOHEMA II experiment. Considering low velocities (around 4 km/s) at shallow depths included in the models LinInterp and NearNeighbour (see Section 4), we calculated station corrections (static terms) and applied them in the second tomographic test with observed travel times (see Section 5).

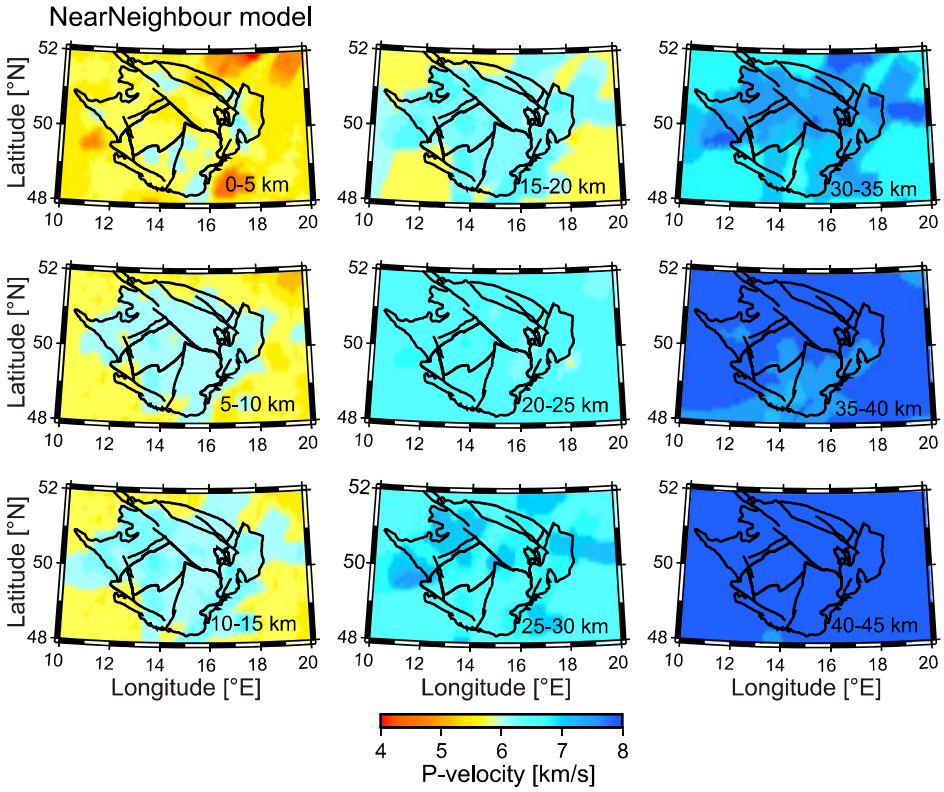

Fig. 3. P-velocities averaged for 5 km thick layers of the 3D NearNeighbour model of the crust. Lines show tectonic units of BM (as shown in Fig. 1) and main faults.

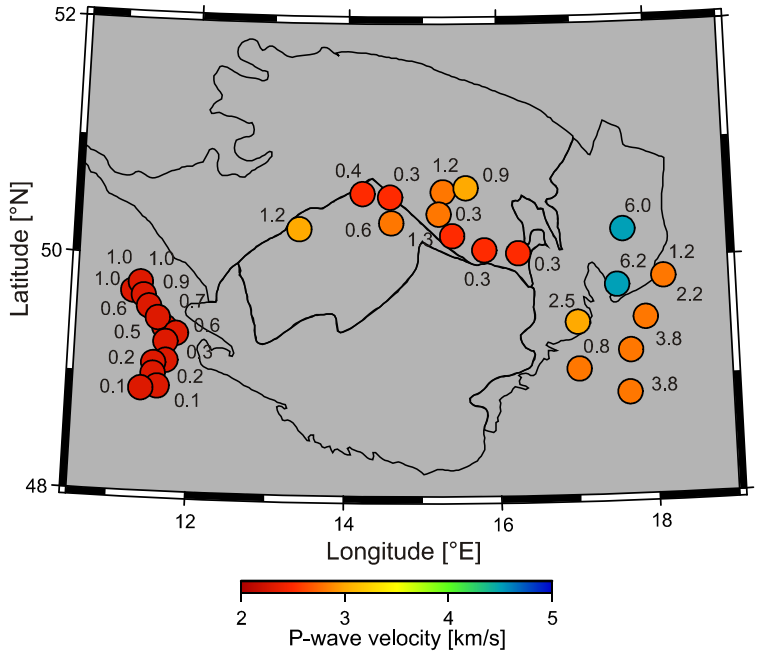

Fig. 4. Sediment thicknesses (numbers in kilometres) beneath stations of the BOHEMA II array and averaged P-velocities of these sediments applied in crustal corrections.

In order to analyse the effects of crustal heterogeneities in the LinInterp and NearNeighbour models on tomographic images of the upper mantle, we invert synthetic and observed travel times. We use non-linear inversion technique based on ACH method (*Aki et al., 1977*; *Evans and Achauer, 1993*). Forward modelling of travel times, considering station elevations above the sea level, is performed by 3D ray-tracing method by *Steck and Prothero (1991)*. An iterative scheme inverts the velocity variations relatively to a reference Earth model, in our case the IASP91 model, which was also used for calculations of theoretical travel times. The damping factor of 100 was applied as a result of tomographic tests (*Karousová et al., submitted to Tectonophysics, 2011*). We employ the station array of the BOHEMA II experiment (Fig. 5a) consisting of 61 permanent and temporary stations *(Babuška et al., 2005*; *Plomerová et al., 2011*; *Geissler et al., submitted to Tectonophysics, 2011*). We have selected 203 teleseismic events (Fig. 5b) with a magnitude higher than 4.5, recorded during a one-year period, which provided 10236 rays. The inversion grid is adjusted according to the station and event distribution. Horizontal grid is of 30×30 km for the whole volume studied. Vertical spacing is set to 45 km in the upper mantle at depths down to 350 km and to 15–20 km in the crust. The shallowest inverted nodes lie at depth of 35 km and thus velocity perturbations in these nodes are affected by both crustal and upper mantle heterogeneities.

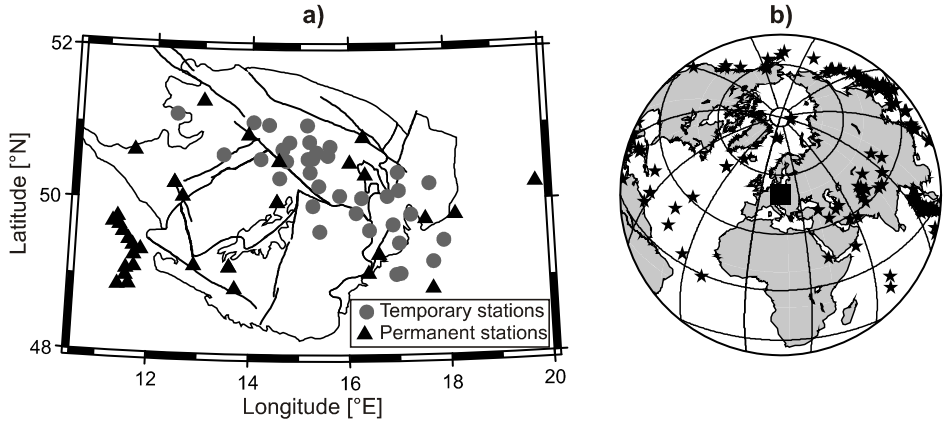

Fig. 5. **a)** Map of seismic stations and **b)** event distribution of BOHEMA II experiment. Black square represents the study area enlarged in Fig. 5a.

4. 3D MODELS OF THE CRUST

The models are plotted in nine 5 km thick layers, whose velocities are averages of values in five depth levels of nodes (Figs. 2 and 3). Similar velocity distributions of both models are observed at the shallowest depths, where velocities are mostly around 5.8 km/s, but there are regions with lower velocities, around 4–5 km/s, in the north-eastern and south-eastern edges of the models, as well as several small-size regions with higher velocities, mainly in the MD unit. Good agreement between the LinInterp and NearNeighbour model at depths from 5 to 20 km is generally observed at their central parts, where velocities vary from 6 to 7 km/s. This velocity range is also valid for rims of the LinInterp model, while velocities at rims of the NearNeighbour model are 5.8 km/s. A layer from 20 to 25 km is characteristic by velocities around a constant value of 6.5 km/s for both models. Velocities of both models at depths between 20 and 35 km range from 6.5 to 8 km/s; however, the models differ significantly in parts, where data are sparse. At depths from 35 to 45 km, velocities are predominantly around 8 km/s, with relatively low velocities (7–7.5 km/s) in southern parts of the models, which corresponds to a Moho deepening in that region (see Fig. 8 later).

5. EFFECTS OF 3D CRUSTAL MODELS ON TOMOGRAPHIC IMAGES OF THE UPPER MANTLE

To study effects of the crustal models on tomography of the upper mantle, we perform two types of tests. By inverting synthetic travel times, we test how crustal heterogeneities are mapped into the upper mantle velocities if no crustal corrections are applied. By inverting observed travel times, we intend to choose the most suitable model of the BM crust for correcting of its effects on teleseismic tomography.

In the first tests (Fig. 6), we invert synthetic data generated by the 3D crustal models LinInterp or NearNeighbour and the upper mantle with no a-priori heterogeneity. Extremes of magnitudes of recovered velocity perturbations lie at the depth of 35 km and are in a range between −6.1% and 7.5% for the LinInterp model and between −3.8% and 3.9% for the NearNeighbour model. Magnitudes of perturbations slightly decrease with depth and their extremes below depths about 150 km are from −1.8% to 2.3% and from −1.2% to 1.1% for the LinInterp and NearNeighbour model, respectively. Velocity perturbation distributions for the LinInterp and NearNeighbour model differ significantly. For example, low- and high-velocity anomalies are observed in recovered velocity perturbations corresponding to the LinInterp crust beneath both the MS and the Brunovistulian units at depth of 35 km, while recovered velocity perturbations corresponding to the NearNeighbour crust show anomalies of nearly opposite signs there. Although the crustal models are very similar in their central parts, the recovered models of the upper mantle differ considerably both in magnitudes and in the distributions of velocity perturbations.

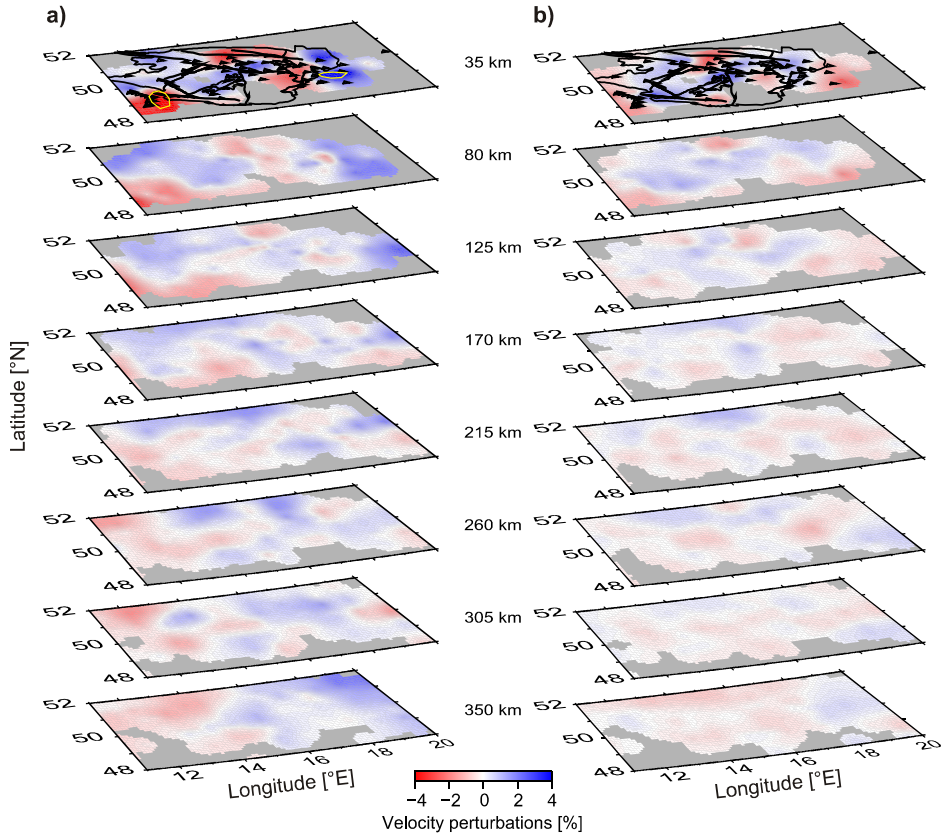

Fig. 6. Recovered P-wave velocity perturbations after inverting only the travel-time residuals generated by: **a)** the LinInterp, and **b)** NearNeighbour crustal models.

According to the first test, neglecting of the crustal corrections can complicate or disallow interpretations of velocity perturbations of the uppermost mantle supposing that the LinInterp and the NearNeighbour models are close to a real structure of the BM crust. Another conclusion of the test is that the NearNeighbour is more conservative than the LinInterp model as it results in generally lower magnitudes of velocity perturbations.

In the second tests (Fig. 7), we inverted the P-wave travel times measured during the BOHEMA II experiment and cleansed of time instabilities and individual picking errors (*Karousová et al., submitted to Tectonophysics., 2011*). These data were inverted (1) without crustal corrections applied, (2) with crustal corrections according to the LinInterp model, and (3) with crustal corrections according to the NearNeighbour model. The inversions with crustal corrections included static terms correcting the travel times for the sediments beneath the stations. The observed travel times were corrected for the crust by subtracting differences between the travel times within the 3D model of the crust, representing the structure which is close to a real one, and the travel times within the IASP91 crust. Velocity perturbations are affected by discrepancies between the crustal model applied and a real velocity structure particularly at depth of 35 km. We expect

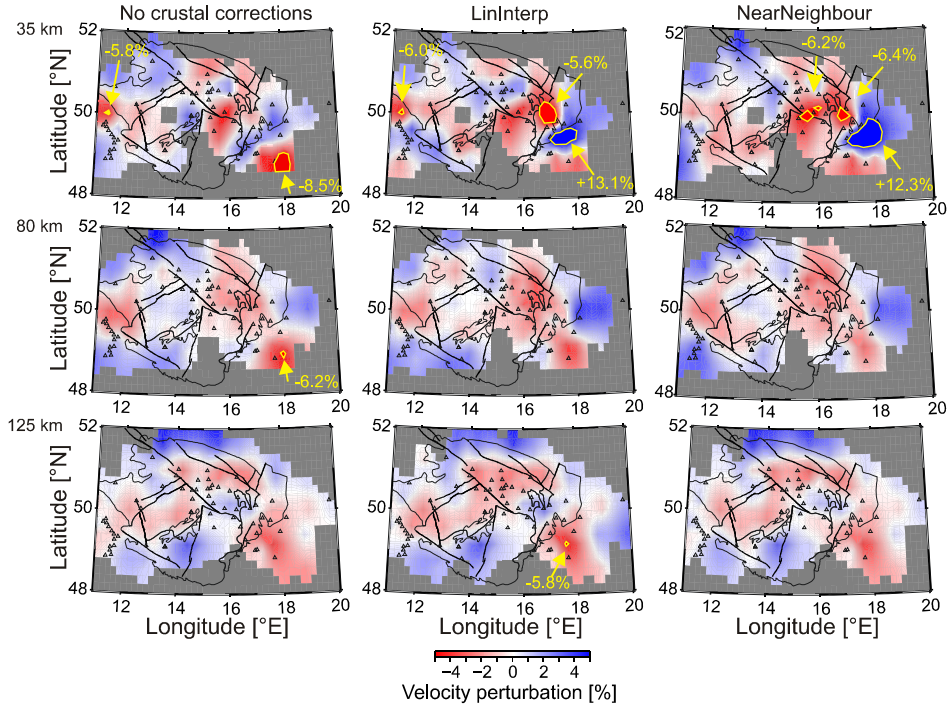

Fig. 7. Images of P-wave velocity perturbations at depth of 35, 80, and 125 km of three inversions of data based on observed P-waves travel times: without crustal corrections (left), with crustal corrections according to the LinInterp model (middle) and with crustal corrections according to the NearNeighbour model (right). Unresolved areas are marked by grey colour. Lines show tectonic units of BM (as shown in Fig. 1) and main faults.

Table 1. Velocity perturbations and variance reductions of data inverted with and without crustal corrections. CC - crustal correction.

Inversion	Variance Reduction [%]	P-Velocity Perturbations [%]					
		Depth of 35 km			Depth of 80–350 km		
		Min	*Max*	*Range*	*Min*	*Max*	*Range*
No CC	82.1	–8.55	4.54	13.10	–6.29	4.55	10.84
CC According to LinInrterp Model	80.3	–7.72	13.14	20.86	–5.85	5.22	11.08
CC According to NearNeighbour Model	81.9	–6.40	12.30	18.70	–5.41	5.20	10.61

a decrease of magnitudes of velocity-perturbation at this depth if the crustal model approximates well the BM crust.

Differences between distributions of recovered velocity perturbations in the inversions performed with or without crustal corrections are observable down to a depth of 125 km (Fig. 7). The result of inversion without crustal corrections is characteristic by majority of perturbations between –5% and 5%. The extremes of velocity perturbations are at depth of 35 km beneath the south-eastern margin of the model with negative perturbations down to –8.5%, and two anomalies with perturbations around –6% at depth of 35 km beneath the western edge of the model and at a depth of 80 km beneath the south-eastern margin of the model. After applying the crustal corrections according to either the LinInterp model or the NearNeighbour model, magnitudes of perturbations increased, particularly beneath the MS unit and the Brunovistulian where the maximum of velocity perturbations attain up to +13% at a depth of 35 km. However, magnitudes of velocity perturbations corresponding to the NearNeigbour model decreased in the western part of the BM compared with velocity perturbations corresponding to inversion without crustal corrections. Ranges of velocity perturbations for all three models are summarized in Table 1. We also compared variance reductions for the inversions. They are very similar, ranging from 80% to 82%.

Though the test showed that the crustal corrections change the recovered velocity perturbations significantly at a depth of 35 km, gross features of the images of the mantle-velocity perturbations remain unchanged in all the models. It indicates that the crustal corrections of teleseismic data in tomography of the upper mantle are the most important for interpreting the uppermost mantle structure down to depths about 100 km.

6. DISCUSSION

Moho depths (Fig. 8) compiled from the 2D velocity models along the CSS profiles described in Section 3 clearly show a thickening of the crust from the north to the south with the deepest Moho at about 40 km beneath the southern Moldanubian. The profile ALP01 (*Brückl et al., 2007*) indicates that the crustal thickening continues further to the south towards the Alps. A thin crust (~30 km) is observed beneath the Saxothuringian unit and beneath the north-eastern extreme of the Moravo-Silesian unit. The local thickening

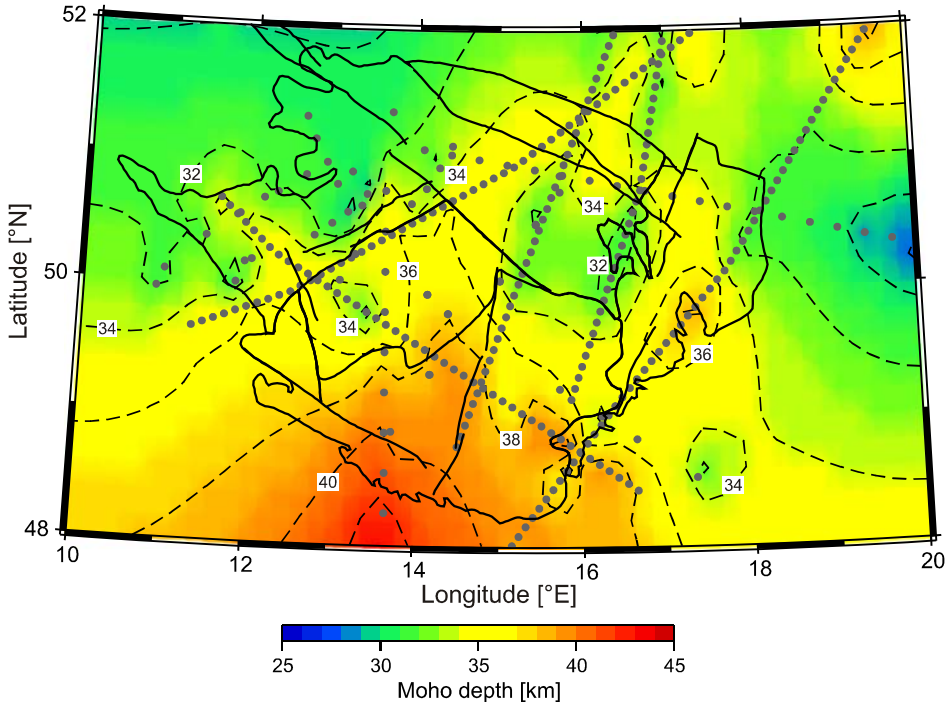

Fig. 8. Compiled Moho depths (dashed isolines) based on the CSS velocity models along the profiles indicated by dotted lines. Solid lines show tectonic units of BM (as shown in Fig. 1) and main faults.

(>36 km) at the eastern limit of the BM might be related to the late Neoproterozoic Brunovistulian block (see Fig. 1). We can say that our representative crustal model is a conservative one that does not include extremely shallow Moho depths of receiver function observations, as discussed bellow.

While selecting our dataset for compilation of the crustal model, we have excluded results based on receiver functions. The main reason are the discrepancies between Moho depths derived from the receiver functions and those from the CSS method along profile CEL09 (Fig. 9); another reason for that is the non-uniqueness of depths of interfaces interpreted by receiver functions alone (e.g., *Julia et al., 1990*). According to the refraction model by *Hrubcová et al. (2005)*, the Moho lies at about 35 km in the Saxothuringian, while *Heuer at al. (2006)* and *Geissler et al. (2005)* observe the Moho depths there in a range from 24 to 32 km. Differences between the depths according to *Geissler et al. (2005)* and *Heuer et al. (2006)* and those of *Hrubcová et al. (2005)* are 5–6 km in the Saxothuringian, on the average, while all the Moho depths in the Teplá-Barrandian are consistent (Fig. 9). *Hrubcová and Geissler (2009)* propose an alternative velocity structure below one station (A03) in the Saxothuringian to remove this inconsistency between the findings from the receiver function stacks and those from the

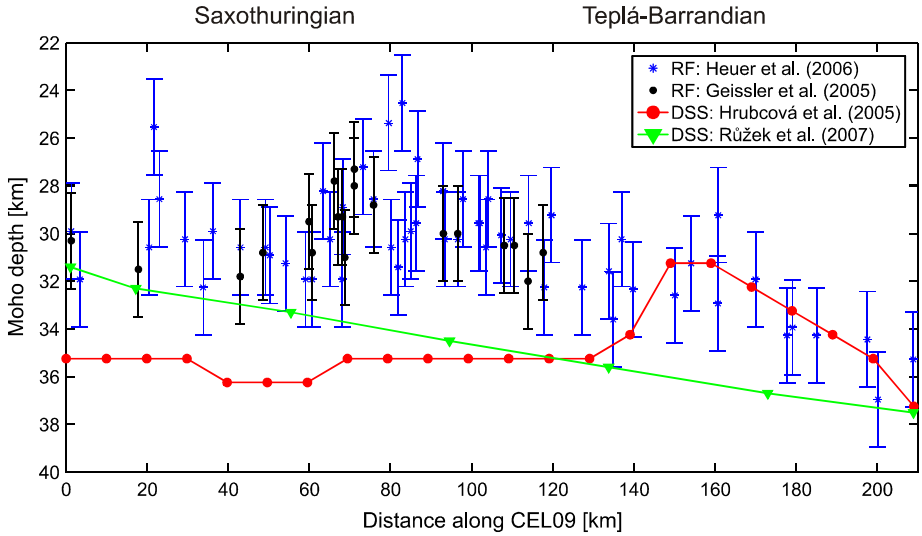

Fig. 9. Comparison of the Moho depths along profile CEL09 from CSS method (*Hrubcová et al., 2005*; *Růžek et al., 2007*) and from receiver functions (along with error bars, *Geissler et al., 2005*; *Heuer et al., 2006*).

refraction measurements, trying to find velocity structure consistent for both methods. They show that data can be explained by a gradient zone with the top of the lower crust at depth of 28 km and the Moho at depths of 32–33 km. We also compare the Moho depths from the receiver functions and those from refraction methods by *Hrubcová et al. (2005)* with relief of the Moho derived along refraction profile CEL09 by *Růžek et al. (2007)*. The Moho is very smooth (Fig. 9), but it does not correlate either with *Hrubcová et al. (2005)* or with *Geissler et al. (2005)* and *Heuer et al. (2006)*. Hence, we want to exploit only those velocity models of the BM crust that are consistent. We conclude that one has to be careful while using crustal parameters of different origin and consider the resolution and limitations of the methods used (*Karousová, 2008*). On the other hand, applying corrections for crustal effects based on all available information on the crust is useful in case of global or broader regional tomographic studies of the deep Earth interior (*Koulakov et al., 2009*). The Moho map of the European Plate by *Grad et al. (2009)*, or velocity model EuCrust-07 by *Tesauro et al. (2008)* are examples of such large-scale models.

Besides the inconsistency between results of different methods, another source of uncertainties in developing a crustal model comes from methods of data interpolation, though the data coverage for compiling a crustal model of the BM is good. This is evident from calculation of the LinInterp model, where data are simply linearly interpolated. In the second tomographic test inverting the observed P-wave travel times corrected for the LinInterp crust, magnitudes of velocity perturbations in the upper mantle increased at depths down to 125 km (see Fig. 7) compared with those from inversion without crustal corrections. It indicates that the LinInterp model is not need to be optimal one for crustal

corrections. Because the published velocity models forming our datasets are the best approximation of velocity distributions in the BM crust, we assume that the largest errors of the LinInterp model are at sites, where data are sparse, and heterogeneities are then a product of the interpolation method. One possibility how to avoid these errors is to complement existing models with a smoothed data. The regional model EuCRUST-07 (*Tesauro et al., 2008*) is not suitable because it does not take into consideration most of recently-published models intersecting the BM. Eventually, we select the reference model IASP91 to complement our velocity models and introduce the nearest neighbour interpolation method, which resulted in the NearNeighbour model. An effect of the crust on teleseismic travel times is calculated as a difference between travel times generated by our 3D model of the crust and travel times according to the reference IASP91 model. Consequently, the sites with sparse data generate only small or no corrections of travel times. This approach guarantees that all heterogeneities appearing in the NearNeighbour model are supported by the data and are not a product of inter/extrapolation. Hence, we believe that we do not project artificial crustal heterogeneities into images of the upper mantle. This seems to be confirmed by smaller magnitudes of velocity perturbations generated by the NearNeighbour model compared to those generated by the LinInterp model in the first tomographic tests inverting the synthetic travel times (Fig. 6).

The second test (Fig. 7) inverting the observed travel times did not show a decrease of magnitudes of velocity perturbations after applying crustal corrections including those for sediments. Both the corrections according to the NearNeighbour and the LinInterp models increased the extremes of velocity perturbations at depth of 35 km (Fig. 7). As mentioned above, we expected a decrease of the perturbations. A reason why a minimization of inter/extrapolation errors does not affect significantly the tomographic images of the upper mantle after applying crustal corrections can be explained by a similarity of the crustal models in the central part of the BM where a density of the BOHEMA II stations is the largest and thus the tomographic inversions have the largest resolutions. Nevertheless, in both types of tomographic tests, inverting either the synthetic or the observed travel-times, the extremes of velocity perturbations are lower after applying corrections according to the NearNeighbour model in comparison with the extremes corresponding to corrections of the LinInterp model (Fig. 7). For this reason, we prefer the NearNeighbour model of the crust.

The second test inverting the observed travel times with crustal corrections also reveals the high-velocity anomaly beneath the MS and the Brunovistulian in the tomographic images (Fig. 7). This anomaly could indicate a significant high-velocity structure in the lower crust or in the uppermost mantle. Such structure is not included in our models because of absence of 2D refraction profiles in this region. The high magnitude of this anomaly (~12–13%) could partly result from our overestimation of effects of the sediments, since boreholes in the Carpathian Foredeep, as the main source of information on their thickness and velocities, do not reach the crystalline basement. Nevertheless, the significant differences between tomographic images, either with or without crustal corrections, confine to the crustal levels.

We consider the NearNeighbour model to be the first attempt to construct a representative 3D model of the crust covering the entire BM and we compare this model with available local models. First, we have compared the NearNeighbour model with the local 1D model of the western Bohemian/Vogtland earthquake swarm region (*Málek et*

al., 2005). The 1D model has low velocities in the shallow crust down to about 2 km; however, such low superficial velocities are missing in our 3D model. The velocity increases from 5.8 to 6.6 km/s between depths of 2 and 10 km in the 1D model, whereas the velocity-depth gradient of the NearNeighbour model is much smaller in these depths. These differences probably originate from the fact that the 1D model by *Málek et al. (2005)* provides a detailed local velocity distribution of the upper crust down to a depth of 15 km, while the 3D NearNeighbour model represents a smoothed model of the entire BM crust. Second, we have compared the NearNeighbour model with local 3D models of the crust beneath the northern part of the BM by *Majdanski et al. (2007*). These local models are based on travel times from seismic experiments CELEBRATION 2000, SUDETES 2003, and POLONAISE'97. Both the models by *Majdanski et al. (2007)* and the NearNeighbour model show northward thickening of the superficial low-velocity layer, interpreted by *Majdanski et al. (2007)* as sediments represented by velocities from 2.5 to 4.7 km/s. We conclude that our NearNeighbour model is consistent with the local models of *Málek et al. (2005)* and *Majdanski et al. (2007)*, but only in well-resolved areas.

7. CONCLUSIONS

We present a first representative three-dimensional model of the crust of the Bohemian Massif (BM). This NearNeighbour model is based on results of near-vertical reflection and wide-angle refraction seismic interpretations as well as on 3D local tomography. Velocities from the 1D reference IASP91 model complement the model data at nodes with no CSS data, which precludes creating artificial heterogeneities that are not supported by the original data. Moho depths in the BM vary between ~40 km beneath the Moldanubian unit and ~28–30 km beneath the Saxothuringian and the northern part of the Moravo-Silesian region.

The credibility of the NearNeighbour model was tested on tomographic inversions of synthetic and observed travel times recorded during the BOHEMA II experiment. According to the first test, where only crustal residuals were inverted, images of the upper mantle velocities were significantly affected by a leakage of velocity perturbations from the crust. Magnitudes of the artificial perturbations are comparable with those caused by heterogeneities of real upper mantle structures. The second test, consisting of inversions of observed P-wave travel times, either with or without crustal corrections, showed that the application of the NearNeighbour model for crustal corrections reduced effects of crustal heterogeneities projected into the upper mantle images in the western part of the BM. In the eastern part of the model, the crustal corrections according to the NearNeighbour model increase the velocity perturbations. This can be caused by a high-velocity anomaly in the lower crust or just beneath the Moho. Such velocity structure cannot be included into the NearNeghbour model because no CSS profile is located in the region. We conclude that according to the performed tomographic tests the crustal corrections are of the great importance especially for interpretations of the uppermost mantle down to depths of 100 km.

Acknowledgements: The authors are grateful to P. Hrubcová, and B. Růžek for providing us with their CSS models and data files. We also thank to M. Wilde-Piórko, E. Sandvol, and an anonymous reviewer for reviewing the manuscript and valuable suggestions how to improve

original version, as well as to G.R. Keller for his editorial work. The research was partly supported by a grant No. 205/071088 of the Grant Agency of the Czech Republic, by a grant No. IAA300120709 of the Grant Agency of the Academy of Sciences of the Czech Republic, and by a grant No. SVV-2011-263308.

References

Aki K., Christoffersson A. and Husebye E.S., 1977. Determination of 3-dimensional seismic structure of lithosphere. *J. Geophys. Res.*, **82(B2)**, 277–296.

Babuška V., Plomerová J., Vecsey L., Jedlička P. and Růžek B., 2005. Ongoing passive seismic experiments unravel deep lithosphere structure of the Bohemian Massif. *Stud. Geophys. Geod.*, **49**, 423–430.

Behr H.J., Dürbaum H.J. and Bankwitz P., 1994. Crustal structure of the Saxothuringian Zone: Results of the deep seismic profile MVE-90 (East). *Z. Geol. Wiss.*, **22**, 647–769.

Beránek B., Dudek A. and Zounková M., 1975. Velocity models of the crust in the Bohemian Massif and the Western Carpathians (Rychlostní modely stavby zemské kůry v Českém masívu a Západních Karpatech). *J. Geol. Sci. Appl. Geophys. (Sborník geologických věd, Užitá Geofyzika)*, **13**, 7–17 (in Czech).

Brückl E., Blebinhaus F., Gosar A., Grad M., Guterch A., Hrubcová P., Keller G., Majdański M., Šumanovac F., Tiira T., Yliniemi J., Hegedüs E. and Thybo H., 2007. Crustal structure due collisional and escape tectonics in the eastern Alps region based on profiles Alp01 and Alp02 from the Alp 2002 seismic experiment. *J. Geophys. Res.*, **112**, B06308, DOI: 10.1029/2006JB004687.

Dallmeyer R.D., Franke W. and Weber K. (Eds.), 1995. *Pre-Permian Geology of Central and Eastern Europe*. Springer-Verlag, Berlin, Heidelberg, New York.

Dudek A., 1980. The crystalline basement block of the outer Carpathians in Moravia: Bruno-Vistullicum. *Rozpravy Čs. Akad. Věd*, **90**, 1–85 (in Czech).

Enderle U., Schuster K., Prodehl C., Schulz A. and Bribach J., 1998. The refraction seismic experiment GRANU95 in the Saxothuringian belt, southeastern Germany. *Geoph. J. Int.*, **133**, 245–259.

Evans J.R. and Achauer U., 1993. Teleseismic velocity tomography using the ACH method: theory and application to continentalscale studies. In: Iyer H.M. and Hirahara K. (Eds.), *Seismic Tomography*. Chapman and Hall, London, U.K., 319–360.

Franke W., 2000. The mid-European segment of the Variscides: tectonostratigraphic units, terrane boundaries and plate tectonic evolution. In: Franke W., Haak V., Oncken O. and Tanner D. (Eds.), *Orogenic Processes: Quantification and Modelling in the Variscan Belt*. Geol. Soc. London Spec. Publ. 179, London, U.K., 35–61.

Grad M., Guterch A., Mazur S., Keller G.R., Špičák A., Hrubcová P. and Geissler W., 2008. Lithosperic structure of the Bohemian Massif and adjacent Variscian belt in central Europe based on profile S01 from SUDETES 2003 experiment. *J. Geophys. Res.*, **113**, B10304, DOI: 10.1029/2007JB005497.

Grad M., Tiira T. and ESC Working Group, 2009. The Moho depth map of the European Plate. *Gephys. J. Int.*, **176**, 279–292.

Geissler W., Plenefisch T. and Kind R., 2005. The Moho structure in the western Eger Rift: A receiver function experiment. *Stud. Geophys. Geod.*, **44**, 188–194.

Heuer B., Geissler W. and Kind R., 2006. Seismic evidence for asthenospheric updoming beneath the western Bohemian Massif, central Europe. *Geophys. Res. Lett.*, **33**, L05311, DOI: 10.1029/2005GL025158.

Hrubcová P., Sroda P., Špičák A., Guterch A., Grad M., Keller G.R., Brückl E. and Thybo H., 2005. Crustal and uppermost mantle stucture of the Bohemian Massif based on CELEBRATION 2000 data. *J. Geophys. Res.*, **110**, B11305, DOI: 10.1029/2004JB003080.

Hrubcová P. and Sroda P., 2008. Crustal structure at the easternmost termination of the Variscan belt based on CELEBRATION 2000 and ALP 2002 data. *Tectonophysics*, **460**, 55–75.

Hrubcová P. and Geissler W., 2009. The crust-mantle transition and the Moho beneath the Vogtland/West Bohemian region in the light of different seismic methods. *Stud. Geophys. Geod.*, **53**, 275–294.

Julia J., Ammon C.J., Herrmann R.B. and Correig A.M., 2000. Joint inversion of the receiver function and the surface-wave dispersion observations. *Geophys. J. Int.*, **143**, 99–112.

Kalvoda J., Bábek O., Fatka O., Leichmann J., Melichar R., Nehyba S. and Špaček P., 2008. Brunovistulian terrane (Bohemian Massif, central Europe) from Late Proterozoic to late Paleozoic: a review. *Int. J. Earth Sci.*, **97**, 497–518.

Karousová H., 2008. *Three-Dimensional Velocity Model of Crust beneath the Bohemian Massif and Its Effects on Results of Teleseismic Tomography of Upper Mantle*. Master Thesis, Charles University, Prague, Czech Republic (in Czech).

Kennett B.L.N. and Engdahl E.R., 1991. Traveltimes for global earthquake location and phase identification. *Geophys. J. Int.*, **105**, 429–465.

Kossmat F., 1927. Gliederung des varistischen Gebirgsbaues. *Abhandlungen des Sächsischen Geologischen Landesamtes*, **1**, 1–39 (in German).

Koulakov I., Kaban M.K., Tesauro M. and Cloetingh S., 2009. P- and S-velocity anomalies in the upper mantle beneath Europe from tomographic inversion of ISC data. *Geophys. J. Int.*, **179**, 345–366.

Linnemann U., Gemmlich M., Tichomirowa M., Buschmann B., Nasdala L., Jonas P., Lützner H. and Bombach K., 2000. From Cadomian subduction to Early Palaeozoic rifting: the evolution of Saxo-Thuringia at the margin of Gondwana in the light of single zircon geochronology and basin development (Central European Variscides, Germany). In: Franke W, Haak W, Oncken O. and Tanner D. (Eds), *Orogenic Processes: Quantification and Modelling in the Variscan Belt*. Geol. Soc. London Spec. Publ., 179, 131–153.

Majdanski M., Grad M. and Guterch A., 2006. 2-D seismic tomographic and ray tracing modelling of the crustal structure across the Sudetes Mountains basing on SUDETES 2003 experiment data. *Tectonophysics*, **413**, 249–269.

Majdanski M., Kozlovskaya E. and Grad M., 2007. 3D structure of the Earth's crust beneath the northern part of the Bohemian Massif. *Tectonophysics*, **437**, 17–36.

Málek J., Horálek J. and Jánský J., 2005. One-dimensional qP-wave velocity model of the upper crust for the west Bohemian/Vogtland Earthquake swarm region. *Stud. Geophys. Geod.*, **49**, 501–524.

Martin, M., Ritter, J.R.R. and CALIXTO working group, 2005. High-resolution teleseismic body-wave tomography beneath SE Romania – I. Implications for three-dimensional versus one-dimensional crustal correction strategies with a new crustal velocity model. Geophys. J. Int., 162, 448-460p.

Matte P., Maluski H., Rajlich P. and Franke W., 1990. Terrane boundaries in the Bohemian Massif - result of large-scale Variscan shearing. *Tectonophysics*, **177**, 151–170.

McCann T., 2008. *Geology of the Central Europe*. Geological Society, London, U.K.

Neunhöfer H., Marillier F. and Panza G.F., 1981. Crust and upper mantle structure in the Bohemian Massif from the dispersion of Rayleigh waves. *Gerlands Beitr. Geofyzik*, **90**, 514–520.

Neunhöfer H., Plešinger A. and Kracke D., 1983. Crust and upper mantle structure between Moxa and Kasperske Hory from Rayleigh waves. *Gerlands Beitr. Geofyzik*, **92**, 284–290.

Novotný O. and Urban L., 1988. Seismic models of the Bohemian Massif and of some adjacent regions derived from deep seismic soundings and surface wave investigations: a review. In: Procházková D. (Ed.), *Induced Seismicity and Associated Phenomena*. Geophys. Inst. of the Czechosl. Acad. Sci., Prague, Czech Rep., 227–249.

Novotný O., Proskuryakova T.S. and Shilov A.V., 1995. Dispersion of Rayleigh waves along the Prague-Warsaw profile. *Stud. Geophys. Geod.*, **39**, 138–147.

Novotný O., Grad M., Lund C.-E. and Urban L., 1997. Verification of the lithospheric structure along profile Uppsala-Prague using surface waves dispersion. *Stud. Gephys. Geod.*, **41**, 15–28.

Patočka F. and Štorch P., 2004. Evolution of geochemistry and depositional settings of Early Paleozoic siliciclastics of the Barrandian (Teplá-Barrandian unit, Bohemian Massif, Czech Republic). *Int. J. Earth Sci.*, **93**, 728–741.

Pharaoh T.C., 1999. Palaeozoic terranes and their lithospheric boundaries within the Trans-European Suture Zone (TESZ): a review. *Tectonophysics*, **314**, 17–41.

Plomerová J., Achauer U., Babuška V. and Granet M., 2003. BOHEMA 2001-2003. Passive seismic experiment to study lithosphere-asthenosphere system in the western part of the Bohemian Massif. *Stud. Geophys. Geod.*, **47**, 691–701.

Plomerová J., Vecsey L., Babuška V., Granet M. and Achauer U., 2005. Passive seismic experiment MOSAIC - a pilot study of mantle lithosphere anisotropy of the Bohemian Massif. *Stud. Geophys. Geod.*, **49**, 541–560.

Plomerová J., Vecsey L. and Babuška V., 2011. Mapping seismic anisotropy of the lithospheric mantle beneath the northern and eastern Bohemian Massif (central Europe). *Tectonophysics*, DOI: 10.1016/j.tecto.2011.08.011 (in press).

Růžek B., Hrubcová P., Novotný M., Špičák A. and Karousová O., 2007. Inversion of travel times obtained during active seismic refraction experiment CELEBRATION 2000, ALP 2002 and SUDETES 2003. *Stud. Geophys. Geod.*, **51**, 141–164.

Růžek B., Holub K. and Rušajová J., 2011. Three-dimensional crustal model of the Moravo-Silesian region obtained by seismic tomography. *Stud. Geophys. Geod.*, **55**, 87–107.

Sandoval S., Kissling E., Ansorge A. and SVEKALAPKO Seismic Tomography Working Group, 2003. High-resolution body wave tomography beneath the SVEKALAPKO array: I. A priori three dimentional crustal model and associated traveltime effects on teleseismic tomographic wave fronts. *Geophys. J. Int.*, **153**, 75–87.

Steck L.K. and Prothero W.A., 1991. A 3-D ray-tracer for teleseismic body-wave arrival-times. *Bull. Seismol. Soc. Amer.*, **81**, 1332–1339.

Tesauro M., Kaban M.K. and Cloetingh S., 2008. EuCRUST-07: A new reference model for the European crust. *Geophys. Res. Lett.*, **35**, L05313, DOI: 10.1029/2007GL032244.

Vrána S., 1997. Geology and petrology of the Moldanubian Zone. In: Vrána S. and Štědrá V. (Eds.), *Geological Model of Western Bohemia Related to the KTB Borehole in Germany. J. Geol. Sci. (Prague)*, **47**,109–123.

Waldhauser F., Kissling E., Ansorge J. and Müller S., 1998. Three-dimensional interface modeling with two-dimensional seismic data: the Alpine crust-mantle boundary. *Geophys. J. Int.*, **135**, 264–278.

Waldhauser F., Lippitch R., Kissling E. and Ansorge J., 2002. High-resolution tomography of the upper mantle structure using a priori three-dimensional crustal model. *Geophys. J. Int.*, **150**, 403–414.

Wendt J.I., Kröner A., Fiala J. and Todt W., 1993. Evidence from zircon dating for existence of approximately 2.1 Ga old crystalline basement in southern Bohemia, Czech Republic. *Geol. Rundsch.*, **82**, 42–50.

Wessel P. and Smith H.F., 1995. New version of Generic Mapping Tools released. *EOS Trans. AGU*, **76**, 329.

Wielandt E., Sigg A., Plešinger A. and Horálek J., 1987. Deep structure of the Bohemian Massif from phase velocities of the Rayleigh and Love waves. *Stud. Geophys. Geod.*, **31**, 1–7.

Wilde-Piórko M., Saul J. and Grad M., 2005. Differences in the crustal and uppermost mantle structure of the Bohemian Massif from teleseismic receiver functions. *Stud. Geophys. Geod.*, **49**, 85–107.

Wilde-Piórko M., Geissler W.H., Plomerová J., Grad M., Babuška V., Brückl E., Cyziene J., Czuba W., England R., Gaczynski E., Gazdová R., Gregersen S., Guterch A., Hanka W., Hegedues E., Heuer B., Jedlička P., Lazauskiene J., Keller G.R., Kind R., Klinge K., Kolínský P., Komminaho K., Kozlovskaya E., Krueger F., Larsen T., Majdanski M., Málek J., Motuza G., Novotný O., Pietrasiak R., Plenefisch Th., Růžek B., Sliaupa S., Sroda P., Swieczak M., Tiira T., Voss P. and Wiejacz P., 2008. PASSEQ 2006-2008: Passive seismic experiment in Trans-European Suture Zone. *Stud. Geophys. Geod.*, **52**, 439–448.

Zulauf G., Dörr W., Fiala J. and Vejnar Z., 1997. Late Cadomian crustal tilting and Cambrian transtension in the Teplá-Barrandian unit (Bohemian Massif, Central European Variscides). *Geol. Rundsch.*, **86**, 571–584.

P2

Seismic tomography of the upper mantle beneath the north-eastern Bohemian Massif (central Europe)

Karousová, H., Plomerová, J. and Vecsey, L.

Tectonophysics, 564–565, 1- 11, doi:10.1016/j.tecto.2012.06.031, 2012

Tectonophysics 564–565 (2012) 1–11

Contents lists available at SciVerse ScienceDirect

Tectonophysics

journal homepage: www.elsevier.com/locate/tecto

Review Article

Seismic tomography of the upper mantle beneath the north-eastern Bohemian Massif (central Europe)

Hana Karousová *, Jaroslava Plomerová, Luděk Vecsey

Geophysical Institute, Academy of Sciences of the Czech Republic, Boční II/1401, 141 31 Prague 4, Czech Republic

ARTICLE INFO

Article history:
Received 18 February 2011
Received in revised form 13 June 2012
Accepted 24 June 2012
Available online 30 June 2012

Keywords:
Bohemian Massif
Passive seismic experiment
Teleseismic tomography
Upper mantle structure

ABSTRACT

We present a 3-D velocity model of the upper mantle beneath the northern and eastern parts of the Bohemian Massif (BM) based on data from passive seismic experiment BOHEMA II (May 2004–June 2005) consisted of 35 temporary stations complemented by data of permanent observatories. The resulting tomographic model, with a variance reduction of 84%, shows relatively small velocity variations, both in size and in amplitude. A small-size high velocity perturbation in the eastern part of the model can be related to the complex structure beneath the Sudetes/Moravo-Silesian unit contact. Similarly to results from the BOHEMA I experiment in the western BM, the presented model from BOHEMA II data confirms the north-southward thickening of the lithosphere. Though in the upper mantle the low perturbations prevail, some inconsistencies among the isotropic velocity perturbation model, Sp receiver function inferences and anisotropic models of the mantle lithosphere domains indicate that both the topography of the lithosphere–asthenosphere boundary and internal velocity structure of the upper mantle beneath the BM can be complex. We tested two regularization techniques: truncated singular value decomposition and damped least square method, results of which lead us to prefer the damped least square method. The truncated singular value decomposition seems to be more sensitive to uneven ray geometry.

Contents

1. Introduction and tectonic setting

The Bohemian Massif (BM, Fig. 1), formed by heterogeneous collage of units (Kachlík, 2003) namely by the Saxothuringian (ST), Teplá-Barrandian (TB), Sudetes, (SU), Moldanubian (MD), Moravo-Silesian (MS) and Brunovistulian (BV), belongs to the European Variscan massifs. The crust of most of the massifs is 'cut' by rifts, which form the European Cenozoic Rift System (ECRIS). In the past, seismic tomography studies of the upper mantle beneath the massifs have focused on a search of decreased velocities, which could be interpreted as uprising plumes. Granet et al. (1995) postulated the idea of the existence of a plume in the European mantle with several small baby plumes beneath most of the massifs. And indeed, such baby plumes were undoubtedly imaged beneath the French Massif Central Granet et al. (1995)) and Rhenish Massif (Ritter et al., 2001), but not beneath the Armorican Massif in the Western Europe (Judenherc and Granet, 1999).

* Corresponding author. Tel.: +420 267 103 021; fax: +420 272 761 549.
E-mail address: hanak@ig.cas.cz (H. Karousová).

0040-1951/$ – see front matter © 2012 Elsevier B.V. All rights reserved.
doi:10.1016/j.tecto.2012.06.031

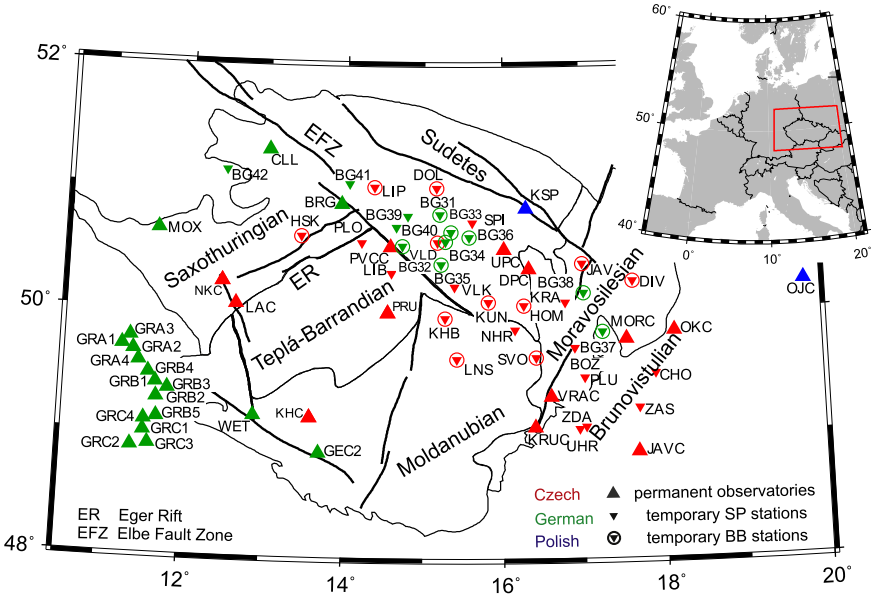

Fig. 1. Location of the area studied within Europe (inset). Distribution of stations of the BOHEMA II array and major tectonic units (fine lines) and faults (bold lines) of the Bohemian Massif (for more details see Fig. 1 of Plomerová et al. (2011-this issue) and Karousová et al. (2012)).

The upper mantle structure beneath the BM (central Europe), with the Eger Rift (ER) in its western part, was expected to be similar to the French Massif Central or the Rhenish Massif. However, tomography images of the BM, based only on observations from permanent observatories, did not have sufficient resolution to confirm or to exclude the existence of a small plume. Therefore, the international passive seismic experiment, BOHEMA I (Plomerová et al., 2003, 2007), was designed to collect teleseismic data at densely instrumented seismic arrays, allowing detailed studies of the upper mantle. When inverted, this data yielded velocity perturbations that did not indicate any 'tube-like' low-velocity heterogeneity (Plomerová et al., 2007), which could be interpreted as a small plume finger. Besides that, studies of body-wave seismic anisotropy have revealed that the mantle lithosphere of the Variscan Massifs consists of several domains, each with its own fossil fabric (Babuška and Plomerová, 2008; Plomerová et al., 2000, 2007, 2011-this issue).

To address the question about the isotropic velocity structure of the upper mantle beneath the whole BM and its relation to the lithosphere domains, two additional temporary arrays were installed in the following experiments: BOHEMA II and BOHEMA III (Babuška et al., 2005). Permanent observatories in central Europe formed the backbone array for all the experiments, with a station spacing of approximately 100 km. The spacing between the stations in the temporary arrays was much smaller — between 10 and 40 km. The temporary arrays of BOHEMA I–III covered step-by-step the whole BM, with an overlap on margins of the individual arrays. This paper concentrates on modeling the isotropic velocity structure of the upper mantle beneath the north-eastern part of the BM from teleseismic data of the BOHEMA II array (Fig. 1).

2. Data

Data used in this study were obtained from the BOHEMA II array consisting of 35 temporary stations belonging to the Geophysical Institute, Prague and to the GFZ, Potsdam (Fig. 1, Geissler et al., 2012-this issue). The array was in operation for about one year – from May 2004 to June 2005 – and covered the northern and eastern parts of the BM. Arrival times were measured on recordings with 20 Hz sampling. Waveforms from 32 permanent seismological observatories in the region were also included into the tomography dataset. Station spacing in the BOHEMA II array was about 30–40 km, on average. We selected 203 events with magnitudes larger than 4.5 located at epicentral distances between 25° and 90° (Fig. 2) relative to the center of the array.

First, we measured manually the arrival time at the first P-wave maximum amplitude (either peak or trough) on each trace of an event and correlated them within the array. Then, the first P-wave onset times were picked on the selected highest-quality recordings. Finally, we calculated the P-wave arrival times at each station in the array. A quality factor for each measurement was determined based on the uncertainty of the picking. Most of measurements were of the highest quality with uncertainty of ± 0.05 s. Based on the quality factor we estimated the average data error to be 0.06 s.

An analysis of P-wave travel-time deviations used for modeling seismic anisotropy beneath the north-eastern BM indicated time instabilities in the dataset (Plomerová et al., 2011-this issue). Therefore, we plotted the relative residuals (see Section 3 for details) for each station in chronological order and examined them in detail. These plots revealed several kinds of time instabilities in P-wave arrival times at some temporary stations. Fig. 3 shows selected types of the instabilities at 7 temporary stations and, for a comparison, also representative measurements from stations HSK, KUN, and LNS which are

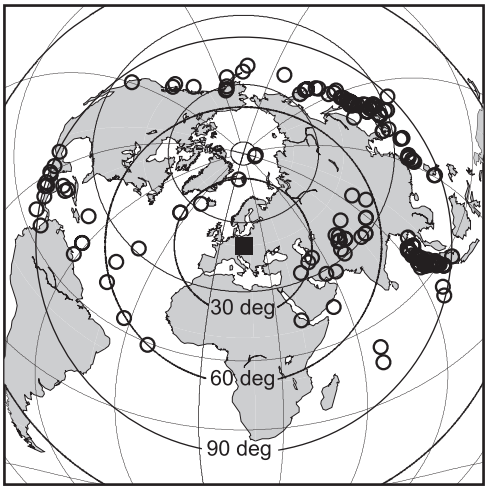

Fig. 2. Distribution of teleseismic events used (circles) relative to the location of the BOHEMA II array (square).

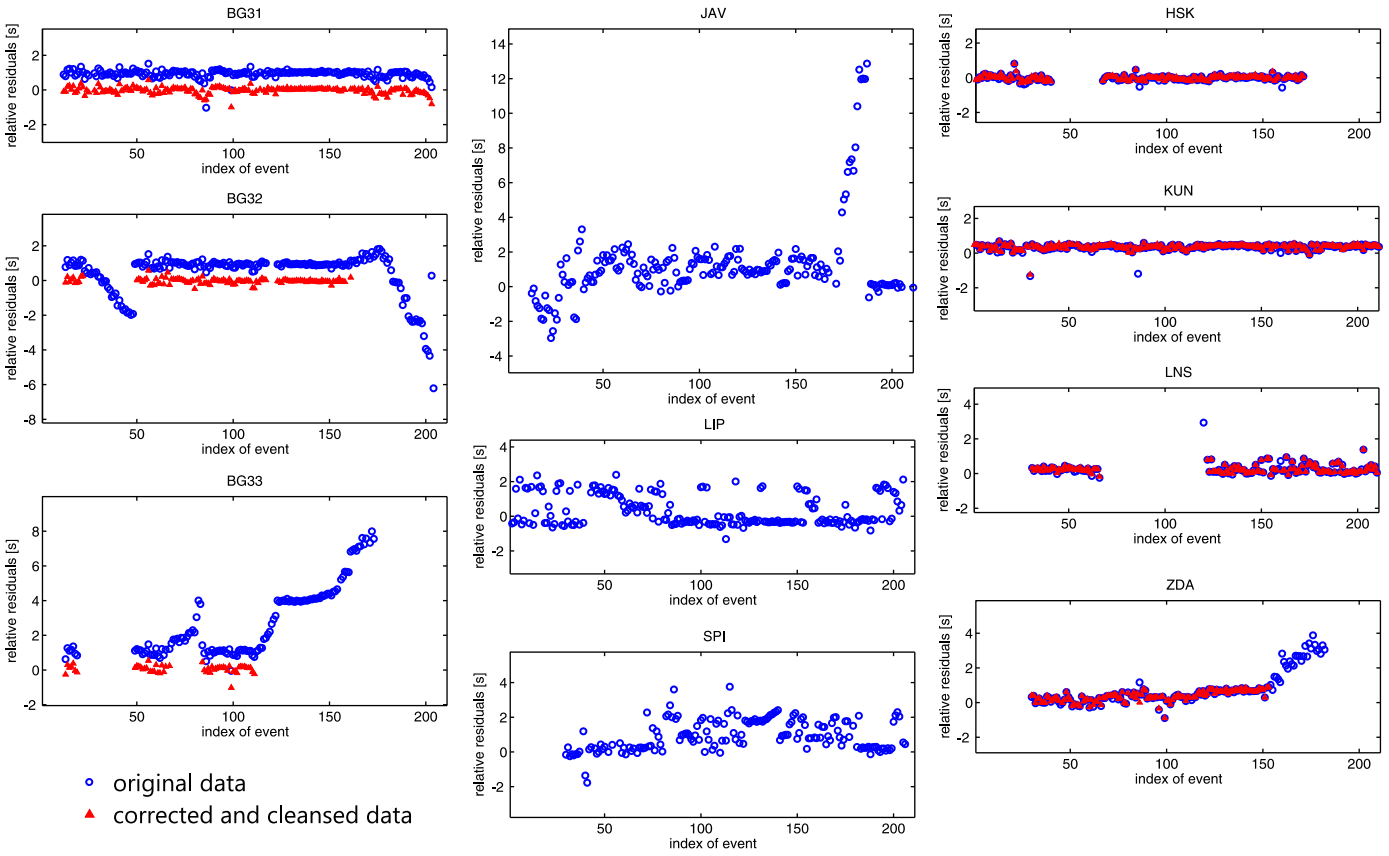

Fig. 3. Relative P-wave residuals (event mean subtracted) at stations BG31, BG32, BG33, JAV, LIP, SPI, and ZDA plotted chronologically to show examples of time instabilities. Relative residuals at stations HSK, KUN, and LNS reflect data stable in time, for a comparison. Only cleansed and corrected data (triangles) were used in the tomographic inversion.

stable in time. Most of the instabilities are attributed to instrumental errors caused by poor synchronization of data acquisition system (DAS) and the Global Position System (GPS). The measurements at six stations (BG31, BG32, BG34, BG35, BG36, BG37) were corrected easily because their recordings were shifted in time by a constant value of 0.975 s due to malfunctioning of the DAS (Geissler, personal communication). On the other hand, diffusion in the residuals of four stations LIP, SPI, JAV, and ZAS clearly indicates uncontrolled time instabilities during the whole period of recordings. Therefore, data from these stations were excluded from the tomography. The measurements at 61 stations were included into the tomographic analysis, with a minimum of 27 P-wave arrivals per event. The final data set of the P-wave arrivals, cleansed of time instabilities and individual picking errors, consists of 10236 high-quality measurements with relative residuals in a range of ± 1.5 s.

3. Tomographic inversion

Seismic tomography inverts travel-time deviations to velocities or velocity perturbations in the Earth's interior by fitting the basic formula

$$\boldsymbol{d} = \mathbf{G}\boldsymbol{m}, \tag{1}$$

where $\boldsymbol{d}$ is a data vector, $\boldsymbol{m}$ is a vector of model parameters, and $\mathbf{G}$ is a matrix coupling data and model parameters.

In regional teleseismic studies, relative travel-time residuals are inverted for velocity perturbations in the upper mantle beneath a seismic array. The velocity perturbations relative to a radial Earth model are searched in a limited volume of the mantle. Velocities outside of the target volume are approximated by the reference model. Differences between observed and calculated travel-times, called absolute residuals, contain errors from source regions (e.g., origin time and hypocenter mislocations), or, effects from lower mantle velocity structure. Local and global tomography studies invert the absolute residuals, but in regional studies, where a part of each ray lies outside of the volume studied, it is necessary to correct for the effects originating outside of the volume. If the seismic array is relatively small in comparison with epicentral distances of teleseismic earthquake foci, these effects disturb observations at all stations similarly and can be suppressed by normalization. Subtracting the mean travel-time residual for each event (an event-referenced residual) from absolute residuals is the most frequently used normalization method for calculating relative residuals. By inverting relative residuals, we are able to resolve velocity perturbations in a volume of the upper mantle densely sampled by up-going seismic rays. The task is non-linear because both parameters – the travel-times and ray paths – change with velocities. The problem can be linearized assuming the velocity perturbations are small (up to 10%) and, thus, affect the ray-paths only a little.

The teleseismic tomography described by Evans and Achauer (1993) forms the basis of the program TELINV used in this study. The program has been originally written by Steck and Weiland (Weiland et al., 1995) and later modified and used by several authors (e.g., Achauer, 1992; Eken et al., 2007; Kissling and Spakman, 1996; Shomali et al., 2006). Observed P-wave travel-times are the input data for this code. The relative residuals are calculated within the program from the absolute residuals by subtracting the residual mean of each individual event. Velocity perturbations are calculated in the orthogonal net of nodes approximating the volume studied. The velocity among adjacent nodes is calculated by trilinear interpolation (Steck and Prothero, 1991). The initial velocity model of the upper mantle and theoretical travel-times are set according to a reference Earth model IASP91 (Kennett and Engdahl, 1991). We run the

TELINV code with three-dimensional ray-tracing implemented by the Simplex method (Steck and Prothero, 1991). The kernel matrix is inverted by Singular Value Decomposition (SVD). The basic equation of the inversion of the TELINV code can be written as:

$$m_{\text{est}} = \left(\mathbf{G}^{\mathrm{T}} W_{\mathrm{D}} \mathbf{G} + \varepsilon^2 I\right)^{-1} \mathbf{G}^{\mathrm{T}} \mathrm{W}_{\mathrm{D}} \boldsymbol{d}, \quad (2)$$

where $\mathbf{m}_{\text{est}}$ are estimated model parameters (i.e., velocity perturbations), $\mathbf{G}$ is matrix of partial derivatives with respect to the model parameters, $\mathbf{W}_{\mathrm{D}}$ is weighting matrix of data, where weights are set according to quality factors assigned to individual arrival time picks, ε^2 is a damping factor, $\mathbf{I}$ is a unit diagonal matrix and $\boldsymbol{d}$ is data vector (i.e., relative residuals) (Menke, 1984). To meet assumptions behind the linearization of the inversion, we perform several iterative cycles. In each cycle, new ray-paths inside of the area studied are traced according to the improved velocity model retrieved in the previous step. We apply four iteration cycles allowing us to reach such data variance which does not decrease with further iterations noticeably and stay above the twice the average data error (see Section 3.2 and Fig. 6).

3.1. Model parameterization and crustal corrections

The BOHEMA II array has an NW–SE elongated shape with a length of about 450 km. We approximate the volume below the array by the 3D grid of nodes with horizontal spacing of 30 km inside the region and of 50 km at its rim (Fig. 4a). These parameters were selected according to the ray geometry and the wavelength of teleseismic P-waves. Outside of the region studied, we added stabilization nodes, which created two frames around the region at distances of 200 and 1000 km relative to the center of the array at 50°N 16°E. Evans and Achauer (1993) recommend choosing a vertical spacing of nodes at least 1.5-times larger than horizontal one to increase number of crossing rays within one block. Therefore, we use a vertical spacing of nodes of 45 km in the upper mantle (Fig. 4b). In the lower parts of the model, at depths below 350 km, we added two stabilizing 100- and 350-km thick layers. These two deepest levels of nodes were not inverted, nor were the nodes at the two out-boarding stabilization frames. The first inverted layer of nodes lies at depth of 35 km to minimize effects of potential inaccuracies of the 3D crustal model applied in the inversion. We tested several different vertical parameterizations with irregular and smaller spacing, but the variance reduction as well as the diagonal terms of the resolution matrix decreased rapidly. In total, we inverted for 2352 model parameters.

Due to the sub-vertical directions of the incoming rays, teleseismic tomography cannot resolve structure of the crust, although the inverted travel-times are affected significantly by its complexities (Arlitt et al., 1999; Sandoval et al., 2003; Waldhauser et al., 2002). Moreover, the spacing between stations often exceeds the size of crustal heterogeneities. Therefore, we follow standard procedure (e.g., Lippitsch et al., 2003; Sandoval et al., 2004) and introduce crustal corrections (Karousová et al., 2012) into the dataset before inverting for the upper mantle velocity structure. Neglecting crustal effects in the inversion would map the heterogeneities from the crust into the mantle, and such false velocity perturbations could mask real upper mantle structures.

Recently, Karousová et al. (2012) compiled a 3D crustal model which can be used to correct for crustal heterogeneities of the BM. The authors showed that when applying model to correct for crustal effects, the leakage of velocity perturbations from the crust into the upper mantle is decreased. In addition, they showed that the inversion variance reduction slightly increased. To apply the crustal corrections, we first calculated travel-times through the 3D model using forward option of the TELINV code. Then, we corrected the observed travel-times for the crustal effects by subtracting the differences between the travel-times within the 3D model of crust, representing the real structure, and travel-times within the IASP91 crust. Thicknesses and average velocities of sediments beneath the stations complemented the 3D model with a-priori calculated station corrections (Karousová et al., 2012).

3.2. Regularization

Due to the regular parameterization of the model space, the number of rays passing through individual nodes/boxes is uneven. Especially in the margins of the model, the rays do not cross-fire or they do not intersect some boxes at all. Consequently, the kernel matrix, representing system of equations in formulae (1), is a singular matrix and thus needs to be regularized for calculating the inverse matrix. Menke (1984) suggests two types of regularizations, a truncated SVD (TSVD) and a damped least square method (DLSQ). We tested both methods and compared their tomography images to evaluate their suitability for inversion of our data.

To use the TSVD regularization, we set damping factor $\varepsilon^2 = 0$ in Eq. (2). The kernel matrix is decomposed into three matrices containing its singular values and eigenvectors. The velocity perturbations derived by the TSVD method can be interpreted as a summation of partial solutions, given by non-zero singular values and related pairs of eigenvectors. Non-zero, but small singular values represent such combination of partial solutions, which is significantly corrupted by data errors or computer round-off errors (Press et al., 1992). To avoid including such misleading partial solutions into the inversion, the decomposed kernel matrix is truncated at the optimal smallest singular value, called a threshold.

To determine the threshold, we searched for a stable inversion with minimum of data RMS, which express root-mean squares of

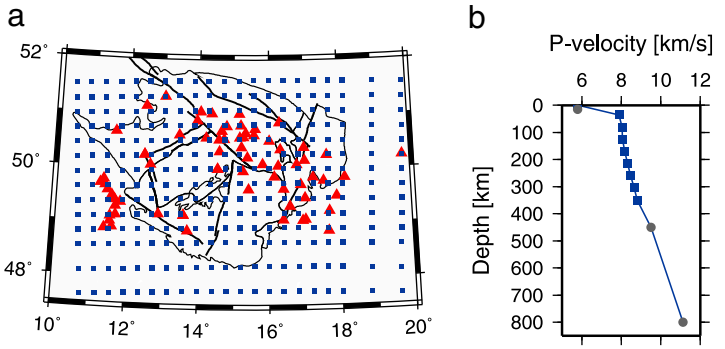

Fig. 4. (a) Horizontal grid of nodes (squares) of model parameterization with spacing of 30–50 km and stations of the BOHEMA II array (triangles). (b) Initial velocity model according to the reference IASP91 model (Kennett and Engdahl, 1991). Squares and circles indicate depths of inverted and fixed nodes, respectively.

differences between travel-times entering into inversion and synthetic travel-times calculated according to perturbed velocity model. We plot a dependence of data RMS after the 1st and 4th iterations on different condition numbers defined as a ratio between the highest and smallest singular values used in the inversions (Fig. 5a). We chose the condition number of 134 for our calculations because the inversion is stable in all four iterations and condition numbers higher than this value did not decrease the data RMS significantly.

The DLSQ is one of the most common regularization methods (e.g., Lippitsch et al., 2003; Martin and Wenzel, 2006; Mercier et al., 2010) and solves Eq. (2) in its original form. A damping factor ε^2 added to the diagonal terms of the kernel matrix ensures that all singular values remain above zero. Since the damping factor increases also small singular values artificially, the method includes partial solutions which could be corrupted by data errors or computer round-off errors in the inversion. Therefore, we define a threshold that is equal to the value of the damping factor to remove the smallest singular values which would be zeroes without damping.

An optimal damping factor was found empirically by constructing a data variance and model length trade-off curve for different damping factors (Fig. 5b). Traditionally, one chooses a value close to the inflection point of the trade-off curve which symbolizes a compromise between complexity of the model and a minimization of data residuals. The increase of data variance between damping factors of 50 and 10 indicates that an inversion using damping factor of 10 is not a stable. As an optimal damping we chose a factor of 100 (Fig. 5b).

In order to verify that we do not invert in the last iteration only for data noise, we tested the dependence of the data RMS from inversions with both types of regularization on number of iterations (Fig. 6). As the data RMS does not fall below the data-error threshold estimated as twice the average data error, we do not invert a noise and stay on safe side of recovered perturbations. Although the data RMS in the final iteration from both regularization methods (TSVD and DLSQ) and the variance reductions are very close (82% and 84%, respectively), velocity perturbations differ considerably (Fig. 7a, b). The TSVD method results in smaller-size velocity anomalies with abrupt changes of polarity compared with the DLSQ method. This feature remains valid even for a smaller condition number of 67, which mimic larger damping. Velocity heterogeneities from the DLSQ method are larger in size and smoother. Synthetic tests indicate that the one-cell anomalies in the TSVD method result from a higher sensitivity to uneven ray distribution. Therefore, we adopt the regularization

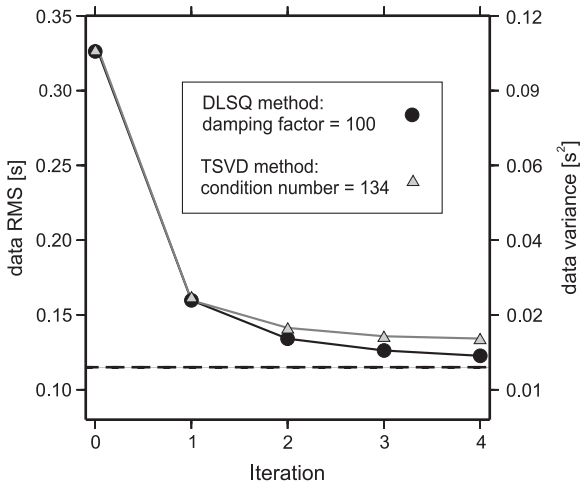

Fig. 6. Data RMS and data variance curves for individual iterations during the inversions with the use of the TSVD (triangles) and DLSQ (circles) methods. The dashed line indicates a data error threshold (0.12 s), defined as twice the picking uncertainties. The data RMS of inversions with optimal parameters remain above the data error threshold for the fourth iteration, which indicates we did not invert the data noise in these inversions.

by DLSQ as the more convenient method for inversion of the BOHEMA II data.

4. Upper mantle velocity structure of the northern and eastern Bohemian Massif

General patterns of upper mantle velocity perturbations retrieved by inversions with two different regularizations – with and without damping – are similar, as shown at three selected depths slices (Fig. 7). In Fig. 8, we plot perturbations in the upper mantle from the preferred DLSQ inversion. Only nodes with a hit-count of at least 10 rays and with the diagonal elements of the resolution matrix in the 4th iteration above 0.25 are considered as resolved and illuminated. As no or only few rays intersect in the crustal and bottom layers of the model, corresponding nodes do not meet the criteria mentioned above and therefore, we do not considered them. Most of the upper mantle of the well-resolved part of the BM, particularly the SU and MS units, is characterized by low-velocity perturbations

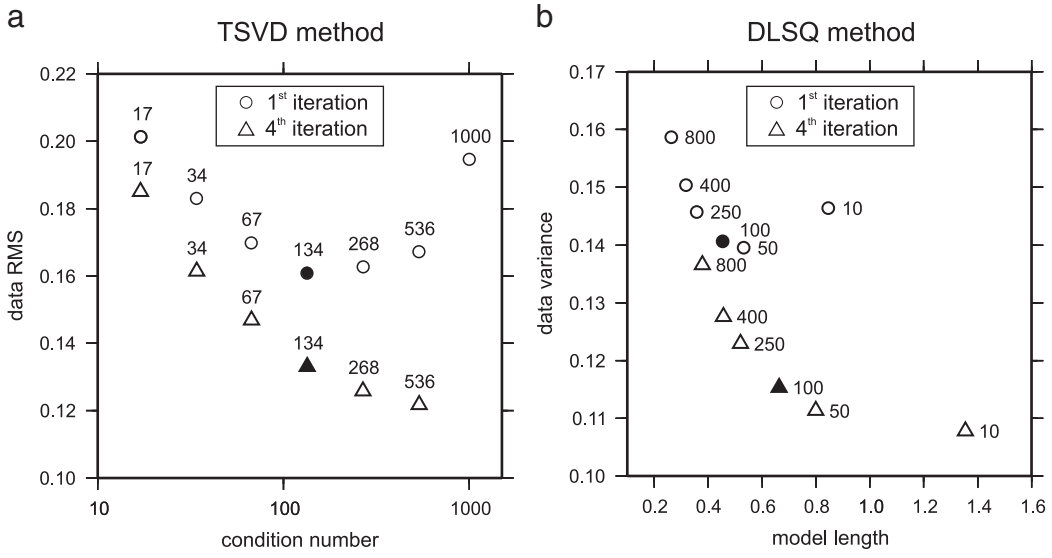

Fig. 5. Relationship between data root mean square (RMS) and condition number for data in the truncated singular value decomposition (TSVD) regularization (a). Trade-off curve for different damping factors in the damped least square (DLSQ) regularization (b). The first (circle) and fourth (triangle) iterations are indicated. The values of condition numbers and damping factors tested are labeled. The filled symbols indicate parameters selected as the optimal ones for the inversions.

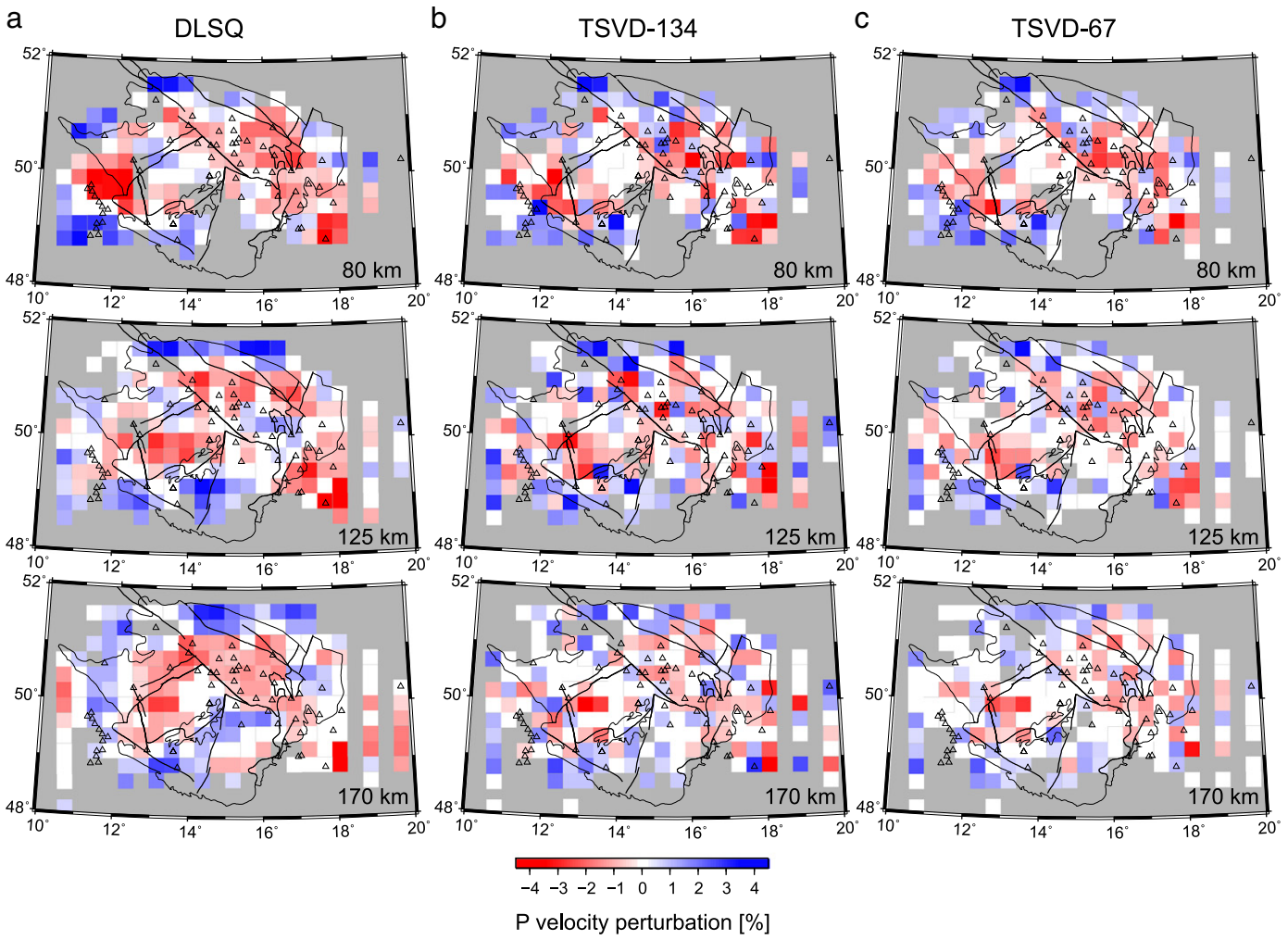

Fig. 7. Velocity perturbations at horizontal slices at three selected depths in the upper mantle from inversions with the DLSQ regularization defined by a damping factor of 100 (a), with the TSVD regularization defined by condition numbers of 134 (b), and of 67 (c). The black lines show tectonic units of the BM and main faults as in Fig. 1. The DLSQ method results in large and smooth heterogeneities, while the TSVD method leads to small-size velocity anomalies with abrupt changes of polarity.

down to ~250 km, relative to the IASP91 reference model. According to images of the damped solution (Fig. 8), this anomaly is distorted by small high-velocity perturbations beneath the boundary between the SU and MS units at depths of 125, 170, and 215 km. The high-velocity anomaly seems to shift towards the north along this boundary with increasing depth. In the south-western part of the model down to 150 km, the well-resolved velocity perturbations are distinguished by a sign change. A negative anomaly at ~50°N 12°E adjoins a positive anomaly in the south. This feature is present in both models with (DLSQ) and without (TSVD) damping (Figs. 7 and 8).

The dominance of the low velocity perturbations in the NE part of the BM mantle is clearly visible also in a cross-section through the model (Fig. 9a) along the NW–SE profile running through the central part of the array from the Sudetes to the MS zone. This cross-section parallels the Elbe Fault Zone (EFZ, Fig. 1). The two types of inversions show the same gross-features (see Fig. S1a, c). Similarly the high-velocity anomaly dipping towards the north-east is observed in vertical cross-sections perpendicular to the EFZ (Figs. 9 and S1b). Velocity perturbations from the TSVD inversion with condition number of 67 show only a slight indication of this anomaly (Fig. S1d).

5. Resolution analyses

Resolution analyses of tomographic models are essential for distinguishing real structures from artifacts caused by methods used and for identifying well-resolved model parameters. Since we prefer the tomographic images from the DLSQ method, we do not rely purely on the resolution matrix, which is distorted by adding the damping factor. Therefore, we analyzed the reliability of tomographic images by evaluating also a hit-count matrix, sensitivity tests, synthetic tests, and tests of parameterization. All resolution and synthetic tests were performed with the ray geometry of the BOHEMA II array, with 3D ray-tracing, and with damping factor of 100 (see Section 3.2).

The hit-count matrix (Fig. S2) gives the number of rays (hit-counts) passing through a box around every particular node. It is a key parameter of resolution, but we have to be aware that even large hit-counts do not necessarily mean high resolution. The well-resolved parts of the model only occur where rays intersect. The region is well sampled by many cross-firing rays in the mantle down to ~200 km. At greater depths, the nodes with large hit-counts shift to the north-east as the majority of events are located in these back azimuths, but rays do not intersect.

To verify sensitivity in the whole volume studied, we apply a checkerboard test (Spakman et al., 1993). For this, we construct a net of alternating anomalies of +3% and −3% in nodes at depths of 80, 170, and 260 km (Fig. S3), leaving the layers in between them unperturbed as well as in the remaining parts of the model (Sandoval et al., 2004). The input anomalies are recovered well at depths of 80 and 170 km (Fig. S3). However in deeper parts of the model, at ~260 km, the low-velocity anomalies in the central part are not resolved successfully.

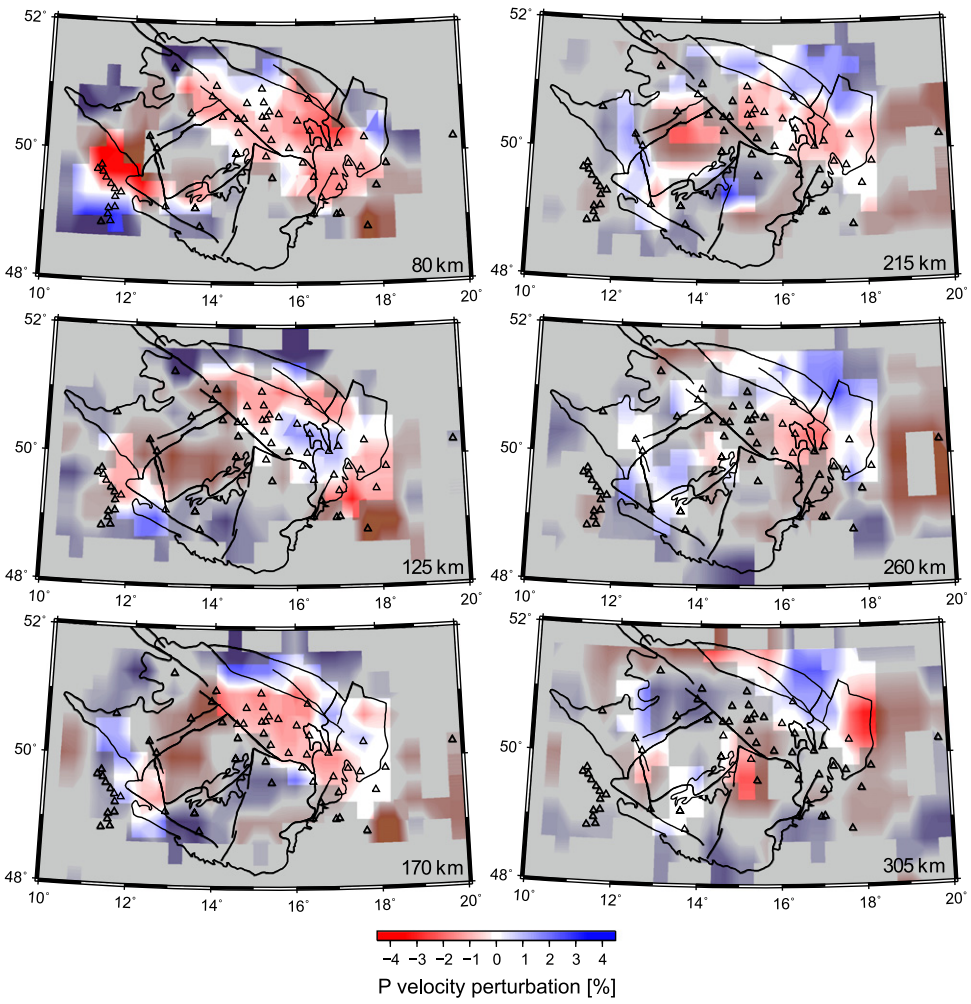

Fig. 8. Final model of the upper mantle velocity perturbations at horizontal slices from inversion with the use of the DLSQ regularization method with damping factor of 100. Regions with well resolved nodes are illuminated, while fairly and poorly resolved areas are shaded with respect to the values of the diagonal elements of resolution matrix. The black lines show tectonic units of the BM and main faults as in Fig. 1. Low velocity perturbations dominate in the well-resolved nodes in the north-western part of the model down to depths of about 250 km. The prevailing trend is distorted by a small high-velocity anomaly beneath the boundary between the SU and MS units (see Fig. 1) at depths 125, 170, and 215 km.

Moreover, perturbations from this layer are mapped down to greater depths at 305 km, due to the well-known vertical smearing dominated in the inversions of teleseismic data.

A synthetic test (Fig. S4) shows artifacts that can also be caused by simple velocity structures. Two velocity anomalies of +3% and −3% were inserted into the central part of the model with the good ray coverage. The high-velocity anomaly extends across two levels of nodes at 80 and 125 km on the north-western part of the model, whereas the low-velocity anomaly occupies nodes at three depth levels from 125 to 215 km on the south-east. To calculate the synthetic travel-times we refined the horizontal parameterization of the model to 10-by-10 km and shifted the center of the model by 10 km towards the north-west. The small-size high-velocity anomaly is well-recovered with only weak vertical smearing (Fig. S4). On the other hand, the larger low-velocity heterogeneity is significantly smeared vertically and shifted to shallower depths. However, the horizontal size of the perturbations is well resolved by the array, in general. We infer from these tests that the ray-geometry of the BOHEMA II array reveals reliably structures at size of about 90-by-120-by-90 km, but it may be less suitable for recovering the upper mantle anomalies larger than about 150-by-120-by-125 km.

We also carried out inversions with an average-and-offset scheme (Evans and Achauer, 1993) to test effects of the horizontal parameterization on resulting perturbations. The parameterization can cause difficulties, if the nodes are located just on a border of two structures with different velocities. Such parameterization would result in averaging the velocities. Therefore, we performed two additional inversions with the half-block shifted parameterizations; i.e., by 15 km to the north and to the east relatively to the central node. Differences among velocity perturbations from all these three inversions are noticeable only in small-size anomalies (Fig. 10) but, in general, the results are similar. The high-velocity heterogeneity beneath the boundary between the SU and MS units in the well-resolved part of the model shifts in dependence on the parameterization used. In order to see if the ray geometry of the BOHEMA II project is able to resolve an anomaly located in a margin of the well-resolved area, we performed a series of additional synthetic tests with different parameterizations, similar to the previous test. In this case, we inserted the 2% high-velocity anomaly at a depth of 125 km located beneath the SU/MS boundary (Fig. 11b). To be as realistic as possible, we added the 10% white noise to the synthetic travel-times. The recovered velocity perturbations (Fig. 11a, c, and d) prove that a modeled high-velocity anomaly can be resolved, although it could be shifted and smeared when an optimal parameterization is not met. This synthetic test (Fig. 11) also verified that the high-velocity anomaly dipping towards the north-east observed in

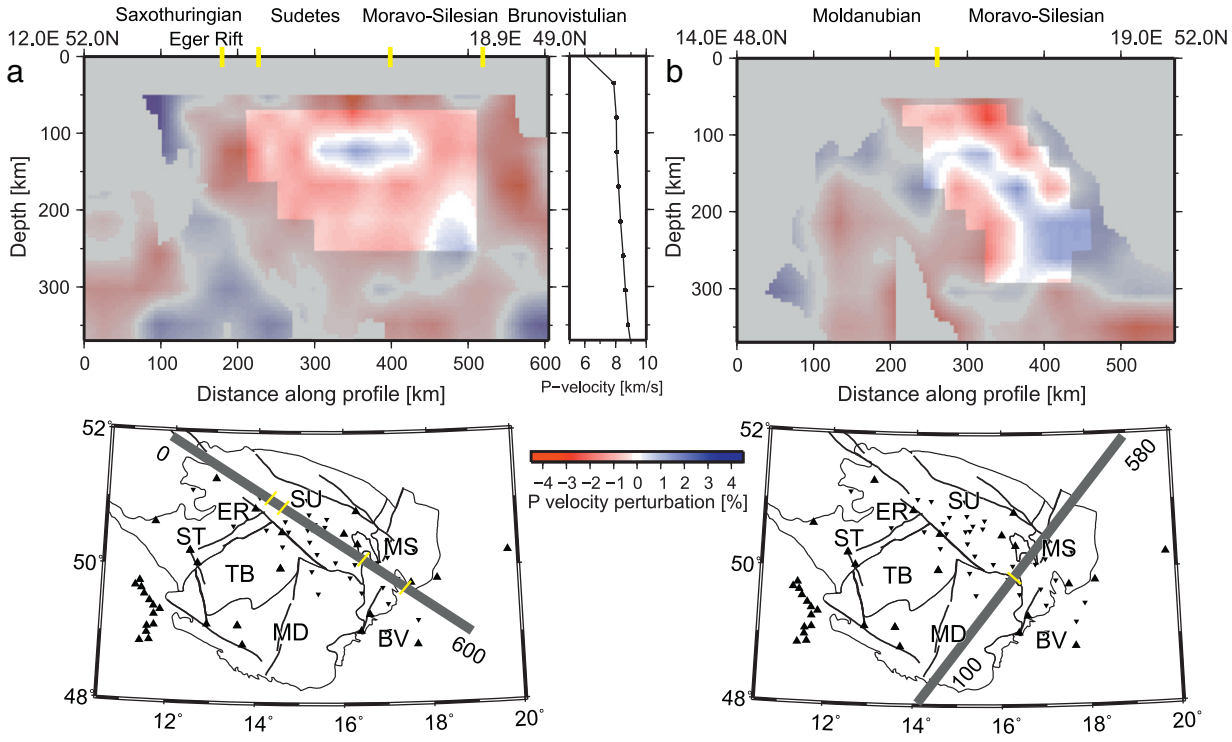

Fig. 9. Cross-sections through the final velocity perturbation model (Fig. 8) along the NW–SE (a) and SW–NE (b) profiles. Resolved areas are indicated as in Fig. 8. The input 1D velocity model is shown for comparison. The yellow marks indicate approximate contacts of the Saxothuringian (ST), Teplá-Barrandian (TB), Sudetes, (SU), Moldanubian (MD), Moravo-Silesian (MS) and Brunovistulian (BV) crustal units, and the Eger Rift (ER).

the vertical cross-section in Fig. 9b is not caused by vertical smearing of an anomaly located at a depth of 125 km, but it could represent real velocity heterogeneity.

6. Discussion

The most robust outcome of the tomography, which does not vary with regularization or parameterization applied, is that low-velocity perturbations prevail in the north-eastern part of the BM down to depths of ~250 km (see Figs. 7 and 8). Similarly, two regional studies (Koulakov et al., 2009 and Piromallo and Morelli, 2003) indicate that the upper mantle beneath the entire BM is characterized by lower velocities, relative to the surrounding area down to these depths. These studies do not exploit only teleseismic data, but include also data from regional events. Moreover, global tomography studies (Amaru, 2007; van der Meer et al., 2010) show the upper mantle beneath the BM as a part of an extensive low-velocity heterogeneity located in central Europe, which continues even deeper to about 400 km

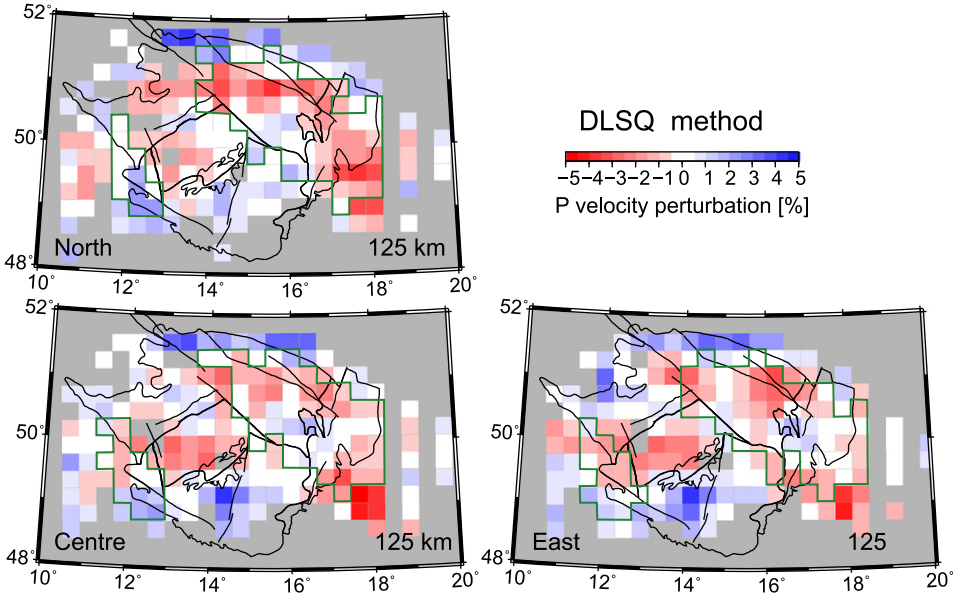

Fig. 10. Velocity perturbations at a depth of 125 km from the DLSQ inversions with a half-block offset scheme (15 km). The center of the model parameterization is shifted to the north and to the east. The green outlines indicate well-resolved parts of the models. The black lines show tectonic units of the BM and main faults as in Fig. 1. Note that the high velocity anomaly beneath the SU/MD/MS units (see Fig. 1) shifts with the model parameterization used.

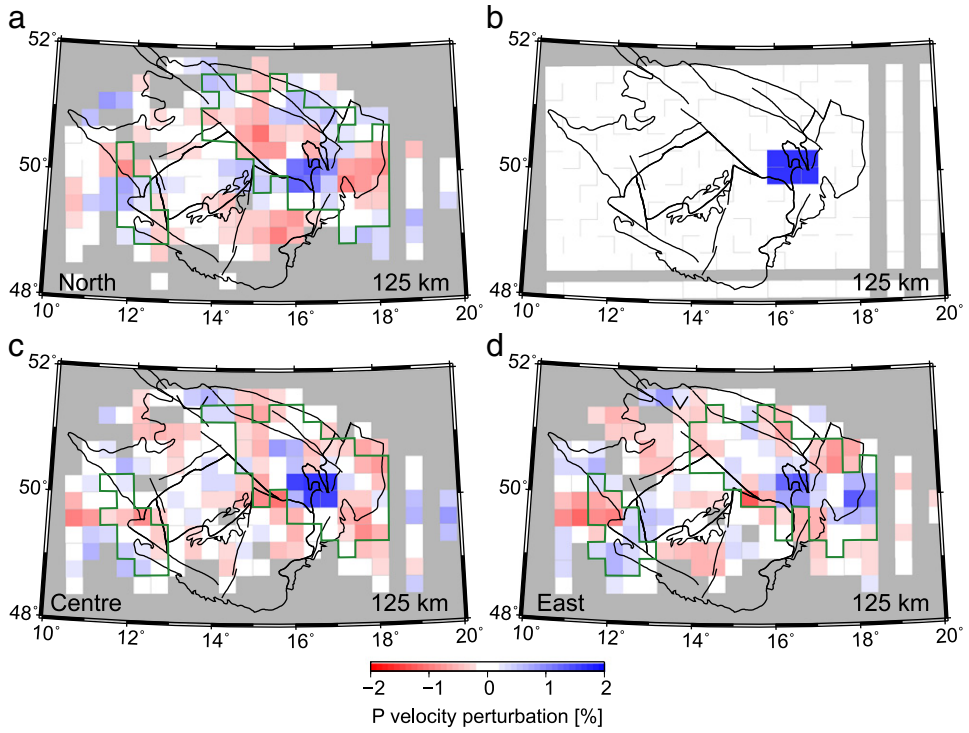

Fig. 11. Test of recovering synthetic high-velocity anomaly (+2%) at a depth of 125 km added into the IASP91 radial Earth model (b). Velocity perturbations calculated with the use of the DLSQ regularization method with central parameterization (c), parameterization with half-block offset towards the north (a) and towards the east (d). The green outlines indicate well-resolved parts of the models. The black lines show tectonic units of the BM and main faults as in Fig. 1. The recovered velocity perturbations prove that a modeled high-velocity anomaly can be resolved, although it would be shifted and smeared when an optimal parameterization is not chosen.

(Fig. 12). The regional teleseismic tomography from the BOHEMA II array indicates relatively small velocity variations, both in size and in amplitude (Fig. 8). Such details are below resolution level of global or regional studies which invert data of permanent observatories only. Thus, our results can be viewed as being in an agreement with these larger-scale investigations.

In comparison to the tomographic studies mentioned above, measurements that incorporate data from dense temporary arrays of stations have higher lateral resolution. Tomographic images from the BOHEMA I experiment (Plomerová et al., 2007; 2011-this issue) and those from this study (Fig. 8) all show a low-velocity anomaly beneath the ER and a high-velocity anomaly southwards from the ER in the well-resolved parts of the models at depths of 80 and 125 km. Such change of velocity-perturbation polarity correlates well with findings of Plomerová et al. (1998) and Plomerová and Babuška (2010) who identified a southward dipping lithosphere–asthenosphere boundary (LAB) beneath the Moldanubian. Moreover, the southward thickening of the lithosphere was also inferred from the Sp receiver functions in the western BM (Geissler et al., 2012-this issue; Heuer et al., 2007).

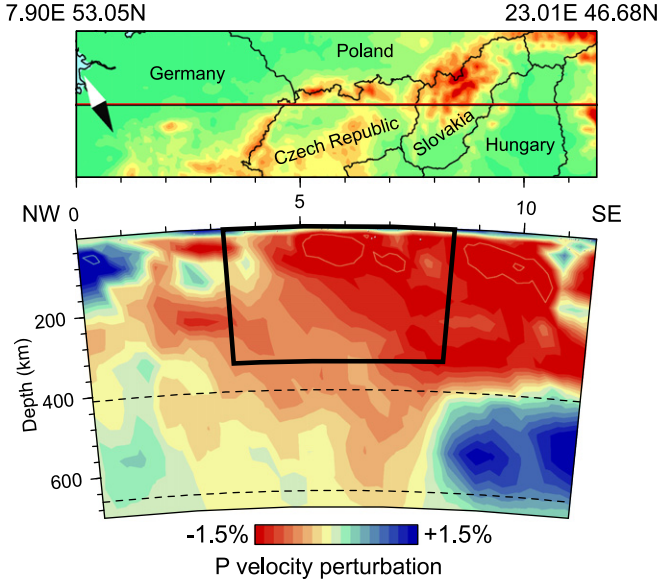

Fig. 12. Cross-section through the velocity model from global tomography (Amaru, 2007) along the NW–SE profile. The target volume of this paper is indicated. The velocities are shown as perturbations relative to the ak135 reference Earth model (Kennett et al., 1995).

While the relief of the LAB in the western BM is confirmed by several independent seismic techniques, the structure of the upper mantle beneath the contact of the SU/MD/MS units seems to be more complex. The depth variations of the LAB proposed by Plomerová et al. (2011-this issue) indicates a thinner lithosphere beneath the contact of SU/MD/MS units compared to that beneath the eastern part of the MS unit. The general low-velocity pattern in the tomographic images is disturbed by a high-velocity heterogeneity (Figs. 8 and 9), indicating a complex structure in the region. Additionally, Geissler et al. (2012-this issue) suggest two alternative interpretations of the LAB depths from the Sp receiver functions in this area and thus, they note that the north-eastern BM might have complicated internal structure.

Another discrepancy between inferences of seismic techniques emerges from a comparison of velocity perturbations with anisotropic studies of the BM upper mantle. Joint inversions of shear-wave splitting parameters and P-wave residuals, resulting in 3D self-consistent models of seismic anisotropy (e.g., Babuška et al., 2008; Plomerová et al., 2000, 2007, 2011-this issue) revealed that the BM mantle lithosphere is formed by domains with consistent olivine fabric. These domains, found also in other European regions, e.g., Baltic Shield or the French Massif Central (Babuška et al., 2002; Plomerová et al., 2002), are often accompanied by changes of the lithosphere and/or crust thicknesses, and

are interpreted as blocks of lithosphere with frozen-in olivine preferred orientation (Babuška and Plomerová, 2006). Eken et al. (2010) observed a remarkable correlation between the division of anisotropic domains and the isotropic velocity heterogeneities retrieved from the tomography of the upper-mantle below the Swedish National Seismological Network (Eken et al., 2007, 2008). However, the domains of the BM mantle lithosphere down to depths of 80–120 km (Geissler et al., 2012-this issue; Plomerová and Babuška, 2010; Plomerová et al., 2011-this issue), characterized by different orientation of dipping symmetry axes, remain hidden in the isotropic images in our study. This can be due to the fact that the BM domains delimited by changes in fossil anisotropy need not vary in average isotropic velocities, or, differences among them are too small to be resolved by isotropic tomography, due to uneven ray geometry of the BOHEMA II array.

The primary goal of the BOHEMA I experiment in the western BM was to detect a potential baby-plume in the upper mantle, predicted beneath the Variscan massifs (Granet et al., 1995). Such a baby-plume was not imaged by the specially designed station array BOHEMA I. We can hardly have better resolution in the western part of the BM using data of the BOHEMA II experiment, designed for other purposes. In spite of that, both tomography experiments result in similar perturbation images. In the future, we plan to increase the resolution of the tomographic images of the whole BM upper mantle by, combining the BOHEMA II dataset with those from temporary arrays of other experiments, namely, BOHEMA I, BOHEMA III, PASSEQ, and ALPASS (Babuška et al., 2005; Brückl et al., 2007; Plomerová et al., 2007; Wilde-Piórko et al., 2008), when data is available.

7. Conclusions

In this study, we present results from high-resolution seismic tomography beneath the north-eastern parts of the Bohemian Massif down to ~250 km. The resulting tomographic model, with a variance reduction of 84%, shows relatively small velocity variations, both in size and in amplitude. Only a small-size high-velocity perturbation in the eastern part of the model can be related to the complex structure beneath the contact of the Sudetes/Moravo-Silesian units. Similarly to the results from the BOHEMA I experiment in the western BM, the presented model from BOHEMA II data indicates the southward thickening of the lithosphere beneath the BM. Though the low perturbations prevail in the upper mantle, some inconsistencies among isotropic velocity perturbation model, Sp receiver function inferences and anisotropic models of the mantle lithosphere domains indicate that both the topography of the lithosphere–asthenosphere boundary and internal velocity structure of the upper mantle beneath the BM are complex.

We tested two different regularization techniques as well as model resolutions. The damped least square method resulted in a smooth velocity perturbation model, which was only slightly sensitive to uneven ray coverage in the regular model parameterization, whereas the truncated singular decomposition method tended to produce unrealistically small-sized anomalies. Therefore, to model the upper mantle velocity structure, we prefer the damped least square regularization. Resolution tests of the BOHEMA II array configuration confirm that the vertical smearing is more distinct than the horizontal one in the case of heterogeneity at size of about 6 times of horizontal node spacing by 3 times of vertical node spacing. On the other hand, smaller heterogeneity at size of about 4 times of horizontal node spacing by 2 times of vertical node spacing are well-recovered in both horizontal and vertical dimensions. To increase resolution of the tomographic images of the BM upper mantle velocities, we plan in near future to combine the BOHEMA II dataset with those from other temporary arrays in the region.

Supplementary data to this article can be found online at http://dx.doi.org/10.1016/j.tecto.2012.06.031.

Acknowledgments

The authors are grateful to U. Achauer, T. Eken and J. Šimkanin for their advice during TELINV code implementation at the early stage of computations and R.C. Liebermann and C. Alexandrakis for English grammar corrections. Consultations and recommendations of E. Kissling are greatly appreciated. Constructive criticism and recommendations of two anonymous reviewers help to improve the manuscript and are greatly acknowledged. The research was partly supported by grant nos. 205/071088 and 210/12/2381 of the Grant Agency of the Czech Republic, by a grant no. IAA300120709 of the Grant Agency of the Academy of Sciences of the Czech Republic and by grant no. SVV-2012-265308. The data acquisition was supported by the project of large research infrastructure Czech Geo, grant no. LM2010008.

References

Achauer, U., 1992. A study of the Kenya Rift using delay-time tomography analysis and gravity modelling. Tectonophysics 209, 197–207.
Amaru, M., 2007. Global Travel Time Tomography with 3-D Reference Models, Geol. Traiectina 274. PhD thesis, Utrecht Univ. 174 pp.
Arlitt, R., Kissling, E., Ansorge, J., 1999. Three-dimensional crustal structure beneath the TOR array and effects on teleseismic wavefronts. Tectonophysics 314, 309–319.
Babuška, V., Plomerová, J., 2006. European mantle lithosphere assembled from rigid microplates with inherited seismic anisotropy. Phys. Earth. Planet. Inter. 158, 264–280. http://dx.doi.org/10.1016/j.pepi.2006.01.010.
Babuška, V., Plomerová, J., 2008. Control of paths of Quaternary volcanic products in western Bohemian Massif by rejuvenated Variscan triple junction of ancient microplates. Studia Geophysica et Geodaetica 52, 607–629.
Babuška, V., Plomerová, J., Vecsey, L., Granet, M., Achauer, U., 2002. Seismic anisotropy of the French Massif Central and predisposition of Cenozoic rifting and volcanism by Variscan suture hidden in the mantle lithosphere. Tectonics 21. http://dx.doi.org/10.1029/2001TC901035.
Babuška, V., Plomerová, J., Vecsey, L., Jedlička, P., Růžek, B., 2005. Ongoing passive seismic experiments unravel deep lithosphere structure of the Bohemian Massif. Studia Geophysica et Geodaetica 3, 423–430.
Babuška, V., Plomerová, J., Vecsey, L., 2008. Mantle fabric of western Bohemian Massif (central Europe) constrained by 3D seismic P and S anisotropy. Tectonophysics 462, 149–163.
Brückl, E., Behm, M., Chvatal, W., Mitterbauer, U., CELEBRATION 2000, ALP 2002, ALPASS Working Groups, 2007. Erkenntnisse über den Tiefbau der Ostalpen aus neuen seismischen Großexperimenten. Beiträge zur Geologie Oberösterreichs, Arbeitstagung GBA, pp. 143–150.
Eken, T., Shomali, H., Roberts, R., Bodvarsson, R., 2007. Upper mantle structure of the Baltic Shield below the Swedish National Seismological Networks (SNSN) resolved by teleseismic tomography. Geophysical Journal International 169, 617–630.
Eken, T., Shomali, Z.H., Roberts, R., Hieronymus, C.F., Bodvarsson, R., 2008. S and P velocity heterogeneities within the upper mantle below the Baltic Shield. Tectonophysics 462, 109–124.
Eken, T., Plomerová, J., Roberts, R., Vecsey, L., Babuška, V., Shomali, H., Bodvarsson, R., 2010. Seismic anisotropy of the mantle lithosphere beneath the Swedish National Seismological Network (SNSN). Tectonophysics 480, 241–258.
Evans, J.R., Achauer, U., 1993. Teleseismic velocity tomography using the ACH method: theory and application to continental scale studies. In: Iyer, H.M., Hirahara, K. (Eds.), Seismic Tomography. Chapman and Hall, London, pp. 319–360.
Geissler, W.H., Skacelová, Z., Kämpf, H., Plomerová, J., Korn, M., Babuška, V., Kind, R., 2012. Lithosphere structure of the NE Bohemian Massif (Sudetes) — a teleseismic receiver function study. Tectonophysics 564-565, 12–37 (this issue).
Granet, M., Wilson, M., Achauer, U., 1995. Imaging a mantle plume beneath the French Massif Central. Earth and Planetary Science Letters 136, 281–296.
Heuer, B., Kämpf, H., Kind, R., Geissler, W.H., 2007. Seismic evidence for whole lithosphere separation between Saxothuringian and Moldanubian tectonic units in central Europe. Geophysical Research Letters 34, 1–5.
Judenherc, S., Granet, M., 1999. Two-dimensional anisotropic tomography of lithosphere beneath France using regional arrival times. Journal of Geophysical Research 104, 13201–13215.
Kachlík, V., 2003. Geological evolution of the Czech Republic territory (in Czech) Supplement to the publication: Preparation of a deep geological repository of a nuclear waste, Surao Praha.
Karousová, H., Plomerová, J., Babuška, V., 2012. A three-dimensional velocity model of the crust of the Bohemian Massif. Studia Geophysica et Geodaetica 56, 249–267. http://dx.doi.org/10.1007/s11200-010-0065-z.
Kennett, B.L.N., Engdahl, E.R., 1991. Traveltimes for global earthquake location and phase identification. Geophysical Journal International 105, 429–465.
Kennett, B.L.N., Engdahl, E.R., Buland, R., 1995. Constraints on seismic velocities in the Earth from traveltimes. Geophysical Journal International 122, 108–124.
Kissling, E., Spakman, W., 1996. Interpretation of tomographic images of uppermost mantle structure: examples from the western and central Alps. Journal of Geodynamics 21, 97–111.

Koulakov, I., Kaban, M.K., Tesauro, M., Cloetingh, S., 2009. P- and S-velocity anomalies in the upper mantle beneath Europe from tomographic inversion of ISC data. Geophysical Journal International 179, 345–366.

Lippitsch, R., Kissling, E., Ansorge, J., 2003. Upper mantle structure beneath the Alpine orogen from high-resolution teleseismic tomography. Journal of Geophysical Research 108, 2376.

Martin, M., Wenzel, F., 2006. High-resolution teleseismic body wave tomography beneath SE-Romania — II. Imaging of a slab detachment scenario. Geophysical Journal International 164, 579–595.

Menke, W., 1984. Geophysical Data Analysis: Discrete Inverse Theory. Academic Press, Inc., College of Oceanography, Oregon State University.

Mercier, J.-P., Bostock, M.G., Cassidy, J.F., Dueker, K., Gaherty, J.B., Garnero, E.J., Revenaugh, J., Zandt, G., 2010. Body-wave tomography of western Canada. Tectonophysics 475, 480–492.

Piromallo, C., Morelli, A., 2003. P wave tomography of the mantle under the Alpine–Mediterranean area. Journal of Geophysical Research 108 (B2), 2065.

Plomerová, J., Babuška, V., 2010. Long memory of mantle lithosphere fabric — European LAB constrained from seismic anisotropy. Lithos 120, 131–143.

Plomerová, J., Babuška, V., Šílený, J., Horálek, J., 1998. Seismic anisotropy and velocity variations in the mantle beneath the Saxothuringicum–Moldanubicum contact in Central Europe. Pure and Applied Geophysics 151, 365.

Plomerová, J., Granet, M., Judenherc, S., Achauer, U., Babuška, V., Jedlička, P., Kouba, D., Vecsey, L., 2000. Temporary array data for studying seismic anisotropy of Variscan Massifs — the Armorican Massif French Massif Central and Bohemian Massif. Studia Geophysica et Geodaetica 44, 195–209.

Plomerová, J., Babuška, V., Vecsey, L., Kouba, D., 2002. Seismic anisotropy of the lithosphere around the Trans-European Suture Zone (TESZ) based on teleseismic body-wave data of the TOR experiment. Tectonophysics 360, 89–114.

Plomerová, J., Achauer, U., Babuška, V., Granet, M., 2003. BOHEMA 2001–2003. Passive seismic experiment to study lithosphere–asthenosphere system in the western part of the Bohemian Massif. Studia Geophysica et Geodaetica 47, 691–701.

Plomerová, J., Achauer, U., Babuška, V., Vecsey, L., 2007. Upper mantle beneath the Eger Rift (Central Europe): plume or asthenosphere upwelling? Geophysical Journal International 169, 675–682.

Plomerová, J., Vecsey, L., Babuška, V., 2011. Mapping seismic anisotropy of the lithospheric mantle beneath the northern and eastern Bohemian Massif (central Europe). Tectonophysics 564-564, 38–53 (this issue).

Press, W.H., Flannery, B.P., Teukolsky, S.A., Vetterling, W.T., 1992. Numerical recipes in Fortran 77, The Art of Scientific Computing2nd edition. Cambridge University Press.

Ritter, J.R.R., Jordan, M., Christensen, U.R., Achauer, U., 2001. A mantle plume below the Eifel volcanic fields, Germany. Earth and Planetary Science Letters 186, 7–14.

Sandoval, S., Kissling, E., Ansorge, J., SVEKALAPKO Seismic Tomography Working Group, 2003. High-resolution body wave tomography beneath the SVEKALAPKO array: I. A priory three dimensional crustal model and associated travel-time effects on teleseismic tomographic wave fronts. Geophysical Journal International 153, 75–87.

Sandoval, S., Kislling, E., Ansorge, J., SVEKALAKO Seismic Tomography working Group, 2004. High-resolution body wave tomography beneath the SVEKALAPKO array — II. Anomalous upper mantle structure beneath the central Baltic Shield. Geophysical Journal International 157, 200–214.

Shomali, Z.H., Roberts, R.G., Pedersen, L.B., the TOR Working Group, 2006. Lithospheric structure of the Tornquist Zone resolved by nonlinear P and S teleseismic tomography along the TOR array. Tectonophysics 416, 133–149.

Spakman, W., Vanderlee, S., van der Hilst, R., 1993. Travel-time tomography of the European Mediterranean Mantle down to 1400 km. Physics of the Earth and Planetary Interiors 79, 3–74.

Steck, L.K., Prothero, W.A., 1991. A 3-D ray-tracer for teleseismic body-wave arrival-times. Bulletin of the Seismological Society of America 81, 1332–1339.

van der Meer, D.G., Spakman, W., van Hinsbergen, D.J.J., Amaru, M.L., Torsvik, T.H., 2010. Toward absolute plate motions constrained by lower mantle slab remnants. Nature Geoscience 3, 36–40.

Waldhauser, F., Lippitsch, R., Kissling, E., Ansorge, J., 2002. High-resolution teleseismic tomography of the upper mantle structure using an a priori three-dimensional crustal model. Geophysical Journal International 150, 403–414.

Weiland, C.M., Steck, L.K., Dawson, P.B., Korneev, V.A., 1995. Nonlinear teleseismic tomography at Long Valley caldera, using three-dimensional minimum travel time ray tracing. Journal of Geophysical Research 100, 20379–20390.

Wilde-Piórko, M., Geissler, W.H., Plomerová, J., Grad, M., Babuška, V., Brückl, E., Cyziene, J., Czuba, W., England, R., Gaczyński, E., Gazdova, R., Gregersen, S., Guterch, A., Hanka, W., Hegedűs, E., Heuer, B., Jedlička, P., Lazauskiene, J., Keller, G.R., Kind, R., Klinge, K., Kolinsky, P., Komminaho, K., Kozlovskaya, E., Krüger, F., Larsen, T., Majdański, M., Málek, J., Motuza, G., Novotný, O., Pietrasiak, R., Plenefisch, T., Růžek, B., Sliaupa, S., Środa, P., Świeczak, M., Tiira, T., Voss, P., Wiejacz, P., 2008. PASSEQ 2006–2008: passive seismic experiment in Trans-European Suture Zone. Studia Geophysica et Geodaetica 52, 439–448.

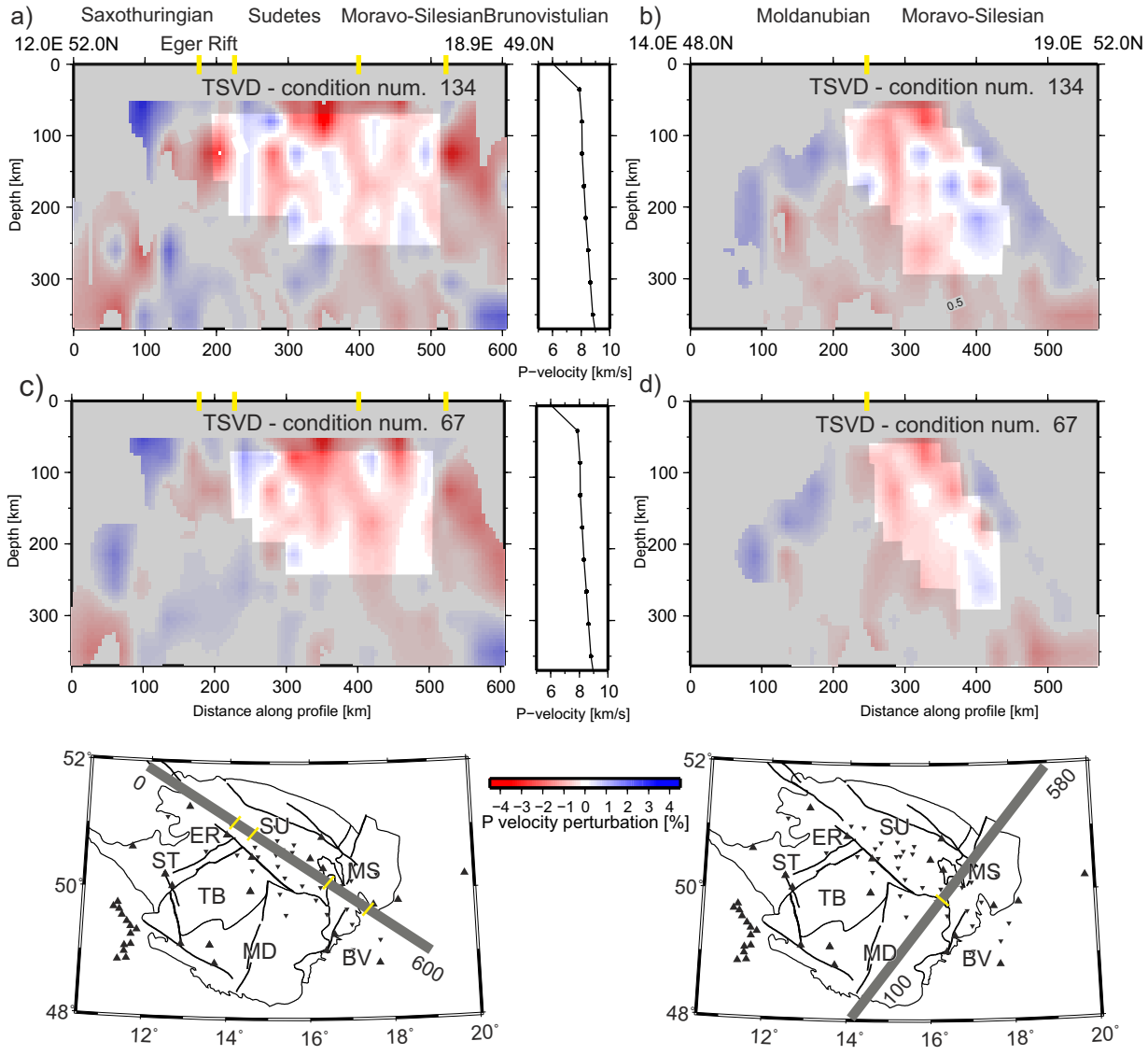

Fig. S1. Cross-sections through the velocity perturbation models from the inversions with the TSVD regularization method along the NW-SE (a,c) and along the SW-NE (b,d) profiles with condition numbers of 134 (a,b) and 67 (c,d). Resolved areas are indicated as in Fig. 8. The input 1D velocity model is shown for comparison. The yellow marks indicate approximate contacts of the Saxothuringian (ST), Teplá-Barrandian (TB), Sudetes, (SU), Moldanubian (MD), Moravo-Silesian (MS), and Brunovistulian (BV) units, and the approximate position of the Eger Rift (ER).

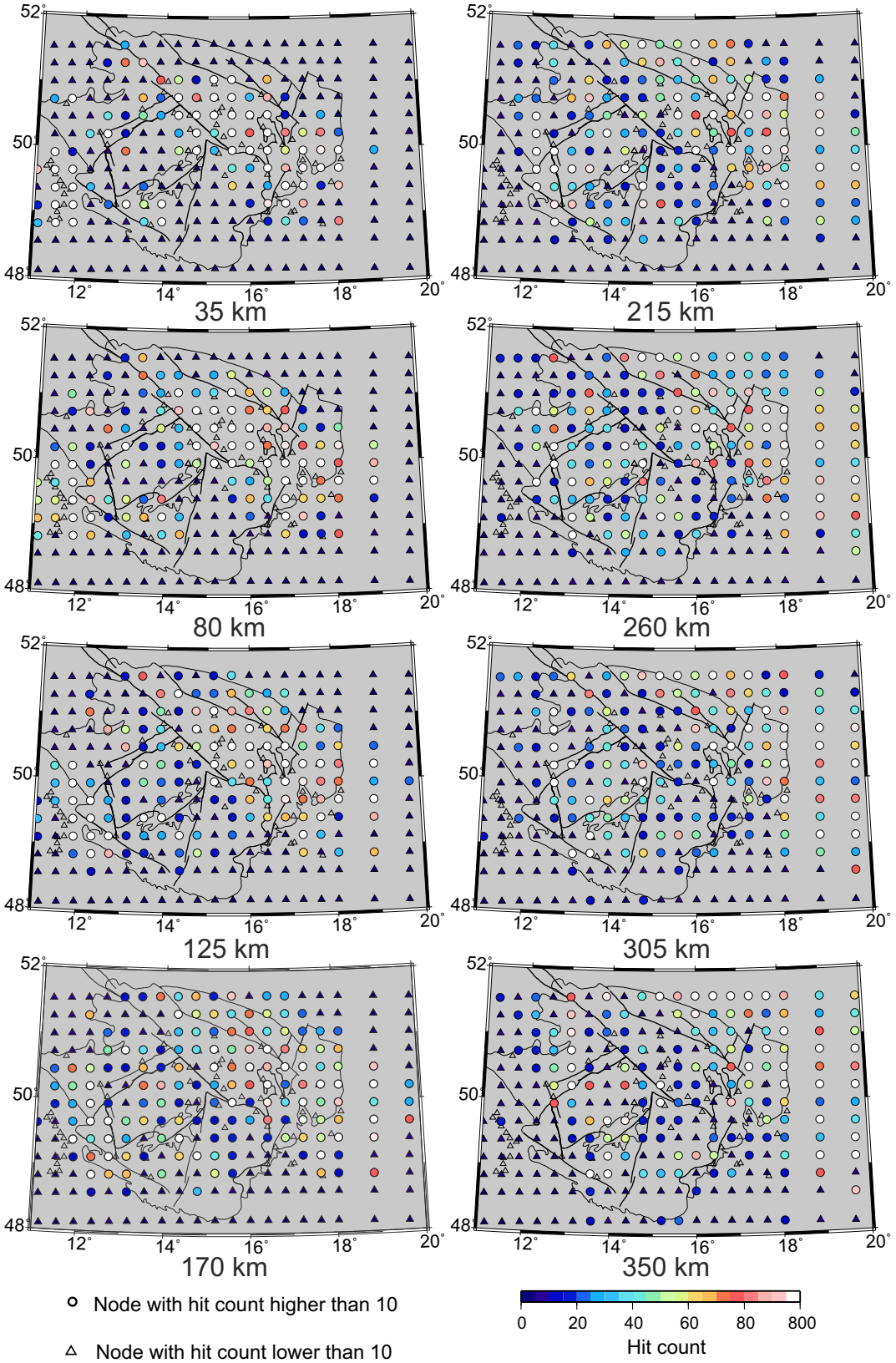

Fig. S2. Ray hit-count at horizontal slices of the model parameterization shown in Figure 4. The black lines show tectonic units of the BM and main faults as in Figure 1. The hit count map reflects that the events from the NE back-azimuths prevail.

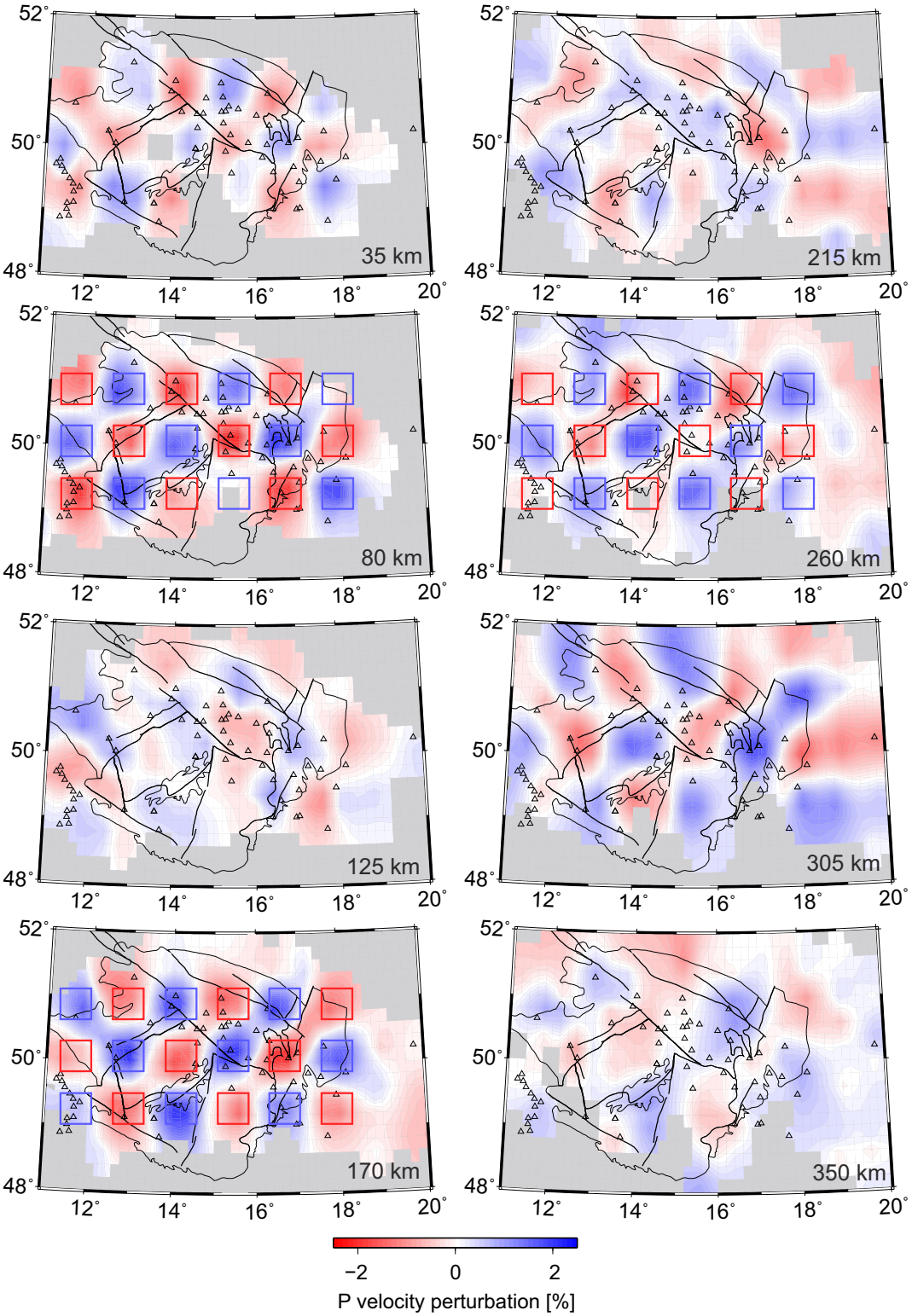

Fig. S3. Checkerboard test indicating recovered synthetic velocity anomalies of +3% (blue squares) and −3% (red squares) added into the IASP91 radial Earth model at depths of 80, 170 and 260 km. The black lines show tectonic units of the BM and main faults as in Figure 1. The test shows good lateral recovery of the input model, but significant vertical smearing especially in deeper parts of the

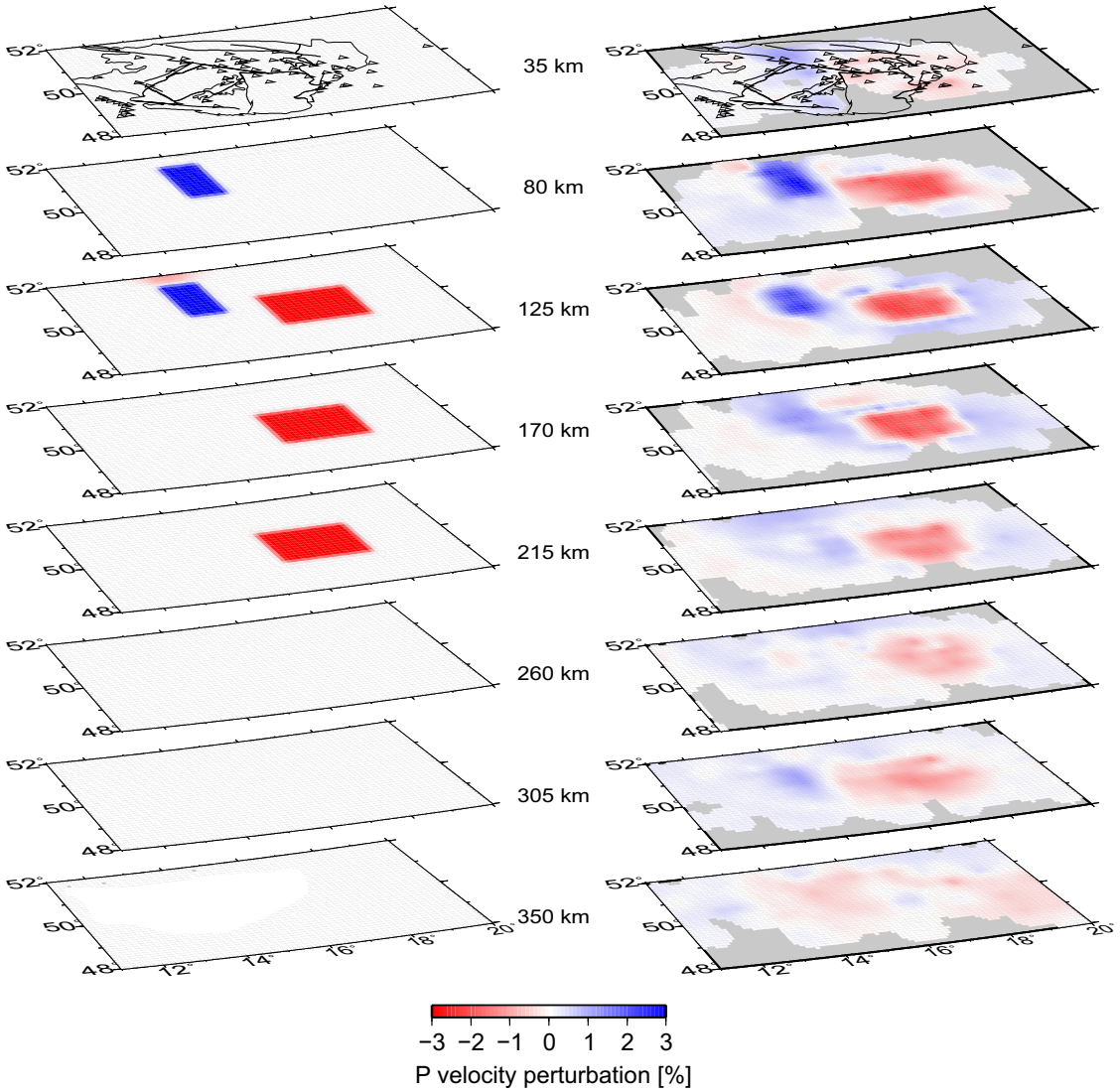

Fig. S4. Test recovering two +3% (blue) and −3% (red) synthetic velocity anomalies added into the IASP91 radial Earth model. The input model is shown on the left, and recovered velocities are shown on the right. The black lines show tectonic units of the BM and main faults as in Figure 1. The test indicates that the small-size velocity anomaly does not suffer from vertical smearing of velocity perturbations as much as the large anomaly.

P3

Upper-mantle structure beneath the southern Bohemian Massif and its surroundings imaged by high-resolution tomography

Karousová, H., Plomerová, J. and Babuška, V.

Geoph. J. Int.; doi: 10.1093/gji/ggt159, 2013

Geophysical Journal International

Geophys. J. Int. (2013) doi: 10.1093/gji/ggt159

Geophysical Journal International Advance Access published May 17, 2013

Upper-mantle structure beneath the southern Bohemian Massif and its surroundings imaged by high-resolution tomography

H. Karousová,[1,2] J. Plomerová[1] and V. Babuška[1]

[1]*Institute of Geophysics, Academy of Sciences, Prague, Czech Republic. E-mail: hana.karousova@gmail.com*
[2]*Department of Geophysics, Faculty of Mathematics and Physics, Charles University, Prague, Czech Republic*

Accepted 2013 April 16. Received 2013 April 12; in original form 2013 January 23

SUMMARY

We present a new velocity-perturbation model of the upper mantle down to 300 km retrieved by teleseismic tomography beneath the southern part of the Bohemian Massif (BM) and its surroundings. Though the upper mantle beneath the BM appears as extensive low-velocity heterogeneity in large-scale tomography studies of Europe, our regional study based on data from passive experiment BOHEMA III and the northern part of the ALPASS array reveals also velocity features at scales of ∼40 km. The most distinct low-velocity perturbations concentrate along the Eger Rift down to ∼200 km, while velocities at greater depths beneath this rift show high-velocity perturbations relative to the overall low-velocity character of the BM mantle. Two significant high-velocity heterogeneities dominate the tomography images. The most distinct and extensive one, located south of the BM, we associate with the eastern Alpine root. The second high-velocity heterogeneity can be traced in horizontal slices down to 215 km beneath the central part of the BM. These positive perturbations seem to shift from the southwestern part of the massif at shallower depths to the northeastern part of the BM at greater depths. The heterogeneity can reflect the lithosphere thickening resulting from the collision of the BM with the Brunovistulian (BV) microplate from the east and the following underthrusting of the BV beneath the Moldanubian part of the BM.

Key words: Body waves; Seismic tomography; Europe.

1 INTRODUCTION

The Bohemian Massif (BM) is the prominent easternmost exposure of the European Variscan Belt (Fig. 1). Its present-day structure represents a collage of microplates and relics of magmatic arcs, resulting from the collision of supercontinents Laurasia (Laurentia–Baltica) and Africa (Gondwana). While the BM was consolidated during the Variscan orogeny in a period between 380 and 300 Ma (e.g. Franke 2000), the Alps resulted from the collision of the African and Eurasian tectonic plates during the Oligocene and Miocene (35–5 Ma). The closure of the Alpine ocean basins lead to the collision of the Adriatic microplate (subplate of Africa) with the European platform, causing a second phase of the Alpine orogenic activity (Brückl *et al.* 2007). Teleseismic tomography (e.g. Lippitsch *et al.* 2003; Koulakov *et al.* 2009; Dando *et al.* 2011; Mitterbauer *et al.* 2011) based on data of permanent and temporary seismic stations helps to understand the structure and tectonic evolution of the region.

The target of three successive seismic passive experiments BOHEMA I–III (Babuška *et al.* 2005) was to gather and exploit teleseismic data from dense temporary arrays of stations for studying velocity structure of the upper mantle beneath the BM. Based on high-quality recordings from these experiments, modelling of seismic anisotropy revealed a domain-like structure of the BM mantle lithosphere, with deep boundaries of the geotectonic units often shifted relative to their surface equivalents (Plomerová *et al.* 2007, 2012; Babuška & Plomerová 2008, 2013).

Primary initiative of isotropic tomographic imaging of the upper mantle beneath the BM was an idea of a possible existence of a mantle plume beneath the Eger Rift (ER) in western part of the BM that belongs to the geodynamically most active part of the massif. The idea stems from similarities between the ER and the Variscan rifts in the French Massif Central and the Rhenish Massif, where small plumes were indicated by tomographic studies (Granet *et al.* 1995; Ritter *et al.* 2001). However, results of the first teleseismic tomography based on data from BOHEMA I (Plomerová *et al.* 2007) did not image any columnar anomaly that could be interpreted as a mantle plume. The broad low-velocity anomaly in the western BM was interpreted by an asthenosphere upwelling beneath the region (Plomerová *et al.* 1998). Tomographic images based on data from passive seismic experiment BOHEMA II, focused on the northeastern part of the BM, showed relatively small velocity perturbations, both in size and in amplitude (Karousová *et al.* 2012b). Generally prevailing low-velocity characteristics of the uppermost mantle beneath the northeastern BM, with only small high-velocity perturbations, are in agreement with other regional tomography

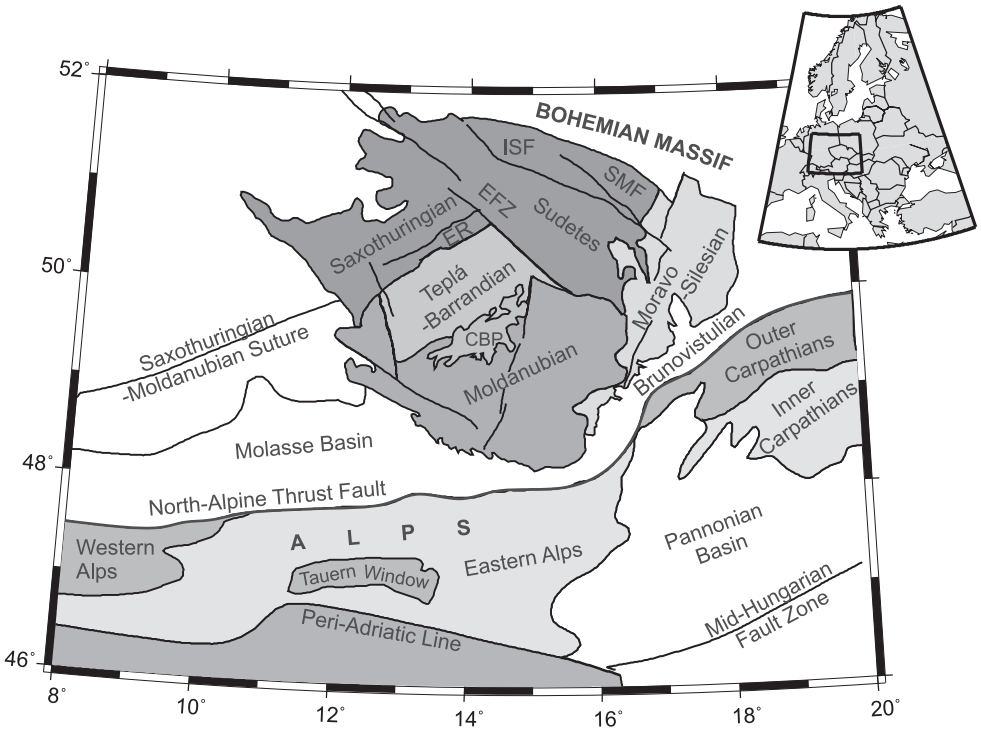

Figure 1. Simplified map of tectonic units in a region of the Bohemain Massif and the Alps: ER, Eger Rift; EFZ, Elbe Falut Zone; ISF, Intra-Sudetic Fault; SMF, Sudetic Marginal Fault; CBP, Central Bohemian Pluton. Redrawn from Plomerová *et al.* (2007) and Brückl *et al.* (2010).

studies (Piromallo & Morelli 2003; Amaru 2007; Koulakov *et al.* 2009), where the BM is a part of an extensive low-velocity region.

This paper focuses on the isotropic tomography of the southern BM and its surroundings down to ∼300 km. Velocity perturbations are retrieved from data of the third passive seismic experiment BOHEMA III (Fig. 2) realized in the massif. To get better resolution at deeper parts of the model, we incorporated also data from the northern part of the ALPASS array (Mitterbauer *et al.* 2011) surveying the upper mantle beneath the Eastern Alps (EA).

2 DATA

P-wave arrival times measured on digital recordings of the BOHEMA III experiment form a core of data set for calculation of velocity images of the upper mantle beneath the southern part of the BM. Temporary stations of the BOHEMA III passive seismic experiment were in operation for about 1 yr, from 2005 July to 2006 July. Contemporarily, seismic stations of the independent ALPASS project (Mitterbauer *et al.* 2011) were installed south of the BM, in the EA. To enhance station coverage of both experiments, we agreed on an exchange of a part of data from both experiments. Because the ALPASS array started its operation about 2 months earlier than the BOHEMA III array, we included into our data set also waveforms from stations running during preceding experiment in the north-eastern part of the BM—the BOHEMA II (Babuška *et al.* 2005). We collected waveforms from 65 temporary seismic stations of the BOHEMA III experiment, the northern part of the ALPASS project and an overlapping part of the BOHEMA II experiment, and from 57 permanent observatories in the region (Fig. 2).

To measure the *P*-wave arrival times, we selected events between 2005 May and 2006 July with a minimal magnitude 4.7 and epicentral distances in a range from 25° to 95° relative to the centre of the array. Because we aimed our attention at obtaining as homogeneous distribution of rays within the investigated upper-mantle volume as possible, we sorted events according to the backazimuth, ray path angle and a signal-to-noise ratio estimated with the use of the short-term average/long-term average (STA/LTA) method. In this way, we managed to assign at least one event to all backazimuth and ray path angle segments and to limit a number of events with dominant backazimuths (Fig. 3).

We resample waveforms of each event to 100 Hz, correct them for the effect of instrument response to simulate WWSSN-SP (World Wide Standardized Seismic Network—short period) sensor. We use a semi-automatic picking procedure incorporated into the Seismic Handler software (Stammler 1993). The procedure consists of two steps. At first we select a station with the strongest signal, where we mark an interval with the *P*-wave coda. Then the waveforms of all the stations of the array are shifted by time differences found by cross-correlation with the signals in the marked interval. Having the waveforms aligned, we select an extreme closest to the first onset that is coherent across the whole station array. In the second step, the time of the selected extreme is determined as a time of the minimum or maximum of the waveforms within the interval for all the stations. To have also absolute arrival times, we measure the first onsets of the *P*-wave arrival on one or several recordings with the clearest signal for each event. From the differences between the times measured at the first onsets and coherent extremes, the absolute arrival times for all the stations were calculated. All the picks are visually inspected and quality classes are assigned to each pick according to time uncertainty of the measurement (±0.05, ±0.10 or ±0.20 s). Due to the pre-selection of the events, the 85 per cent of the picks are of the highest quality (Table 1).

To avoid time instabilities, we analysed the measured *P*-wave arrival times as described in Karousová *et al.* (2012b). For some of the stations, we detected time instabilities that were mostly attributed to

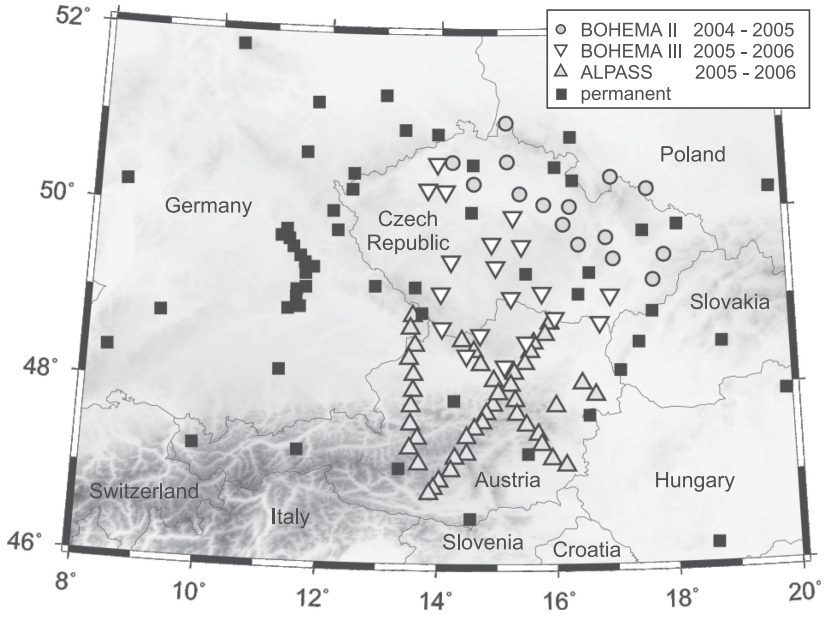

Figure 2. Location of temporary stations and permanent observatories included in several passive seismic experiments in a topography map of the region.

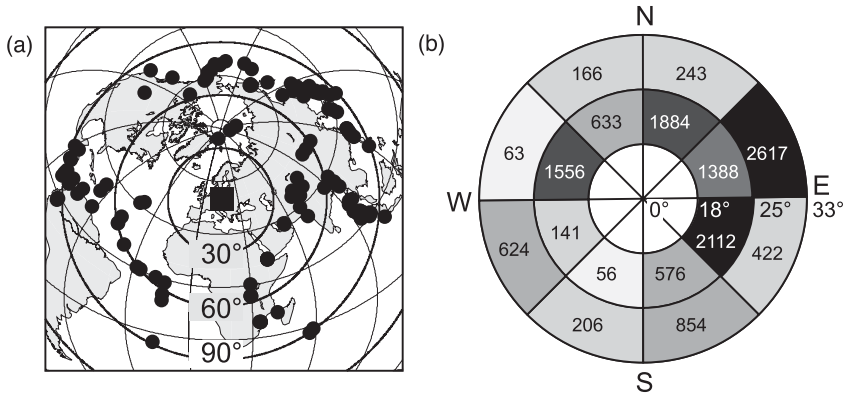

Figure 3. (a) Teleseismic events used (circles) and a location of the region studied (square). (b) Distribution of a number of rays corresponding to *P*-wave residuals entering the inversion sorted into bins according to their backazimuth and approximate ray path angle in the volume studied.

Table 1. Classifications of the *P*-wave arrival times according to quality of measurements.

Quality classes	Error (s)	Number of measurements
1	±0.05	11 460
2	±0.10	1542
3	±0.20	539

poor time synchronization between the Global Positioning System (GPS) and the data acquisition system. Stable time-shifts were then corrected, while unstable ones were removed from the data set used in the tomography. The cleansed data set consists of 13 541 *P*-wave arrivals from 168 events measured on 136 stations with the average error of ±0.062 s.

Traveltime residuals are affected by errors both in event mislocations and time origins, and by heterogeneities along paths outside of the volume studied. Because the ray paths from a distant event to the station array are similar, we can remove such effects by traveltime normalization, in which an event reference residual is subtracted from all traveltime residuals (e.g. Evans & Achauer 1993). We tested several types of normalizations with conclusion that differences in resulting velocity perturbations were small and visible only in the margins of the model. Therefore, we selected the most robust normalization and calculated the reference residual as an average for each event with at least 45 measurements. The relative residuals entering the tomographic inversion vary between −2 and 2 s.

Crustal heterogeneities cannot be resolved by the teleseismic tomography because ray paths of teleseismic waves are nearly vertical at shallow depths and do not intersect there. Moreover, the wavelengths of teleseismic phases are too large to 'see' details in the heterogeneous crust. The importance of crustal corrections was highlighted in many studies, for example, Arlitt *et al.* (1999), Waldhauser *et al.* (2002), Martin *et al.* (2005), Karousová *et al.* (2012a), showing also a possible projection of crustal heterogeneities into the upper-mantle structure. Therefore, we compiled a 3-D crustal model to minimize crustal effects on velocity images of the upper mantle retrieved by teleseimic tomography. The 3-D crustal model used for crustal corrections is the same as that in a tomographic study of the northern and eastern part of the BM (Karousová *et al.* 2012a,b) extended southwards by a model of Behm *et al.* (2007). Both models are based on data and results from controlled-source seismic experiments, for example, CELEBRATION 2000, ALP 2002 and SUDETES 2003 (e.g. Hrubcová *et al.* 2005; Majdanski *et al.* 2006; Brückl *et al.* 2007; Grad *et al.* 2008).

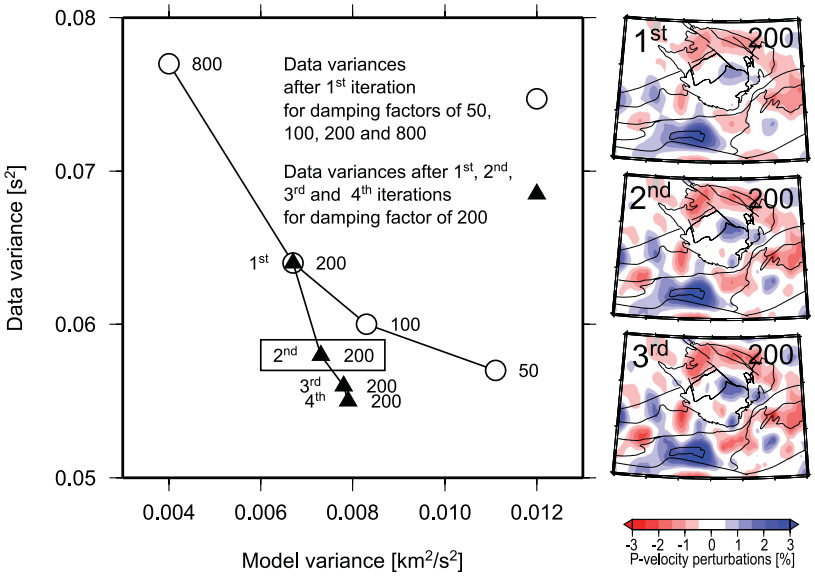

Figure 4. Trade-off curves between the data and model variances to determine a damping factor. The damping factor of 200 was selected for final calculations as a compromise between data and model variances. A part of the trade-off curve for damping factor 200 for the first to fourth iterations (triangles), along with a comparison of velocity perturbations at depth of 145 km after the first, second and third iterations are shown as well (right-side column). We prefer velocity perturbations after the second iteration because the following iterations lead to one-cell perturbations in less resolved regions.

To avoid sudden variations caused by extrapolation near edges of the models, we combined Moho depths from well-resolved regions of both models and interpolated velocities from the two models. Velocities of the reference earth model IASP91 (Kennett & Engdahl 1991) were used at sites where data were missing and at parts of the model from the Moho depth down to the 60 km. The model does not include information on very shallow sediment layers (down to ∼100 m), which are not resolved in 2-D velocity profiles from the active seismic experiments. Therefore, we have calculated station terms for individual stations according to unpublished sources with approximate thicknesses and *P*-wave velocities of sediments. The crustal corrections were calculated as differences of traveltimes of waves propagating through the 3-D crustal model and those propagating through the crust of the reference IASP91 model. Crustal corrections are smooth and compensate traveltime deviations mainly for regional effects of the Moho depth.

3 METHOD

To retrieve velocity perturbations in the upper mantle, we use a tomographic code based on a modified non-linear inversion scheme known as the Aki–Christoffersson–Husebye (ACH) method (Aki *et al.* 1977; Evans & Achauer 1993). The task is solved by a weighted damped least-square method, where the inverse of kernel matrix is computed by truncated singular value decomposition. Governing equation of the technique is described, for example, in Menke (1984). In the forward-modelling part of the code, the 3-D ray tracing bending technique Simplex (Steck & Prothero 1991), where ray paths are distorted by sinusoidal signals, is applied. Resulting perturbations are calculated in several iteration cycles, in which the ray paths, within the volume studied, and traveltime residuals are updated according to the improved velocity model.

We discretize the model by a grid of nodes with a regular horizontal spacing of 40 km and with depth increasing vertical spacing of 30, 40 and 50 km according to a ray geometry (see Fig. 7), given by the station and event distributions, and a dominant wavelength of the teleseismic *P* waves. Total number of inverted nodes, at depths from 25 to 305 km, is 3800. The perturbations at the first inverted depth of 25 km cannot be resolved due to lack of ray intersections. However, these perturbations, at nodes at the margin of the model, tend to absorb imperfect crustal corrections and data errors which would be otherwise projected to the deeper parts of the model. As an initial velocity model for the inversions and for calculation of theoretical traveltimes, we used the IASP91 reference earth velocity model (Kennett & Engdahl 1991). The input residuals are weighted according to the quality classes determined for each event-station pair during the picking procedure (Section 2).

The damping factor and number of iterations control both stability and complexity of the solution (Lippitsch *et al.* 2003). We selected these parameters according to the trade-off curves and synthetic tests with the main criterion that resulting velocity perturbations must have a physical meaning (Karousová *et al.* 2012b). The damping factor of 200 was selected in a close vicinity of the inflection point of the trade-off curve based on the data and model variances (Fig. 4). Main features of tomographic images after the second, third and fourth iterations remain unchanged (Fig. 4), which indicates a stability of the solution. We prefer velocity perturbations after the second iterations because the following iterations lead to several one-cell anomalies in less resolved parts of the model. Standard deviation of the final residuals is 0.24 s, which is highly above our estimate of the picking error. The difference between the estimate of data error and standard deviation of the final residuals can be explained by well-known limitations of the isotropic teleseismic traveltime tomography, for example, imperfect crustal corrections, velocity model simplification or neglecting seismic anisotropy.

4 RESULTS

4.1 Tomography images of the upper mantle

We present *P*-velocity perturbations of the final model of the BM, relative to the background velocity model IASP91, in eight horizontal slices at depths from 55 to 305 km (Fig. 5). The perturbations are considered as well-resolved if diagonal elements of resolution

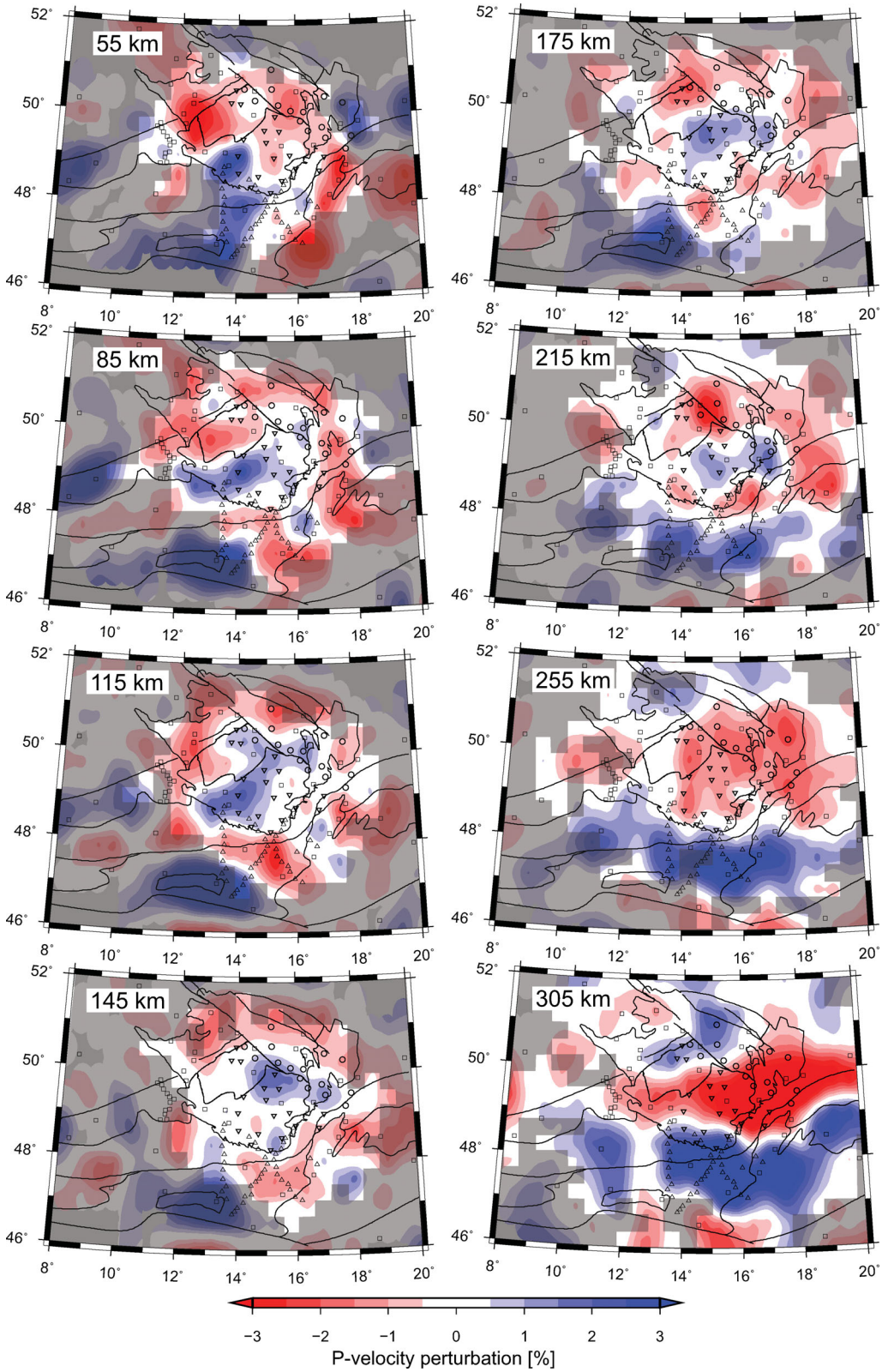

Figure 5. Horizontal depth sections of the final *P*-velocity perturbation model. Regions with well-resolved nodes are illuminated, while fairly and poorly resolved areas are shaded. High-resolution regions are defined at nodes with the diagonal elements of resolution matrix higher than 0.15. The black lines mark tectonics units and main faults as in Fig. 1. Stations are denoted by symbols as in Fig. 2. Low velocities prevail in the BM except of the elongated high-velocity heterogeneity beneath the Moldanubian unit (see Fig. 1) at depths from 55 to 215 km. Significant high-velocity perturbations exist south of the BM, which at depth below ∼200 extend beneath the Eastern Alps and the western part of the Pannonian Basin.

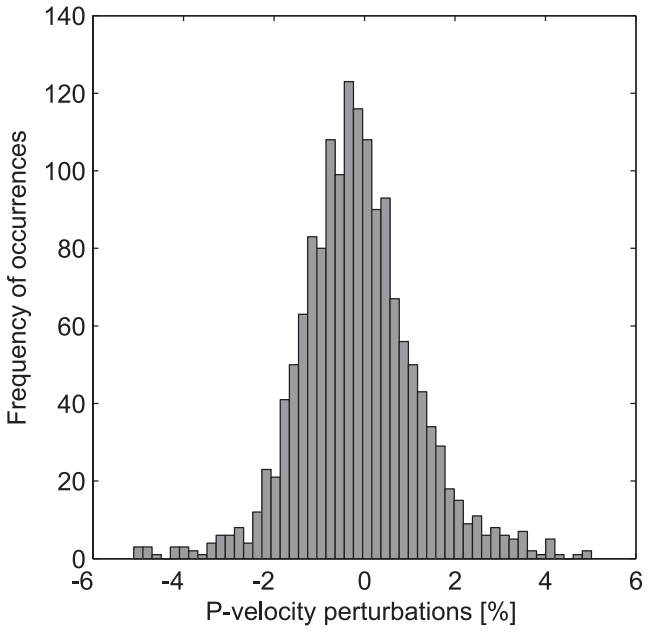

Figure 6. Histogram of *P*-velocity perturbations recovered by the inversion after the second iteration.

matrix are larger than 0.15. This threshold value was selected according to several tests. Velocities of synthetic models were not recovered at sites where diagonal elements of the resolution matrix were lower than 0.15. We show only perturbations calculated from more than 10 rays per a cell. A majority of velocity perturbations in the well-resolved parts of the model vary between −2 and +2 per cent (Fig. 6) for the selected damping factor of 200. The data variance reduction of the final model attains 58 per cent after the second iteration.

The best-resolved part of the model is a volume beneath the south–central BM and its nearest surroundings, particularly southwards to the Alps. Due to the ray geometry, the region of the EA is not fully resolved in the lithospheric depths down to 145 km. In general, several localized heterogeneities occur in the upper six mantle layers of the model, while at depths of 255 km and below, two extensive, sharply bounded heterogeneities dominate. Amplitudes of the velocity perturbations beneath the BM decrease in images at depths between 145 and 215 km. Large amplitudes of perturbations at deep parts of the model are probably result of combination of several effects: the real velocity distribution, mapping of velocities from beneath the model, for example, from a 'slab graveyard' in Mitterbauer *et al.* (2011) and Dando *et al.* (2011) and by a well-known transmitting of velocity perturbation artefacts down to the lowest parts of the model.

Overall, the upper mantle beneath the whole BM appears as a low-velocity region. A distinct low-velocity heterogeneity occurs in the upper two layers beneath the geodynamically active ER (Fig. 1). In deeper layers, these negative perturbations shift from the SW end of the rift to its NE part. The outer parts of the massif, as well as the Teplá-Barrandian unit (TB, Fig. 1), show mainly negative anomalies in all layers down to 215 km. Similarly, the low-velocity perturbations prevail down to 215 km beneath the Saxothuringian, Sudetic and Moravo-Silesian units of the BM. A low-velocity region in the SE of the BM belongs to the Western Carpathians. It can be traced in all layers except of the deepest one. The most intensive low-velocity heterogeneity of the EW elongated shape extends in the central part of the model at a depth of 305 km.

There are two significant regions of the model with high-velocity perturbations in the upper mantle. The strongest one relates to the Alps. The second one, characterized by positive perturbations in the slices from 85 to 215 km is located in the central and southwestern parts of the BM [the Moldanubian (MD) unit, see Fig. 1]. This relatively high-velocity heterogeneity seems to shift from the southwestern part of the massif at shallower depths to the northeast at greater depths. Weak positive perturbations occur also beneath the northern rim of the BM at the well-resolved deep parts of the model.

The strongest high-velocity heterogeneity related to the Eastern Alpine root is centred beneath the Tauern Window down to 175 km. Though these velocity perturbations at the lithosphere depths are less resolved in comparison with perturbations beneath the BM, both their intensity and location is meaningful. At depth ∼200 km and downwards, this high-velocity heterogeneity broadens and spreads from the EA to the western part of the Pannonian Basin. The heterogeneity is sharply bounded on the north by the low-velocity upper mantle beneath the BM.

4.2 Resolution analysis and synthetic tests

A model resolution depends on the ray geometry within the volume studied. We used several proxies for visualization of the ray distribution, such as derivative weighted sums (DWS), ray paths and diagonal elements of the resolution matrix.

The DWS are defined as sums of weighted ray lengths for each cell normalized by the space diagonal of the cell (Sandoval *et al.* 2004). The rays were weighted according to picking errors of corresponding traveltime residuals. Individual values of the DWS depend on number of rays intersecting each cell. In comparison with a simple and often used cell-hit-count approach, the DWS provide us with more advance information by considering differences in lengths of the rays in each cell, for which the velocity perturbations are calculated. Regions with good ray sampling, indicated by large values of the DWS, correlate well with the size of the station array (Fig. S1). The well-sampled volume shifts slightly northeastwards with the increasing depth due to the prevailing event backazimuths.

Degree of resolution of a cell perturbation depends not only on the number and lengths of rays within a cell, but also on diversity of ray intersections with respect to their backazimuths and ray path angles. We show the diversity of the intersections in projection into horizontal planes (Fig. 7). The ray intersections define a depth limit, at which velocity perturbations can be well-resolved and interpreted. Size of the area where rays with different backazimuths intersect enlarges with depth. This is also evident from a map of diagonal elements of the resolution matrix (Fig. S2), which quantitatively evaluates the trade-off between the DWS and the 3-D distribution of ray paths. A shallow depth limit is controlled by station spacing, while a deep one is given by a total aperture of a station array. From the figures of the DWS and ray path distribution or resolution matrix, we conclude that well-resolved velocity perturbations lie beneath the TB, MD, southern parts of Sudetes and Moravo-Silesian units.

To address a reliability of the two high-velocity perturbations retrieved in the low-velocity BM and in the EA, we perform synthetic tests. We search how the array recovers a west–east-oriented band of synthetic low-velocity perturbations (−3 per cent) relative to the IASP91 reference model, to test whether the SW–NE orientated high-velocity perturbations in the central part of the BM (Fig. 5) can be considered as real ones, or whether they appear due to the smearing caused by the station configuration. The second anomaly

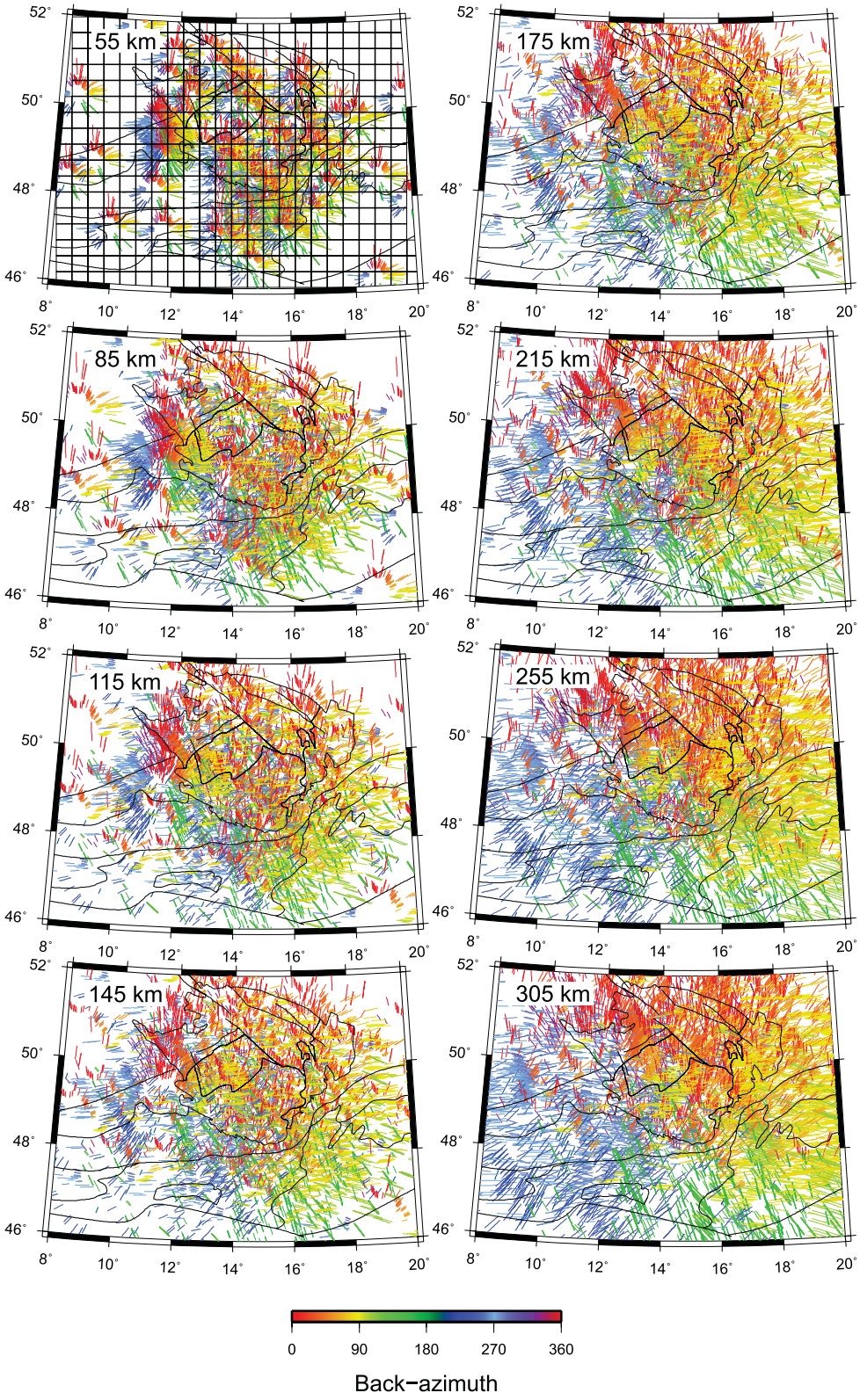

Figure 7. *P*-wave ray paths in the volume studied marked according to their backazimuths and projected into the horizontal depth slices. The horizontal parametrization of the model is indicated by the black net at the depth section of 55 km. The black lines show tectonic units and main faults as in Fig. 1.

of +5 per cent perturbations relative to background model mimics effects of the steep lithospheric slab beneath the EA (Lippitsch *et al.* 2003) on velocity images of the upper mantle beneath the BM and shows resolving capability of the data for such heterogeneity at the margin of our model. These anomalous perturbations were inserted to depths from 115 to 215 km. The synthetic traveltimes, computed by the 3-D ray tracing, contain 5 per cent of the Gaussian noise.

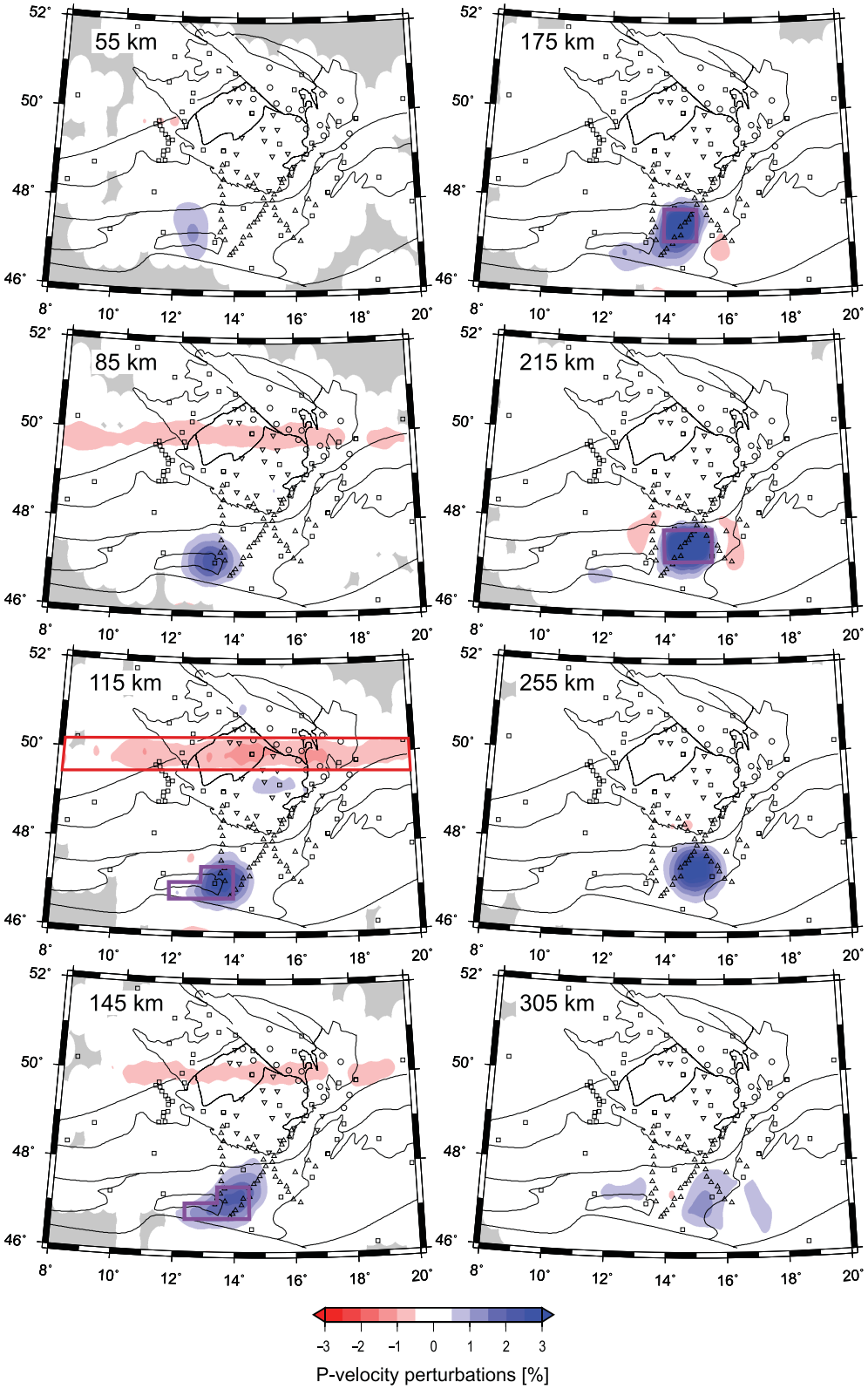

Figure 8. Test of recovering two synthetic velocity anomalies added into the IASP91 radial earth model. The positive +5 per cent synthetic heterogeneity (blue), contoured at depths from 115 to 215 km simulates the East Alpine root according to tomography by Lippitsch *et al.* (2003). The negative −3 per cent band (red), contoured at 115 km was introduced to check a potential SW–NE smearing due to array geometry. Both anomalies are recovered well, particularly in their horizontal dimensions. Amplitudes of the high-velocity anomaly were recovered better than those of the low-velocity anomaly. The black lines show tectonic units and main faults as in Fig. 1. Stations are denoted by symbols as in Fig. 2.

Results of the test (Fig. 8), with variance reduction of 80 per cent, show that horizontal boundaries of both anomalies are recovered well without artefacts due to uneven station or event distributions. The synthetic west–east negative anomaly added in nodes at a depth of 115 km is blurred into the neighbouring depth slices and thus the recovered velocity perturbations attain only about a half of the inserted amplitudes. On the other hand, the amplitudes of the velocity perturbations beneath the EA are recovered more accurately, reaching values of +4.7 per cent. Nevertheless, the velocity perturbations at depths of 55, 85, 255 and 305 km are products of vertical smearing. Note that a shape of velocity perturbations at depth of 305 km does not correspond to any inserted anomaly. The test showed an ability of the ray geometry used to resolve a significant steep heterogeneity at the southern margin of the model and no indications of a horizontal smearing in the SW–NE direction.

5 DISCUSSION

Three relatively small-scale regional tomographic studies of velocity perturbations in the upper mantle beneath the BM and its vicinity have been carried out up to now. The first one (Plomerová *et al.* 2007) concentrated on the western part of the BM and did not confirm an existence of a potential asthenospheric plume proposed there in analogy with the French Massif Central and the Rhenish Massif according to the 'baby-plume' concept (Granet *et al.* 1995; Ritter *et al.* 2001). The second tomography (Karousová *et al.* 2012b) mapped velocity perturbations in the northeastern part of the BM. The resulting tomographic model, with a variance reduction of 84 per cent has shown only relatively small velocity variations, both in size and in amplitude. The authors relate a small-size high-velocity perturbation in the eastern part of the model to the complex structure of the upper mantle beneath the Sudetes/Moravo-Silesian crustal unit contact. The third model, we present in this paper, has the highest resolution in the south–central part of the BM. Structural studies of the continental lithosphere and the upper-mantle velocities require minimum model depths of about 250–300 km, which calls for a station array of a lateral extent which at least double the depth extent of the model, in general. Therefore, we included into the studies also data from permanent observatories both in the BM and its surroundings and thus outer frames of the three velocity-perturbation models are about the same. However, well-resolved regions are not identical at all depths. Nevertheless, the tomographic images in overlapping parts of the models are similar and all of them show a low-velocity character of the upper mantle beneath the BM, as a part of a large low-velocity region (Fig. 9) in global, or, large-scale regional tomography (e.g. Piromallo & Morelli 2003; Amaru 2007; Koulakov *et al.* 2009), based on data reported to the International Seismological Centre (ISC) from relatively sparsely distributed permanent observatories.

In this study, we discuss results of the high-resolution velocity tomography in the south–central part of the BM in the light of other high-resolution studies of the region based on data from several passive seismic experiments covering the BM and a broader region of the central and EA by dense networks of temporary seismic stations (Lippitsch *et al.* 2003; Plomerová *et al.* 2007; Dando *et al.* 2011; Mitterbauer *et al.* 2011; Karousová *et al.* 2012b). Naturally, we limit our discussion only to the well-resolved parts of the model (Fig. 5).

The three upper layers reflect gross features of the mantle lithosphere of the BM. In case of the less well-resolved structure beneath the Alps, we mainly refer to depths below 145, where the EA root is imaged best. Amplitudes of velocity perturbations are larger in

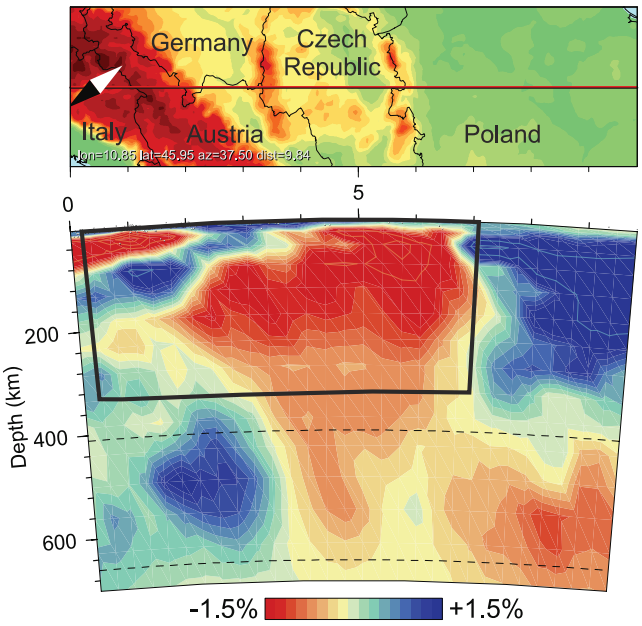

Figure 9. Vertical cross-section through the velocity model from a large-scale tomography by Amaru (2007) along the NW–SE profile (see also Fig. 10e—dashed line). The target volume of this paper is indicated by a box. The velocities are shown as perturbations relative to the ak135 reference earth model (Kennett *et al.* 1995).

layers representing the lithosphere of the BM, with the thickness between ∼80 km along the ER d ∼140 km beneath the MD unit (e.g. Plomerová & Babuška 2010). The upper mantle beneath the BM is characterized in the tomographic images of Piromallo & Morelli (2003) by relatively low velocities without indications of the high-velocity anomaly beneath the central part of the MD unit. The high-velocity heterogeneity beneath the EA is significant down to the depths of 150 km in the Piromallo & Morelli model (2003), while down to depths of 400 km the amplitudes are smaller. Traveltimes from regional earthquakes are also included in their inversion. We have to admit that in any teleseismic tomography, without additional rays from regional events, the velocity perturbations suffer from vertical smearing due to the steep-ray geometry, namely in the lowermost layers. Moreover, resulting perturbation can be affected by a leakage of anisotropic fabric of the lithosphere (e.g. Babuška & Plomerová 2013; see also Fig. 11), or even by the mantle structure beneath the bottom on the model (Dando *et al.* 2011).

The topmost layer (Fig. 5) shows a low-velocity feature beneath the geodynamically active western ER that correlates well with the lithosphere thinning to about 80 km (e.g. Plomerová & Babuška 2010 and reference therein). Also the mantle lithosphere of the TB unit (Figs 1 and 5) appears as a low-velocity block resistant to a subduction and playing a role of a 'median' massif during the Variscan orogeny (Franke 2000). The positive gravity anomaly of the whole TB unit (e.g. Švancara *et al.* 2008) should thus be caused by the relatively high-density crust. The high-velocity anomaly in the central BM is discussed below.

For additional visualization of our results and their discussion, we construct three cross-sections (Fig. 10) through the final model (Fig. 5) along two profiles, identical with those in previous structural studies of the mantle lithosphere (Plomerová *et al.* 2007; Karousová *et al.* 2012b; Babuška & Plomerová 2013) and along another one, running in the SW–NE direction through the EA and the eastern rim

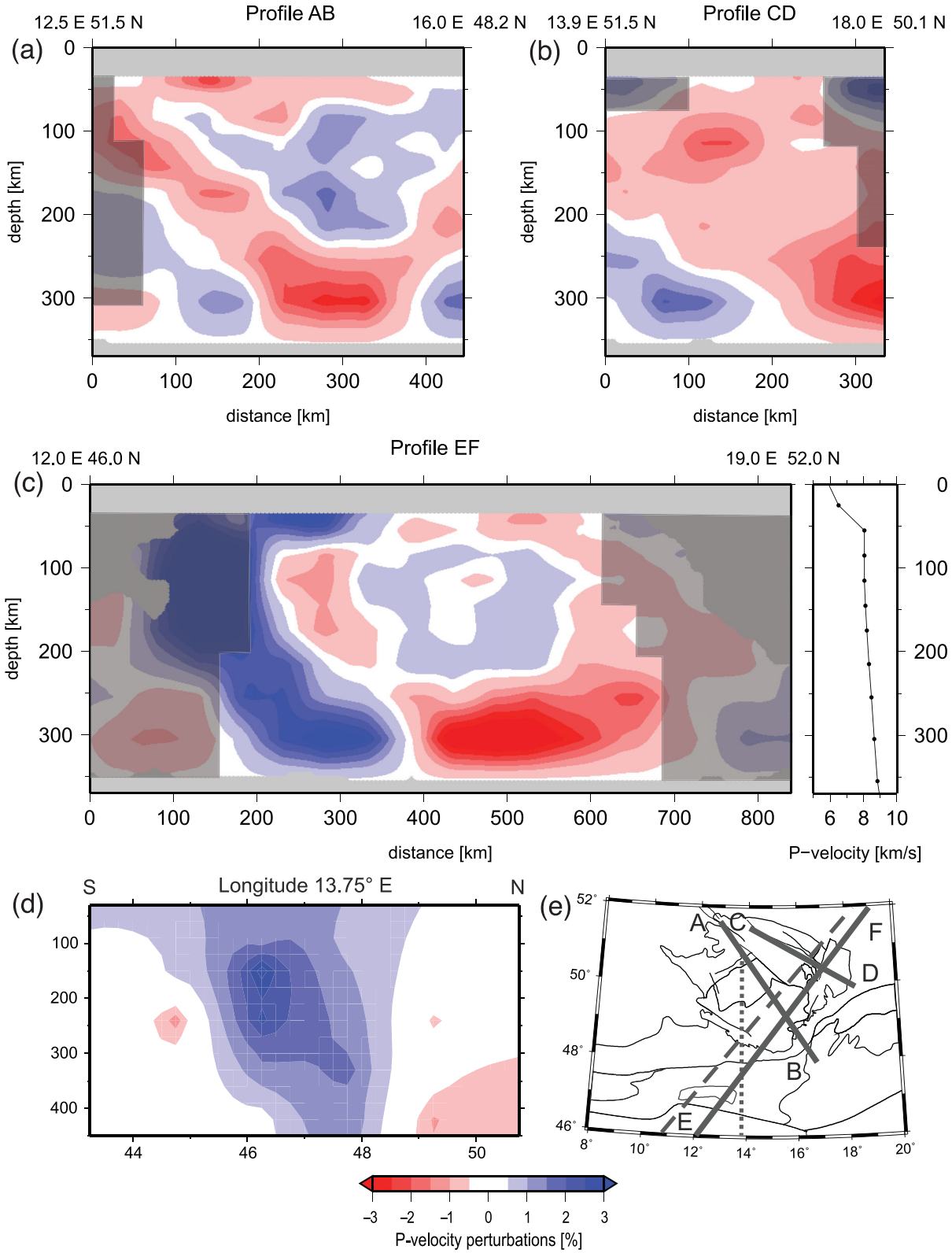

Figure 10. Vertical cross-sections (a, b, c) along profiles AB, CD and EF (see part e—full lines) through the final *P*-velocity perturbation model (see Fig. 5). Well-resolved regions are illuminated, while fairly and poorly resolved areas are shaded with respect to the values of the diagonal elements of resolution matrix. (d) Cross-section through the model by Aric *et al.* (1989) along profile marked by dotted line in part (e); (e) Map of the region with tectonic units and main faults as in Fig. 1 along with all the profiles.

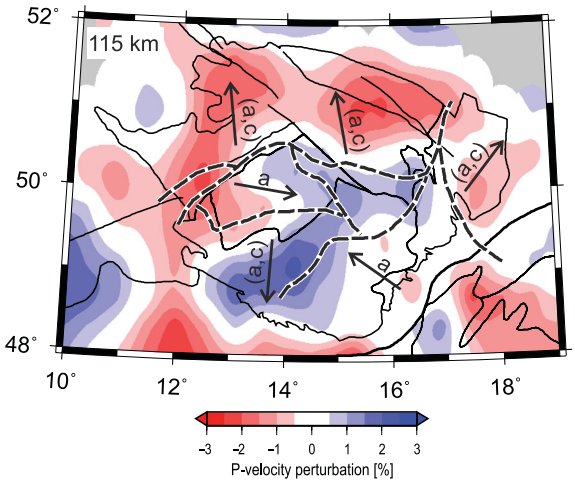

Figure 11. Comparison of isotropic distribution of *P*-velocity perturbations at depth of 115 km and boundaries (dashed) of anisotropic domains with inclined symmetry axes retrieved in the BM by a joint inversion of body wave anisotropic parameters (Plomerová *et al.* 2007, 2012; Babuška *et al.* 2008; Babuška & Plomerová 2013). Directions of fast axes (lineation) *a* or dip directions of foliations (*a*,*c*) of individual anisotropic models are indicated by arrows in each domain.

of the BM as a parallel continuation of profile C–C' of Lippitsch *et al.* (2003) with about 40 km westward offset.

The northernmost cross-section (Fig. 10b) shows the prevailing low velocities in the northeastern BM down to the bottom of the model. The small-size high-velocity perturbation near the NW end of the cross-section at a depth of ∼250 km and deeper underlays the low-velocity structures beneath the ER and its NE continuation beneath the Sudetes region (Fig. 1).

Cross-section AB (Fig. 10a) is oriented normal to the ER and to other SW–NE-oriented tectonic features of the BM (see Fig. 1). This section cuts the central high-velocity heterogeneity revealed beneath the MD unit in the velocity-perturbation images at depths down to ∼200 km. This SW–NE elongated heterogeneity (Fig. 5) parallels the mantle contact of the Brunovistulian (BV) and MD lithosphere domains (Babuška & Plomerová 2013). Thus, from the isotropic point of view, we can interpret the high-velocity heterogeneity as a lithosphere thickening due to the underthrusting of the BV beneath the MD as a consequence of the BV microplate collision with the eastern rim of the BM during the Variscan orogeny. However, at least a part of this heterogeneity can be an artefact, due to neglecting anisotropic structure of the BM. The mantle lithosphere of the massif consists of several large anisotropic domains with high-velocity directions dipping in different azimuths (e.g. Babuška & Plomerová 2013). The positive perturbations in the central part of the AB cross-section (Fig. 10a) can be affected by the convergently dipping high-velocity directions (Fig. 11) retrieved in the anisotropic models of the TB and BV domains, though the structure of the MD, with high velocities dipping southwards, can partly dilute moderate anisotropic effects imposed on the isotropic velocity tomographic model. Eken *et al.* (2012) attempted to clean their isotropic images of upper-mantle velocities beneath the Baltic Shield from anisotropic artefacts by inverting traveltime residuals corrected for anisotropic effects. Unfortunately, the domains of the BM are much smaller in comparison with the lithosphere domains of the Baltic Shield. Thus selecting rays for tomography, which travel to the stations only through one domain with a consistent fabric, would be difficult.

The third cross-section EF (Fig. 10c) intersects the EA and continues northeastwards through the BM. The EA lithosphere root naturally exhibits the largest positive perturbations in the model. In the central part of the cross-section, weaker positive perturbations are related to the eastern rim of the MD/BV 'heterogeneity' shown in cross-section AB (Fig. 10a) and discussed above. The synthetic test demonstrates (Fig. 8) that reliability of resolution of the strong heterogeneity related to the EA root is sufficient in the presented model retrieved from the BOHEMA III and from a part of the ALPASS data. The steep northward-dipping high-velocity heterogeneity seems to detect the Adriatic lower lithosphere subduction in collision with the Eurasia Plate in region of the EA (Handy *et al.* 2010; Munzarová *et al.* 2013).

Several decades back, various studies have been attempting, with the use of different techniques, to understand the Eurasia–Africa plate collision and to model dynamics of the subducting lithosphere particularly in the Alpine area. Since Babuška *et al.* (1990) suggested to abandon a model of the continuously subducting Eurasian Plate along the whole Alpine chain, a broad debate on a configuration of the EA subduction and particularly its polarity has started (e.g. Kissling 1993; Kissling *et al.* 2006; Lippitsch *et al.* 2003; Schmid *et al.* 2004; Brückl *et al.* 2010). The broad lithosphere root of a triangular shape reflects a complex structure of the collision beneath the EA (Babuška *et al.* 1990; Babuška & Plomerová 1992) and indicates a very steep sinking of both the Eurasian and Adriatic plates and also a flip from the SE-oriented subduction in the Western Alps (WA) to the northward-dominant subduction in the EA. Several large-scale traveltime tomography studies aimed at answering these questions as well (e.g. Wortel & Spakman 2000; Amaru 2007). In the NNE–SSW cross-section through the tomography by Amaru (2007), the high-velocity perturbations associated with the subduction beneath the Alps dips southwards (Fig. 9). On the other hand, already in a small-scale tomography by Aric *et al.* (1989), with a limited resolution from a nowadays point of view, the steep slightly northward-dipping subduction can be identified (Fig. 10d). That tomography data set includes besides the ISC data also traveltime residuals from temporary Eastern Alpine Network.

Tomography study by Lippitsch *et al.* (2003), in which data from the TRANSALP transect across the EA has been incorporated, shows significantly more detailed structures in the EA. According to the authors, the high velocities imaged beneath the EA represent the north Adriatic lower lithosphere subducted down to ∼250 km. A similar steep northward to vertically dipping slab below the EA is resolved to the same depth in the ALPASS tomography by Mitterbauer *et al.* (2011). Though the resolution of this tomography in the BM is lower in comparison with the tomography based on the targeted BOHEMA experiments, the upper mantle beneath the BM appears as a low-velocity region there as well, and moreover, weak small-size high-velocity perturbations within the massif correlate with the high-velocity heterogeneity in the south–central BM identified in our model (Fig. 5).

Velocity perturbations in the upper mantle beneath the BM form also a part of the tomographic model by Dando *et al.* (2011) based on data collected during the Carpathian Basin project. Reliable low-velocity perturbations beneath the BM dominate in their model at depth from ∼350 to ∼600 km, being sharply separated on the south from the broad high-velocity heterogeneity extending down to the mantle transition zone. The boundary between the large high- and the low-velocity heterogeneity runs north of the North Alpine Thrust Fault (see Fig. 1) and follows the ridge of the Western Carpathians. Dando *et al.* (2011) interpret the deep heterogeneity as a graveyard of a detached lithosphere probably triggering the extension of the

Pannonian Basin. Though the resolution of their model at shallow depths beneath the BM is much lower than the resolution of our model from the BOHEMA III data, similar features exist in both of them. The strongest phenomenon is the steep East Alpine root imaged down to ~350 km depth by Dando *et al.* (2011).

6 CONCLUSION

The high-resolution tomography of the southern part of the BM and its surroundings images the massif as a part of an extensive large-scale low-velocity region in the upper mantle beneath central Europe. The low-velocity perturbations in our model concentrate in the shallow mantle layers beneath the ER and move from the SW end of the rift towards its NE continuation. The ray geometry allows us to resolve small-scale features (~40 km) in the upper mantle and reveals high-velocity heterogeneity beneath the MD part of the BM. We interpret this prominent feature as a manifestation of lithosphere thickening reflecting the collision of the BV microplate with the eastern rim of the BM during the Variscan orogeny and a consequent underthrusting of this microplate beneath the MD unit. We associate the strongest high-velocity heterogeneity, located near the southern margin of the model and well-resolved in its deeper parts, with the Eastern Alpine lithosphere root. Our tomographic images indicate the northward dip of this subduction. The low-velocity upper mantle beneath the BM is sharply separated from the extensive high-velocity heterogeneity beneath the EA, which extends towards the east, beneath the Pannonian Basin at the bottom of the model and may relate to delaminated parts of downwelling lithosphere residing within the transition zone.

ACKNOWLEDGEMENTS

The authors are grateful to E. Kissling for his valuable advice related to the TELINV code, and for his recommendations and consultations during the tomography computations. L. Vecsey is acknowledged for providing us with his arrival time picking software and a help with preparing the data set. The research was partly supported by grants No. 210/12/2381 of the Grant Agency of the Czech Republic, No. SVV-2013-267308 of Ministry of Education, Youth and Sports, Czech Republic and No.111-926 10/253101 of the Grant Agency of Charles University. Data acquisition from permanent observatories was supported by the project of large research infrastructure CzechGeo, Grant No. LM2010008.

REFERENCES

Aki, K., Christoffersson, A. & Husebye, E.S., 1977. Determination of 3-dimensional seismic structure of lithosphere, *J. geophys. Res.,* **82**(B2), 277–296.

Amaru, M., 2007. Global travel time tomography with 3-D reference models, *Geol. Traiectina,* **274,** *PhD thesis,* Utrecht Univ. 174.

Aric, K., Gutdeusch, R., Leichter, B., Lenhardt, W., Plomerová, J., Babuška, V., Pajdušák, P. & Nixdorf, U., 1989. *Structure of the Lithosphere in the Eastern Alps from P-Residual Analysis,* Vol. 317, pp. 1–26, Zentralanstalt für Metereologie und Geodynamik, Wien.

Arlitt, R., Kissling, E. & Ansorge, J., 1999. Three-dimensional crustal structure beneath the TOR array and effects on teleseismic wavefronts, *Tectonophysics,* **314,** 309–319.

Babuška, V. & Plomerová, J., 1992. The lithosphere in central Europe—seismological and petrological aspects, *Tectonophysics,* **207,** 141–163.

Babuška, V. & Plomerová, J., 2008. Control of paths of quaternary volcanic products in western Bohemian Massif by rejuvenated Variscan triple junction of ancient microplates, *Stud. Geophys. Geod.,* **52,** 607–629.

Babuška, V. & Plomerová, J. 2013. Boundaries of mantle–lithosphere domains in the Bohemian Massif as extinct exhumation channels for high-pressure rocks, *Gondwana Res.,* **23,** 973–987.

Babuška, V., Plomerová, J. & Granet, M., 1990. The deep lithosphere in the Alps: a model inferred from P residuals, *Tectonophysics,* **176,** 137–165.

Babuška, V., Plomerová, J., Vecsey, L., Jedlička, P. & Růžek, B., 2005. Ongoing passive seismic experiments unravel deep lithosphere structure of the Bohemian Massif, *Stud. Geophys. Geod.,* **3,** 423–430.

Babuška, V., Plomerová, J. & Vecsey, L., 2008. Mantle fabric of western Bohemian Massif (central Europe) constrained by 3D seismic P and S anisotropy, *Tectonophysics,* **462**(1–4), 149–163.

Behm, M., Brückl, E., Chwatal, W. & Thybo, H., 2007. Application of stacking and inversion techniques to three-dimensional wide-angle reflection and refraction seismic data of the Alps, *Geophys. J. Int.,* **170,** 275–298.

Brückl, E., Behm, M., Chvatal, W. & Mitterbauer, U., CELEBRATION, 2000 & ALP 2002 & ALPASS Working Groups, 2007. Erkenntnisse über den Tiefbau der Ostalpen aus neuen seismischen Großexperimenten, in *Beiträge zur Geologie Oberösterreichs, Arbeitstagung GBA,* pp. 143–150.

Brückl, E., Behm, M., Decker, K., Grad, M., Guterch, A., Keller, G.R. & Thybo, H., 2010. Crustal structure and active tectonics in the Eastern Alps, *Tectonics,* **29,** 1–17.

Dando, B.D.E., Stuart, G.W., Houseman, G.A., Heged, E., Brückl, E. & Radovanovi, S., 2011. Teleseismic tomography of the mantle in the Carpathian–Pannonian region of central Europe, *Geophys. J. Int.,* **186,** 11–31.

Eken, T., Plomerová, J., Vecsey, L., Babuška, V., Roberts, R., Shomali, H. & Bodvarsson, R., 2012. Effects of seismic anisotropy on P-velocity of the Baltic Shield, *Geophys. J. Int.,* **188,** 600–612.

Evans, J.R. & Achauer, U., 1993. Teleseismic velocity tomography using the ACH method: theory and application to continental scale studies, in *Seismic Tomography,* pp. 319–360, eds Iyer, H.M. & Hirahara, K., Chapman and Hall, London.

Franke, W., 2000. The mid-European segment of the Variscides: tectonostratigraphic units, terrane boundaries and plate tectonic evolution, in *Orogenic Processes: Quantification and Modelling in the Variscan Belt,* Vol. **179,** pp. 35–61, eds Franke, W., Haak, V., Oncken, O. & Tanner, D., *Special* Publication of the Geological Society, London.

Grad, M., Brückl, E., Majdański, M., Behm, M. & Guterch, A., CELEBRATION 2000 & ALP 2002 Working Groups, 2008. Crustal structure of the Eastern Alps and their forelands: seismic model beneath the CEL10/ALP04 profile and tectonic implications, *Geophys. J. Int.,* **177,** 279–295.

Granet, M., Wilson, M. & Achauer, U., 1995. Imaging a mantle plume beneath the French Massif Central, *Earth planet. Sci. Lett.,* **136,** 281–296.

Handy, M.R., Schmid, S.M., Bousquet, R., Kissling, E. & Bernoulli, D., 2010. Reconciling plate-tectonic reconstructions of Alpine Tethys with the geological–geophysical record of spreading and subduction in the Alps, *Earth-Sci. Rev.,* **102,** 121–158.

Hrubcová, P., Środa, P., Špičák, A., Guterch, A., Grad, M., Keller, G.R., Brückl, E. & Thybo, H., 2005. Crustal and uppermost mantle structure of the Bohemian Massif based on CELEBRATION 2000 data, *J. geophys. Res.,* **110,** B11305, doi:10.1029/2004JB003080.

Karousová, H., Plomerová, J. & Babuška, V., 2012a. A three-dimensional velocity model of the crust of the Bohemian Massif, *Stud. Geophys. Geod.,* **56,** 249–267.

Karousová, H., Plomerová, J. & Vecsey, L., 2012b. Seismic tomography of the upper mantle beneath the north-eastern Bohemian Massif (central Europe), *Tectonophysics,* **564–565,** 1–11.

Kennett, B.L.N. & Engdahl, E.R., 1991. Traveltimes for global earthquake location and phase identification, *Geophys. J. Int.,* **105,** 429–465.

Kennett, B.L.N., Engdahl, E.R. & Buland, R., 1995. Constraints on seismic velocities in the Earth from traveltimes, *Geophys. J. Int.,* **122,** 108–124.

Kissling, E., 1993. Deep structure of the Alps—what do we really know? *Phys. Earth planet. Inter.,* **79,** 87–112.

Kissling, E., Schmid, S.M., Lippitsch, R., Ansorge, J. & Fügenschuh, B., 2006. Lithosphere structure and tectonic evolution of the Alpine arc: new evidence from high-resolution teleseismic tomography, in *Eurpean*

Lithosphere Dynamics, Vol. **32,** pp. 129–145, eds Gee, D.G. & Stephenson, R.A., Memoirs of Geol. Soc.

Koulakov, I., Kaban, M.K., Tesauro, M. & Cloetingh, S., 2009. P- and S-velocity anomalies in the upper mantle beneath Europe from tomographic inversion of ISC data, *Geophys. J. Int.,* **179,** 345–366.

Lippitsch, R., Kissling, E. & Ansorge, J., 2003. Upper mantle structure beneath the Alpine orogen from high-resolution teleseismic tomography, *J. geophys. Res.,* **108,** B82376, doi:10.1029/2002JB002016.

Majdanski, M., Grad, M. & Guterch, A., SUDETES 2003 Working Group, 2006. 2-D seismic tomographic and ray tracing modelling of the structure across the Sudetes Mountains basing on SUDETES 2003 data, *Tectonophysics,* **413,** 249–269.

Martin, M. & Ritter, J.R.R., CALIXTO Working Group, 2005. High-resolution teleseismic body wave tomography beneath SE-Romania—I. implications for three-dimensional versus one-dimensional crustal corrections strategies with a new crustal velocity model, *Geophys. J. Int.,* **162,** 448–460.

Menke, W., 1984. *Geophysical Data Analysis: Discrete Inverse Theory,* Academic Press, Inc., College of Oceanography, Oregon State University.

Mitterbauer, U. *et al.*, 2011. Shape and origin of the East-Alpine slab constrained by the ALPASS teleseismic model, *Tectonophysics,* **510,** 195–206.

Munzarová, H., Plomerová, J., Babuška, V. & Vecsey, L., 2013. Upper-mantle fabrics beneath the Northern Apennines revealed by seismic anisotropy, *Geochem. Geophys. Geosyst.,* **14,** doi:10.1002/ggge.20092.

Piromallo, C. & Morelli, A., 2003. P wave tomography of the mantle under the Alpine-Mediterranean area, *J. geophys. Res.,* **108,** B22065, doi:10.1029/2002JB001757.

Plomerová, J. & Babuška, V., 2010. Long memory of mantle lithosphere fabric—European LAB constrained from seismic anisotropy, *Lithos,* **120,** 131–143.

Plomerová, J., Vecsey, L. & Babuška, V., 2012. Mapping seismic anisotropy of the lithospheric mantle beneath the northern and eastern Bohemian Massif (central Europe), *Tectonophysics,* **564–565,** 38–53.

Plomerová, J., Babuška, V., Šílený, J. & Horálek, J., 1998. Seismic anisotropy and velocity variations in the mantle beneath the Saxothuringicum-Moldanubicum contact in central Europe, *Pure appl. Geophys.,* **151,** 365–394.

Plomerová, J., Achauer, U., Babuška, V. & Vecsey, L., 2007. Upper mantle beneath the Eger Rift (central Europe): plume or asthenosphere upwelling? *Geophys. J. Int.,* **169,** 675–682.

Ritter, J.R.R., Jordan, M., Christensen, U.R. & Achauer, U., 2001. A mantle plume below the Eifel volcanic fields, Germany, *Earth planet. Sci. Lett.,* **186,** 7–14.

Sandoval, S., Kislling, E. & Ansorge, J., SVEKALAKO Seismic Tomography Working Group, 2004. High-resolution body wave tomography beneath the SVEKALAPKO array—II. Anomalous upper mantle structure beneath the central Baltic Shield, *Geophys. J. Int.,* **157,** 200–214.

Schmid, S.M., Fügenschuh, B., Kissling, E. & Schuster, R., 2004. Tectonic map and overall architecture of the Alpine orogeny, *Eclogae Geol. Helv.,* **97,** 93–117.

Stammler, K., 1993. Seismichandler: programmable multichannel data handler for interactive and automatic processing of seismological analyses, *Comput. Geosci.,* **19**(2), 135–140.

Steck, L.K. & Prothero, W.A., 1991. A 3-D ray-tracer for teleseismic body-wave arrival-times, *Bull. seism. Soc. Am.,* **81,** 1332–1339.

Švancara, J., Havíř, J. & Conrad, W., 2008. Derived gravity field of the seismogenic upper crust of SE Germany and West Bohemia and its comparison with seismicity, *Stud. Geophys. Geod.,* **52,** 567–588.

Waldhauser, F., Lippitsch, R., Kissling, E. & Ansorge, J., 2002. High-resolution teleseismic tomography of the upper mantle structure using an a priori three-dimensional crustal model, *Geophys. J. Int.,* **150,** 403–414.

Wortel, M.J.R. & Spakman, W., 2000. Subduction and slab detachment in the Mediterranean-Carpathian region, *Science,* **290,** 910–917.

SUPPORTING INFORMATION

Additional Supporting Information may be found in the online version of this article:

Figure S1. Depth slices with derivative weighted sums (DWS) for nodes with more than 10 hit counts.

Figure S2. Depth slices with diagonal elements of resolution matrix, representing a quantitative evaluation of a trade-off between the DWS and the 3-D distribution of ray paths (http://gji.oxfordjournals.org/lookup/suppl/doi:10.1093/gji/ggt159/-/DC1)

Please note: Oxford University Press is not responsible for the content or functionality of any supporting materials supplied by the authors. Any queries (other than missing material) should be directed to the corresponding author for the article.

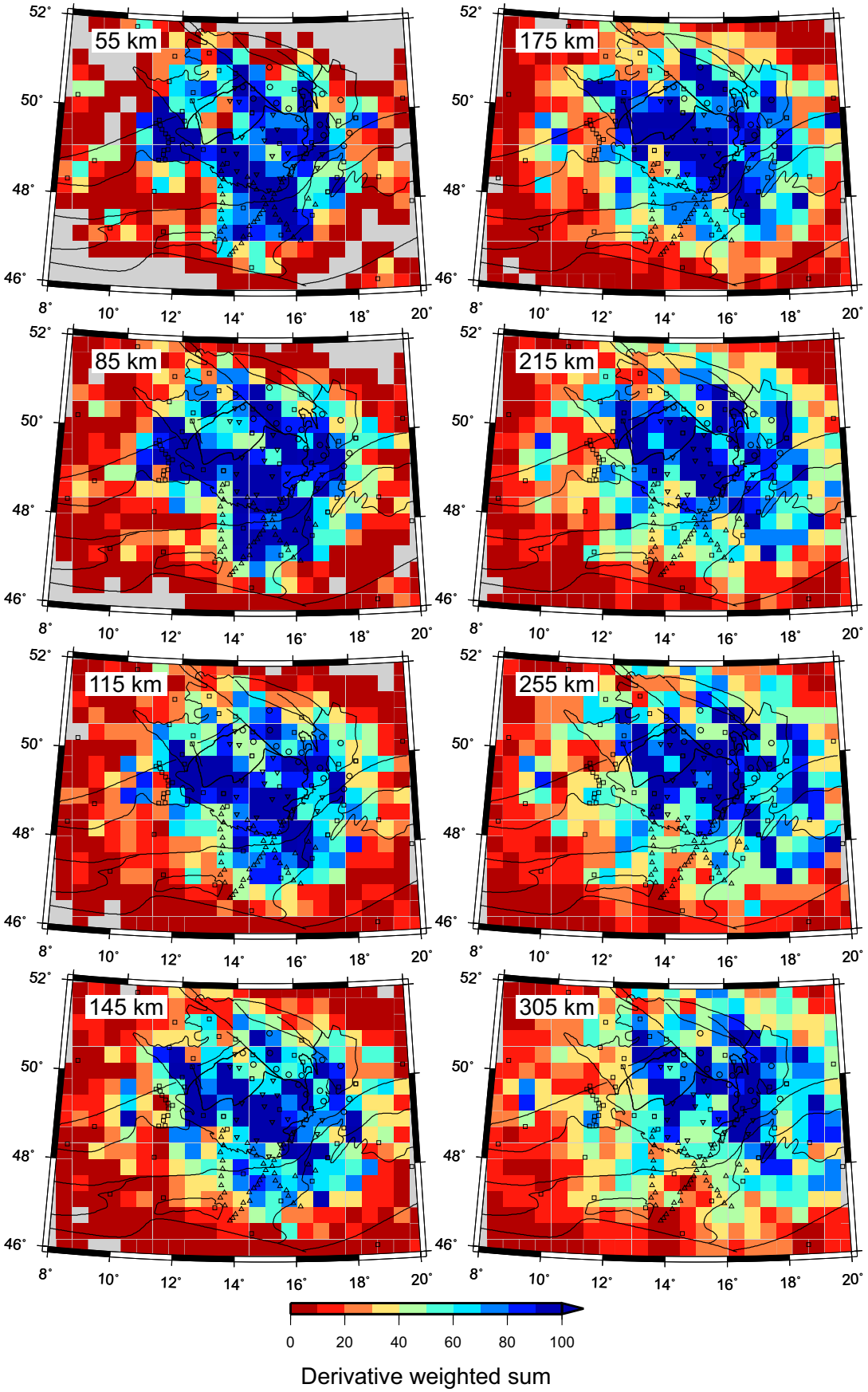

Fig. S1. Depth slices with derivative weighted sums (DWS) for nodes with more than 10 hit counts. Regions with good ray sampling, indicated by large values of the DWS, correlate well with the size of the station array. The black lines show tectonic units and main faults as in Fig. 1. Stations are denoted

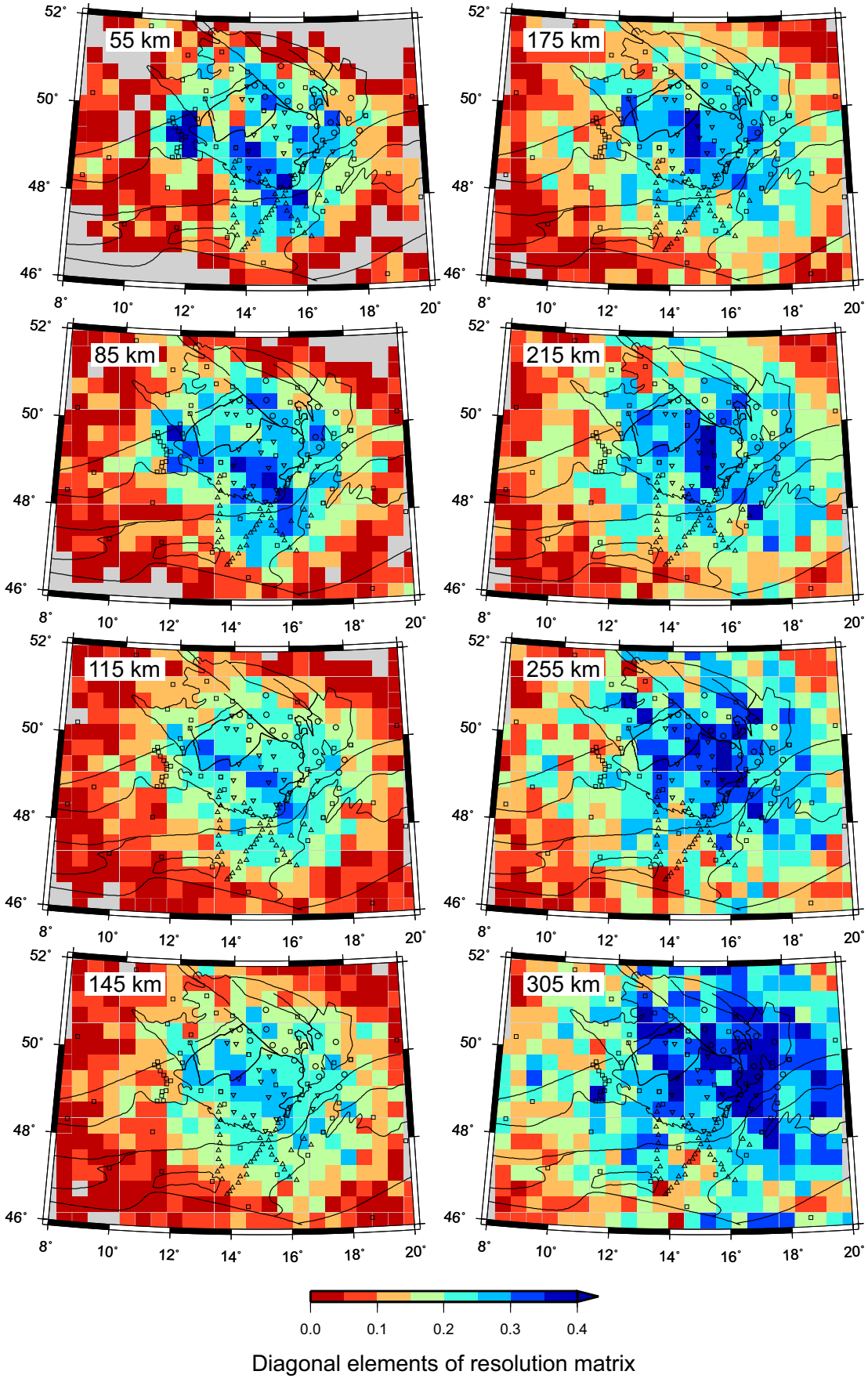

Fig. S2. Depth slices with diagonal elements of resolution matrix, representing a quantitative evaluation of a trade-off between the DWS and the three-dimensional distribution of ray paths. The black lines show tectonic units and main faults as in Fig. 1. Stations are denoted by symbols as in Fig. 2.

P4

TELINV2012 - User's Guide

Karousová, H.

http://www.ig.cas.cz/en/research-teaching/software-download

TELINV2012 - User's Guide

by Hana Karousová, Prague 2013

27th September 2013

Contents

1 Introduction

The TELINV2012 tomography code runs in two modes. In the inversion mode, teleseismic travel-time residuals are inverted for three-dimensional velocity structure of the upper mantle. In the forward modelling mode, synthetic travel times are calculated for a supplied velocity model. The code enables one-dimensional or three-dimensional ray tracing. The latter one is implemented according to the Simplex ray-tracing technique (Steck and Prothero, 1991). The velocity perturbations are searched at nodes among which velocities are linearly interpolated. The velocity perturbations are calculated in subsequent iteration steps, in which the ray paths and travel-time residuals are updated.

Authors of the original and then modified versions of the TELINV code are J. Taylor, E. Kissling, U. Achauer, C. M. Weiland, L. Steck, H. Shomali and probably also many other users of the code (e.g., Weiland et al., 1995; Arlitt et al., 1999; Lippitsch et al., 2003; Sandoval et al., 2004; Shomali et al., 2006; Eken et al., 2007). This version of the code - TELINV2012 is based on the TELINV99 code, which is a version lastly revised by E. Kissling. The latest modifications were implemented by H. Karousová and H. Munzarová under supervision of E. Kissling and J. Plomerová. The code is written in FORTRAN77 with several subroutines in FOTRAN95 (however, compiled with ifort). The TELINV2012 code is complemented with comments and error and warning messages. We added an analysis of input travel-time residuals, corresponding ray geometry and outputs of the code. A part of the TELINV2012 package are auxiliary GMT, Matlab and Fortran scripts for simple visualization of input data and final model parameters and for preparation of some input files. The purpose of this User's guide is to describe the most important parts of the tomographic code and to provide a step-by-step guide to inversion and modelling of travel-time residuals.

2 Description of the code

The structure of the TELINV2012 is shown in a simplified flowchart (Fig. 1). At first, the code reads input files in order: *telinv2012input.inp, station.inp, velocity_model.inp, travel_time.inp and use_node.inp* (Section 4.1). These files contain control parameters, e.g., damping factor, number of iterations, locations of seismic stations, phase identifications, e.g., ray parameters and back-azimuths, travel times, initial velocity model and grid of nodes, in which velocity perturbations are searched. In the code, crustal corrections, additional station corrections and travel-time normalization of the input data can be applied. After these data adjustments, the input data are analyzed providing a user with a basic statistics. Because the code's ability to reveal time instabilities is limited, we recommend to check the data set a-priori (out of the code).

After travel-time calculation, the code flow splits in dependence on its mode. In case of the forward solution, synthetic travel times and other outputs are created and the program stops. In case of the inversion mode, velocity perturbations are calculated in several iterative steps. The number of iterative steps is determined by a user. The inversion can be calculated with or without data weighting and model smoothing.

2.1 Input travel-time data

The *travel_time.inp* (Section 4.1.3) contains the teleseismic travel-time data in three columns representing observed (measured) travel times, theoretical travel times and their differences: travel-time residuals. Each ray, associated with a travel-time residual, is identified by a ray parameter, back-azimuth and coordinates of a seismic station. Absolute values of the travel-time residuals have to be smaller than

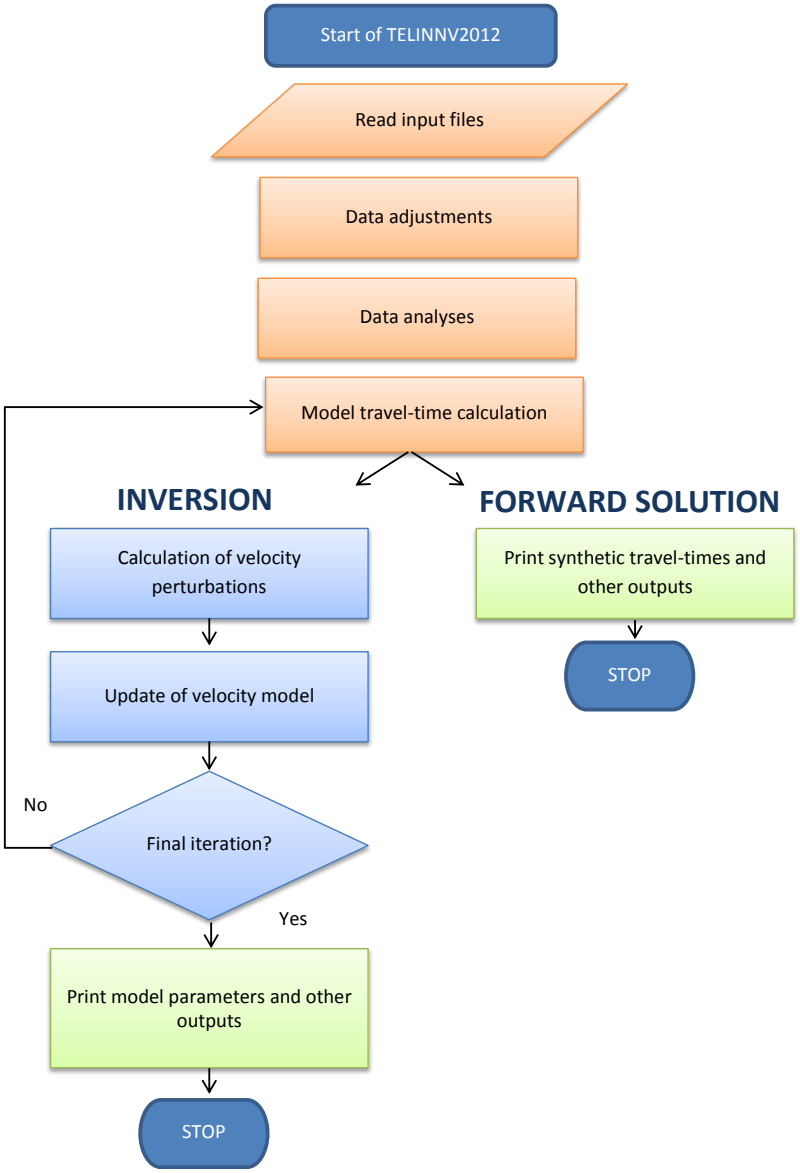

Figure 1: Simplified flowchart of the TELINV2012 code

pre-defined tolerance value ***ttr_tol*** defined in *telinv2012input.inp* (Section 4.1.5). The tolerance values ***ttr_tol***, ***cc_tol*** and ***shift_tol*** (see Section 2.2.2) serve as a simple control of the input data.

Data weighting

The code allows data weighting according to measurement uncertainty (i.e., picking error). In the *travel_time.inp*, quality classes 1, 2 or 3 are assigned to each travel time. The "1" quality class indicates data of the highest quality. Analogically, the "3" quality class indicates data of the lowest, but still acceptable quality. Users are asked to assign time uncertainties (***q1***, ***q2***, ***q3***) of observed travel times to each quality class. If switch ***do_weight*** is set to 1, the data weighting according to these uncertainties is applied in an inversion (see Section 2.6). If switch ***do_weight*** is set to 0, all qualities are set to 1 regardless of the originally assigned values in the *travel_time.inp* and no data weighting is applied. The most important information for data weighting subroutines is a ratio among the time uncertainties ***q1***, ***q2***, ***q3***. The values of time uncertainties affect mainly data statistics, particularly the average data error. The switch ***do_weight*** and time uncertainties ***q1***, ***q2***, ***q3*** are defined in *telinv2012input.inp* (Section 4.1.5).

2.2 Travel-time data adjustments

The code allows application of crustal corrections, additional corrections at individual stations and calculation of relative travel-time residuals. Because the calculation of relative residuals could be biased by uncorrected crustal structure, additional station corrections and crustal corrections are applied before relative residuals are calculated. Nevertheless, we recommend performing all data adjustments a-priori because these travel-time modifications are simple and do not provide many options.

2.2.1 Crustal corrections

Crustal corrections are differences between travel times calculated according to a "true" 3D crustal model (e.g., according to results from control source seismic) and travel times calculated according to an 1D reference crustal model (e.g., IASP91), which should be identical with the crust of an initial velocity model used in inversion.

The travel times of rays progatating through crustal models can be calculated by the forward modelling option of this code (Section 3). Because crustal heterogenities are smaller and more complex than those in the upper mantle, node spacings in of the crustal models have to be smaller (e.g., 5 km). Note that the ray-tracing of this code is adapted for teleseismic waves.

If crustal corrections were not applied out of the code, they should be added in *travel_time.inp* (Section 4.1.3) as the last column and the ***crust_3D*** switch should be set to 1 in the *telinv2012input.inp* file (Section 4.1.5). The crustal corrections are then subtracted from observed travel times and according to them travel-time residuals are re-calculated. Absolute values of the crustal corrections have to be smaller than pre-defined tolerance value ***cc_tol***, which is defined in *telinv2012input.inp*.

If the travel times are already corrected for the crustal structure, set the ***crust_3D*** switch to 0 in *telinv2012input.inp*.

2.2.2 Additional station corrections

Additional station corrections are systematic time shifts applied to travel-time residuals at selected stations. Reasons for usage of the station corrections can be varied, e.g., to correct travel times for sediments

beneath the station not considered in crustal corrections or to correct known time shift at station. The station corrections can be inserted in *station.inp* (Section 4.1.1). If switch ***ishift*** is set to 1 in the *telinv2012input.inp* file (Section 4.1.5), the station corrections are applied to observed travel times and the travel-time residuals are re-calculated. For example, if a user wants to correct for a time delay due to sediment cover with lower velocities than those in a reference model he/she has to insert a positive value into *station.inp* because station corrections are subtracted from the observed travel times. Absolute values of the additional station corrections have to be smaller than pre-defined tolerance value ***shift_tol***, which is defined in *telinv2012input.inp*.

2.2.3 Calculation of relative travel-time residuals

To minimize effects due to event mislocations, origin time inaccuracy and velocity heterogeneities along ray paths outside of the target volume, a travel-time normalization is often applied. The code calculates relative residuals with use of the most common normalization, which is the removal of a weighted event residual mean from travel-time residuals of individual stations (Achauer et al., 1986). Such calculated relative residuals are then inverted for velocity perturbations. If switch ***inorm*** is set to 1 in the *telinv2012input.inp* file (Section 4.1.5), the observed travel times in *travel_time.inp* (Section 4.1.3) are then replaced by a summation of the relative residuals and theoretical travel times, according to the reference model, and the travel-time residuals are replaced by the relative residuals.

2.3 Analysis of input data

This section is an overview of analyses and checks of the input data. The data are analyzed after the adjustments, which are applied in dependence on switches ***crust_3D***, ***ishift*** and ***inorm*** in the *telinv2012input.inp* file (Section 4.1.5). A user can define several complementary parameters in the *telinv.include* file (Section 4.1.6) to adapt an analysis to *travel_time.inp*. For example, a user can define a tolerance limit for a number of rays per station. If the input data are in conflict with these parameters, the code prints out only warnings to log file *telilnv2012.out* (Section 4.2.4).

The tolerances for travel-time residuals ***ttr_tol***, crustal correction ***cc_tol*** and station corrections ***shift_tol*** defined in *telinv2012input.inp* are of a higher importance. If data are in conflict with the tolerances, the program stops and a user is asked to either adapt the tolerance level or the input data.

2.3.1 Main analysis

The main analysis is designed as a basic statistics of the input data entering the inversion. Because optimal ray geometry requires an even volume illumination, a number of rays and travel-time residuals is analyzed in dependence on back-azimuths. A user can define back-azimuth segments (Fig. 2), for which characteristic quantities are calculated.

- Travel-time residuals
  - minimum, maximum, average, variance and standard deviation of travel-time residuals
  - station averages of travel-time residuals
  - station averages of travel-time residuals corresponding to rays with back-azimuths in pre-defined segments controlled by parameter ***n_baz_bins*** (Fig. 2)

- Number of rays

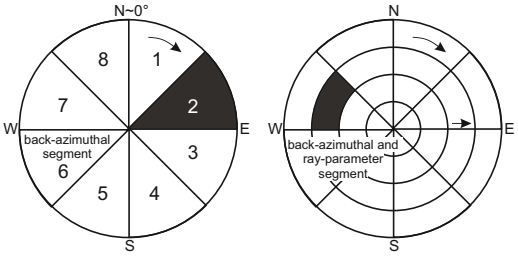

Figure 2: On the left, back-azimuth segments for parameter $n\_baz\_bins = 8$. Size of the back-azimuth segments is $360/n\_baz\_bins$. The lower limit of the first segment is at 0^{o} (towards the North). Numbering of the back-azimuth segments, used in output files, is clock-wise. On the right, back-azimuth and ray-parameter segments with parameters defined as $n\_baz = 8$ and $n\_ray\_param = 4$.

  - number of rays for each station

    In an ideal state, a number of rays per stations would be equal to the number of events used.
  - stations with the minimum and maximum of numbers of rays
  - average number of observations per station
  - number of rays in pre-defined back-azimuth segments (Fig. 2)
  - back-azimuth segments with the minimum and maximum of numbers of rays
  - average number of rays per back-azimuth segment

- Additional corrections at individual stations

  - minimum, maximum and average of station corrections

  Analysis of additional station corrections is done if switch $ishift = 1$.

- Crustal corrections

  - minimum, maximum and average of crustal corrections for the whole station array
  - averages of crustal corrections for each station

  Analysis of crustal corrections is done if switch $crust\_3D = 1$.

- Data Quality

  - numbers of travel times with quality classes 1, 2 and 3
  - average error of travel-time residuals
  - averages of travel-time residuals for each quality class
  - average errors of travel-time residuals for each station

  Analysis of data quality is done if switch $do\_weight = 1$.

Input parameters for main analysis:

n_baz_bins number of back-azimuth segments

The size of the segments is $360/n\_baz\_bins$ and the lower limit of the first segment is at 0^{o} (towards the North).

Recommended value is 8.

neqs_limit minimum number of rays per station

If the number of rays for a station is less than the ***neqs_limit*** parameter, the program prints a warning.

Recommended value is 10% of events.

n_data_limit minimum number of rays per back-azimuth segment

If the number of rays for a back-azimuth segment is less than ***n_data_limit*** parameter, the program prints a warning.

Recommended value is $n\_rays/(2 \cdot n\_baz\_bins)$.

These parameters can be defined in *telinv.include* (Section 4.1.6). Results of the analysis can be find in the *telinv2012.out* file, *input_info_ray_distribution.plo*, *input_info_station.plo* (Sections 4.2.4, 4.2.5, 4.2.6). Results of station and ray analyses in the files with suffix *plo* can be plotted with GMT scripts *plot_info_station.gmt* and *plot_ray_distribution.gmt* (Sections 5.1.1, 5.1.3).

2.3.2 Check of travel-time residuals of near-by events

The travel-time residuals entering the inversion should be cleansed of effects from sources outside the target volume. If absolute travel-time residuals are used in the inversion, effects of mislocation and origin time errors can identidied by this analysis. Event residual means are sorted into small segments according to back azimuth and ray paramater. A user control sizes of these segments by parameters ***n_baz*** and ***n_ray_param***. Events with back-azimuths and ray parameters in one segment are considered as close ones. Therefore, the size of the segment must be chosen carefully. Reference residuals of each segment are similar/close if standard deviations and differences between average and the minimum or maximum of the event residual means are smaller than pre-defined values ***ref_bin_std_limit*** and ***ref_bin_ext_limit***. According to these pre-defined tolerance values, warnings are printed to *telinv2012.out*.

Input parameters for additional check travel-time residuals:

n_baz number of back-azimuth segments

The size of the back-azimuth segments is then $360/$***n_baz***, analalogically to segments based on the ***n_baz_bins*** parameter, described above.

Generally, it may differ from the ***n_baz_bins*** parameter.

n_ray_param number of ray-parameter segments

The size of the ray-parameter segments is then

$$\frac{rayparam\_max - rayparam\_min}{n\_ray\_param} \tag{1}$$

.

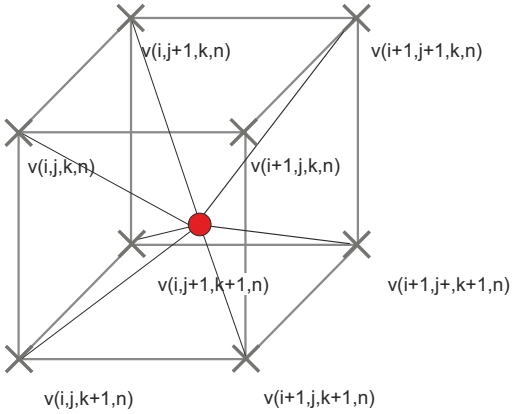

Figure 3: Velocity in an arbitrary point (circle) of the velocity model is calculated by a linear interpolation from velocities at the 8 nearest nodes (crosses). Velocity at a node is a function of node coordinates $\boldsymbol{xn(i)}$, $\boldsymbol{yn(j)}$, $\boldsymbol{zn(k)}$ and a number of iteration ($\boldsymbol{n}$).

rayparam_min minimum ray parameter in the dataset

rayparam_max maximum ray parameter in the dataset

ref_bin_std_limit tolerance limit of standard deviation of the event residual mean

ref_bin_ext_limit tolerance limit of difference between the average and the minimum or maximum of the event residual means

Results of the analysis are provided in two output files: *input_info_ref_res_bins.out* and *input_info_ref_res.out* (Sections 4.2.8, 4.2.7).

2.4 Model parameterization

Each velocity model is defined by an orthogonal grid of nodes in the Cartesian coordinate system, with an origin approximately in the center of a station array. Coordinates [km] and velocities [km/s] are set in the *velocity_model.inp* (Section 4.1.2). The velocities among these nodes are calculated by a linear interpolation (Fig. 3). The node coordinates are defined by a vector $[\boldsymbol{xn(i)}, \boldsymbol{ynt(j)}, \boldsymbol{zn(k)}]$, where $i \in \langle 1, nx \rangle$, $j \in \langle 1, ny \rangle$, $k \in \langle 1, nz \rangle$ and $\boldsymbol{nx}$, $\boldsymbol{ny}$ and $\boldsymbol{nz}$ are numbers of nodes in $\boldsymbol{x}$, $\boldsymbol{y}$ and $\boldsymbol{z}$ directions. The $\boldsymbol{x}$ direction is positive eastward, the $\boldsymbol{y}$ direction is positive northward and the $\boldsymbol{z}$ direction is positive downward (Figure 4 , 5).

2.4.1 Top and bottom of the velocity model

The shallowest nodes at depth of $\boldsymbol{zn(1)}$ must be above the largest station elevation. Because the direction of the vertical axis is positive downwards, the shallowest vertical coordinate is negative.

The bottom of the model is called $\boldsymbol{zlayerdepth} = \boldsymbol{zn(nz)} + 5$ (Fig. 4). Velocity ***vhalf*** at depth ***zlayerdepth*** is defined as a velocity at most southern and eastern node at depth of ***zlayerdepth***, $[\boldsymbol{xn(nx)}, \boldsymbol{yn(ny)}, \boldsymbol{zn(nz)}]$.

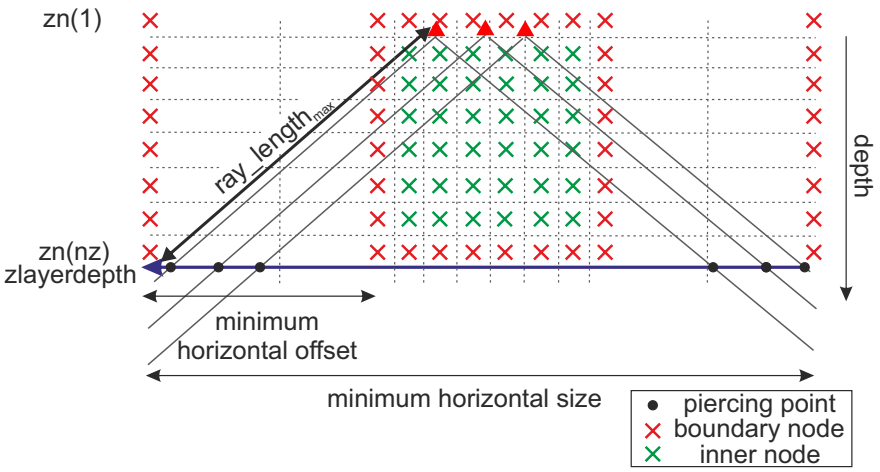

Figure 4: Vertical cross-section through the model parameterization. The nodes are indicated with crosses. The green crosses mark nodes, in which velocity perturbations can be searched. While the red crosses mark the boundary nodes, where velocities of the initial model are fixed. A cell is a volume around a node bounded by planes (dashed lines) at half-distances between neighbouring nodes. Solid black lines show ray paths close to the boundary nodes and black circles indicate ray piercing points. Seismic stations are marked with red triangles.

2.4.2 Horizontal size of the velocity model

Rays are allowed to enter the model only at the ***zlayerdepth***. Horizontal offsets between the piercing points and corresponding stations are given by ray parameters and back-azimuths. The minimum horizontal size of the velocity model has to be selected in dependence on the distances between the ending piercing points (Fig. 4). Because the ray parameter is defined as

$$rayp = \frac{sin(g\,(x,y,z))}{v\,(x,y,z)} \tag{2}$$

where $\boldsymbol{g}$ is an angle of ray path at $[\boldsymbol{x},\ \boldsymbol{y},\ \boldsymbol{z}]$ from the vertical and $\boldsymbol{v}$ is a velocity at $[\boldsymbol{x},\ \boldsymbol{y},\ \boldsymbol{z}]$, a minimum horizontal offset (Fig. 4) between boundary and inner nodes is

$$offset_{min} = zlayerdepth \cdot tan\,(asin\,(rayp_{max} \cdot vhalf)) \tag{3}$$

where $\boldsymbol{rayp}_{max}$ is the largest ray parameter in the data set.

2.4.3 Other limitations for horizontal nodes

Nodes at the margin of the model have to be set according to station distribution. Station coordinates must lie within limits ***xmin***, ***xmax***, ***ymin*** and ***ymax***, defined as:

$$xmin = xn\,(3) + dx/2 \tag{4}$$

$$xmax = xn\,(nx-2) - dx/2 \tag{5}$$

$$ymin = yn\,(3) + dy/2 \tag{6}$$

$$ymax = yn\,(ny-2) - dy/2 \tag{7}$$

where $dx = xn(3) - xn(2)$ and $dy = yn(3) - yn(2)$.

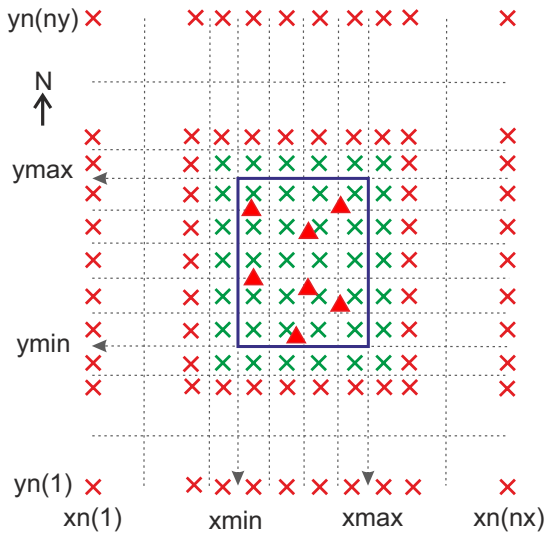

Figure 5: Horizontal parameterization of the model. The blue rectangle, defined by *xmin*, *xmax*, *ymin* and *ymax*, depends on the station locations, which have to fit inside the rectangle. For detailed description see Fig.4.

2.4.4 Optimal node spacing

The optimal spacing among nodes depends on wave lengths of teleseismic phases and station distribution. The frequency content of teleseismic body waves implies typical wave lengths of around 10 km. Therefore, a node spacing at least twice larger than the typical wave length is recommended. A spacing between the inner nodes can generally be irregular, but this may complicate the interpretation of the resulting velocity perturbations. Therefore, regular (equal) spacing is recommended, at least in horizontal dimensions (spacing in x direction is equal to spacing in y direction). Otherwise, the shape of velocity heterogeneities can be biased by the parameterization. The ratio between vertical and horizontal spacing is recommended to be around 1.5 (Evans and Achauer, 1993). Generally, small spacing can lead to a very complex model and too large spacing can lead to a very smooth model without any details. For this reason, several model parameterization should be tested together with regularization parameters (Section 2.6).

The horizontal parameterization and station distribution can be plotted by the auxiliary GMT script *plot_map_sta_nodes.gmt* (Section 5.1.2).

2.4.5 Initial velocity model

The initial velocities assigned to the model nodes should be set according to a 1D velocity model, whose velocities are good estimates of the real velocities. If the initial velocity model significantly differs from the real velocity structure, assumptions allowing us to linearize the tomography task will not be fulfilled. Velocities at boundary nodes (Figs. 4 and 5) should be set according to the Earth velocity model used for the calculation of the theoretical travel times. The velocity model can be created

and plotted with Matlab script *SyntheticSeismic3DModel* (Section 5.3.1) or using the Fortran script *create_TELINV_velocity_model.f* (Section 5.3.1) and GMT script *plot_synthetic_model.gmt* (Section 5.1.6).

2.4.6 Inverted nodes

In dependence on ray geometry, one has to define a subset of the model nodes where the velocity perturbations are searched. These nodes are called inverted nodes. The velocity perturbation at a node depends on the distribution of ray paths in the cell, which is a volume around the node bounded by planes at half-distances between neighbouring nodes. In case of regular horizontal and vertical spacings, the inner nodes lie in the center of the cell. The distribution of the inverted nodes has to be selected by a user according to the ray path distribution following these rules:

- Velocities should be inverted at nodes, whose cells are intersected by rays and are in their vicinity because the distribution of the intersected cell can vary due to changes in ray paths according to updates of velocities in subsequent iterations.
- The number of inverted nodes has to be smaller than the number of rays because the code can solve only over-determined problems.
- The velocity perturbations cannot be inverted at boundary nodes.
- Nodes next to boundary nodes should have fixed velocities. These nodes guaruntee that all inner cells have approximatelly the same volume (Fig. 5).

To visualize ray distribution, we recommend to run the program in the forward modelling mode (Section 3) and then to plot discretized ray paths with auxiliary GMT script *plot_ray_paths_2D_layers.gmt* (Section 5.1.4). According to the distribution of ray intersections, one can define which nodes will be inverted and which will remain fixed. Distribution of the inverted nodes is controlled by parameters ***i1z*** and ***inz***, defined in *telinv2012input.inp* (Section 4.1.5), and by positions of '1' in matrices of *use_node.inp* (Section 4.1.4). ***i1z*** and ***inz*** determine depths of nodes in which velocity perturbations are inverted.

2.5 Calculation of travel times

The travel times within the 3D velocity model can be calculated either along straight line (1D ray tracing) from a station to a ray piercing point (Fig.4) or along a more complex ray path perturbed by a simplex algorithm (3D ray tracing). The Simplex ray-tracing technique (Steck and Prothero, 1991) calculates the final ray path as a linear combination of three basic ray paths: a straight line and its horizontally and vertically distorted versions. The ray paths are repetitively distorted by sinusoidal signals of different amplitudes and wave lengths until the optimal ray path with the shortest travel time is found. The ray tracing in both cases (1D and 3D options) considers station elevations. As mentioned above, the velocity in an arbitrary point of the model is calculated by a linear interpolation among the velocities at the 8 nearest nodes (Fig.3).

The ray path is within the model discretized by points, whose number depends on the length of each ray and on the parameter ***scale1*** [km], which is defined in *telinv2012input.inp* (Section 4.1.5).

$$n\_points = 2^b + 1 \tag{8}$$

$$b = log_2 \left(int \left(\frac{ray\_length}{scale1} \right) \right) + 1 \tag{9}$$

where ***n_ points*** is the number of points along a ray path, ***ray_ length*** is the length of the ray. The largest value of exponent ***b*** in the equation (9) is 7 (may be changed in future update of the code) implying that the maximum of number of points is 129.

Along the starting straight ray paths, the points are distributed regularly. Spacing between points along a ray should be significantly smaller than node spacing in the velocity model because only then distortions in ray paths can reflect changes due to velocity perturbations. The minimum number of ray segments within a cell is 2. Moreover, there is a condition that the ***scale1*** parameter has to be at least 4-times smaller than space diagonal of corresponding cell. This condition prevents defining insuficiently poor discretization along ray paths.

Note the maximum number of points affects the smallest reasonable ***scale1***, which depends on the longest ray path.

$$scale1_{min} \sim int \left(\frac{ray\_length_{max}}{2^6} \right) = int \left(\frac{\sqrt{offset^2_{min} + zlayerdepth^2}}{64} \right) \tag{10}$$

where $\boldsymbol{ray\_length}_{max}$ is the longest ray in the data set and $\boldsymbol{offset}_{min}$ is minimum offset between boundary and inner nodes. There is no lower limit for the ***scale1***. This limitation of the maximum number of points along ray path means that the model size has to be selected together with node spacing.

2.6 Inversion

The detailed description of the inversion flow includes:

1. reading input files (Section 4.1):
   - observed travel times ***tt_ obs***, theoretical travel times ***tt_ theo*** and their differences: travel-time residuals ***tt_ diff***
   - initial velocity model $\boldsymbol{v}_{initial}$
   - ray geometry: station coordinates, ray parameters and back-azimuths
   - positions of nodes, where velocity perturbations are searched
2. data adjustment
3. data analyses
4. calculation of model smoothing matrix $\boldsymbol{W}_M$ [unitless], only when $smooth = 1$
5. calculation of data weighting matrix $\boldsymbol{W}_D$ [unitless]
6. calculation of travel times $\boldsymbol{tt}_{iter}$ through a velocity model $\boldsymbol{v}_{iter}$ [km/s] reflecting velocity after the previous iteration

   The subscript ***iter*** is an index of iteration. In case of the first iteration, travel times $\boldsymbol{tt}_{initial}$ are calculated according to the initial velocity model $\boldsymbol{v}_{initial}$; see Section 2.5.
7. for iterations > 1: travel-time residuals ***tt_ diff*** are re-calculated of according to updated ray paths resulting from the velocity model adjustments according to results of precending iteration

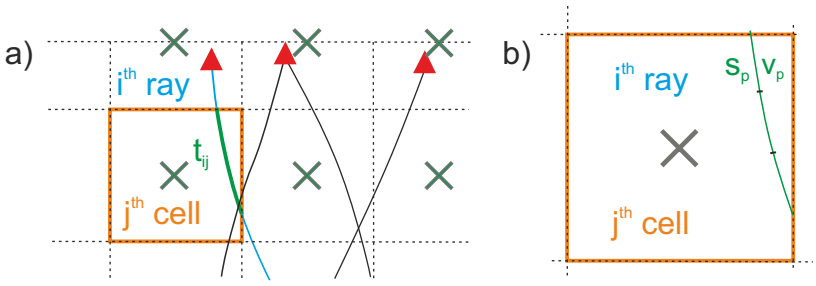

Figure 6: Matrix $\boldsymbol{A}$ consists of travel times corresponding to wave propagations along ray paths through cells around inverted nodes. Nodes are marked with crosses, stations with triangles and cells with dashed squares. t_{ij} is a time of wave propagation along ray segment of the i-th ray in the j-th cell. On the right side, a detail of travel-time calculation is shown. Travel times corresponding to the i-th ray segment in the j-th cell are sums of partial travel times t_p, which are calculated as $t_p = \frac{s_p}{v_p}$, where s_p is the length of ray sub-segment and v_p is the velocity at the center of the ray sub-segment.

$$tt\_diff_{iter+1} = tt\_obs - tt\_theo - (tt_{iter} - tt_{initial}) \tag{11}$$

where $\boldsymbol{tt}_{initial}$ are travel times calculated for initial velocity model $\boldsymbol{v}_{initial}$ while $\boldsymbol{tt}_{iter}$ are travel times calculated for updated velocity model $\boldsymbol{v}_{iter}$.

8. calculation of matrix $\boldsymbol{A}_{iter}$ [s], which is updated after each iteration

$$A_{ij} = t_{ij} \tag{12}$$

$$t_{ij} = \sum_{p=1}^{Q} t_p = \sum_{p=1}^{Q} \frac{s_p}{v_p} \tag{13}$$

t_{ij} travel time [s] corresponding to the i-th ray in the j-th cell (Fig.6)

t_p partial travel time corresponding to the p-th sub-segment of ray path in the j-th cell

s_p length of the p-th sub-segment of the i-th ray in the j-th cell

v_p velocity in a center of the p-th sub-segment of i-th ray in the j-th cell

Q number of ray sub-segments

9. calculation of velocity adjustments in two steps $\triangle \boldsymbol{v}_{iter}$

$$m_{est} = \left(A^T W_D A + \varepsilon^2 W_M\right)^{-1} A^T W_D tt_{diff} \tag{14}$$

$$\triangle v_{iter} = m_{est} \cdot (-1) \cdot v_{iter} \tag{15}$$

m_{est} estimates of model parameters [unitless]

ε^2 (theta) damping factor [unitless]

$\triangle v$ velocity adjustments [km/s] of velocity model v_{iter}

10. updates of velocity model

$$v_{iter+1} = \triangle v_{iter} + v_{iter} \tag{16}$$

11. repeating procedures from the 6^{th} point until the pre-defined maximum number of iterations, defined in telinv2012input.inp, is reached.

$$iter = iter + 1 \tag{17}$$

12. calculation of parameters for evaluation of model resolution: hit counts, derivative weighted sums (DWS), resolution matrix
13. calculation of final travel-time residuals according to the final velocity model
14. printing output files

2.6.1 Weighting matrix

The weight of each travel time (ray) is indirectly proportional to its time uncertainty (see Section 2.1). Data of the highest quality with the smallest error have the largest weights. The weights are normalized in such way that the sum of the weights is equal to the number of rays. In the weighting matrix, off-diagonal terms result from the comparison of weights of travel times along rays of an event.

2.6.2 Smoothing matrix

The smoothing matrix stabilizes the inversion by additional requirements to model parameters. The searched velocity perturbations in the inverted nodes should be equal to averages of perturbations at the neighbouring inverted nodes in horizontal planes. Because velocity perturbations are smeared in the vertical direction due to steep ray paths, additional coupling of model parameters in the vertical would not be favourable. The matrix is built according to the study of Ammon and Vidale (BSSA,1993).

2.6.3 Selection of regularization parameters

In most cases, many velocity perturbations are not well-resolved due to uneven ray geometry. The matrix $\boldsymbol{A}$ is then singular and its regularization is necessary. The code options offer two regularization parameters: the damping factor ε^2 (***theta***) and the smallest singular value ***small_sv*** for pseudo-inversion of the matrix $A^T W_D A + \varepsilon^2 W_M$. The main purpose of the regularization is to get velocity perturbations within a realistic range of velocities. For the upper mantle, velocity perturbations not exceeding 5 % are expected. The values of damping factor and the smallest singular value depend mainly on ray distribution and input travel-time residuals. The damping factor is traditionally selected as a trade-off between data and model variances. Note that the trade-off curve provides only a rough extimates of inversion parameters and amplitudes of final velocity perturbations should be tested.

The pseudo-inversion of the kernel matrix is implemented by a truncated singular value decomposition. Selection of the singular values above chosen threshold for a calculation of inverse matrix is an alternative regularization method to a usage of the damping factor. From that reason, we recommend to set one of the parameters - either the damping factor ***theta*** or the smallest singular value ***small_sv*** - to relatively small value in comparison to the other one. The damping factor ***theta*** and the smallest singular value

small_ sv are defined in *telinv2012input.inp* (Section 4.1.5). The data and model variances for each iteration are stored in output files *variances_ data.out* and *variances_ model.out* (Sections 4.2.13, 4.2.14).

2.6.4 Number of iterations

During consequent iterations, ray paths change due to velocity model updates. Therefore, a higher number of iterations reduces demands on linerization of the task. The maximum/optimal number of iterations is reached when the velocity adjustments are insignificant. Significance of model improvement is defined by model variances after each iteration and by differences in figures of velocity perturbations after each iteration. Usually 3-5 iterations are sufficient if data quality is high. Variances of the velocity adjustments $\triangle v_{iter}$ after each iteration are printed in file *variances_ model.out* (Section 4.2.14). Note that every iteration will increase the complexity of the final velocity model.

2.6.5 Model assessment options

1. number of hit counts per cell

   This is one of the most common proxy for ray distribution. However, it counts only numbers of rays passing each cell, we calculate also derivative weighted sum.

2. derivative weighted sums (DWS)

   Compared to hit count, the DWS (Sandoval et al., 2004) also considers differences in ray lengths within each cell and in weights. It is calculated as

   $$DWS_j = \frac{\sum s_{ij} w_i}{L_j} \tag{18}$$

   s_{ij} lengths [km] of ray segments for the i-th ray and j-th cell

   w_i weight of the i-th ray

   L_j space diagonal of the j-th cell

3. ray paths

   The discretized ray paths can be plotted by auxiliary GMT script *plot_ ray_ paths_ 2D_ layers.gmt*. The plots complement the DWS or hit counts with information about back-azimuth distribution of ray paths.

4. resolution matrix

   It shows capabilities of the ray geometry and distribution of inverted nodes to resolve the velocity perturbations. It is calculated as

   $$R = \left(A^T W_D A + \varepsilon^2 W_M\right)^{-1} A^T W_D A \tag{19}$$

   The most important parts are diagonal elements of the resolution matrix (Menke, 1984), allowing to compare resolution of velocity perturbations at all nodes. In case of optimal ray-geometry, resolution matrix would become unity matrix. Off-diagonal terms show a level of mutual dependency of searched model parameters (velocity perturbations). For these off-diagonal terms, resolving width function RW (Michelini and McEvilly, 1991) is calculated as

$$RW_i = \|r_j\|^{-1} \sum_{j=1}^{m} d_{ij} R_{ij}^2 \tag{20}$$

where $\|r_j\|^{-1}$ is L^2 norm of the j-th averaging kernel, the d_{ij} are distances in kilometers between nodes and R is the resolution matrix from equation (19).

Hit counts, DWS, diagonal elements of resolution matrix are stored together with final velocity model in output file *combi_output* (Section 4.2.1). Resolution width RW is printed only in case of extended output in *reswidth.out* (Section 4.2.11).

3 Step-by-step guide

Input files (Section 4.1) and their preparation are common for both modes, the forward modelling and the inversion, though their purposes differ essentially. The forward solution produces primarily synthetic travel times according to the given velocity model. The synthetic travel times are necessary for synthetic tests (Section 3.2). The other purpose of the forward modelling mode is to provide basic statistics of the input travel time residuals, stations, events and ray path distributions. These analyses check input data and help with selection of optimal control parameters for the inversion mode (Section 2.6), where velocity perturbations relative to inital velocity model are calculated.

3.1 Forward modelling and inversion modes

1. Choose the origin of the Cartesian Coordinate System at the center of the station array.
2. Create a *station.inp* (Section 4.1.1) with geographical and Cartesian coordinates of all stations.
3. Create a *travel_time.inp* (Section 4.1.3).
4. Create an initial *velocity_model.inp* (Section 4.1.2). Auxiliary Fortran, GMT and Matlab scripts (Sections 5.2.1,5.1.6, 5.3.1) can be used to prepare and visualize the velocity model.
5. Create a *use_node.inp* (Section 4.1.4) file with a use of a Fortran script (Section 5.2.2).
6. Define control parameters in *telinv2012input.inp* (Section 4.1.5). For forward modelling set *modinv* to 0. For inversion set *modinv* to 1.
7. Define main control parameters in *the telinv.include* file (Section 4.1.6), which is located in a sub-directory *src* (Section 4.1.6).
8. Compile and run the code.

   There are two equivalent options:

   (a) Write "sh makefile" to the command line in sub-directory *src* to compile the code, then write "sh run.sh" to the command line in a working directory to run the program.

   or

   (b) Write "sh compile.sh" to the command line in a working directory. This command compiles the code and runs the program at once.

9. The current stage of the forward modelling is printed on screen and ends with message according to the mode:

   END of FORWARD SOLUTION

   or

   END of INVERSION

Output files in case of the forward modelling:

- *telinv2012.out* - a log file with information about the input parameters (Section 4.2.4)
- *forward_sol.out* - a file with synthetic travel times according to a given velocity model (Section 4.2.2)
- *final_residuals.out* - a file with input travel-time residuals after adjustments (Section 2.2), e.g., crustal corrections (Section 4.2.3)
- *input_info_ray_distribution.plo* - a file with the number of rays in back-azimuth segments (Section 4.2.5)
- *input_info_station.plo* - a file with detailed station information (Section 4.2.6)
- *raypaths.out* - a file with ray-path coordinates (Section 4.2.9)
- created only when ***ioutext*** = 1 in *telinv2012input.inp*:
  - *input_info_ref_res.out* - a file with detailed event information (Section 4.2.7)
  - *input_info_ref_res_bins.out* - a file with information about near-by events (Section 4.2.8)
  - *velmod.out* - file with the initial velocity model (Section 4.2.11)

Output files in case of the inversion:

- *telinv2012.out* - a log file with information about the input and output parameters and the final velocity model (Section 4.2.4)
- *combi_output* - a file with the initial and final velocity perturbation model, number of hit counts, DWS and diagonal elements of resolution matrix (Section 4.2.1)
- *final_residuals.out* - a file with a part of travel-time residuals that was not explained by the final velocity model (Section 4.2.3)
- *input_info_ray_distribution.plo* - a file with number of rays in back-azimuth segments (Section 4.2.5)
- *input_info_station.plo* - a file with detailed station information (Section 4.2.6)
- created only when ***ioutext*** = 1 in *telinv2012input.inp*:
  - *input_info_ref_res.out* - a file with detailed event information (Section 4.2.7)
  - *input_info_ref_res_bins.out* - a file with information about near-by events (Section 4.2.8)
  - *resol.out* - a file with diagonal elements of resolution matrix (Section 4.2.10)
  - *reswidth.out* - a file with resolution widths (Section 4.2.11)
  - *velmod.out* - a file with the initial and final velocity models (Section 4.2.11)

3.2 Synthetic test

The syntetic test is an inversion with a synthetic *travel_time.inp*. To create the synthetic *travel_time.inp*, one needs two kinds of synthetic travel times. The first synthetic travel times, usually with additional noise, substitute the observed travel times. These "observed" travel times are calculated by the forward modelling with synthetic *velocity_model.inp*. The second synthetic travel times substitute the theoretical travel times. These "theoretical" travel times are calculated by the forward modelling with initial *velocity_model.inp*.

1. Create two velocity models: synthetic and initial.

2. Prepare remaining input files, with control parameters set to the forward modelling, following steps in Section 3.1. The *travel_time.inp* serves only for defining the ray geometry.

3. Run the forward modelling with synthetic velocity model and save the outputs.

   - Define a name of the *velocity_model.inp* to the synthetic velocity model in *telinv2012input.inp*.
   - Define the level of noise added to synthetic travel times in *telinv2012input.inp*.
   - Create a directory frw_SYN and move there all the outputs of the forward modelling.
   - *forward_sol.out* in a directory frw_SYN contains the "observed" travel times.

4. Run the forward modelling with initial velocity model and save the outputs.

   - Define a name of the *velocity_model.inp* to the initial velocity model in telinv2012input.inp.
   - Create a directory frw_INITIAL and move there all the outputs of the forward modelling.
   - *forward_sol.out* in a directory frw_INITIAL contains the "theoretical" travel times.

5. Use an auxililary shell script *make_synthetic_input.csh* (Section 5.4.1) to create the synthetic *travel_time.inp*.

   - The "observed" travel times can be chosen with or without the additional noise.

6. Run the inversion mode with sythetic *travel_time.inp*, following steps in Section 3.1.

4 Input/Output formats

4.1 Input files

The *telinv2012input.inp*, *station.inp*, *velocity_model.inp*, *travel_time.inp* and *use_node.inp* files are read by a compiled program, while dimensions of the important parameters have to be defined in file *telinv.include* before the compilation of the code.

Legend for the description of the formats: [CH] - character; [R] - real; [I] - integer, all input parameters are read in free format.

4.1.1 station.inp

This file contains station information including geographical and Cartesian coordinates. Conversion from geographical into the Cartesian coordinates is not performed in the code. Name of the file is defined in *telinv2012input.inp* (Section 4.1.5). Number of lines is equal to a total number of stations (*nsts*) plus one line of a header. Station order in *station.inp* is coupled with station indexes in the *travel_time.inp* file (Section 4.1.3).

- header: lon0= ***lon0*** lat0= ***lat0***

  lon0 [R], ***lat0*** [R] define the origin of coordinate system. Latitude, positive to the north, and longitude, positive to the east, are both in degrees. These values have to match corresponding values ***orlon***, ***orlat*** in the *telinv2012input.inp* file (Section 4.1.5).

- Then 8 columns with station codes, coordinates and additional time shifts follow:

1. ***stn*** [CH*4] defines a station code
2. ***lon*** [R] defines a station longitude [degree]
3. ***lat*** [R] defines a station latitude [degree]
4. ***elev*** [R] defines a station elevation, positive above sea level [m] (Example: 326 means 326 m above the sea level.)
5. ***x*** [R] is station's x coordinate, positive eastwards [km]

   It must lie within limits of ***xmin*** and ***xmax*** defined by parameterization of model in the *velocity_model.inp* (Fig.5) and must be identical with x station coordinate in the *travel_time.inp* (Section 4.1.3).
6. ***y*** [R] is station's y coordinate, positive northwards [km]

   It must lie within limits of ***ymin*** and ***ymax*** defined by parameterization of model in the *velocity_model.inp* (Fig.5) and must be identical with y station coordinate in the *travel_time.inp*.
7. ***z*** [R] is station's z coordinate, positive downwards [km]

   It must lie within limits ***zn(1)*** and ***zlayerdepth*** defined by parameterization of model in the *velocity_model.inp* (Fig.4) and must be identical with z station coordinate in the *travel_time.inp*. (Example: -0.326 means 326 m above the sea level.)
8. ***shift*** [R] defines additional time corrections at individual stations [s]

   The additional station corrections (Section 2.2.2) will be applied only if ***shift=1***. The absolute values of ***shift*** must be smaller than ***shift_tol***. Both parameters, ***ishift*** and ***shift_tol***, are defined in the *telinv2012input.inp* (Section 4.1.5).

Example:

```
lon0= 15.0 lat0= 49.0
A102 13.5420 48.8135 645.0000 -106.9300 -19.6847 -0.6450 0.0000
A103 13.5106 48.6719 552.0000 -109.5410 -35.3622 -0.5520 0.0000
A104 13.5885 48.4804 528.0000 -104.2080 -56.7347 -0.5280 0.0000
A105 13.4896 48.3280 452.0000 -111.8460 -73.5152 -0.4520 0.0000
```

A106 13.5743 48.1461 550.0000 -105.9540 -93.8336 -0.5500 0.0000
A107 13.5665 47.9643 523.0000 -106.9150 -114.0090 -0.5230 0.0000
...

4.1.2 velocity_model.inp

Name of this file is defined in *telinv2012input.inp* (Section 4.1.5). In this file, initial velocities [km/s] and node coordinates [km] are defined.

1. line: ***nx ny nz***

   nx [I] ***ny*** [I] ***nz*** [I] Numbers of nodes in x, y, and z directions must be identical with ***n_x_nodes***, ***n_y_nodes*** *and* ***n_z_nodes***, respectively, defined in *telinv2012input.inp*.

2. line: ***xn(1) xn(2) ... xn(nx)***

   xn [R] Vector with x-node coordinates sorted from west to the east, positive eastwards [km].

3. line: ***yn(1) yn(2) ... yn(ny)***

   yn [R] Vector with y-node coordinates sorted from south to north, positive northwards [km].

4. line: ***zn(1) zn(2) ... zn(nz)***

   zn [R] Vector of z-node coordinates sorted from shallow to deep, positive downwards [km].

Starting at the 5^{th} line, velocities at nodes are defined in blocks at depth ***zn(N)***, where N is from 1 to ***nz***. Header of the block is "layerN". Velocities at the first line of the block are defined for the northernmost nodes from the west to the east. Therefore, we look at the velocities of each depth slice as at a map. The north-western node is the upper-left corner.

Rules for setting of the model parameterization and initial velocities (Section 2.4).

- Initial velocities are usually set according to an Earth's reference velocity model (IASP91, PREM, ak135).
- First vertical coordinate is negative and above the highest station elevation.
- Set vertical size of the model to the ***zlayerdepth*** to approximately the horizontal size of the station array as the first rought estimate. Then adapt the depth extent of the model according to ray intersections in deep layers.
- Horizontal distance between boundary and inner nodes equals to a minimum horizontal offset at least (Fig.4).
- Station coordinates lie within a region defined by ***xmin***, ***xmax***, ***ymin*** and ***ymax*** (Fig.5).
- Node spacing is at least twice the wave length of teleseismic waves.
- Horizontal spacing among inner nodes should be regular and equidistant.
- Ratio between vertical and horizontal node spacings should be around 1-1.5.

Example:

4 5 3
-1000 -500 250 1000
-1200 -700 -300 100 1200
-2 20 40
layer1
5.8 5.8 5.8 5.8
5.8 5.8 5.8 5.8
5.8 5.8 5.8 5.8
5.8 5.8 5.8 5.8
5.8 5.8 5.8 5.8
layer2
...

4.1.3 travel_time.inp

Name of this file is defined in *telinv2012input.inp* (Section 4.1.5). This file contains parameters of each ray and corresponding travel-time residual. The file contains a header and then 11 or 12 columns.

- header: "Eq sta x y z rayp baz tt_obs tt_pred tt_diff qua (crc)"

  The 1st character of the 1st line must be capital E.

- columns:

1. event index [I]
2. station index [I]

   Station index equals the order of station in the *station.inp* (Section 4.1.1).
3. x station coordinate [km], [R]

   Station cordinates in the travel_time.inp are identical with those in the *station.inp* (Section 4.1.1)
4. y station coordinate [km], [R]
5. z station coordinate [km], [R]
6. ray parameter [s/km], [R]
7. ray back-azimuth in [degrees], [R]
8. observed travel time [s], [R]

   In case, relative residuals are used, the observed travel times are represented by a sum of relative residuals and theoretical travel times.
9. theoretical travel time [s], [R]
10. travel-time residual = difference between travel times in the 8^{th} and 9^{th} columns [s], [R]
11. quality of the measurement [I]

    Quality classes 1, 2 or 3 have to be assigned to each travel-time residual. '1' indicates the highest quality of the measurement, '3' indicates the lowest quality of the measurement. If the travel times cannot be distinguished by quality, set all qualities to 1.

12. crustal corrections [s], [R] - optional

    Crustal corrections (Section 2.2.1) are considered only when the SWITCH ***crust_3D*** = 1. The absolute values of crustal corrections have to be smaller than ***cc_tol*** defined in *telinv2012input.inp* (Section 4.1.5).

Example:

Eq sta x y z rayp baz tt_obs tt_pred tt_diff weight crust_corr
97 114 365.103 -108.272 -0.549 0.0599847 250.633 626.1432 625.6750 0.4682 1 -0.0728
97 115 -30.530 169.847 -0.311 0.0615136 244.591 610.9017 610.5390 0.3627 1 -0.2827
97 117 -200.909 88.876 -0.430 0.0625927 242.788 599.0382 598.8420 0.1962 1 -0.3659
97 118 -65.344 137.298 -0.275 0.0616934 244.293 608.0756 607.7320 0.3436 2 -0.3170
97 120 116.862 -145.027 -0.260 0.0614236 247.858 610.8484 610.8590 -0.0106 1 -0.0565
...

4.1.4 use_node.inp

The name of this file is defined in *telinv2012input.inp* (Section 4.1.5). The file contains '1' or zeros '0' for each node. The '1' stands for inverted nodes, where velocity perturbations relative to a reference model are searched for. The '0' stands for nodes, which are not inverted and where velocities are fixed to the initial ones. The boundary nodes must be always fixed. The total number of '1' in the *use_node.inp* have to be smaller than the number of rays. In case of the forward mode, one can set all numbers to 0. In case of the inversion mode, follow the rules for selection of inverted nodes in Section 2.4.6.

The format of *use_node.inp* is similar to the format of *velocity_model.inp* (Section 4.1.2) without first 4 lines. The zero in the first column and first row is assigned to nodes in the first depth layer (the shallowest one) in the north-western corner of the model. The *use_node.inp* file can be created with a use of auxiliary Fortran script *create_use_node.f* (Section 5.2.2).

Example:

layer1
0 0 0 0 0 0 0 0
0 0 0 0 0 0 0 0
0 0 0 0 0 0 0 0
0 0 0 0 0 0 0 0
0 0 0 0 0 0 0 0
0 0 0 0 0 0 0 0
layer2
0 0 0 0 0 0 0 0
0 0 0 0 0 0 0 0
0 0 1 1 1 0 0 0
0 0 0 1 1 1 0 0
0 0 0 0 0 0 0 0
0 0 0 0 0 0 0 0
...

4.1.5 telinv2012input.inp

This file has a fixed name and contains names of other input files and control parameter.

1. title of the project [CH]
2. name of *station.inp* file [CH] (Section 4.1.1)
3. name of *velocity_model.inp* file [CH] (Section 4.1.2)
4. name of *travel_time.inp* file [CH] (Section 4.1.3)
5. name of *use_node.inp* file [CH] (Section 4.1.4)
6. ***nsts*** [I] defines number of stations in the *station.inp*

   It is allowed to have stations in the *station.inp,* which are not included into the *travel_time.inp.* If no travel time is assigned to a station, only warning will be printed in *telinv2012.out* file.
7. ***neqs*** [I] defines the maximum of event index in the *travel_time.inp*

   To allow further excluding of the events without their re-numbering, the total number of events may be smaller than ***neqs*** parameter.
8. ***n_data*** [I] defines a number of travel-time residuals in *travel_time.inp*
9. ***do_weight*** [I] ***q1*** [R] ***q2*** [R] ***q3*** [R]

   do_weight is a SWITCH, which controls data weighting (see Section 2.1)

   - If ***do_weight*** = 1 then data weighting is applied according to the quality classes.
   - If ***do_weight*** = 0 then no data weighting is applied.

   q1, ***q2***, ***q3*** define accuracies/errors of travel-time residuals in seconds. ***q1*** indicates data with the highest quality (smallest error), ***q2*** indicates data with the medium quality and ***q3*** indicates data of the lowest quality (largest error).
10. ***inorm*** [I] is a SWITCH, which defines whether a normalization of the travel-time residuals is applied (Section 2.2)

    - If ***inorm*** = 0 then normalization of travel-time residuals is not applied. It is recommended to make all data corrections outside of the code.
    - If ***inorm*** = 1 then normalization of travel-time residuals is applied.
11. ***ttr_tol*** [R] defines a limit for maximum or minimum of travel-time residuals in seconds.

    The ***ttr_tol*** parameter serves as a basic control of data entering the inversion and it is able to find a rewriting errors etc. The travel-time residuals in *travel_time.inp* must be in absolute value smaller than ***ttr_tol***. If the absolute values of residuals are larger than ***ttr_tol***, the program STOPS! If this is the case, check your data set for time instabilities and outliers and /or adapt the tolerance level according to the data set. The normal value of ***ttr_tol*** can be around 2 s for residuals reflecting only velocity perturbations of the upper mantle. Example: travel-time residuals are in range from -1.54 s to 2.1 s, then ***ttr_tol*** should be at least 2.2.
12. ***crust_3D*** [I] ***cc_tol*** [R]

    crust_3D is a SWITCH, which defines whether to apply crustal corrections (Section 2.2)

- If ***crust_ 3D*** = 1 then crustal corrections are contained in *travel_ time.inp* and will be applied. Warning: When the switch ***crust_ 3D*** is set to 1, crustal corrections must be in the *travel_ time.inp* (Section 4.1.3)!
- If ***crust_ 3D*** = 0 then crustal corrections are not applied even if they are in the *travel_ time.inp*.

cc_ tol defines a tolerance of crustal corrections in seconds.

Crustal corrections, if they are supplied in *travel_ time.inp*, have to be in absolute value smaller than ***cc_ tol***. If the absolute values of crustal corrections are larger than ***cc_ tol***, the program STOPS! If this is the case, check crustal corrections and adapt the tolerance level according to them.

13. ***ishift*** [I] ***shift_ tol*** [R]

ishift is a SWITCH, which defines whether to apply additional corrections at individual stations

- If ***ishift*** = 1 then additional station corrections will be applied.
- If ***ishift*** = 0 then no additional corrections at individual stations will be applied.

shift_ tol defines a station correction tolerance in seconds

Station corrections, defined in *station.inp*, in absolute value have to be smaller than ***shift_ tol***. If the absolute values of additional station corrections are larger than ***shift_ tol***, the program STOPS! If this is the case, check station corrections and adapt the tolerance level according to them.

14. ***orlat*** [R] ***orlon*** [R] define origin of Cartesian coordinate system

The latitude, positive to the north, and longitude, positive to the east, are defined in degrees. These values have to be identical with values in header of *station.inp*.

15. ***n_ x_ nodes*** [I] ***n_ y_ nodes*** [I] ***n_ z_ nodes*** [I]

n_ x_ nodes, ***n_ y_ nodes*** and ***n_ z_ nodes*** define numbers of nodes in the velocity model in x, y, and z directions, respectively. These values must be identical with those in the *velocity_ model.inp*.

16. ***i1z*** [I] ***inz*** [I]

i1z defines an index of the 1^{st} inverted layer of nodes and ***inz*** defines a number of layers with fixed nodes from the bottom of the model. Note that boundary nodes cannot be inverted, therefore, ***i1z*** > 1 and ***inz*** > 1.

17. ***nodes2*** [I] defines the total number of inverted nodes.

The total number of inverted nodes is determined by a sum of '1' in the *use_ node.inp* (Section 4.1.4) at all inverted depths, which are controlled by parameters ***i1z*** and ***inz*** (above).

18. ***i3d*** [I] is a SWITCH, which controls type of ray tracing.

- If ***i3d*** = 1 then 3D Simplex ray tracing is applied (recommended).
- If ***i3d*** = 0 then ray tracing is calculated along straight lines.

19. ***scale1*** [R] controls a step s_p length [km] along ray path (Fig.6).

Follow the rules in Section 2.5.

20. ***signois*** [R] defines a signal-to-noise ratio indicating a level of Gaussian noise added to synthetic travel times. This parameter is used only in forward modelling mode of the code. Default value is 0.05 (5%).

21. ***modinv*** [I] ***npass*** [I]

    modinv is a SWITCH, which controls whether the code performs a forward modelling or inversion of travel-time residuals

    - If ***modinv*** = 0 then the code calculates travel times for given velocity model: FORWARD MODELLLING.
    - If ***modinv*** = 1 then the code inverts the travel-time residuals for velocity perturbations: INVERSION.

    npass defines the number of iterations in the case of inversion mode (See Section 2.6.4).

22. ***smooth*** [I] is a SWITCH, which controls smoothing of velocity perturbations (Section 2.6.2)

    - If ***smooth*** = 1 then smoothing of model parameters is applied (recommended).
    - If ***smooth*** = 0 then no smoothing of model parameters is applied.

23. ***small_sv*** [R] defines the smallest singular value of the kernel matrix used for inversion of travel-time residuals. See Section 2.6.3.

24. ***theta*** (ε^2) [R] defines a damping factor (Section 2.6.3)

25. ***ioutext*** [I] is a SWITCH, which controls extended output

    - If ***ioutext*** = 1 then extended output files are created.
    - If ***ioutext*** = 0 then no extended outputs are created.

4.1.6 telinv.include file

The *telinv.include* file declares global parameters and sets dimensions for the important parameters, necessary for a compilation of the code. The user should modify only parameters listed bellow. These parameters are defined in the upper part of the file. Modification of other parts of the file can significantly damage the functions of the code.

Essential parameters for a compilation of the code to be modified:

nsta_exact [I] number of stations, e.g., number of lines of *station.inp* without header (Section 4.1.1)

nev_exact [I] the largest event index in *travel_time.inp* (Section 4.1.3)

nx_exact [I] number of x nodes as in *velocity_model.inp* (Section 4.1.2)

ny_exact [I] number of y nodes as in *velocity_model.inp*

nz_exact [I] number of z nodes as in *velocity_model.inp*

ndat_exact [I] number of data, i.e., number of lines of *travel_time.inp* without header

nodes2_exact [I] total number of inverted nodes, i.e., sum of ones in the *use_node.inp* in inverted layers defined by ***i1z*** and ***inz*** values in *telinv2012input.inp* (Section 4.1.5)

Parameters for main input analysis to be modified (Section 2.3.1):

n_baz_bins [I] number of back-azimuth segments

neqs_limit [I] minimum number of events per station

n_data_limit [I] minimum number of rays per back-azimuth segment

Parameters for analysis of near-by events to be modified (Section 2.3.2):

n_baz [I] number of back-azimuth segments

n_rayparam [I] number of ray-parameter segments

rayparam_min [R] the smallest ray parameter in *travel_time.inp* [s/km]

rayparam_max [R] the largest ray parameter in *travel_time.inp* [s/km]

ref_bin_var_limit [R] tolerance limit for variance of event residual means in a segment [s] (Fig.2)

ref_bin_ext_limit [R] tolerance limit for difference between average of event residual means in a segment and minimum/maximum of event residual means in a segment [s]

Additional parameters for 3D ray tracing :

n_har [I] defines the number of harmonics used in 3D ray tracing

amp [R] defines the amplitude of raypath diturbed in both horizontal and vertical directions [km]

ar [R] defines the amplitude of raypath disturbed in vertical direction [km]

cf [R] defines the smallest difference between travel times of tested ray paths [s]

4.2 Outputs

4.2.1 combi_output

The file contains results of the inversion such as the absolute velocities after each iteration and velocity perturbation for the last successful (complete) iteration. The file contains a header and columns with the results. Number of the columns depends on a number of iterations set in *telinv2012input.inp*. This file is produced only in case of the inversion mode. The parameters in the file can be plotted by auxiliary GMT script *plot_combi_output.gmt* (Section 5.1.5).

- header: "x(km) y(km) z(km) velinit(km/s) node_index vel_iter_1 ... vel_iter_final vel_per(%) nhit dws res"

1. ***x*** node coordinate [km]
2. ***y*** node coordinate [km]
3. ***z*** node coordinate [km]
4. ***velinit*** - initial velocity model [km/s]
5. ***node_index*** - index of each inverted node

6. ***vel_iter_ 1*** - velocity model after first iteration [km/s]
7. ***vel_iter_ 2*** - velocity model after first iteration [km/s]

   Note that number of columns varies according to the number of iterations.
8. ***vel_iter_ (N-1)*** - velocity model after first iteration [km/s]
9. ***vel_iter_ N*** - the final velocity model [km/s]
10. ***vel_per*** - velocity perturbations [%] calculated as $vel\_per = \frac{vel\_iter\_final - vel\_init}{vel\_init} \cdot 100\%$
11. ***nhit*** - number of hit counts: the number of ray paths propagating through the cell
12. ***dws*** - derivative weighted sums (DWS) defined as sums of weighted ray lengths in each cell normalized by the space diagonal of the cell (Sandoval et al. 2004)
13. ***res*** - diagonal elements of resolution matrix

4.2.2 forward_sol.out

This file contains synthetic travel times according to a velocity model with and without Gaussian noise of level ***signois***, defined in *telinv2012.input.inp*. The format of *forward_ sol.out* is similar to *travel_ time.inp* and the first seven columns are identical. The eighth, ninth and tenth columns contain travel times with noise, without noise and differences of these travel times, respectively. This output serves also for preparation of synthetic *travel_ time.inp*. This file is printed only in the case of the forward modelling mode.

4.2.3 final_residuals.out

Contents of the file differ for the forward modelling (1) mode and inversion (2). The format of the file is similar to *travel_ time.inp*. The first seven columns are identical with those in *travel_ time.inp*. The eighth, ninth and tenth columns contain travel times and travel-time residuals modified according to the mode of the code.

1. Forward modelling:

   The file contains the input travel times from the input *travel_ time.inp* (Section 4.1.3) after adjustments according to the switches in the *telinv2012.input.inp* file (Section 4.1.5). The adjustments are described in Section 2.2.
2. Inversion:

   The file contains remaining travel-time residuals (the tenth column), which cannot be explained by the final 3D velocity model retrieved by the inversion. The observed travel-times after adjustments according to switches in *telinv2012input.inp* (Section 4.1.5) are in the eighth column. The theoretical travel-times to the zlayerdepth (Fig.4) of the model are in the ninth column.

4.2.4 telinv2012.out

This file is the most important output file. It is a log file with information about all the input parameters and input files, their basic statistics, messages from the important subroutines, and in case of inversion mode it contains the whole *combi_ output* file. The file contains possible warnings due to input data or parameters. Error messages appear only if the program crashes.

4.2.5 input_info_ray_distribution.plo

The file contains the numbers of rays per back-azimuth segments. The format of the file is self-explanatory. The file serves for plotting a rose diagram of back-azimuth distribution by auxililary GMT script *plot_ray_distribution.gmt* (Section 5.1.3).

4.2.6 input_info_station.plo

The file contains important station characteristics: station code, geographical and Cartesian coordinates, number of recorded events, additional corrections at individual stations, average crustal correction, average data error, average travel-time residual, average travel-time residual in each back-azimuth segment. A format of the file is self-explanatory. The file serves for plotting a map of stations with required parameters by auxiliary GMT script *plot_info_station.gmt* (Section 5.1.1).

4.2.7 input_info_ref_res.out

The file contains travel-time characteristics for each event in 8 columns. This file is a part of the analysis of travel-time residuals of near-by events. The file is printed only in the case when extended output is asked (***ioutext*** = 1).

1. index of the event
2. event residual mean - calculated as average from travel times of an event
3. standard deviation of relative residuals of an event

   Relative residuals are travel-time residuals from which event residual means are subtracted.
4. minimum relative residual of the event
5. maximum relative residual of the event
6. average back-azimuth of the event
7. average ray parameter of the event
8. number of travel times for the event

4.2.8 input_info_ref_res_bins.out

The file contains characteristics for each back-azimuth and ray-parameter segment in 10 columns. This file is a part of the analysis of travel-time residuals from near-by events (Section 2.3.2). The file is printed only in case when extended output is asked (***ioutext*** = 1).

1. index of the segment
2. lower limit of back-azimuth segment
3. upper limit of back-azimuth segment
4. lower limit of ray-parameter segment
5. upper limit of ray-parameter segment
6. average of event residual means within the segment

7. standard deviation of event residual means within the segment
8. minimum of event residual means in the segment
9. maximum of event residual means in the segment
10. number of events per segment

4.2.9 raypaths.out

This file contains the Cartesian coordinates of all ray paths. Each ray is introduced by a header with index, the number of points describing the ray path and back-azimuth of the ray. The coordinates of points along the ray path are in following lines:

1. index of point along ray path
2. x Cartesian coordinate of the ray path [km]
3. y Cartesian coordinate of the ray path [km]
4. z Cartesian coordinate of the ray path [km]

The file serves for plotting of ray paths by auxiliary GMT script *plot_rays_paths_2D_layers.gmt* (Section 5.1.4).

4.2.10 resol.out

This file contains diagonal elements of the resolution matrix (Section 2.6.5). The format of the file is similar to the format of input *velocity_model.inp* or *use_node.inp*. The file is created only if ***ioutext*** = 1.

4.2.11 reswidth.out

The file contains additional information about the resolution matrix, particularly about the resolution width (Section 2.6.5). The format of the file is similar to the format of input *velocity_model.inp* or *use_node.inp*. The file is created only if ***ioutext*** = 1.

4.2.12 velmod.out

The file contains initial velocity model and velocity models after each iteration. The file is created only if ***ioutext*** = 1.

4.2.13 variances_data.out

This file contains variances of travel-time residuals entering the iteration of the inversion. There are two types of variances. First one does not consider different data weighting (all ***weights*** = 1), while the second variance considers data weighting. The file is created only in the case of the inversion mode.

4.2.14 variances_model.out

This file contains variances of model adjustments after each iteration. The final velocity is the sum of initial velocity and velocity adjustments after each of the iterations: $v_{final} = v_0 + \triangle v_1 + \triangle v_2 + \cdots + \triangle v_N$, where N is the number of iterations.

There are two kinds of model adjustments - partial and total:

1. partial model adjustment relates to each individual iteration, e.g. $\triangle v_3$ in case of the 3^{rd} iteration
2. total model adjustment is sum of partial adjusments relative to the initial velocity model v_0, which is $\triangle v_1 + \triangle v_2 + \triangle v_3$ in case of the 3^{rd} iteration

In case of the first iteration, these adjustments are identical. In following iterations, the total adjustments are sums of the partial adjustments. The partial adjustment should decrease with the number of iterations. On the other hand, the total model adjustment usually increases with iterations. The file is created only in case of the inversion mode.

5 Auxiliary scripts

5.1 GMT scripts

5.1.1 plot_info_station.gmt

The script plots basic input information for each station based on the output file *input_info_station.plo* (Section 4.2.6).

5.1.2 plot_map_sta_nodes.gmt

The script plots a map with node and station distributions based on *station.inp* (Section 4.1.1) and the *velocity_model.inp* files (Section 4.1.2).

5.1.3 plot_ray_distribution.gmt

The script plots a rose diagram of back-azimuth distribution of rays. File *input_info_ray_distribution.plo* is the input.

5.1.4 plot_ray_paths_2D_layers.gmt

The scripts plots ray paths projected into depths defined by vertical parameterization of velocity model. File *raypaths.out* is the input.

5.1.5 plot_combi_output.gmt

The scripts plots final velocity perturbations or perturbations of preceding iterations, hit counts, DWS and diagonal elements of resolution matrix. File *combi_output* is the input.

5.1.6 plot_synthetic_model.gmt

The script plots synthetic velocity perturbations calculated from two velocity models - synthetic and initial (Section 3.2) - created by forward modelling. The velocity models - *velmod.out (Section 4.2.12)* and station file *input_info_station.plo* (Section 4.2.6) are inputs for the script.

5.1.7 plot_per_vertical.csh

The script plots vertical cross-sections through the final velocity perturbation model. The interpolation of the velocities is calculated by Fortran code *invel_inv_combi2012.f*. The *combi_output* is the input file.

5.2 Fortran scripts

5.2.1 create_TELINV_velocity_model.f

The script creates *velocity_model.inp* (Section 4.1.2).

5.2.2 create_use_node.f

The script creates *use_node.inp* (Section 4.1.4).

5.3 Matlab script

5.3.1 VelModelTools1.1.zip

Package of Matlab scripts created by Jan Chyba allows:

1. creating the input *velocity_model.inp* file with Cartesian parameterization and velocities according to IASP91 model
2. creating and plotting synthetic *velocity_model.inp* file with velocity anomalies relative to the IASP91 model
3. 2D plotting P-wave velocity dependence on a depth
4. 2D plotting different parameters, e.g., velocity perturbations, hit counts, etc., in horizontal slices
5. 3D plotting different parameters, e.g., velocity perturbations, hit counts, etc.

5.4 Shell scripts

5.4.1 make_synthetic_input.csh

This script creates a synthetic *travel_time.inp*. The inputs are *travel_time.inp*, and two *forward_sol.out* files with "observed" and theoretical travel times. See Section 3.2 for instructions on using these files.

6 Installation of TELINV2012

Download the *TELINV2012.tar.gz* package from http://www.ig.cas.cz/en/research-teaching/software-download, unpack it in working directory. The code itself with example input files is located in the directory TELINV2012_example. The Fortran codes can be found in sub-directory *src*. To run the code, one has to re-compile the code. There are two equivalent options:

1. Write "sh makefile" to the command line in the sub-directory src to compile the code, then write "sh run.sh" to the command line in the main directory (TELINV2012_example) to run the program.

   or

2. Write "sh compile.sh" in directory TELINV2012_example with all input files. This command compiles the code and runs the program at once.

To prepare input files and run the program, follow the instructions according to step-by-step guide (Section 3). The code was compiled with ifort Fortran compiler and succesfully run on MacOS 10.6.8 and on Linux SUSE Linux Enterprise Server 10 (x86_64).

Time demands depend strongly on total number of rays, inverted nodes and iterations. The inversion took about 7 hours in case of 13541 rays, 4024 inverted nodes and 2 iterations, while inversion is finished in about 1 hour in case of 5541 rays, 2400 inverted nodes and 2 iterations.

7 Additional notes

- **back-azimuth segment** - a pre-defined range of back-azimuths (Fig.2)
- **boundary nodes** - nodes at the shallowest (***zn(1)***), deepest (***zn(nz)***), most western (***xn(1)***), eastern (***xn(nx)***), northern (***yn(ny)***) and southern (***yn(1)***) parts of the model
- **cell** - a volume around a node limitted by planes at half-distances between neighbouring nodes

  If the node spacing is equidistant at all dimensions, nodes lie in the centers of the cells.
- **inverted node** - a node, where velocity perturbation is searched by an inversion of travel-time residuals
- **fixed node** - a node, where velocity is fixed to the initial velocity and does not change during an inversion
- **piercing point** - a point where a ray intersects a depth called ***zlayerdepth*** representing a bottom of the model (Fig.4)
- **ray parameter** - an invariant for a ray depending on ray path angle at a point and velocity at this point (Section 2.4)
- **event residual mean** - an average residual calculated from all travel-time residuals of the event
- **travel-time residual** - a difference between the observed (measured) and theoretical travel times
- **relative residual** - travel-time residual from which an event residual mean is subtracted

8 References

Ammon, J.A., Vidale, J.E., 1993. Tomography without rays. Bull. Seismol. Soc. Am., 83, 509-528.

Achauer, U., Greene, L., Evans, J.R., Iyer, H.M., 1986. Nature of the magma chamber underlying the Mono Craters area, eastern California, as determined from teleseismic travel time residuals. J. Geophys. Res., 91, 873-891.

Arlitt, R., Kissling, E., Ansorge, J., 1999. Three-dimensional crustal structure beneath the TOR array and effects on teleseismic wavefronts. Tectonophysics 314, 309–319.

Eken, T., Shomali, H., Roberts, R., Bodvarsson, R., 2007. Upper mantle structure of the Baltic Shield below the Swedish National Seismological Networks (SNSN) resolved by teleseismic tomography. Geophysical Journal International 169, 617–630.

Evans, J.R., Achauer, U., 1993. Teleseismic velocity tomography using the ACH method: theory and application to continental scale studies. In: Iyer, H.M., Hirahara, K. (Eds.), Seismic Tomography. Chapman and Hall, London, pp. 319–360.

Karousová, H., Plomerová, J., Babuška, V., 2012b. Seismic tomography of the upper mantle beneath the north-eastern Bohemian Massif (central Europe). Tectonophysics, 564–565, 1-11, doi:10.1016/j.tecto.2012.06.031.

Karousová, H., Plomerová, J., Babuška, V., 2013. Upper-mantle structure beneath the southern Bohemian Massif and its surroundings imaged by high-resolution tomography. Geoph. J. Int.; 1-13, doi: 10.1093/gji/ggt159.

Lippitsch, R., Kissling, E., Ansorge, J., 2003. Upper mantle structure beneath the Alpine orogen from high-resolution teleseismic tomography. Journal of Geophysical Research 108, 2376.

Menke, W., 1984. Geophysical Data Analysis: Discrete Inverse Theory. Academic Press, Inc., College of Oceanography, Oregon State University.

Michelini, A., McEvilly, T.V., 1991. Seismological studies at Parkfield, I, Simultaneous inversion for velocity structure and hypocenters using cubic B-splines parameterization. Bull. Seismol. Soc. Am., 81, 524-552.

Sandoval, S., Kislling, E., Ansorge, J., SVEKALAKO Seismic Tomography working Group, 2004. High-resolution body wave tomography beneath the SVEKALAPKO array — II. Anomalous upper mantle structure beneath the central Baltic Shield. Geophysical Journal International 157, 200–214.

Shomali, Z.H., Roberts, R.G., Pedersen, L.B., the TOR Working Group, 2006. Lithospheric structure of the Tornquist Zone resolved by nonlinear P and S teleseismic tomography along the TOR array. Tectonophysics 416, 133–149.

Steck, L.K., Prothero, W.A., 1991. A 3-D ray-tracer for teleseismic body-wave arrivaltimes. Bulletin of the Seismological Society of America 81, 1332–1339.

Weiland, C.M., Steck, L.K., Dawson, P.B., Korneev, V.A., 1995. Nonlinear teleseismic tomography at Long Valley caldera, using three-dimensional minimum travel time ray tracing. Journal of Geophysical Research 100, 20379–20390.